

POLITECNICO DI TORINO

Collegio di Ingegneria Chimica e dei Materiali

**Corso di Laurea Magistrale
in Ingegneria Chimica e dei Processi Sostenibili**

Tesi di Laurea Magistrale

**Optimization of the oxidative dehydrogenation of ethane to
ethylene over NiO-SnO₂ catalysts in an industrial-scale
packed-bed reactor**



**Politecnico
di Torino**

Relatori

Dr. Jeroen Poissonnier
Prof. Joris Thybaut
Prof. Stefania Specchia

Candidato

Lucas Iván Garbarino

Luglio 2021

[This page was intentionally left in blank]

Sommario

I. Introduzione

Nella società odierna, è risaputo che la domanda mondiale di energia è in costante aumento a causa della crescita della popolazione mondiale e del tenore di vita. Tuttavia, è anche vero che le fonti energetiche convenzionali hanno un'origine fossile e quindi sono limitate. Il crescente sfruttamento e consumo di idrocarburi sta generando effetti indesiderati nel nostro pianeta, come l'emissione costante di gas a effetto serra che deriva dal cambiamento climatico con i suoi effetti di conseguenza a breve e lungo termine [1]. In questo modo, è necessario sostituire gradualmente l'uso di idrocarburi con fonti di energia rinnovabili, non solo per la produzione di energia stessa, ma anche per la produzione chimica di materie prime.

Il settore petrolchimico sta attualmente sviluppando nuove tecnologie per aumentare il valore aggiunto dei componenti chiave del gas naturale (paraffine $C_1 - C_4$), trasformandoli in olefine. Questi ultimi hanno una particolare struttura chimica con uno o più doppi legami che li rendono chimicamente reattivi verso la produzione di molti composti di interesse commerciale come resine, fibre sintetiche, una vasta gamma di plastiche, ecc. Quando si tratta di olefine, l'etilene è senza dubbio uno dei composti più richiesti al mondo grazie alla sua versatilità alla produzione chimica di prodotti ad alto valore aggiunto.

Essendo il principale elemento costitutivo dell'industria petrolchimica, il consumo mondiale di etilene è in costante aumento. Attualmente, la produzione mondiale è di circa 1.5×10^8 tonnellate all'anno e si prevede che affronterà un tasso di crescita annuo compreso tra il 3,7 e il 4% [2], come mostrato in Figura 1.3.

Attualmente, la tecnologia dominante per la produzione di etilene è lo steam cracking. Il principio di funzionamento di questa tecnologia si basa sulla pirolisi degli idrocarburi più pesanti per produrre quelli più leggeri (olefine), al costo di una quantità significativa di energia [3]. Considerate il cuore di un impianto convenzionale di olefine, le fornaci di cracking sono responsabili della conversione delle materie prime in composti a più alto valore aggiunto. In questo modo, attraverso le fornaci vengono distribuiti diversi bruciatori per fornire calore sufficiente a indurre una serie di reazioni radicaliche in presenza di vapore. Ciò implica che si raggiungeranno temperature da 750°C a 1000°C e quindi la frazione di idrocarburi più pesanti viene di conseguenza convertita in quella contenente degli idrocarburi più leggeri. La corrente risultante è una miscela di una vasta gamma di prodotti ad alto valore aggiunto, uno dei quali etilene. A valle delle fornaci di cracking, si svolgono una serie di complesse fasi di separazione per purificare i prodotti desiderati. Sebbene si tratti di un processo ben consolidato per la produzione di etilene, la formazione di coke, la bassa selettività e l'eccessivo consumo di energia, sono solo alcuni degli svantaggi che hanno prevalso nonostante i miglioramenti dell'efficienza. Questo scenario sta quindi incentivando una costante ricerca di alternative più sostenibili.

La fattibilità di processi alternativi per la produzione di etilene sono strettamente legati alla disponibilità di materie prime a basso costo, e la loro competitività rispetto ai processi convenzionali dipende da questo aspetto. Ad esempio, negli Stati Uniti la materia prima per la produzione di etilene, i.e. il greggio, sta diventando sempre più scarsa poiché le frazioni più leggere adatte alla produzione di nafta si stanno esaurendo. Perciò, dovrebbero invece essere usati degli idrocarburi più pesanti; lo svantaggio è che comporterebbe, inevitabilmente, costi

più elevati [4]. Fortunatamente, negli Stati Uniti, il gas naturale proveniente da giacimenti non convenzionali ha standardizzato i prezzi, creando un vantaggio competitivo e una soluzione per evitare l'uso di oli più pesanti come materia prima per la produzione di etilene.

In questo scenario promettente, la deidrogenazione ossidativa dell'etano è diventata sempre più interessante all'interno della comunità scientifica, data una serie di vantaggi che questa tecnologia presenta rispetto ad altre alternative. Le basse temperature di lavoro, il numero limitato di prodotti indesiderati e l'accesso a materie prime a basso costo, sono solo alcuni punti importanti per considerare questa tecnologia come una potenziale alternativa per la produzione industriale di etilene.

I.a. Obiettivi della tesi

Questo documento ha lo scopo di studiare la deidrogenazione ossidativa dell'etano (DIO-C₂) in un reattore catalitico multi-tubolare a letto fisso, al fine di determinare le condizioni operative ottimali per la produzione di etilene. A tal fine, viene utilizzato un catalizzatore a base di nichel (NiO-SnO₂) per dimostrare le sue prestazioni e quindi considerarlo un potenziale candidato per la produzione industriale di etilene.

Il lavoro presentato in questo documento può essere suddiviso in due sezioni principali. Nella prima sezione, un'analisi a livello di reattore comporta un'ottimizzazione multi-obiettivo in cui vengono testati dei parametri operativi importanti. A questo proposito, un modello di reattore pseudo-eterogeneo viene risolto numericamente al fine di ottenere una descrizione bidimensionale dettagliata delle prestazioni del reattore in termini di selettività dell'etilene e conversione finale dei reagenti. In questo modo, i profili di concentrazione e temperatura lungo il reattore a letto fisso vengono generati sia sulla coordinata radiale che assiale in un singolo tubo del reattore. A causa della complessità matematica coinvolta nel modello pseudo-eterogeneo, un'ottimizzazione multi-parametrica sarebbe notevolmente costosa dal punto di vista computazionale. Pertanto, un modello più semplice è proposto attraverso un disegno sperimentale (DoE), in cui un insieme di equazioni multi-parametriche algebriche sono sviluppate secondo la metodologia della superficie di risposta (RSM). Le equazioni di governo sono progettate e verificate dal punto di vista statistico tramite i test ANOVA, dove la significatività statistica di ogni parametro è valutata tramite i *t* test. Una volta verificato il modello, l'obiettivo è quello di utilizzarlo per studiare l'intero spettro delle variabili indipendenti e delle sue rispettive interazioni; quindi, identificando delle configurazioni promettenti per massimizzare le prestazioni del reattore.

La seconda sezione del presente documento prevede l'implementazione del modello in un simulatore commerciale (i.e. ASPEN Plus[®]) allo scopo di stabilire uno schema di modellazione completo del caso di studio. A questo scopo, il reattore catalitico è modellato all'interno del software di simulazione tramite un blocco predefinito dall'utente (USER2). In questo senso, è possibile incorporare dei processi aggiuntivi a valle del reattore catalitico, sia per migliorare l'integrazione energetica, sia per modellare ulteriori processi fondamentali per produrre etilene di grado polimerico (i.e. assorbimento di CO₂ con soluzione di ammine e distillazione criogenica). Il sistema risultante è ulteriormente ottimizzato all'interno dell'ambiente di simulazione per raggiungere gli standard commerciali del prodotto di interesse, riducendo al minimo sia le perdite di prodotto che i requisiti energetici.

Infine, il processo complessivo viene confrontato con la tecnologia convenzionale attualmente utilizzata per la produzione mondiale di etilene. A questo proposito vengono presi in considerazione importanti parametri di sostenibilità, i.e. il consumo energetico e le emissioni

di CO₂, al fine di valutare la fattibilità di una graduale innovazione tecnologica all'interno del settore petrolchimico.

II. Deidrogenazione ossidativa dell'etano (DIO-C₂)

Con l'obiettivo di migliorare la sostenibilità dell'industria di olefine, la deidrogenazione ossidativa dell'etano è stata riconosciuta come un'interessante via alternativa per la produzione di etilene. DIO-C₂ è semplicemente una combinazione di deidrogenazione dell'etano accoppiata alla combustione dell'idrogeno dove viene prodotta dell'acqua [5]. Questa sequenza di reazioni è rappresentata nella Tabella 2.1.

Anche se la deidrogenazione dell'etano è endotermica, la combustione dell'idrogeno è molto più esotermica; pertanto, il meccanismo di reazione complessivo risulta altamente esotermico. Inoltre la combustione dell'idrogeno migliora lo spostamento dell'equilibrio verso la produzione di etilene [6]. Sfortunatamente, la DIO-C₂ presenta anche una serie di reazioni collaterali in cui avviene l'ossidazione parziale o totale della frazione di idrocarburi. Le reazioni indesiderate sono presentate nella Tabella 2.2. È importante sottolineare che ogni prodotto collaterale (CO e CO₂) deriva da una reazione di combustione altamente esotermica. Di conseguenza, il controllo della stabilità termica in un reattore, su scala industriale, rappresenta una delle principali sfide di questo processo. Gli ossidi di carbonio (CO_x) sono termodinamicamente più stabili delle olefine, quindi il catalizzatore deve essere abbastanza sensibile da fermare l'ossidazione prima che vada verso l'ossidazione totale [6].

Nonostante ciò, la DIO-C₂ presenta numerosi vantaggi per quanto riguarda lo steam cracking:

- Meccanismo di reazione altamente esotermico;
- minimizzazione della formazione di prodotti collaterali;
- processo catalitico;
- fasi di purificazione più semplici dell'effluente a valle del reattore catalitico;
- assenza di formazione di coke.

Al fine di massimizzare questi vantaggi su scala industriale, la scelta di un catalizzatore adeguato è di fondamentale importanza.

II.a. Ossidi di nichel a base di stagno (NiO-SnO₂)

Il catalizzatore a base di vanadio è stata una delle configurazioni più promettenti nella DIO-C₂. Tuttavia, la sua sintesi ha presentato dei problemi di riproducibilità e una considerevole richiesta energetica, direttamente collegata al costo finale di produzione. Inoltre, ulteriori prodotti indesiderati, i.e. CO, sono presenti nel meccanismo di reazione, quindi la complessità della sua eventuale applicazione su scala industriale viene aumentata [7]. Queste osservazioni sono state le motivazioni principali per lo sviluppo di catalizzatori alternativi.

A questo proposito, gli ossidi di nichel hanno mostrato un vantaggio promettente quando vengono inseriti degli etero atomi nella struttura dell'ossido, come Nb o Sn. In questo lavoro, la DIO-C₂ viene studiata su scala industriale utilizzando NiO-SnO₂ come catalizzatore. È stato dimostrato che questa configurazione è facile da sintetizzare, con elevata riproducibilità e sufficientemente efficace a temperature relativamente basse (< 480°C). Inoltre, sono state osservate solo tracce di CO [8].

II.b. Cinetica

Uno dei passaggi più importanti nello sviluppo di un processo chimico, specialmente quelli che coinvolgono la catalisi, è la formulazione del modello cinetico. Avere una conoscenza dettagliata della cinetica di processo è un fattore chiave per la progettazione e la classificazione dei reattori chimici su scala industriale. Un modello cinetico richiede espressioni matematiche in grado di riprodurre, con una certa accuratezza, le osservazioni sperimentali.

Lo sviluppo di un modello cinetico per la DIO-C₂ sul catalizzatore NiO-SnO₂ è un passo principale per studiare il processo su scala industriale [9]. Il primo passo per costruire un modello cinetico è quello di definire uno schema di reazione basato su osservazioni a scala di laboratorio. A tal proposito, si tratta di tre reazioni: (i) ossidazione parziale dell'etano in etilene, (ii) ossidazione totale dell'etano in anidride carbonica e (iii) ossidazione totale dell'etilene in anidride carbonica.

II.b.a. Formalismo Eley-Rideal (ER)

Il principio di questo formalismo consiste nell'adsorbimento di una singola molecola sulla superficie del catalizzatore mentre un'altra reagisce direttamente in fase gassosa senza essere adsorbita [8, 10]. Questo modello è stato costruito utilizzando le seguenti ipotesi: (i) c'è solo un tipo di sito attivo sulla superficie del catalizzatore; (ii) l'ossigeno e l'acqua sono adsorbiti esclusivamente nei siti attivi; (iii) si considera l'approccio allo stato stazionario; (iv) le reazioni superficiali sono le fasi determinanti nella velocità di reazione; (v) le reazioni superficiali sono irreversibili. Queste reazioni coinvolgono ossigeno adsorbito ed etano o etilene presenti nella fase gassosa. Il meccanismo di reazione del modello è stato presentato nella Tabella 2.4

II.c. Modello di reattore

Una progettazione concettuale di una configurazione di reattore adatta per condurre la DIO-C₂ è un passo cruciale per proseguire la sua applicazione a livello industriale. Poiché il processo è esotermico, un reattore multi-tubolare con camicia di raffreddamento è una configurazione adeguata quando si tratta di migliorare l'efficienza di rimozione del calore [11]. Una corretta gestione del calore generato è di fondamentale importanza per massimizzare la resa del prodotto ed evitare la disattivazione permanente del catalizzatore [12, 13].

Durante la progettazione di un reattore a letto fisso, le prestazioni del reattore sono generalmente previste sulla base della modellazione di un singolo tubo; si presume pertanto che ogni tubo si comporti in modo simile in termini di concentrazione e profili di temperatura, perdita di carico, ecc. [14, 15].

Detto questo, lo studio della DIO-C₂ in questo lavoro è stato fatto seguendo un approccio rigoroso presentato in lavori precedenti [10, 16]. Questa metodologia consente di simulare il comportamento non adiabatico/non isoterma di un reattore a letto fisso che approssima più accuratamente le condizioni reali. Il trasferimento di calore all'interno del reattore è effettuato tramite una stima di parametri di trasporto effettivi, i.e. conducibilità termica effettiva (k_{eff}) e coefficiente di trasferimento del calore alle pareti (h_w). Questi parametri descrivono il trasferimento di calore dal *bulk* del letto fisso e i fenomeni di trasporto di calore nell'interfaccia tra il catalizzatore e le pareti della tubazione. Per calcolare questi parametri è stata utilizzata una serie di correlazioni ingegneristiche affidabili (vedere Appendice B).

L'idrodinamica in un reattore a letto fisso su scala industriale viene intrapresa risolvendo l'equazione di Navier-Stokes, compresi i termini aggiuntivi proposti da Darcy e Forchheimer

(NSDF) [17, 18]. Quest'ultima equazione è semplificata considerando la componente della velocità assiale (v_z) in funzione della coordinata assiale e radiale, mentre la componente di velocità radiale (v_r) viene trascurata. L'idrodinamica è quindi descritta dall'equazione di continuità e dalla NSDF semplificata nella sua forma bidimensionale; rispettivamente, rappresentate dalle equazioni (2.11-12) [19]. Le condizioni iniziali e al contorno sono rappresentate dalle equazioni (2.13-17).

Sebbene per semplicità sia comune assumere una frazione di vuoto (ε_b) costante sulla coordinata radiale del letto fisso, per un rapporto tra il diametro della particella e il diametro della tubazione inferiore a 11, l'effetto alle pareti inizia ad essere non trascurabile [20]. Pertanto, un'espressione matematica per descrivere radialmente il profilo di ε_b è richiesta quando $d_t/d_p < 11$. In questo lavoro il profilo è costruito utilizzando il modello empirico sviluppato da de Klerk [21].

Una descrizione matematica del modello pseudo-eterogeneo prevede profili di concentrazione e temperatura basati sul principio della conservazione di massa ed energia, compresi coefficienti di trasporto effettivi. A questo scopo, le espressioni di governo sia in fase gassosa che solida sono rappresentate dalle equazioni (2.20-23) [10, 15, 19]. Le loro corrispondenti condizioni iniziali e al contorno, sono rappresentate dalle equazioni (2.24-30) [10].

II.c.a. Subroutine di Fortran

Lo sviluppo di un modello pseudo-eterogeneo è in grado di descrivere con precisione la fluidodinamica e i fenomeni di trasporto coinvolti in un singolo tubo riempito dalle particelle catalitiche. Inoltre, a questo modello non reattivo, viene aggiunto un meccanismo cinetico per progettare completamente una descrizione matematica per la DIO-C₂ utilizzando il catalizzatore NiO-SnO₂.

Le equazioni di governo del modello sono state codificate in una subroutine scritta nel linguaggio di programmazione Fortran[®]. Poiché è stato proposto un modello bidimensionale, il codice è in grado di stimare i profili di temperatura e concentrazione lungo le coordinate radiali e assiali, che risulta essere l'output del codice.

Il risolutore è stato condensato in un file .exe per facilitare l'inserimento di diverse impostazioni per ogni simulazione. In questo senso, dei file .txt ausiliari vengono utilizzati per stabilire varie configurazioni parametriche in diverse condizioni operative (ad esempio composizione dell'ingresso, diametro delle particelle del catalizzatore, flusso di massa, temperatura operativa e pressione, ecc.). Questo strumento è stato la principale fonte di acquisizione dei dati utilizzata in questo lavoro allo scopo di eseguire un'ottimizzazione multi-obiettivo a livello di reattore.

III. Progettazione di modelli multi-parametrici

La complessità matematica di un modello pseudo-eterogeneo bidimensionale garantisce un'elevata precisione, ad un costo computazionale molto elevato. Tuttavia, ai fini di una simulazione su scala industriale, in cui sono inclusi diversi processi anche a valle del reattore catalitico, potrebbe essere implementato un modello più semplice che comporti un abbassamento del costo computazionale che resti in grado di produrre risultati affidabili con la massima precisione possibile rispetto al modello complesso. In altre parole, la sensibilità verso diverse configurazioni parametriche dovrebbe essere statisticamente equivalente in entrambi i modelli, osservando lo stesso effetto da cui all'interno del dominio vengono imposte condizioni identiche.

III.a. Metodologia della superficie di risposta

La funzione principale della RSM è sviluppare un insieme di equazioni del modello di regressione tra variabili indipendenti (fattori) e un insieme di variabili dipendenti predefinite (risposte). La significatività statistica e l'accuratezza del modello sono verificate attraverso un'analisi della varianza (ANOVA). Grazie alla sua semplicità e alla sua vasta gamma di applicazioni, viene utilizzato un modello polinomiale di second'ordine che include termini lineari delle variabili indipendenti, così come tutti i termini quadratici e termini di interazioni [22]. Pertanto, un'espressione multi-parametrica di secondo ordine è rappresentata dall'equazione (1),

$$y = \beta_0 + \sum_{i=1}^j \beta_i F_i + \sum_{i,k=1}^j \beta_{ik} F_i F_k + \sum_{i=1}^j \beta_{ii} F_i^2 + \dots + \epsilon \quad (1)$$

dove β_0 , β_i , β_{ik} e β_{ii} sono dei coefficienti polinomiali calcolati con il metodo dei minimi quadrati [23].

Lo studio RSM è stato applicato alla fine di trovare la configurazione ottimale per la DIO-C₂. Il primo passo è stato quello di selezionare con precisione l'insieme dei fattori che descrivono il processo chimico e le risposte più importanti. Queste risposte includono le variabili da massimizzare, cioè la selettività dell'etilene e la conversione dell'etano e dell'ossigeno; oltre alla ricostruzione del profilo di temperatura sia nella fase gassosa che nella fase solida. L'intervallo dei fattori e delle risposte utilizzati in questo lavoro è riassunto nelle Tabella 1 e Tabella 2. Il software commerciale JMP 15[®] è stato utilizzato per l'analisi RSM, l'analisi statistica della regressione e l'ottimizzazione del processo a livello di reattore.

Tabella 1 – Fattori e risposte per lo sviluppo delle equazioni multi-parametriche in grado di descrivere la DIO-C₂ in un reattore a letto fisso su scala industriale.

Fattori		Unità	Range	
Descrizione	Nomenclatura			
Frazione molare di etano all'ingresso	Y _{C₂H₆}	[%]	2	8
Frazione molare di ossigeno all'ingresso	Y _{O₂}	[%]	8	14
Temperatura del bagno	T _{bath}	[°C]	380	480
Rapporto tra il diametro della tubazione e delle particelle catalitiche	d _t /d _p	[-]	3	9
Flusso di massa	MF	[kg m ⁻² hr ⁻¹]	5×10 ³	15×10 ³

Tabella 2 - Risposte per lo sviluppo delle equazioni multi-parametriche in grado di descrivere la DIO-C₂ in un reattore a letto fisso su scala industriale.

Risposte		Unità	Range	
Descrizione	Nomenclatura			
Conversione molare di etano	$X_{C_2H_6}$	[%]	0	100
Conversione molare di ossigeno	X_{O_2}	[%]	0	100
Selettività dell'etilene	$S_{C_2H_4}$	[%]	0	100
Temperatura della fase gassosa	T_g	[°C]	200	650
Temperatura della fase solida	T_s	[°C]	200	650

Per quanto riguarda il dominio per ciascun fattore, la loro selezione è stata effettuata sulla base di considerazioni pratiche. La miscela di gas di ingresso è composta principalmente da azoto molecolare (N₂) che fornisce un'atmosfera inerte. I valori del rapporto C₂H₆/O₂ sono stati rigorosamente selezionati per evitare la regione esplosiva dell'alimentazione [24]. In questo modo, $Y_{C_2H_6}$, Y_{O_2} e T_{bath} sono stati considerati nello studio del meccanismo cinetico. Per quanto riguarda i restanti fattori (d_i/d_p e MF), la loro rilevanza nella massimizzazione delle prestazioni del reattore è stata dimostrata in base a quello riportato in letteratura [10, 15, 19]. Ulteriore informazione sulle dimensioni e le condizioni di funzionamento del reattore catalitico, sono state riassunte nella Tabella 3.3.

Utilizzando questa configurazione, 44 simulazioni sono richieste da JMP 15[®] al fine di ottenere dati sufficienti per eseguire lo studio. L'elenco completo delle simulazioni è riportato nell'Appendice C (si noti come vengano anche aggiunti i risultati del modello pseudo-eterogeneo sotto le condizioni predefinite).

I profili di concentrazione e temperatura calcolati utilizzando il modello complesso sono propriamente manipolati per ottenere dei dati utili per la costruzione del modello. Mentre il profilo di temperatura di entrambe le fasi è determinato direttamente dal modello pseudo-eterogeneo, la concentrazione di ciascuna specie (in kmol m⁻³) deve essere manipolata per determinare conversione di etano e di ossigeno come mostrato dall'equazione (2),

$$X_n = \frac{F_n^{in} - F_n^{out}}{F_n^{in}} \times 100 \rightarrow n = C_2H_6, O_2 \quad (2)$$

dove ci sono rappresentati, rispettivamente, la portata molare di ingresso (F_n^{in}) e uscita (F_n^{out}) del componente n una volta raggiunte le condizioni di stato stazionario.

La selettività dell'etilene è calcolata come indicato dall'equazione (3),

$$S_{C_2H_4} = \frac{F_{C_2H_4}^{out}}{F_{C_2H_6}^{in} - F_{C_2H_6}^{out}} \times 100 \quad (3)$$

Lo studio è stato effettuato considerando un totale di 25 punti assiali per un singolo tubo del reattore in una posizione radiale adimensionale fissa ($r_{dss} = 0,5$). Questi punti sono stati presi strategicamente considerando le zone critiche lungo il reattore in cui è più probabile che vengano prodotti degli hot spots e quindi le zone in cui il modello può deviare considerevolmente dalle normali condizioni operative [25, 26]. La Figura 3.4 illustra le coordinate assiali scelte.

III.b. Convalida del modello

L'analisi statistica inizia con una valutazione della significatività statistica dei parametri del primo ordine e dei rispettivi parametri di secondo ordine (cioè termini quadratici e di interazione). L'obiettivo di questo passaggio è quello di rimuovere gli elementi meno significativi dalle equazioni del modello e fornire informazione utile su quali parametri hanno un effetto più rilevante verso l'obiettivo di ogni risposta.

Dopo questa procedura, il passo successivo consiste nel generare i coefficienti di regressione utilizzando il metodo dei minimi quadrati. Dopodiché dei t test vengono eseguiti per valutarne la significatività statistica del valore calcolato per ciascun coefficiente del modello, ad un livello di confidenza del 95%.

Al fine di quantificare l'adattamento tra i valori previsti e osservati, il coefficiente di determinazione (R^2) viene calcolato e confrontato con la sua forma più rigorosa per i sistemi multi-variabile (R^2 adj.). Il grado di significatività globale di ogni modello di regressione è quantificato attraverso l' F -value, dove un valore di 4.05 è considerato come la soglia minima per un'adeguatezza accettabile dal punto di vista statistico.

A causa della diversa natura delle risposte considerate in questo lavoro, è necessario un approccio diverso per la stima della composizione del prodotto a valle del reattore rispetto al profilo di temperatura della fase solida. Mentre nella conversione dei reagenti e della selettività dell'etilene è rilevante solo l'ultima coordinata assiale ($L_{re} = 2.6$ m), la temperatura della fase solida deve essere monitorata in ogni punto assiale per verificare la stabilità termica.

Detto questo, le Tabelle 3.5-8 riassumono i risultati dei test ANOVA per ogni equazione del modello. Tutte le equazioni del modello hanno raggiunto un'elevata precisione nel prevedere i dati generati dal codice Fortran, essendo notevolmente preciso nella stima del profilo di temperatura di entrambe le fasi. Questa osservazione potrebbe essere collegata al fatto che, a $L_{re} = 2,6$ m, c'è un'attività molto meno intensa all'interno del reattore rispetto a coordinate assiali inferiori [10, 15, 16]. Pertanto, la temperatura finale della fase gassosa dipenderà principalmente dalla temperatura del bagno, essendo molto meno influenzata dai fattori rimanenti. Ulteriore informazione riguardo allo studio ANOVA si trova nelle Tabelle D.1-4 messe in Appendice D.

Le espressioni matematiche che governano il modello in condizioni di uscita del reattore sono rappresentate dall'equazione (4) per la conversione dell'etano ($X_{C_2H_6}$), l'equazione (5) per la conversione dell'ossigeno (X_{O_2}), l'equazione (6) per la selettività dell'etilene ($S_{C_2H_4}$) e l'equazione (7) per la temperatura della fase gassosa (T_g). La denominazione del fattore normalizzato (F_i) corrisponde, in ordine alfabetico, a $Y_{C_2H_6}$, Y_{O_2} , T_{bath} , d_i/d_p e MF .

$$X_{C_2H_6} = 72.99 + 20.38 F_a - 10.11 F_b - 8.77 F_c + 4.30 F_d - 6.23 F_a^2 - 12.10 F_e^2 - \dots \\ \dots - 4.54 F_a F_b + 4.37 F_a F_c + 2.58 F_a F_d + 3.08 F_b F_c + 2.92 F_b F_d \quad (4)$$

$$X_{O_2} = 65.99 + 23.97 F_a + 19.31 F_b - 8.28 F_c - 6.52 F_d - 14.37 F_e^2 + 6.50 F_a F_b \quad (5)$$

$$S_{C_2H_4} = 51.16 - 12.93 F_a + 4.48 F_b + 4.07 F_c - 1.65 F_d + 3.81 F_a F_b + 2.35 F_a F_c - \dots \\ \dots - 1.40 F_a F_d - 2.85 F_b F_c \quad (6)$$

$$T_g = 431.62 + 50.76 F_a + 0.55 F_c + 0.61 F_d + 2.86 F_a^2 - 0.93 F_a F_b + 0.79 F_a F_c + \dots \\ \dots + 0.46 F_a F_d + 0.50 F_c F_d \quad (7)$$

Per quanto riguarda la temperatura della fase solida, poiché tutti i punti assiali sono ugualmente importanti per lo studio della stabilità termica, viene adottato un approccio diverso. Il profilo di temperatura fornito dal codice Fortran è stato confrontato con il profilo fornito dal modello al fine di trovare possibili incongruenze e quantificare l'errore locale. Le equazioni di governo di quest'ultimo sono in totale 25, i.e. un'equazione multi-parametrica per la stima del valore di temperatura locale in ciascun punto assiale della discretizzazione. Il modello ha dimostrato un'elevata accuratezza nel descrivere il profilo di temperatura nella fase solida lungo la discretizzazione assiale. L' F -value è stato stimato ad ogni coordinata assiale, osservando un range di valori di almeno due ordini di grandezza più elevati rispetto al valore minimo, i.e. 4.05, in tutti i casi.

In particolare, le osservazioni hanno dimostrato che gli hot spots, se presenti, sono sempre localizzati nel primo 30% della lunghezza totale del reattore, il che è congruente ai risultati trovati in letteratura [15, 19].

IV. Ottimizzazione a livello di reattore

Una volta che il modello di regressione è stato costruito e verificato dal punto di vista statistico, il passo successivo consiste nell'eseguire un'ottimizzazione multi-obiettivo per massimizzare le prestazioni del reattore. L'obiettivo principale è massimizzare la selettività dell'etilene sotto la massima conversione possibile di etano e ossigeno.

Inoltre, deve essere concessa una verifica delle condizioni di stabilità termica all'interno del letto catalitico. A tal fine, ogni combinazione efficace di fattori non deve causare la formazione di hot spots. Per hot spot, si intende un surriscaldamento di almeno 15 °C rispetto a T_{bath} in almeno un punto del letto fisso. Anche se l'hot spot non è considerato critico, cioè la temperatura finale non supera i 500 °C in grado di causare la disattivazione del catalizzatore, può comunque causare le instabilità termiche all'interno del reattore [26, 27]. Una disposizione multi-parametrica accettabile dovrebbe quindi soddisfare le condizioni rappresentate dall'equazione (8).

$$X_{C_2H_6} \rightarrow \max \cup X_{O_2} \rightarrow \max \cup S_{C_2H_4} \rightarrow \max \cup T_s, T_g \rightarrow T_{bath} \forall Dom(L_{re}) \quad (8)$$

IV.a. Effetti sulla conversione dell'etano

È stato osservato che la conversione dell'etano è altamente influenzata da T_{bath} , dove le alte temperature di esercizio migliorano la conversione di questo reagente. Al contrario, valori più elevati, sia di $Y_{C_2H_6}$ che di MF , indurranno un abbassamento nella conversione dell'etano; ciò è previsto poiché ci sarebbe, rispettivamente, un eccesso di etano e un tempo di residenza più breve all'interno del reattore pur mantenendo costanti gli altri fattori (vedere Figura 4.1).

Come suggerito dall'equazione (4), gli effetti di interazione sono importanti per prevedere la conversione dell'etano. Pertanto, nella Figura 4.2 viene mostrata una serie di grafici di superficie in cui questi effetti sono visualizzati. Per semplicità, i restanti fattori che non sono contabilizzati sono stati mantenuti ai rispettivi valori a livello zero; cioè $T_{bath} = 430^\circ\text{C}$, $d_v/d_p = 6$, $MF = 1 \times 10^4 \text{ kg m}^{-2} \text{ hr}^{-1}$, $Y_{O_2} = 11\%$ e $Y_{C_2H_6} = 5\%$.

I risultati indicano che i valori di $X_{C_2H_6}$ sono compresi tra il 15 e il 100%, sempre all'interno del dominio scelto. Il modello prevede che valori elevati della risposta siano osservati a (i) diametro delle particelle intermedie ($d_v/d_p \approx 6$); (ii) frazione molare minima di etano ($Y_{C_2H_6} \approx 2\%$) ad alta frazione molare di ossigeno nell'alimentazione ($Y_{O_2} > 13\%$); (iii) elevata temperatura di operazione ($T_{bath} = 480^\circ\text{C}$); e (iv) tempi di residenza lunghi ($MF = 5 \times 10^3 \text{ kg m}^{-2} \text{ hr}^{-1}$). Una configurazione dei fattori opposta rispetto a quella riportata diminuirà, di conseguenza, la reattività dell'etano fino a raggiungere circa un 15% di conversione.

IV.b. Effetti sulla conversione dell'ossigeno

L'influenza dei diversi fattori in questa risposta ha mostrato alcuni aspetti in comune per quanto riguarda la conversione dell'etano. Ciò è totalmente prevedibile a causa della loro similitudini come variabili indipendenti. In realtà, solo $Y_{C_2H_6}$ e Y_{O_2} hanno mostrato un comportamento opposto verso la conversione dell'ossigeno, come si può osservare nella Figura 4.1.

Un approccio simile rispetto alla risposta precedente indica che X_{O_2} può assumere valori compresi tra il 3% al 100%. Il modello indica che valori elevati di X_{O_2} possano essere ottenuti nelle configurazioni che prevedono (i) diametri intermedi di particelle ($d_v/d_p \approx 6$); (ii) alta frazione molare di etano ($Y_{C_2H_6} > 3\%$) a bassa frazione molare di ossigeno ($Y_{O_2} < 13\%$) nell'alimentazione; (iii) alta temperatura ($T_{bath} > 390^\circ\text{C}$); e (iv) tempi di residenza lunghi ($MF < 14.5 \times 10^3 \text{ kg m}^{-2} \text{ hr}^{-1}$).

IV.c. Effetti sulla selettività dell'etilene

Fino a questo momento, è stato dimostrato che le due specie reattive sono influenzate in modo praticamente analogo dai fattori, che potrebbero potenzialmente definire le condizioni operative del reattore. Tuttavia, la Figura 4.1 indica che la selettività dell'etilene è inversamente influenzata da alcuni fattori; ciò è indicato anche dal segno di ciascun coefficiente nell'equazione multi-parametrica che modella la risposta (e.g. -12.33 e 20.38 sono, rispettivamente, coefficienti di regressione per T_{bath} nel modello per $S_{C_2H_4}$ e $X_{C_2H_6}$). Il diametro delle particelle influenzerà anche in modo diverso la selettività verso l'etilene, anche se il suo effetto è meno intenso e meno significativo rispetto ai casi precedenti.

Detto ciò, Figura 4.4 illustra che i valori di selettività dell'etilene sono compresi tra il 13% ad un massimo del 66%. Inoltre, il modello indica che le reazioni di sovraossidazione sono ridotte al minimo durante il funzionamento del reattore a (i) bassa d_v/d_p ; (ii) alta concentrazione di etano nell'alimentazione, preferenzialmente in atmosfera a basso contenuto di ossigeno

($Y_{C_2H_6} \approx 8\%$ e $Y_{O_2} < 9\%$); (iii) bassa temperatura del bagno termico ($T_{bath} < 390^\circ C$) e (iv) basso tempo di residenza ($MF > 13 \times 10^3 \text{ kg m}^{-2} \text{ hr}^{-1}$).

IV.d. Effetti sul profilo di temperatura

I risultati finora analizzati hanno permesso di elaborare conclusioni basate su una serie di equazioni multi-parametriche in grado di descrivere la composizione finale dell'effluente del reattore catalitico. Tuttavia, una corretta descrizione dei profili di temperatura sia in fase gassosa che solida richiede stime dei valori intermedi all'interno del letto catalitico. A questo punto, Figura 4.1 indica che T_{bath} è l'unico fattore che ha un'influenza rilevante sulla temperatura del gas e della fase solida a $L_{re} = 2,6 \text{ m}$, condizione che differisce nel primo 30% della lunghezza complessiva del reattore, come mostrato in Figura 4.5.

Il calore che deve essere dissipato dal reattore dipenderà dalle velocità di reazione. Nel primo 30% della lunghezza del letto, la concentrazione dei reagenti è massima e quindi la velocità di reazione sarà più elevata rispetto alle coordinate assiali più a valle. L'effetto diretto di ciò è un tasso di generazione di calore più elevato e, quindi, è necessario un tasso di dissipazione del calore più efficace per evitare la produzione di hot spots. Tuttavia, poiché i reagenti vengano gradualmente consumati lungo il reattore, la differenza tra questi due parametri diventerà sempre meno pronunciata con la coordinata assiale fino a raggiungere il punto in cui il calore generato viene dissipato alla stessa velocità. Questo fenomeno spiega l'assenza di formazione di hot spots a $L_{re} > 0,75 \text{ m}$. Per quanto riguarda $Y_{C_2H_6}$ e Y_{O_2} , valori più elevati portano ad un'attività più intensa all'interno del reattore, causando una notevole differenza tra T_{bath} e la temperatura di entrambe le fasi, i.e. T_g e T_s .

L'influenza dei diversi parametri nella stabilità termica del letto catalitico è implicitamente presa in considerazione dal modello multi-parametrico. Figura 4.6 illustra come la significatività statistica dei principali fattori si evolve lungo la coordinata assiale.

IV.e. Effetto combinato

A causa della natura multi-fattoriale del caso di studio, diventa sfidante trovare una configurazione di reattore unica in cui tutti i risultati desiderati siano raggiunti contemporaneamente. Invece, generalmente bisogna stabilire un compromesso tra le variabili ad ottimizzare per ottenere un punto ottimale dal punto di vista pratico. In particolare, in questo studio è necessario un compromesso tra selettività verso i prodotti desiderati e conversione delle materie prime. Come spiegato nella Sezione 4.1.3, una combinazione fattoriale che indurrà un'elevata conversione di etano e ossigeno sposterà anche il meccanismo di reazione verso la formazione di CO_2 .

Al fine di limitare il dominio e ridurre la variabilità, alcune condizioni al contorno sono imposte in base alla loro influenza relativa, non solo a livello di reattore, ma anche tenendo conto dei processi a valle del reattore. A questo proposito, alcuni criteri sono predefiniti:

- Il criterio di selettività è previsto come $S_{C_2H_4} > 62,1\%$. Secondo la definizione data nell'equazione (3.7), in quest'ultima condizione il rapporto di resa massica del prodotto (kg di CO_2 per kg di etilene prodotto) rimane al di sotto dell'unità;
- si preferisce un basso tempo di residenza dei reagenti all'interno del reattore;

- analogamente, $Y_{C_2H_6}$ dovrebbe essere preferenzialmente pari all'8% per garantire una produttività accettabile e ridurre al minimo i costi di separazione a valle del reattore, vale a dire il costo associato alla separazione della frazione inerte della miscela di gas;
- i restanti fattori, i.e. d_t/d_p , Y_{O_2} e T_{bath} non hanno un criterio specifico di selezione oltre al raggiungimento delle condizioni sopra riportate e alla stabilità termica.

Date queste condizioni, Figura 4.8 illustra una serie di grafici in cui viene evidenziata una regione operativa ottimale. Si vuole far notare che è stata preselezionata una configurazione specifica per la simulazione di processo in ASPEN Plus. Questa disposizione, tuttavia, può essere modificata in base alla performance complessiva del processo, vale a dire includendo le fasi di separazione a valle del reattore, dove viene condotta un'ulteriore analisi per stimare il consumo energetico e le emissioni di CO₂. A questo proposito Tabella 3 indica la configurazione ottimale del fattore e il risultato atteso.

Tabella 3 - Condizioni di funzionamento ottimali e risultati della DIO-C₂ a livello di reattore.

Parametri		Regione ottimizzata	Risultato atteso		
Fattore	Unità		Risposta	Unità	
$Y_{C_2H_6}$	[%]	[7 - 8]	$X_{C_2H_6}$	[%]	[40 - 45]
Y_{O_2}	[%]	[8 - 10.4]	X_{O_2}	[%]	[55 - 59]
d_t/d_p	[-]	[4.7 - 6.6]	$S_{C_2H_4}$	[%]	[62.1 - 64]
T_{bath}	[°C]	[385 - 392]	T_s	[°C]	[381 - 395]
MF	[kg m ⁻² hr ⁻¹]	[8.5×10 ³ - 10×10 ³]	T_g	[°C]	[380 - 393]

Tutte le possibili combinazioni fattoriali presentate nella Tabella 3 devono essere sottoposte ad un'analisi di stabilità termica. A questo scopo, ogni configurazione avrà il suo profilo di temperatura che non dovrebbe presentare degli hot spots secondo le condizioni fornite nella Sezione 4.1.5. Pertanto, tutti i profili sono stati studiati per verificare se la regione ottimale preselezionata potrebbe portare alla formazione di hot spots (vedere Figura 4.9). Fortunatamente, l'area illustrata nella Figura 4.8 non ha presentato delle instabilità termiche di nessun tipo, i.e. critiche e non critiche.

V. Integrazione del modello di reattore e simulazione di processo

Il processo ottimizzato per la produzione di etilene su scala industriale è simulato in ASPEN Plus[®]. A quello scopo, un blocco di simulazione personalizzabile viene utilizzato per l'applicazione del modello sviluppato. Poiché le equazioni di governo derivano dal modello del reattore pseudo-eterogeneo, il meccanismo cinetico e i fenomeni di trasporto sono implicitamente presi in considerazione dal formalismo matematico del nuovo modello. In questo modo, non solo considerazioni fisico-chimiche, ma anche condizioni operative (ad esempio lunghezza del reattore, diametro delle particelle del catalizzatore, numero di tubi, ecc.) sono incluse in un unico blocco.

Con l'obiettivo di studiare un processo completo di produzione dell'etilene, delle sezioni di separazione a valle vengono studiate e ottimizzate in ASPEN Plus[®] (i.e. assorbimento di CO₂ con soluzione di ammine e separazione criogenica). Un'ulteriore sezione nell'ambiente di

simulazione è stata destinata a sfruttare il calore di reazione del meccanismo di reazione che si svolge nel reattore catalitico. Pertanto, il calore sensibile del flusso del prodotto è integrato in una rete di scambiatori di calore (HEN) in cui viene prodotto vapore ad alta e bassa pressione. In questo modo, si tiene conto di una valutazione completa sia del fabbisogno energetico netto che delle emissioni di CO₂ per confrontare le prestazioni di questa tecnologia alternativa rispetto ai numeri comuni riportati per la tecnologia convenzionale, i.e. lo steam cracking.

V.a. Modello di reattore

Il modello di reattore semplificato viene implementato in ASPEN Plus attraverso un blocco USER2, seguendo la procedura presentata nella Figura 5.1. A questo punto, l'utente dovrà fornire un insieme di dati per eseguire la simulazione, e.g. specificazioni delle correnti. Inoltre, è obbligatorio inserire un blocco di calcolo per la generazione dei risultati del modello. In questo lavoro, il modello del reattore è costituito da due correnti; l'alimentazione e la corrente dei prodotti del reattore catalitico. Una corretta manipolazione dell'equazioni di governo deve essere condotta per generare risultati adeguati durante l'implementazione del modello in ASPEN Plus, come rappresentato dalle equazioni (5.1-11).

La configurazione parametrica per eseguire il blocco è stata identificata nella Figura 4.8. In tali condizioni, il flusso di alimentazione è stato definito per una capacità di etano di ca. 40 tonnellate all'ora. Ulteriore informazione in quanto riguarda alla configurazione del reattore e l'input richiesto per eseguire il modello sono riassunti nelle Tabelle 5.2-3. Si noti che alcuni parametri si riferiscono a specifiche del flusso di alimentazione (e.g. temperatura, pressione e composizione molare), mentre altri stanno per ulteriori calcoli come il numero di tubi richiesti per una certa portata nell'alimentazione. La performance del reattore e ulteriori dati sulle correnti sono stati riassunti nelle Tabelle 5.3-4.

V.b. Blocco di generazione del vapore

Questa sezione ha lo scopo di stimare il risparmio energetico netto generando del vapore tramite il calore di reazione liberato nella DIO-C₂. Il blocco di simulazione è illustrato nella Figura 5.2. Sono state create due sezioni analoghe che sono costituite dalle stesse unità, ma a condizioni operative diverse. Le specifiche di pressione e temperatura del vapore sono, rispettivamente, 40 bar a 250°C e 2,5 bar a 125°C per vapore ad alta e bassa pressione.

I dettagli tecnici di ciascuna unità e le specifiche del flusso sono stati riassunti nelle Tabelle 5.5-6. Da questo blocco, è importante evidenziare che 46,1 e 33,8 tons hr⁻¹ di vapore ad alta e bassa pressione viene generato grazie a quanto è esotermo il processo. Questi flussi di massa rappresentano 7,04 e 6,62 GJ per tonnellata di etilene prodotta.

V.c. Blocco di compressione

In questa sezione vengono quantificati i requisiti di compressione per la simulazione del processo. Figura 5.3 illustra come evolve il fabbisogno energetico e le emissioni di CO₂ in funzione del rapporto di compressione. In questo documento, la pressione in uscita dal compressore è stata fissata a 2 bar. Questa scelta è in accordo con le condizioni operative più comuni di pressione per il processo a valle del blocco del reattore catalitico (i.e. l'assorbimento di CO₂), in cui sia l'assorbitore che l'unità di recupero operano a pressioni inferiori a 2 bar [28]. Per simulare questa parte del processo è stato utilizzato un compressore a due stadi, in cui è

richiesto un consumo specifico di elettricità di 0,97 GJ per tonnellata di etilene prodotta. Questo blocco anticipa uno dei principali limiti di questo processo: l'elevata diluizione nella corrente di alimentazione. Questo fatto comporta direttamente notevoli spese energetiche dovute alla necessità di comprimere la frazione inerte dell'alimentazione, cioè l'87,1% di N₂. Infine, ulteriori specifiche operative del blocco sono riassunte nella Tabella 5.8.

V.d. Blocco di separazione CO₂

La separazione dell'anidride carbonica dalla corrente di prodotto è un passo cruciale nel processo di purificazione dell'etilene. L'efficienza di rimozione di questo blocco dovrebbe essere superiore al 99%, questo perché anche tracce di CO₂ potrebbero portare a una significativa formazione di ghiaccio nel processo a valle, cioè alla distillazione criogenica. Un processo molto utilizzato per questo scopo è la tecnologia di "addolcimento dei gas acidi", in cui la CO₂ viene assorbita chimicamente con una soluzione a base di ammina all'interno di una colonna di assorbimento a letto fisso, anche nota come assorbitore. In questo lavoro la monoetanolamina (MEA) viene utilizzata come assorbente. Il blocco di separazione della CO₂ è stato diviso in due sottosezioni. In questo modo, la sezione di assorbimento e desorbimento (stripping) vengono simulate sotto diversi pacchetti termodinamici, selezionati per ogni processo in particolare. Questa distinzione è illustrata nella Figura 5.4.

L'assorbitore è l'unità principale del processo, dove la CO₂ viene assorbita chimicamente nella soluzione di ammina. Per la sua implementazione in ASPEN Plus, sono state considerate configurazioni comuni per i processi di addolcimento presenti in letteratura [29, 30]. A questo proposito, importanti parametri di set up dell'assorbitore sono riassunti in Tabella 5.8. L'altezza del letto nelle colonne di assorbimento è un parametro chiave durante la progettazione di esse poiché influenza direttamente i fenomeni di trasferimento di massa tra entrambe le fasi. Un'altra variabile importante è la portata richiesta della soluzione di MEA per ottenere un'elevata capacità di rimozione. A questo scopo, la progettazione delle colonne è stata ottimizzata tramite un'analisi di sensibilità, in cui la capacità di rimozione della CO₂ è stata valutata in funzione di questi ultimi parametri (vedere Figura 5.5). L'analisi è stata effettuata per rimuovere il contenuto di CO₂ dalla corrente di prodotto del reattore catalitico, la cui portata di gas è di 482 tons hr⁻¹ con una frazione massica di CO₂ pari al 2,5%.

L'analisi di sensibilità ha concluso che l'altezza minima del letto per ottenere un'elevata rimozione di CO₂ è di 7 m. La portata molare dell'ammina è stata definita a $7,5 \times 10^3$ kmol hr⁻¹ per garantire sia un'elevata rimozione della CO₂ sia un'adeguata stabilità idrodinamica all'interno della colonna. Queste condizioni di lavoro garantiscono una rimozione dell'anidride carbonica del 99,2% e perdite di MEA inferiori all'1%. Ulteriori parametri operativi sono riportati nella Tabella 5.10.

La simulazione della sezione di stripping comprende il trattamento di preriscaldamento del flusso di alimentazione (vedere Figura 5.4). Quest'ultimo passaggio è stato condotto attraverso due scambiatori di calore. Il primo costituisce una configurazione molto comune in questi tipi di processi, in cui il calore sensibile del flusso di coda dello stripper è sfruttato per preriscaldare l'alimentazione. Il secondo ha la funzione di sfruttare il carico termico rimanente dell'effluente del reattore. In questo senso, si ottengono notevoli risparmi energetici, i.e. 30 GJ hr⁻¹ in totale (vedere Tabella 5.10).

Lo stripper è costituito da un condensatore parziale raffreddato ad acqua e un ribollitore di tipo *kettle*. La colonna opera a pressione ambiente. L'ottimizzazione di questo blocco si basa su tre parametri: capacità di desorbimento di CO₂, recupero di MEA e richiesta energetica. Pertanto, viene effettuata un'analisi di sensibilità per valutare l'effetto di una variabile discreta (i.e.

numero di stadi) e variabili continue, i.e. rapporto del distillato e prodotto di coda ($B:F$), rapporto di reflusso molare (RR) e richiesta energetica al ribollitore.

Lo studio di ottimizzazione ha stabilito che 11 stadi sono sufficienti per garantire un elevato grado di desorbimento di CO_2 alla più bassa richiesta energetica al ribollitore. Per quanto riguarda le variabili continue, $B:F$ e RR hanno mostrato buoni risultati quando definite a 0,97 e 0,1, rispettivamente. Da un punto di vista pratico, la capacità massima di rimozione dello stripper è stata osservata al 98%.

Le perdite di MEA di questa unità sono state quantificate in ca. 2% mentre la capacità di desorbimento della CO_2 è stata determinata al 98%. Tuttavia, 37.6 GJ hr^{-1} è la richiesta energetica al ribollitore per soddisfare queste condizioni di lavoro. Ulteriori dettagli sono stati riassunti nella Tabella 5.11.

V.e. Blocco di separazione criogenica

La corrente di interesse proveniente dal processo di addolcimento è, in termini pratici, privo di CO_2 , i.e. meno dell'1% in massa. La miscela di gas risultante viene quindi alimentata ad un'unità di disidratazione per eliminare il contenuto di acqua disciolta all'interno della fase gassosa. La corrente risultante è composta principalmente da componenti correlate all'aria, cioè N_2 e O_2 , che costituiscono il 90% in massa. Il restante 10% è costituito dalla frazione di idrocarburi, che richiede un rigoroso processo di separazione per ricircolare l'etano non reattivo al reattore catalitico e ottenere una frazione di etilene di standard commerciali, cioè una purezza superiore al 99% in massa. Ciò detto, l'ambiente di simulazione relativo a questo blocco è presentato nella Figura 5.7.

V.e.a. L'unità flash

La purificazione degli idrocarburi inizia con una liquefazione criogenica in un serbatoio flash. La motivazione di una separazione preliminare a monte della distillazione criogenica è giustificata dalla marcata differenza di punto di ebollizione tra la frazione di idrocarburi (rispettivamente, 184.6 K e 169.3 K per l'etano puro e l'etilene) rispetto a N_2 (77.35 K) e O_2 (90.2 K). In questo senso si prevede che la maggior parte della frazione di azoto molecolare sia separata dalla corrente principale.

Viene effettuata un'analisi di sensibilità per identificare il valore di temperatura più adatto per il funzionamento dell'unità flash (vedere Figura 5.9). A questo proposito, l'obiettivo è di massimizzare la separazione dell'aria riducendo al minimo sia le perdite di idrocarburi che il consumo energetico.

I risultati dell'analisi di sensibilità indicano che la maggior parte del contenuto di N_2 può essere eliminato nell'unità flash senza avere perdite significative nella frazione di idrocarburi. Più specificamente, una temperatura operativa inferiore a 108 K (-165°C) garantisce una separazione superiore al 99% e al 98% del contenuto originale di N_2 e O_2 , rispettivamente. La frazione di idrocarburi ha registrato meno del 2.5% di perdite di etilene; mentre meno dell'1% rispetto all'etano. È importante sottolineare che, anche se le prestazioni del processo sono soddisfacenti, il costo energetico richiesto è notevole. Tuttavia, una opportuna integrazione termica è in grado di ridurre il consumo energetico totale a 5.6 GJ per tonnellata di etilene prodotta, che rappresenta quasi la metà del valore raggiunto senza l'integrazione energetica.

Ulteriori dettagli sulle specifiche dei flussi e i parametri di funzionamento degli scambiatori di calore sono riportati, rispettivamente, nelle Tabella 5.12-13.

V.e.b. Distillazione criogenica

Come presentato nella Figura 5.7, il processo simulato è costituito da due colonne di distillazione criogenica. La corrente liquida che entra nella prima colonna di distillazione è costituita da un 66% di etano, 30.7% d'etilene e 3.3% d'aria. La frazione rimanente dell'aria è stata completamente sciolta nella miscela di idrocarburi e la sua separazione è, quindi, complessa. Ciò giustifica l'uso di un'unità di separazione più avanzata come una colonna di distillazione. Nella seconda colonna di distillazione, comunemente nota come C₂-splitter, la frazione idrocarburica composta da una miscela C₂H₆/C₂H₄ viene distillata. Quest'ultima unità sarà successivamente considerata come un punto potenziale per l'integrazione dei processi.

A causa della natura simile di entrambe le unità di separazione, è stato seguito un approccio simile per la loro ottimizzazione. Il primo passo è stato quello di individuare i gradi di libertà di entrambi i processi, come mostrato in Tabella 5.14

L'obiettivo di ottimizzazione della prima colonna di distillazione è quello di ottenere un prodotto di coda con una purezza superiore al 99% rispetto alla fase degli idrocarburi. La motivazione è stata quella di evitare che tracce d'aria possano finire nella corrente di etilene allo splitter, il che potrebbe difficolare il raggiungimento degli standard di qualità. Allo stesso tempo, le perdite di idrocarburi nel distillato devono essere ridotte al minimo. Sotto queste condizioni, l'analisi di sensibilità delle variabili discrete ha dimostrato che siano necessarie almeno 18 stadi, favorendo la performance se si alimenta la colonna nel settimo stadio. Per quanto riguarda le variabili continue, B:F = 0.96 e RR = 1 hanno presentato buoni risultati.

Il disegno dello splitter segue lo stesso approccio della prima colonna di distillazione. A questo punto, è importante comprendere che questa dovrebbe essere l'ultima fase di separazione prima di ottenere una frazione di etilene di grado polimerico, mentre la frazione di etano dovrebbe anche essere abbastanza pura da essere ricircolata al reattore catalitico o ad altri processi.

L'obiettivo principale di ottimizzazione di quest'ultima unità di distillazione è quello di produrre un etilene di grado polimerico al distillato, i.e. con una purezza superiore al 99%. Tuttavia, le condizioni operative di questa colonna sono molto più intense rispetto alla precedente. L'analisi di sensibilità indica che siano necessarie almeno 65 stadi per soddisfare gli standard di purezza. Inoltre, RR pari a 16 garantisce un'elevata purezza dell'etilene al distillato sotto un considerevole carico energetico al condensatore, i.e. 3.93 GJ per tonnellata di etilene prodotta.

Le specifiche di entrambe le unità criogeniche sono riassunte nella Tabella 5.17. Inoltre, ulteriori dettagli sulle correnti coinvolte in entrambe le colonne di distillazione sono riportati nella Tabella 5.15 e nella Tabella 5.17.

La sezione criogenica è l'ultimo blocco della simulazione di processo. Le correnti di prodotti principali di questo blocco sono quattro:

- Due correnti residui ricchi in azoto ed ossigeno, una delle quali ottenuta dalla separazione nell'unità flash, mentre l'altra risulta dalla prima colonna di distillazione;
- il prodotto di coda allo splitter, il cui componente principale è l'etano e;
- la corrente di distillato allo splitter dove si produce dell'etilene di grado polimerico.

Ciascuna corrente avrà ovvie destinazioni e/o ulteriori trattamenti. La corrente d'aria può essere ricompresa per essere immagazzinata o miscelata con etano prima di essere ricircolata nel reattore catalitico. L'etano non reagito può avere la sua destinazione come materia prima per un'ulteriore produzione di etilene. Infine, l'etilene di grado polimerico viene solitamente immagazzinato su serbatoi sferici ad alta pressione e temperatura normale (i.e. 1.83 MPa e 243 K) per la sua commercializzazione.

VI. Risultati e discussione

I risultati della simulazione di processo sono stati illustrati al fine di stimare il consumo netto di energia per tonnellata di etilene prodotta alla capacità simulata dell'impianto. La matrice energetica è stata valutata al fine di identificare i blocchi operativi più costosi dal punto di vista energetico. Come riferimento, dei valori riportati in letteratura per lo steam cracking sono stati presi in considerazione per valutare la sostenibilità della DIO-C₂. Detto ciò, un impianto di steam cracking opera ad un consumo energetico di 15-25 GJ per tonnellata di etilene [31].

Inoltre, è stato condotto uno studio analogo per contrastare le emissioni di CO₂ legate a entrambe le tecnologie. Al fine di ottenere una stima accurata di quest'ultimo parametro, il consumo netto di energia è stato classificato in base alle utility utilizzate all'interno del processo. Per quanto riguarda la tecnologia convenzionale, i valori comuni sono stati segnalati come 1.2-2 tonnellate di CO₂ per tonnellata di etilene prodotta se compresi i processi di separazione a valle [32, 33].

Il consumo energetico complessivo è stato suddiviso in tre categorie: elettricità, riscaldamento e raffreddamento. Inoltre, quest'ultimo è suddiviso in refrigerazione criogenica e raffreddamento convenzionale. Questa distinzione è di fondamentale importanza in quanto avrà un'influenza rilevante nel valutare le emissioni di CO₂. Detto questo, Figura 6.1 illustra la distribuzione dell'energia secondo le suddette utility.

I risultati dell'analisi hanno indicato un consumo lordo di energia di 25,60 GJ per tonnellata di etilene (vedere Figura 6.2). Questo consumo è, infatti, superiore ai valori comuni riportati per lo steam cracking. Tuttavia, se si considera la generazione di vapore a valle del reattore catalitico, lo scenario energetico cambia. In questo modo, il carico termico del vapore ad alta pressione è sufficientemente alto da coprire, non solo il pretrattamento dell'alimentazione, ma anche il carico termico al ribollitore dello stripper. Tuttavia, pur ottenendo una riduzione del 30,7% (vedere Figura 6.3), il fabbisogno energetico è ancora considerevolmente elevato. Un ulteriore passo nell'integrazione energetica è stato preso date le assomiglianze nelle specifiche del vapore prodotto e il così detto vapore di diluizione, i.e. materia prima cruciale nello steam cracking. Quindi, il consumo netto di energia può essere ulteriormente ridotto a 11-12 GJ per tonnellata di etilene, che risulta essere inferiore al consumo legato allo steam cracking. Tabella 6.1 mette in confronto la distribuzione del consumo energetico del processo simulato con un impianto di cracking termico di etano proposto da V. P. Haribal et al. [31].

La quantificazione delle emissioni totali del processo, siano dirette che indirette, è di fondamentale importanza per l'implementazione di questa nuova tecnologia. In questo lavoro, si è ipotizzato che il gas naturale sia la principale fonte di energia per eseguire ogni processo all'interno dell'ambiente di simulazione. In questo modo, le emissioni di CO₂ possono essere stimate in base all'energia fornita dal gas naturale come fonte primaria.

Il primo contributo alle emissioni complessive del processo è osservato a livello di reattore. Contrariamente allo steam cracking, il reattore catalitico produce direttamente CO₂ come prodotto collaterale. Anche se non è un contributo legato al consumo di energia, costituisce una frazione non trascurabile del totale di CO₂ prodotto nel processo complessivo, i.e. 0.95 tonnellate di CO₂ per tonnellata di etilene prodotto.

Per quanto riguarda alle emissioni nette a valle del reattore catalitico, Figura 6.2 anticipa i processi ad alta intensità energetica. La generazione netta di vapore ha contribuito a ridurre al minimo le emissioni lorde a livello di reattore grazie all'integrazione del processo, i.e. 4,9 tonnellate all'ora di CO₂.

Per quanto riguarda la produzione di elettricità, le turbine a gas sono di solito la tecnologia dominante quando il gas naturale viene utilizzato come fonte di energia primaria. La potenza utile erogata da quest'unità è stata stimata tramite l'equazione (6.3) [28]. I risultati hanno dimostrato che le emissioni di CO₂ legate al fabbisogno di elettricità sono di 3.5 tonnellate all'ora.

Le emissioni del blocco di separazione criogenica sono state stimate direttamente dal database delle utility in ASPEN Plus. A tale proposito, la stima è stata effettuata a seconda del regolamento UE-2007/589/CE che stabilisce orientamenti europei per il monitoraggio e la comunicazione delle emissioni di gas a effetto serra [34]. Sotto le suddette condizioni, ASPEN Plus ha stimato una produzione di 52.5 kg di CO₂ per GJ richiesto nei processi criogenici. Detto questo, la Tabella 6.1 indica un costo di raffreddamento di 6.76 GJ per tonnellata di etilene prodotta, i.e. la somma del contributo del serbatoio flash e dello splitter.

Infine, Figura 6.4 riassume le emissioni di CO₂ legate a ciascun blocco del processo. I risultati sono stati osservati entro il margine di 1,1-1,15 tonnellate di CO₂ per tonnellata di etilene, il cui rappresenta una diminuzione nelle emissioni di almeno 0.05 tonnellate all'ora rispetto alla tecnologia convenzionale.

VII. Conclusioni

Durante lo sviluppo di questa tesi, è stata eseguita un'ottimizzazione dettagliata del processo della DIO-C₂ per studiare la sua implementazione su scala industriale. Un modello pseudo-eterogeneo complesso descrive il principio di funzionamento di un reattore catalitico multi-tubulare a letto fisso in cui NiO-SnO₂ viene utilizzato come catalizzatore. Questo modello tiene conto sia delle limitazioni di trasporto che del complesso meccanismo cinetico, il che lo rende molto più accurato rispetto alle formulazioni più semplici, e.g. modelli pseudo-omogenei.

Tuttavia, una descrizione così rigorosa del principio di funzionamento del reattore viene pagata con un costo computazionale considerevole, il che rappresenta la sfida principale per condurre un'ottimizzazione multi-obiettivo del processo. Come soluzione, un modello multi-parametrico è progettato e verificato statisticamente, con l'obiettivo di ridurre il costo computazionale durante lo studio della DIO-C₂ sotto diverse configurazioni parametriche. In questo lavoro, il nuovo modello è costruito usando un approccio RSM in cui le equazioni di governo sono espressioni algebriche più semplici, indicando che il modello può essere eseguito con minime risorse computazionali. Ciò influisce direttamente sul tempo richiesto per condurre una simulazione; mentre il modello pseudo-eterogeneo richiede da 6 a 24 ore per raggiungere convergenza, il modello multi-parametrico viene risolto in pochi secondi, ottenendo così una riduzione del tempo di almeno quattro ordini di grandezza.

Nonostante la matematica più semplice, la non idealità del modello pseudo-eterogeneo, cioè i limiti di trasporto e il complesso meccanismo cinetico, sono intrinsecamente coperte dal modello multi-parametrico. Infatti, il suo disegno deriva interamente dai dati generati tramite il codice Fortran. Inoltre, i test ANOVA hanno concluso che la perdita di informazione durante questa procedura è statisticamente trascurabile.

Durante l'ottimizzazione multi-obiettivo, è stato determinato che la selettività dell'etilene raggiunge un massimo del 66%. Questo valore, tuttavia, si ottiene a un costo di riduzione sia della conversione dell'etano che dell'ossigeno (rispettivamente del 35% e del 30%), finendo così in un costo operativo più elevato. Avendo conto di questa osservazione, è stato stabilito un compromesso abbassando la selettività dell'etilene fino al 62,2%, per aumentare $X_{C_2H_6}$ e X_{O_2} al 47% e 56%, rispettivamente. Queste prestazioni a livello di reattore si ottengono stabilendo il

seguinte set-up parametrico: $d_t/d_p = 4.7$, $T_{\text{bath}} = 392^\circ\text{C}$, $MF = 9900 \text{ kg m}^{-2} \text{ hr}^{-1}$, $Y_{\text{O}_2} = 10.3\%$ e $Y_{\text{C}_2\text{H}_6} = 8\%$.

La simulazione di processo in ASPEN Plus è stata condotta secondo un approccio rigoroso per l'ottimizzazione del processo, la stima del consumo energetico e delle emissioni di CO_2 . Il blocco del reattore definito dall'utente ha dimostrato che 5 reattori catalitici di 20.000 tubi sono necessari per coprire una capacità di etano di 40 tonnellate all'ora nelle condizioni operative sopra riportate. Secondo la letteratura [35, 36, 37], questa è la capacità di alimentazione di almeno una fornace di cracking industriale. Tuttavia, data l'elevata diluizione richiesta nella corrente di alimentazione, la portata di massa complessiva aumenta a 510 tonnellate all'ora dove l'81.7% corrisponde alla frazione inerte (N_2). Questo punto rappresenta chiaramente uno dei principali limiti del processo dal punto di vista del consumo specifico di energia nel blocco di compressione e separazione criogenica (i.e. rispettivamente, 1.4 e 5.6 GJ per tonnellata di etilene).

Il calore sviluppato nella DIO- C_2 è stato un fattore chiave per ridurre al minimo la richiesta netta di energia. Il carico termico dell'effluente del reattore è stato sufficiente per produrre, rispettivamente, 46.1 e 33.8 tonnellate all'ora di vapore ad alta pressione (250°C a 40 bar) e vapore a bassa pressione (120°C a 2.5 bar). In sintesi, le richieste energetiche sia per il pretrattamento dell'alimentazione, sia per il blocco di separazione della CO_2 (i.e. carico termico al ribollitore), è totalmente coperto dal vapore generato. Questa frazione costituisce il 24% del consumo totale di energia.

L'integrazione di processo è stata giustificata da due punti di vista operativi. Il primo riguarda l'uso di una colonna di frazionamento dell'etilene (C_2 -splitter) già installata in un impianto di steam cracking, con l'obiettivo di ridurre al minimo il consumo specifico di energia per la produzione di etilene di qualità polimerica. Il secondo viene giustificato da un'ulteriore integrazione energetica utilizzando il vapore generato, come materia prima per le fornaci di cracking, i.e. vapore di diluizione.

Poiché la scala di produzione del processo simulato è ca. un ordine di grandezza inferiore rispetto a un impianto di steam cracking, il consumo di energia nell'ultima unità criogenica può essere ridotto da 3.4 volte se si segue la via sopra riportata. Si tratta quindi di un requisito fondamentale per ridurre al minimo sia la richiesta energetica che le emissioni di CO_2 .

La frazione di vapore generato non integrata all'interno del processo stesso, può essere integrata nello steam cracking come vapore di diluizione. In questo modo, questa utility può contribuire ad abbassare la richiesta di energia del processo convenzionale. Questo può essere anche visto come un miglioramento nel fabbisogno energetico netto della DIO- C_2 . Nelle attuali condizioni operative, questo risparmio aggiuntivo rappresenta circa 8 GJ per tonnellata di etilene prodotta.

Riassumendo, l'applicazione della DIO- C_2 su scala industriale ha presentato una riduzione del 15% sul consumo specifico di energia rispetto allo steam cracking. Questo risultato si ottiene se si considera uno scenario ottimistico in cui viene utilizzato come riferimento un impianto molto efficiente dove le richieste energetiche arrivano a 15 GJ per tonnellata di etilene prodotta. Per quanto riguarda le emissioni di CO_2 , i risultati indicano una riduzione di 50 kg per tonnellata di etilene. Si noti che questo valore potrebbe migliorare se idrocarburi più pesanti vengono utilizzati come materia prima nello steam cracking (i.e. nafta). Tuttavia, l'integrazione del processo è, a priori, possibile solo se si considera un impianto di cracking termico di etano. Questo viene giustificato dal fatto che, le impostazioni operative e la composizione dell'alimentazione dello splitter, sono equivalenti rispetto al processo simulato.

Infine, l'implementazione della DIO-C₂ utilizzando NiO-SnO₂ come catalizzatore ha dimostrato miglioramenti promettenti sui parametri di sostenibilità al sostituire del 10% della produzione totale di etilene in un impianto convenzionale di cracking termico di etano.

VII. a. Lavori futuri

Anche se il modello multi-parametrico ha mostrato un'elevata precisione rispetto al complesso modello pseudo-eterogeneo, la limitazione principale rimane la sua formulazione unidimensionale. In questo senso, tutte le conclusioni elaborate in questa tesi sono state formulate secondo l'osservazione ad una coordinata radiale fissa ($r_{dss} = 0.5$). Tuttavia, le condizioni di lavoro a basse d_v/d_p causano un'elevata eterogeneità in quanto riguarda al profilo della frazione di vuoto radiale all'interno del letto fisso. A questo proposito, la correlazione di de Klerk [21] dimostra che cambiamenti significativi sulla frazione di vuoto possono essere ottenuti se viene selezionata una coordinata radiale diversa. Ciò avrà un effetto sui fenomeni di trasporto all'interno del tubo del reattore, influenzando la stima finale delle prestazioni del reattore catalitico.

Come lavoro futuro, la costruzione di un modello multi-parametrico è proposta a diverse coordinate radiali. In questo senso, sarà eventualmente possibile una completa ricostruzione del modello del reattore pseudo-eterogeneo, utilizzando equazioni algebriche più semplici. È importante ricordare che la progettazione di un modello bidimensionale avrà un considerevole costo computazionale associato, soprattutto durante la fase di acquisizione dei dati, identificata come il principale collo di bottiglia della procedura.

Per quanto riguarda il processo stesso, la resa dell'etilene e la diluizione della corrente di alimentazione sono state le principali sfide per l'applicazione della DIO-C₂ su scala industriale. Si propone pertanto di condurre studi futuri con lo scopo di migliorare questi due aspetti. In questo modo, viene proposta la costruzione di un modello multi-parametrico che includa ulteriori variabili indipendenti, ad esempio la temperatura di ingresso, la pressione di lavoro e/o la densità del catalizzatore nel letto fisso. Per quanto riguarda la diluizione dell'alimentazione, dovrebbero essere condotte ulteriori ricerche con la possibilità di sostituire l'N₂ come frazione inerte. Un'alternativa potenziale dovrebbe preservare alcune qualità dell'N₂ (i.e. basso costo e elevata disponibilità), ma alla stessa volta garantire una separazione semplice dalla frazione di idrocarburi, dal punto di vista tecnico ed energetico.

I miglioramenti sopra riportati a livello di reattore potrebbero essere la motivazione principale per condurre un'analisi più ampia del processo. In questo senso, ricerche future dovrebbero concentrarsi sull'aumento della percentuale di sostituzione della tecnologia convenzionale. Eventualmente, il processo studiato in questa tesi potrebbe essere presentato come un'alternativa per una completa sostituzione dello steam cracking come tecnologia dominante.

Un'ulteriore raccomandazione riguarda lo sviluppo di un'analisi tecno-economica. La stima sia degli investimenti di capitale che dei costi operativi dovrebbe essere il passo successivo dopo un'estensione del modello proposto in questo lavoro, i.e. la formulazione bidimensionale. Questo contributo futuro sarebbe un fattore chiave per l'implementazione di questa tecnologia su scala industriale.

Infine, è importante sottolineare che questo approccio di modellazione può essere implementato per valutare diverse configurazioni di catalizzatori per la DIO-C₂. I nuovi catalizzatori dovrebbero mantenere alcuni attributi del NiO-SnO₂, i.e. basse temperature di lavoro ed elevata riproducibilità; ma migliorandone altri, e.g. la minimizzazione della produzione di CO₂ a livello di reattore.

[This page was intentionally left in blank]

Contents

Sommario	I
List of Tables	A
List of Figures	C
1. Introduction	1
1.2 Conventional processes	3
1.3 Innovative processes.....	5
1.4 Objective.....	6
2. State of the art	7
2.1 Oxidative dehydrogenation of ethane (ODH-C ₂)	7
2.1.1 Advantages	8
2.2 Catalysis in ODH-C ₂	9
2.2.1 Nickel oxides.....	10
2.2.2 Tin-based nickel oxides (NiO-SnO ₂)	11
2.3 Kinetics.....	11
2.3.1 Experimentation	12
2.3.2 Eley - Rideal formalism (ER).....	13
2.3.3 Kinetic parameters estimation.....	15
2.4 Reactor model.....	15
2.4.1 Fortran subroutine	18
3. Multiparametric model design	21
3.1 Design of experiments.....	22
3.1.1 Response Surface Methodology.....	23
3.2 Multiparametric analysis	25
3.3 Parameter significance and model robustness.....	29
3.3.1 Ethane conversion	29
3.3.2 Oxygen conversion.....	32
3.3.3 Ethylene selectivity	35
3.3.4 Gas-phase temperature	38
3.3.5 Solid-phase temperature.....	41
4. Optimization at reactor level	43
4.1 Sensitivity analysis for the decision variables.....	43
4.1.1 Effects on ethane conversion.....	45
4.1.2 Effects on oxygen conversion	46

4.1.3 Effects on ethylene selectivity.....	47
4.1.4 Effects on the temperature profile.....	49
4.1.5 Hot spots.....	51
4.1.6 Combined effect.....	52
5. Reactor model integration and process simulation	55
5.1 User-defined reactor model	55
5.1.1 Excel model specifications.....	56
5.1.2 Fortran subroutine	59
5.2 Process simulation	59
5.2.1 ODH-C ₂ reactor block.....	59
5.2.2 Steam generation block	61
5.2.3 Compression block.....	64
5.2.4 CO ₂ separation block.....	65
5.2.5 Cryogenic separation block.....	73
6. Results and discussion	85
6.1 Energy distribution and process comparison.....	85
6.2 Analysis of CO ₂ emissions	90
7. Conclusions.....	93
7.1 Future work.....	94
References	97
Appendix	105
A. Nomenclature.....	105
B. Effective transport parameters.....	109
C. Design of experiments: data acquisition.....	111
D. Analysis of variance (ANOVA)	113
E. Process simulation in ASPEN Plus®	118
Acknowledgements.....	119

List of Tables

Table 2.1 – Main reactions involved in ODH-C ₂ [5].....	7
Table 2.2 – Undesired reactions involved in ODH-C ₂	8
Table 2.3 – Operating set-up for performing experiments at 1 bar.	13
Table 2.4 – Elemental steps for the ODH-C ₂ using NiO-SnO ₂ as catalyst. Activation energies for direct and inverse reactions, i.e. E_a^d and E_a^i respectively, are expressed in (kJ mol ⁻¹); while pre-exponential factors are expressed in (mmol g _{cat} ⁻¹ s ⁻¹) [8].	13
Table 3.1 – Factors for the development of the multiparametric equations able to describe the ODH-C ₂ in an industrial-scale packed-bed reactor.	26
Table 3.2 – Responses for the development of the multiparametric equations able to describe the ODH-C ₂ in an industrial-scale packed-bed reactor.	26
Table 3.3 – Reactor configuration for ODH-C ₂ using NiO-SnO ₂ as catalyst.....	27
Table 3.4 – Experimental design under a central composite design scheme.....	27
Table 3.5 – Summary of fit for ethane conversion	30
Table 3.6 – Summary of fit for oxygen conversion.	33
Table 3.7 – Summary of fit for ethylene selectivity.....	36
Table 4.1 – Governing equations of the multiparametric model.	44
Table 4.2 – Optimized operating conditions and performance of the catalytic reactor.....	54
Table 5.1 – Excel workbook variables for the ODH-C ₂ reactor model. SI is the unit settings given by default.....	56
Table 5.2 – ODH-C ₂ reactor model pre-defined parameters.	60
Table 5.3 – ODH-C ₂ reactor model: operating conditions and performance.	60
Table 5.4 – ODH-C ₂ reactor model: component mass flow rate.....	61
Table 5.5 – General information of the steam generation block.	63
Table 5.6 – Stream parameters of the steam generation block ¹	63
Table 5.7 – Compression block: operative conditions.	65
Table 5.8 – Fixed parameters of the absorber unit.	67
Table 5.9 – Absorber final operative conditions and overall performance.	69
Table 5.10 – Operating specification and performance of the pre-heating system in the stripping section.....	70
Table 5.11 – Optimized stripper specifications and performance.	72
Table 5.12 – Stream specifications of the flash unit.	76

Table 5.13 – Specification and performance of the pre-cooling system in the cryogenic block. Location: upstream the flash unit (see Figure 5.7).....	77
Table 5.14 – Specifications of independent variables for both distillation columns located downstream the flash unit.	78
Table 5.15 – Stream specifications of the first cryogenic distillation column.	80
Table 5.16 – Summary of operative specifications and performance of the cryogenic distillation section.....	83
Table 5.17 – Stream specifications of the C ₂ -splitter.....	84
Table 6.1 – Comparison of energy demand between a small-scale ethylene production plant using ODH-C ₂ technology and an industrial scale ethane steam cracking process.	89
Table 6.2 – Natural gas specification to estimate CO ₂ emissions [28].....	91
Table C.1 – Configuration of the 44 simulations suggested by JMP 15 [®] . Results are shown for L _{re} = 2.6 m.	111
Table D.1 – Analysis of variance (ANOVA) for the construction of the regression model for ethane conversion. The study has been carried out at L _{re} = 2.6 m.	114
Table D.2 – Analysis of variance (ANOVA) for the construction of the regression model for oxygen conversion. The study has been carried out at L _{re} = 2.6 m.....	115
Table D.3 – Analysis of variance (ANOVA) for the construction of the regression model for ethylene selectivity. The study has been carried out at L _{re} = 2.6 m.	116
Table D.4 – Analysis of variance (ANOVA) for the construction of the regression model for gas-phase temperature. The study has been carried out at L _{re} = 2.6 m.	117

List of Figures

Figure 1.1 – Evolution of the energy mix in the European Union from 1990 to 2015 [43].	1
Figure 1.2 – Percentage of ethylene consumption to produce ethylene-derivatives in the EU (including Norway). From left to right: low-density polyethylene, linear low-density polyethylene, ethylene glycol monobutyl ether, ethylene oxide, ethylene dichloride and “Others” includes less common by-products [44].	2
Figure 1.3 – Ethylene consumption worldwide forecast. Adaptation from [45].	2
Figure 1.4 – Natural gas production in the United States [41].	3
Figure 1.5 – Block flow diagram of thermal steam cracking [12].	4
Figure 1.6 – Block flow diagram of the methanol-to-olefin process (MTO) [51].	5
Figure 2.1 – Variation of the ethylene selectivity as a function of the oxidation state of the promoter. Conditions have guaranteed 10 % of ethane molar conversion for each catalyst composition. Adaptation from [64].	10
Figure 2.2 – Reaction scheme for the ODH of ethane using a Ni-Sn-O catalyst where k_i represent rate constants [9].	12
Figure 2.3 – Steps for the simulation of the reactor performance under a set of user-defined parameters. An in-house code developed in Fortran is used as simulation machine.	19
Figure 3.1 – Scheme of a multi-tubular packed-bed reactor. The figure shows the axial symmetry of one tube as well as the dimensionless radial coordinate used for the multiparametric study in this work.	21
Figure 3.2 – Experimental design stages. Adaptation from [72].	23
Figure 3.3 – Scheme of a three-factor central composite design [22].	25
Figure 3.4 – Axial cross-section of a reactor tube filled with catalyst pellets. Selected axial points for the model development are shown. From left to right: $L_{re} = [0.0564, 0.11, 0.15, 0.23, 0.33, 0.39, 0.51, 0.72, 0.79, 0.86, 1.02, 1.18, 1.26, 1.34, 1.50, 1.66, 1.88, 2.02, 2.15, 2.27, 2.41, 2.49, 2.54, 2.56, 2.6]$.	28
Figure 3.5 – From left to right, ethane conversion prediction plot and its respective plot of residuals.	30
Figure 3.6 – Ethane conversion along the catalytic bed in a single reactor tube. (a) Represents the 29 th experiment; (b) represents the 17 th experiment and (c) represents the 3 rd experiment. See Appendix C for further details regarding each reactor configuration.	31
Figure 3.7 – Ethane conversion along the catalytic bed in a single reactor tube. (a) Represents the 6 th experiment and (b) represents the 12 th experiment. See Appendix C for further details regarding each reactor configuration.	32

Figure 3.8 – From left to right, oxygen conversion prediction plot and its respective plot of residuals.....	33
Figure 3.9 – Oxygen conversion along the catalytic bed in a single reactor tube. (a) Represents the 29 th experiment; (b) represents the 17 th experiment and (c) represents the 3 rd experiment. See Appendix C for further details regarding each reactor configuration.	34
Figure 3.10 – Oxygen conversion along the catalytic bed in a single reactor tube. (a) Represents the 27 th experiment; (b) represents the 10 th experiment and (c) represents the 15 th experiment. See Appendix C for further details regarding each reactor configuration.	35
Figure 3.11 – From left to right, ethylene selectivity prediction plot and its respective plot of residuals.....	36
Figure 3.12 – Ethylene selectivity along the catalytic bed in a single reactor tube. (a) Represents the 29 th experiment; (b) represents the 17 th experiment and (c) represents the 3 rd experiment. See Appendix C for further details regarding each reactor configuration.	37
Figure 3.13 – Ethane conversion along the catalytic bed in a single reactor tube. (a) Represents the 33 rd experiment and (b) represents the 12 th experiment. See Appendix C for further details regarding each reactor configuration.....	37
Figure 3.14 – From left to right, gas-phase temperature prediction plot and its respective plot of residuals.	39
Figure 3.15 – Gas and solid-phase temperature along the catalytic bed in a single reactor tube. (a) Represents the 29 th experiment; (b) represents the 17 th experiment and (c) represents the 3 rd experiment. See Appendix C for further details regarding each reactor configuration.	40
Figure 3.16 – Temperatures profiles of both gas and solid phase. (a) Represents the 10 th experiment; (b) represents the 38 th experiment and (c) represents the 27 th experiment. See Appendix C for further details regarding each configuration.	41
Figure 4.1 – Prediction profiler showing linear effects of independent factors on each model response at $L_{re} = 2.6$ m.	44
Figure 4.2 – Response surface plots for ethane conversion showing the interaction between two independent factors. The remaining factors (absents on each plot) have been maintained constant at a value equal to their respective zero level (0).....	46
Figure 4.3 – Response surface plots for oxygen conversion showing the interaction between two independent factors. The remaining factors (absents on each plot) have been maintained constant at a value equal to their respective zero level (0).....	47
Figure 4.4 – Response surface plots for oxygen conversion showing the interaction between two independent factors. The remaining variables have been maintained constant at a value equal to their respective zero level (0).	48
Figure 4.5 – Prediction profiler showing linear effects on both gas and solid-phase temperature at $L_{re} = 0.23$ m.	49
Figure 4.6 – Statistic significance evolution of $Y_{C_2H_6}$, Y_{O_2} , d_t/d_p , MF and T_{bath} along the reactor tube. Significance limit has been established at $Prob > F$ of 0.05.	50

Figure 4.7 – Temperature profile along the catalytic bed under different configurations. (a) Parameters are set at $T_{\text{bath}} = 380 \text{ }^\circ\text{C}$, $\text{MF} = 5000 \text{ kg m}^{-2} \text{ hr}^{-1}$, $Y_{\text{C}_2\text{H}_6} = 8 \%$, $Y_{\text{O}_2} = 14 \%$ and $d_t/d_p = [3, 6, 9]$ correspond to (i), (ii) and (iii), respectively. (b) Parameters are set at $T_{\text{bath}} = 470 \text{ }^\circ\text{C}$, $\text{MF} = 7000 \text{ kg m}^{-2} \text{ hr}^{-1}$, $Y_{\text{C}_2\text{H}_6} = 6 \%$, $Y_{\text{O}_2} = 10 \%$ and $d_t/d_p = [3, 6, 9]$ correspond to (i), (ii) and (iii), respectively. In both cases, $T_{\text{hs}} = T_{\text{bath}} + 15 \text{ }^\circ\text{C}$.	51
Figure 4.8 – Overlaying technique through a series of contour plots. Constrains are defined as: $S_{\text{C}_2\text{H}_4} > 62.1 \%$, $X_{\text{C}_2\text{H}_6} > 30 \%$ and $X_{\text{O}_2} > 50\%$. Dots stand for indicating the direction on which pre-defined conditions are accomplished.	53
Figure 4.9 – Thermal stability verification.	54
Figure 5.1 – Information pathway while using an USER2 block in ASPEN Plus [®] .	55
Figure 5.2 – Steam generation block.	62
Figure 5.3 – Energy specific consumption and CO ₂ emissions as function of a two-stage compressor discharge pressure. The feed (510 tons hr ⁻¹) enters the compressor unit after the steam generation block at 35°C.	64
Figure 5.4 – CO ₂ separation block. (a) represents the CO ₂ absorption section (thermodynamic package: AMINES); while (b) represents the stripping section for CO ₂ desorption and MEA recovery (thermodynamic package: eNRLT).	66
Figure 5.5 – CO ₂ removal capacity of the absorber as a function of (a) number of theoretical stages and (b) amine solution molar flow rate. Temperature and pressure conditions are 45°C and 2 bar, respectively.	68
Figure 5.6 – Sensitivity analysis of stripper performance parameters as a function of discrete and continuous variables. Molar RR was maintained fixed at 0.1. Under these conditions, MEA losses were, on average, between 1-2%.	71
Figure 5.7 – Cryogenic separation block (thermodynamic package: Peng-Robinson).	74
Figure 5.8 – Product stream vapor fraction as a function of the mean temperature at 1.3 bar. The stream is constituted by 87.14% of N ₂ , 6% of O ₂ , 2.2% of C ₂ H ₄ and 4.66% of C ₂ H ₆ in mass bases.	75
Figure 5.9 – Sensitivity analysis of the flash unit without considering the heat integration. (a) illustrates the overall performance of the flash tank while (b) compares the cooling duty of three different scenarios as a function of the operative temperature. The mass flow rate of the feed stream is 472 tons hr ⁻¹ , whose composition is constituted by 87.14% of N ₂ , 6% of O ₂ , 2.2% of C ₂ H ₄ and 4.66% of C ₂ H ₆ in mass bases.	75
Figure 5.10 – Sensitivity analysis of discrete variables for a cryogenic distillation column design. Purity in the column product streams is plotted as a function of (a) number of stages and (b) tray location of the feed stream.	79
Figure 5.11 – Sensitivity analysis of continuous variables for a cryogenic distillation column design. Air purity in the distillate and condenser duty is plotted as a function of (a) molar reflux ratio and (b) bottom-to-feed ratio. Condenser duty and its working temperature are plotted in (a) and (b), respectively.	80

Figure 5.12 – Sensitivity analysis of discrete variables for a C ₂ -splitter design. Purity in the column product streams is plotted as a function of (a) number of stages and (b) tray location of the feed stream.....	82
Figure 5.13 – Sensitivity analysis of continuous variables for a C ₂ -splitter design. Ethylene recovery and its mass fraction in the distillate are plotted as a function of (a) bottom-to-feed ratio (<i>B:F</i>) and (b) molar reflux ratio (<i>RR</i>). The refrigeration load at the condenser is plotted in both graphs.	82
Figure 6.1 – Energy distribution of the ODH-C ₂ at industrial scale using NiO-SnO ₂ as catalyst. The heating utility does not consider the generated steam.....	86
Figure 6.2 – Specific energy consumption of an ethylene production process using ODH-C ₂ technology. Values does not represents net results (i.e. steam generation is not included)....	87
Figure 6.3 – Specific energy consumption of an ethylene production process using ODH-C ₂ technology. Net energy requirements are reported with net steam generation. Negative values indicates the remaining heat load after considering the energy integration.	88
Figure 6.4 – Net specific CO ₂ emissions of an ethylene production process using ODH-C ₂ technology. Note that the category “Steam generation” has been identified with a different colour to indicate emission savings due to a process integration.	92
Figure E.1 – Block flow diagram of the overall process for ethylene production by the ODH-C ₂ using NiO-SnO ₂ as catalyst.	118

[This page was intentionally left in blank]

Chapter 1

1. Introduction

In nowadays society, it is common knowledge that the worldwide energy demand is constantly increasing due to the growth of global population and living standards. Nevertheless, it is also a fact that conventional energy sources have a fossil origin and thus they are limited. The increasing exploitation and consumption of hydrocarbons are generating undesired effects in our planet such as constant emission of greenhouse gases that derives on climate change with its consequently short-term and long-term effects [1]. In this way, it is necessary to gradually replace the use of hydrocarbons with renewable energy sources, not only for energy production itself, but also for chemical feedstock manufacturing. The meaning of the word “gradually” is essential since the necessary technology to achieve worldwide sustainability using renewable sources of energy is still under development given its complexity and costs [38, 39, 40].

When it comes to follow the path towards a sustainability, one should consider both the availability and the negative impact an energy source has while using it to produce goods and services. As a matter of facts, natural gas is becoming more and more interesting within the industrial sector. Nowadays, both petrochemical and chemical sector are centring their attention on natural gas as an alternative to oil as feedstock. The main reason is related to the increasing availability of low-cost natural gas and thus its competitiveness towards the use of conventional oil [41]. Furthermore, although having a fossil origin, it has been widely proved that natural gas emits 50 to 60 percent less carbon dioxide comparing with other fossil fuels (e.g. coal) combusted by power plants [42]. In fact, Europe has already considered the implementation of natural gas within its energy matrix in order to support the insertion of renewable energy sources to gradually decreased the petroleum consumption (see Figure 1.1).

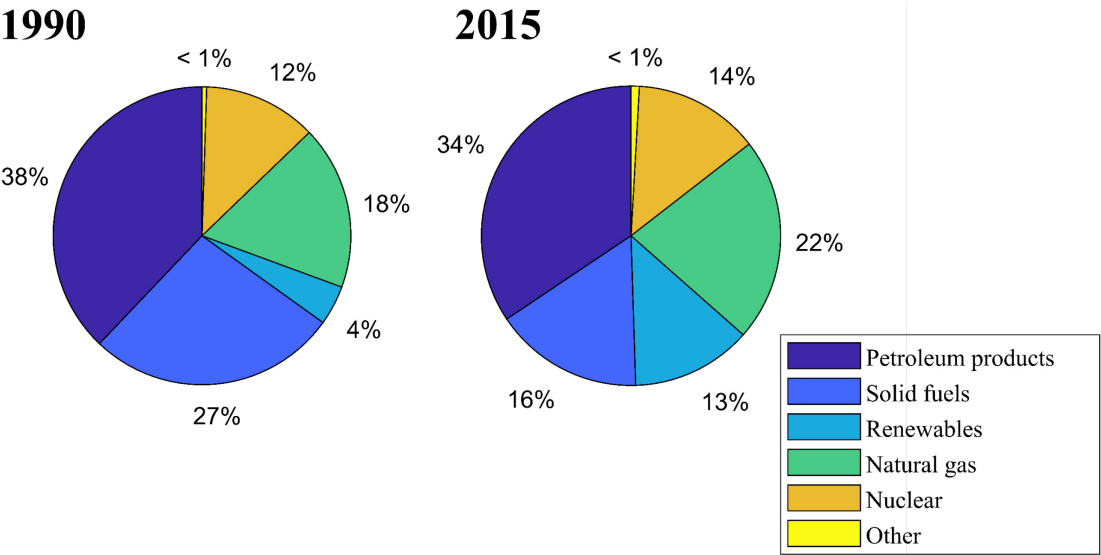


Figure 1.1 – Evolution of the energy mix in the European Union from 1990 to 2015 [43].

The petrochemical sector is currently developing new technologies to increase the added value of the key components of natural gas (C₁ – C₄ paraffines) by transforming them into highly-valued olefins. These latter ones have a particular chemical structure with one or more double-bonds which make them chemically reactive towards the production of many compounds of interest such as resins, synthetic fibers, a wide range of plastics, among others. When it comes to olefins, ethylene is undoubtedly one of the most worldwide demanded compounds due to its versatility towards higher-added value chemical production (see Figure 1.2).

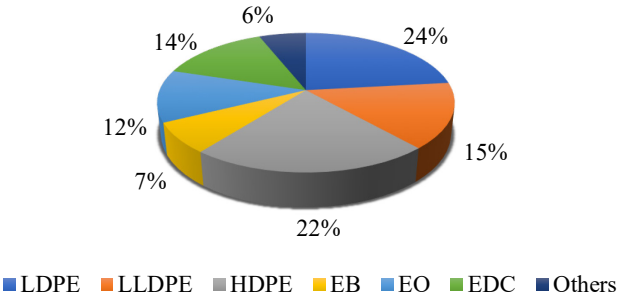


Figure 1.2 – Percentage of ethylene consumption to produce ethylene-derivatives in the EU (including Norway). From left to right: low-density polyethylene, linear low-density polyethylene, ethylene glycol monobutyl ether, ethylene oxide, ethylene dichloride and “Others” includes less common by-products [44].

Being the major building block within the petrochemical industry, the worldwide ethylene consumption of ethylene is constantly increasing due to the rising of living standards as well as the global population growth. Currently, the worldwide production is approximately 1.5×10^8 tons per year and it is expected to face an annual growing rate between 3.7 and 4%, as shown by Figure 1.3 [2].

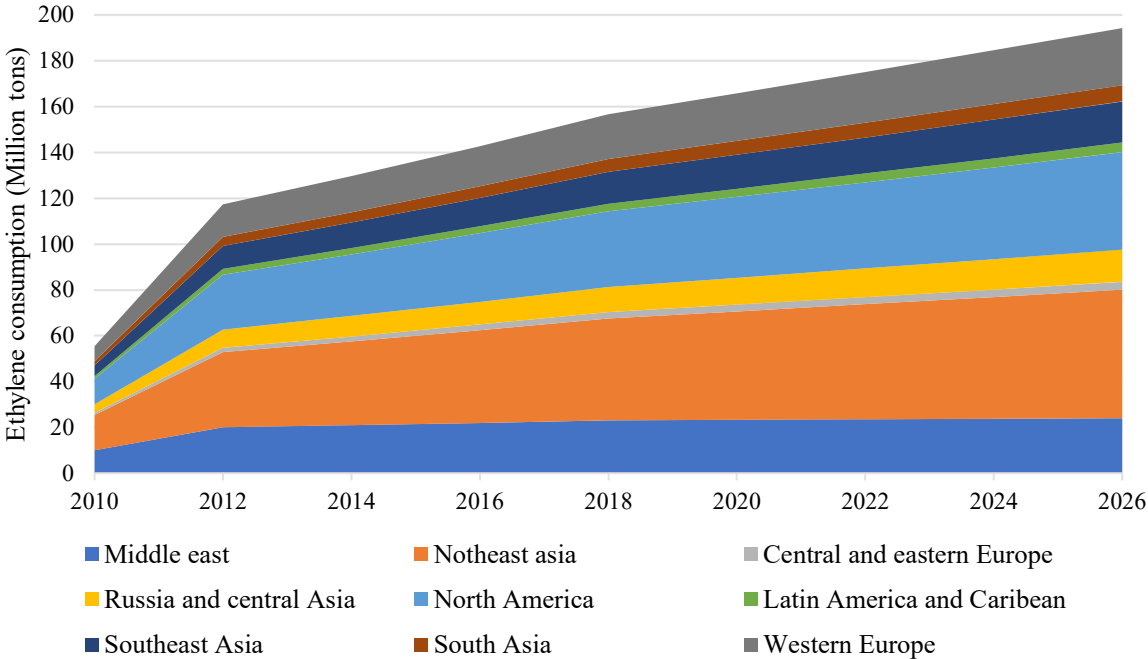


Figure 1.3 – Ethylene consumption worldwide forecast. Adaptation from [45].

The feasibility of alternative processes for ethylene production are strictly linked to the availability of cheap chemical feedstocks and their competitiveness with respect to conventional processes depend on this aspect. For instance, in North America the primary raw material for ethylene production (i.e. crude oil) is becoming scarcer since the lighter crudes suitable for naphtha production are depleting. As a matter of facts, heavier oils should be used instead; nevertheless, higher costs would inevitably be involved [4]. Fortunately, in US, natural gas from shale deposits has been equilibrating the volatile prices of natural gas, creating a competitive advantage and a solution to avoid the use of heavier hydrocarbons as feedstock for ethylene production. Hence, most of the American chemical companies use ethane as raw material for their products while competitors are mostly using naphtha as feedstock (see Figure 1.4). In 2013, a capital investment of US\$ 71.3 billion was announced by chemical companies to expand the production of ethylene and its derivatives in the United States [41].

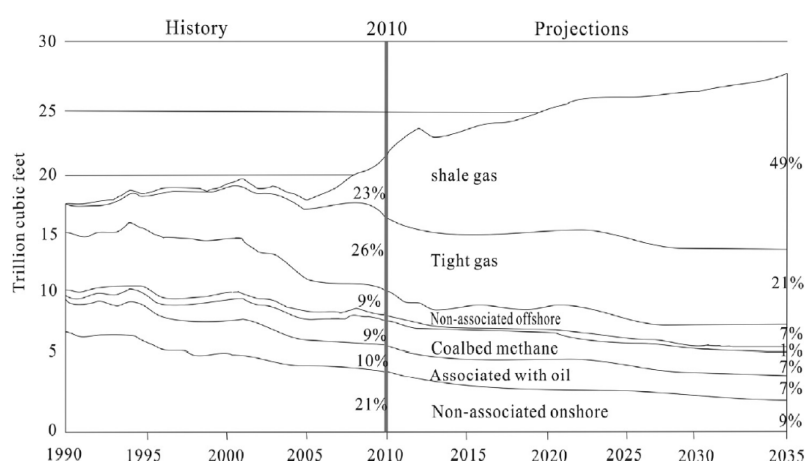


Figure 1.4 – Natural gas production in the United States [41].

Even considering the shale gas revolution, there are still uncertainties which does not allow the industrial sector to totally replace conventional processes. In this scenario, oxidative dehydrogenation of ethane seems to be a promising alternative for ethylene production. However an industrial scale application requires a low cost catalyst able to provide high conversion and selectivity towards ethylene formation.

1.2 Conventional processes

Declining of crude oil reservoirs as well as social awareness have not prevented steam cracking to be the dominant process for ethylene production, covering more than 97% of the annual worldwide manufacturing of this building block [46]. Steam cracking utilizes gaseous and liquid hydrocarbons feedstocks (such as ethane, gas oil and naphtha) for light olefins production. While ethane is still the most used chemical feedstock in steam cracking, more than 80% of ethylene in Asian-Pacific region and Europe is produced by thermal cracking of naphtha. Due to its high endothermicity and complex product-separation, it is a remarkable energy intensive process (e.g. for thermal cracking of naphtha, up to 40.000 MJ of heat per metric tonne of ethylene) [32].

Most of the thermal cracking plants are roughly composed by the same four sections: gas-fired cracking furnaces, quench units, compression and chilling section, and separation units. A simplified scheme of a light olefin production plant is shown in Figure 1.5 [3].

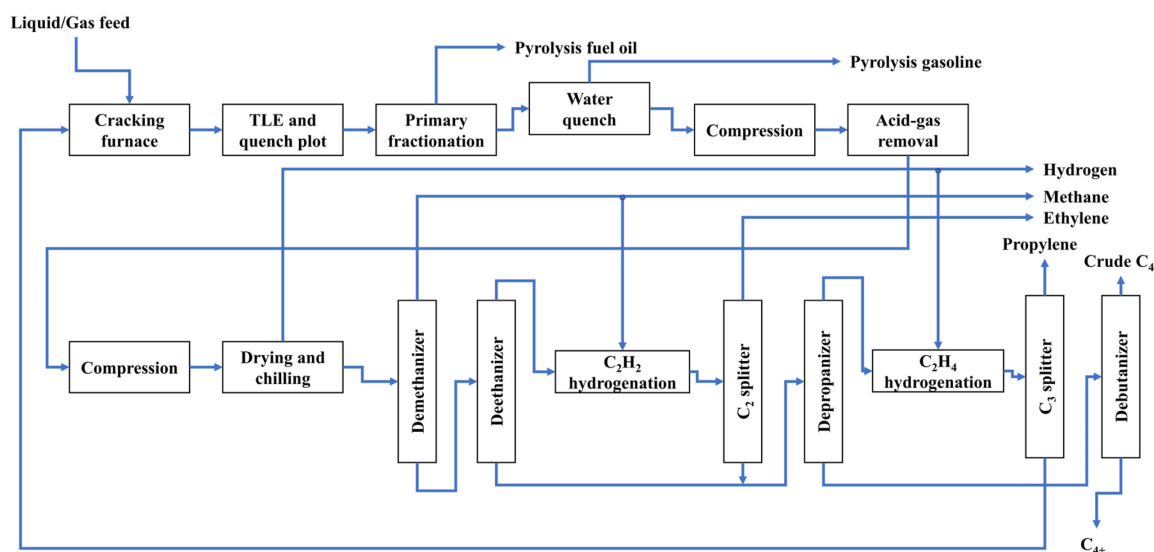


Figure 1.5 – Block flow diagram of thermal steam cracking [12].

Considered as the heart of an olefin plant, cracking furnaces are responsible for the conversion of raw feedstocks into a higher added value compounds. In this way, several burners are distributed along the furnace to provide sufficient heat to induce a series of radically-chemical reactions in the presence of steam. This implies that temperatures in the range of 750-1000°C are reached and therefore heavier hydrocarbons are consequently cracked into lighter ones producing the desired products.

The resulting hydrocarbon mixture leaving the furnace at approximately 800-900°C is quickly cooled down within the quench section to avoid the propagation of undesired secondary reactions (i.e. aromatization and polyaromatics formation, also known as coke formation) and thus maximizing the yield of valuable products. The cracked hot gas is consequently cooled down in a very short period of time via indirect quenching to 300-425°C using a complex heat exchanger known as Transfer Line Exchanger (TLE). Once completed this step, the product mixture is further cooled down till temperatures below ambient conditions by direct quenching [3, 32].

The final step involves separations processes. Among all possible options, cryogenic distillation is currently used at industrial scale. Although, there are promising alternatives to this process, their implementation at big-scale is not yet feasible [47, 48]. These processes are remarkably expensive in terms of energy consumption and capital cost. Thus, the total cooling energy required will depend on the design of the distillation columns and the proper configuration of operating parameters.

Although being a well-rooted process for ethylene production, coke formation, low selectivity and excessive energy consumption are just some drawbacks that have prevailed in spite of efficiency improvements. This scenario is therefore enhancing a constant search for greener and more sustainable alternatives.

1.3 Innovative processes

As introduced in the previous section, the major challenges to be faced with respect to conventional ethylene production is the high energy consumption rate and its link to CO₂ emissions. It has been already proven that a typical oil-to-olefin plant could generate more than 4 tons of CO₂ per ton of olefin produce. Therefore, by taking into account the annual production of this chemical, reducing this number close to zero emissions will be equivalent to take 42 million cars out of the road [49]. However, how to accomplish such goal is still unsolved.

One alternative to steam cracking is methanol-to-olefin process (MTO) which uses methane as feedstock (see Figure 1.6). Therefore, natural gas is generally used as feed to convert the hydrocarbon source into synthesis gas which is further converted to methanol and then to dimethyl ether (DME). In the presence of catalyst, DME is finally converted to the desired olefins. MTO process utilizes a fluidized bed reactors which presents several advantages such as constant catalyst activity, coke burning with air and better heat recovery from the exothermal reactions involved in the process [50]. Since propylene and ethylene are produced, the yield ratio can be adjusted according to their respective market demand and pricing by modifying reactor operating conditions. Unfortunately, MTO process also presents a series of disadvantages such as the access to a cheap chemical feedstock for methanol production and inefficiencies linked to the pre-production of syngas. This aspect is crucial towards the competitiveness of the process with respect to steam cracking.

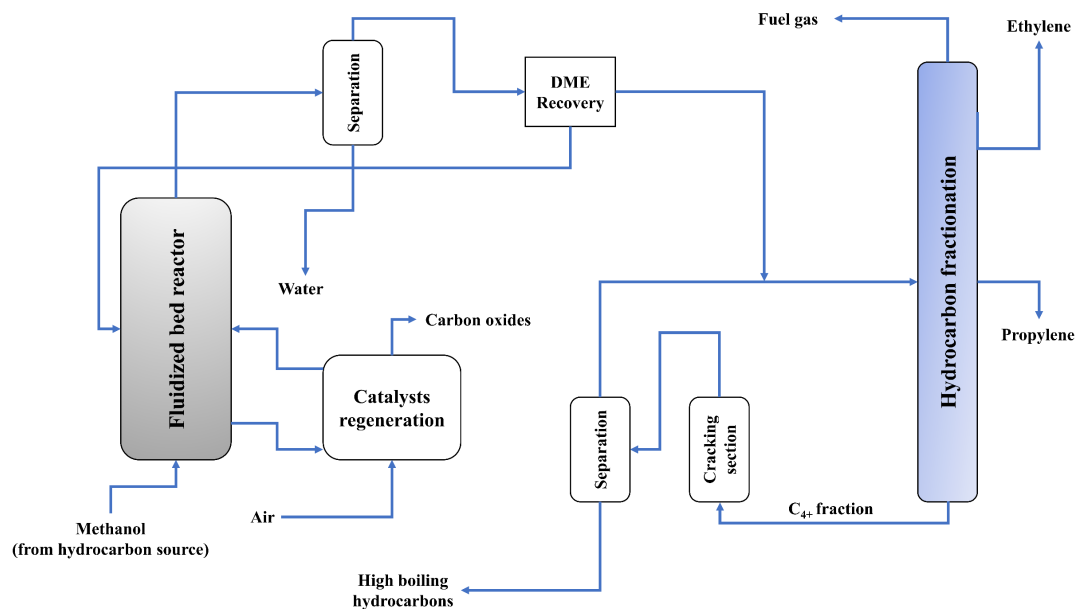


Figure 1.6 – Block flow diagram of the methanol-to-olefin process (MTO) [51].

Another promising alternative to conventional processes is oxidative coupling of methane (OCM). In this process, methyl radicals are formed as a result of methane partial oxidation. Ethane is therefore produced and through a further dehydrogenation, ethylene is obtained [4]. Although OCM has been studied since 1980, there are still challenges towards its industrial application linked to poor methane conversion and product selectivity [51]. On the one hand, recent improvements regarding a more effective catalyst have maintained the OCM as a feasible

method for ethylene production in the near future [52]. On the other hand, the synthesis of a suitable catalyst for using methane-rich feeds from shale gas is still under development [4].

In addition to the previously mentioned alternatives, the oxidative dehydrogenation of ethane has become more and more interesting within the scientific community given a series of advantages this technology presents with respect to other alternatives. Low working temperatures, limited number of side-products and access to cheap feedstock are just some important points for considering this technology as a potential alternative for industrial ethylene production.

1.4 Objective

This document has the purpose of studying the oxidative dehydrogenation of ethane (ODH-C₂) in a multi-tubular packed-bed catalytic reactor in order to determine the optimal operating conditions for ethylene production. For that purpose, a NiO-SnO₂ catalyst is utilized in order to evaluate its performance and thus considering it as a potential candidate for industrial production of ethylene.

The work presented in this document can be divided into two main sections. In the first section, an industrial reactor-level analysis involves a multi-objective optimization where important parameters are tested. On this matter, a pseudo-heterogeneous reactor model is numerically solved in order to obtain a detailed two-dimensional description of the reactor performance in terms of ethylene selectivity and final conversion of reactants. In this way, concentration and temperature profiles along the packed-bed reactor are generated throughout the radial and axial coordinate of a single reactor tube. Due to the complex mathematics involved in the pseudo-heterogeneous model, a parametric optimization would be remarkable time-consuming at a high computational cost. Therefore, a simpler model is proposed through a design of experiments (DoE) where a set of algebraic multiparametric equations are developed using the response surface methodology (RSM) approach. The objective is to utilize the new model to explore the full spectrum of relevant independent variables and their respective interactions; thus, identifying promising configurations to maximize the reactor performance.

The second section of this work involves the implementation of the model into a commercial simulator (i.e. ASPEN Plus[®]) with the aim of establishing a complete modelling framework of the case-study. At that scope, the catalytic reactor is modeled via an user-defined unit operation block (USER2). It follows the incorporation of additional processes, aiming to improve the overall energy integration of the simulation framework, and to simulate key processes for the production of polymer-grade ethylene, i.e. CO₂ absorption with amine solutions and cryogenic distillation. The resulting system is further optimized within the simulation environment aiming to achieve olefin commercial standards by minimizing both, product losses and energetic requirements.

After the conclusion of the previous sections, the overall ODH-C₂ process is compared with the conventional technology currently used for worldwide ethylene production. On this matter, important sustainability parameters are considered (i.e. energy consumption and greenhouse gas emissions) in order to evaluate the feasibility of a gradual technological innovation within the petrochemical sector.

Chapter 2

2. State of the art

In this chapter, the oxidative dehydrogenation of ethane is described in detail in order to provide a proper background of the case-study for a complete comprehension of the content included in the following chapters.

2.1 Oxidative dehydrogenation of ethane (ODH-C₂)

Aiming to improve the sustainability of the olefin industry, oxidative dehydrogenation of ethane has been recognized as an attractive alternative route for ethylene production. ODH-C₂ is simply a combination of dehydrogenation of ethane coupled to hydrogen combustion where water is produced [5]. These sequence of reactions are represented enlisted in Table 2.1.

Table 2.1 – Main reactions involved in ODH-C₂ [5].

Reaction	ΔH_{298K}^0 (kJ mol ⁻¹)
$C_2H_6 \leftrightarrow C_2H_4 + H_2$	136.4
$H_2 + \frac{1}{2}O_2 \rightarrow H_2O$	-286
$C_2H_6 + \frac{1}{2}O_2 \rightarrow C_2H_4 + H_2O$	-149.6

Even though the dehydrogenation of ethane is endothermic, the combustion of hydrogen is much more exothermic; therefore, the overall reaction mechanism results highly exothermic. Furthermore the hydrogen combustion enhances the displacement of the equilibrium towards ethylene production [6]. Unfortunately, the ODH-C₂ also presents a series of side reactions where either partial or total oxidation of the hydrocarbon fraction takes place. Undesired reactions are enlisted in Table 2.2. It is important to point out that each side product (i.e. CO and CO₂) derives from a combustion reaction which is highly exothermic. Consequently, the thermal stability control in an industrial-scale reactor represents one of the main challenges of this process.

Table 2.2 – Undesired reactions involved in ODH-C₂.

Reaction	ΔH_{298K}^0 (kJ mol ⁻¹)
$C_2H_6 + \frac{7}{2} O_2 \rightarrow 2 CO_2 + 3 H_2O$	-1429
$C_2H_4 + 3 O_2 \rightarrow 2 CO_2 + 2 H_2O$	-1323
$C_2H_6 + \frac{5}{2} O_2 \rightarrow 2 CO + 3 H_2O$	-863
$C_2H_4 + 2 O_2 \rightarrow 2 CO + 2 H_2O$	-757

The carbon oxides (i.e. carbon monoxide and carbon dioxide) are thermodynamically more stable than olefins, thus catalyst must be sensitive enough to stop the oxidation before its evolution towards total oxidation or, simply, overoxidation [6]

Nevertheless, there has been experimental evidence of some catalysts whose reaction mechanisms produces negligible amounts of carbon monoxide, leaving only carbon dioxide as the main side product. As reported elsewhere [53], nickel oxide-based catalyst (i.e. Ni-Me-O, where Me a metal compound such as Li, Al, Sn, Nb, among others) have proven that C₂H₄, CO₂ and H₂O are the only observable products during experimentation.

2.1.1 Advantages

It should be clear by now the fact that, due to the high exothermicity of ODH-C₂, there will be remarkable energy saving at reactor level. However, the use of a proper catalyst is also a crucial step to operate at relatively low temperatures. There have been previous reports where high ethylene yields have been observed over chlorine-promoted nonreducible oxides (e.g. LiCl/MgO) where temperatures beyond 600°C are required [54]. The use of γ -Al₂O₃-supported vanadium oxides catalyst have also presented good performances at similar temperature ranges [55]. Although being an exothermic process, operating at such high temperature is often undesired since it enhances catalyst deactivation at thermal stress in the reactor structure.

Nevertheless, some novel catalyst configurations have been recently studied (e.g. NiO-SnO₂) where much lower temperatures are required to achieve high ethylene yields (i.e. 350-400°C) [56]. In this way, the above mentioned drawbacks are minimized and the temperature difference with respect to steam cracking is enlarged [3, 32, 46]. The heat required for this latter endothermic process is mainly generated by fossil fuel combustion (e.g. natural gas) and thus a significant reduction on CO₂ emissions should be guaranteed.

Since steam cracking is not a catalytic process, a wide range of products can be formed depending of the initial feedstock. Even though most of them have a commercial value (e.g. propylene, butadiene, among others) [57], the cost and complexity in terms of separation processes downstream the steam cracker increases. Consequently, ODH-C₂ represents another advantage in this aspect if considering that side products formation is limited.

Another important advantage regards coke formation. This undesired side product in steam cracking is mainly composed by poly-nuclear aromatics. Its formation can be minimized by diluting the feedstock with steam but this will not prevent periodic shutdowns for maintenance,

resulting in higher capital and operative cost [32]. However, the presence of molecular oxygen in ODH-C₂, together with the fact of working at low temperatures, will definitely take coke formation out of the equation.

One last consideration involves the shale gas revolution. As anticipated before, the access to abundant and cheap feedstock is crucial towards the implementation of alternative technologies at industrial scale, such as the one considered in this work.

2.2 Catalysis in ODH-C₂

Selective heterogeneous catalysis for oxidation processes produces approximately 25% of the most important organic chemicals and intermediates for well-known consumer goods, e.g. acrylonitrile, phthalic anhydride, propylene oxide and ethylene. Great efforts have been made to develop selective oxidation processes using efficient catalysis. The terminology “selective catalyst” implies matter preservation, higher yield of the desired product and last, but not least, environmental preservation [58].

There have been reported several studies regarding catalysts of different nature, i.e. different chemical composition where researchers have focused in some chemical features a catalyst should have for oxidation processes. These characteristics have been organized within a total of seven principles for a deeper understanding of the metal oxide catalyst behaviour and catalyst design, as reported by R. K. Grasselli [59]:

- **Lattice oxygen:** this form of oxygen in some metal oxides can be more versatile and selective oxidizing agent for hydrocarbons than molecular oxygen;
- **M-O bonds:** reducible metal oxides must have M-O bonds of intermediate strength for a good performance. Too strong bonds could lead to an absence of reaction while too weak ones to an overoxidation;
- **Host structure:** a proper three-dimensional structure must be guaranteed to enhance M-O bonds, rapid electron transfer and O² diffusion;
- **Redox:** the catalyst should be able to rapidly replace the lattice oxygen that has been removed for oxidation. This re-addition is performed by molecular oxygen;
- **Multi-functionality:** Effective catalysts are generally multi-metallic (usually bi-metallic) and, at least, bi-functional;
- **Site isolation:** the active oxygen present in the catalyst surface must be properly located to enhance its selectivity towards the desired product. This distribution must take care about the density of active oxygen on the domains, i.e. active surface;
- **Phase cooperation:** when a multi-functionality feature cannot be incorporated in a single-phase catalysts, two or more phases are hence considered in order to provide this latter feature.

Among the seven principles, site isolation establishes the importance of having spatially isolated active sites on the catalyst to avoid overoxidation reactions (i.e. formation of CO_x) and thus there must be a limit with respect to the number of hydrocarbon species interacting with lattice oxygen. This surface-located form of oxygen has introduced a significant breakthrough in the study of selective heterogeneous oxidation catalysis which was firstly mentioned in the 1950s [59]. Previous works have shown how lattice oxygen can act as a more efficient oxidizing

agent with respect to its molecular form (i.e. O_2) [58, 59]. The concept relies on the reaction of a reducible metal oxide with hydrocarbons where surface-located oxygen species, defined as $[O^{2-}]_L$, are able to react with two hydrogen atoms coming from the hydrocarbon and thus producing water. In a latter stage, $[O^{2-}]_L$ is regenerated by molecular oxygen.

2.2.1 Nickel oxides

The synthesis of a novel catalysts able to efficiently oxidize ethane into ethylene has been studied for years. However, the possibility to exploit cheap feedstocks (e.g. ethane from shale gas) has lately intensified the research in this area. In this sense, several materials have been developed and carefully analysed as reported elsewhere [53, 60, 61, 62].

The simplest nickel-based catalyst is pure nickel oxide (NiO) which is able to activate ethane at relatively low temperatures, i.e. starting from 300°C . However the selectivity towards ethylene is considerably low [63]. Therefore, the use of NiO in ODH- C_2 is very limited and its performance is easily overcome by other metal oxides such as multi-metallic vanadium-based catalysts.

Despite the questionable results regarding NiO, particular attention has been centred on bi-metallic nickel oxides promoted by other elements such as Li^{1+} , Mg^{2+} , Nb^{5+} , Al^{3+} , Sn^{4+} , among others. In the majority of these mixed oxides, the dopant either contracts or expands the NiO lattice which indicates a formation of a solid solution. Additionally, studies have demonstrated that the dissolution of lower/equal to nickel valence cations (e.g. Li^{1+} , Mg^{2+}) increases a non-stoichiometric form of oxygen in nickel oxides while higher-valence promoters (e.g. Nb^{5+} , Al^{3+} , Sn^{4+}) act as electron donors having hence, an opposite effect. Non-stoichiometric oxygen in NiO catalyses C_2 -to- CO_x reactions and thus its reduction/elimination is favourable in terms of maximization of ethylene selectivity [53, 64]. On this matter, Figure 2.1 shows a correlation between the valence of the promoter (i.e. dopant cation) and ethylene selectivity.

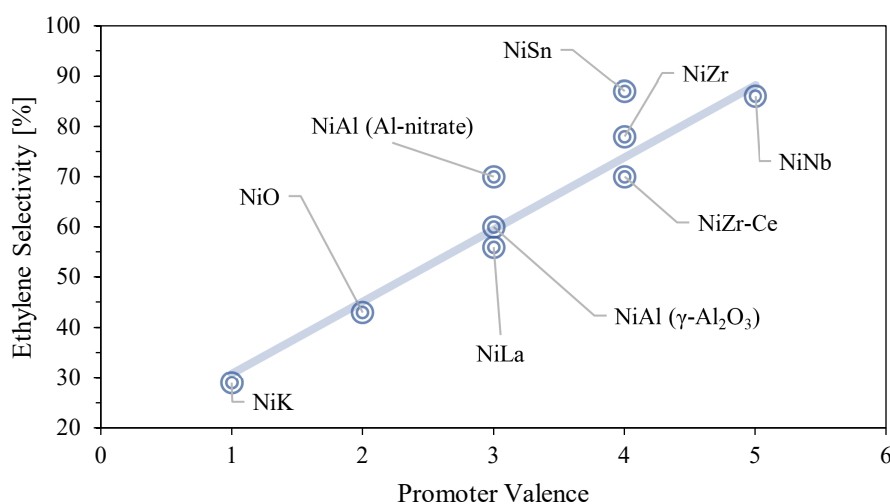


Figure 2.1 – Variation of the ethylene selectivity as a function of the oxidation state of the promoter. Conditions have guaranteed 10 % of ethane molar conversion for each catalyst composition. Adaptation from [64].

Another important parameter to be considered is the acidic/basic character of the catalyst. It has been reported that acidity has an effect on the nature of the nickel active sites and it can influence the adsorption/desorption of ethane, oxygen and ethene [53, 55, 61, 64]. In this way, it has been observed that catalysts present higher ethylene selectivity at high acid characteristics of the promoter. Generally, acidity is determined through the concept of isoelectric point (IEP) where the lower the value, the higher the acidity and vice versa. A previous work [64] has reported that low IEP enhances ethene selectivity for several Ni-based catalysts and thus acid/basic characteristics of the promoters modify the characteristic of nickel species (i.e. specific Lewis acidity). In other words, both the strength and the number of acid sites located in the catalyst surface will influence the ethylene selectivity.

2.2.2 Tin-based nickel oxides (NiO-SnO₂)

Multi-metallic vanadium-based catalyst has been a promising configuration in ODH-C₂. However, its synthesis remains challenging from the standpoint of its reproducibility and energy demand, which is directly linked to the final manufacturing cost. To sum up, additional side-products (i.e. CO) is within the reaction mechanism, which increases the complexity of its eventual application at industrial scale [7]. These observations have been the main motivation for developing alternative configurations to overcome these drawbacks.

On this regard, nickel oxides have shown a promising performance when doped with Nb- or Sn-. In this work, the ODH-C₂ is studied at industrial scale by using NiO-SnO₂ as catalyst. This configuration has proven to be sufficiently effective at relatively low temperatures (< 480°C), where negligible amounts of CO are produced [8].

2.2.2.1 Synthesis

NiO-SnO₂ catalyst was previously synthesized according to what has been proposed by B. Solsona et al. [65, 66]. The catalyst was therefore prepared through an evaporation at 60 °C utilizing a stirred ethanolic solution of nickel nitrate, i.e. Ni(NO₃)₂·6H₂O and tin (II) oxalate (SnC₂O₄). As an additive, oxalic acid was used maintaining an oxalic acid in (Ni + Sn) molar ratio equal to 0.65. The final stage of the synthesis includes a drying process at 120 °C and a calcination using static air for 2 hr at 500 °C.

Following the synthesis process, a catalyst characterization needs to be carried out. This step plays a key role in catalyst development since it allows a deep understanding of the final composition, physical micro/nano-structure, porosity and surface properties.

Further details regarding the synthesis of the catalyst and the respective characterization procedures are out of the scope of this work as they have been fully covered elsewhere [8].

2.3 Kinetics

One of the most important steps in the development of a chemical process, especially those involving catalysis, is the formulation of the kinetic model. Having a detailed knowledge of the process kinetics is a key factor towards the design and rating of chemical reactors at industrial scale. A kinetic model requires mathematical expressions capable of reproducing, with certain

accuracy, the experimental observations. Hence, the size of the catalytic reactor, that is necessary to accomplish a certain yield, will be strictly linked to the reaction kinetics [67].

In accordance with the previous paragraph, the development of the kinetic model for the ODH-C₂ on NiO-SnO₂ catalyst is a key factor to study the process at industrial scale [9]. The first step to construct the kinetic model is to define a reaction scheme (see Figure 2.2) based on observations at laboratory scale.

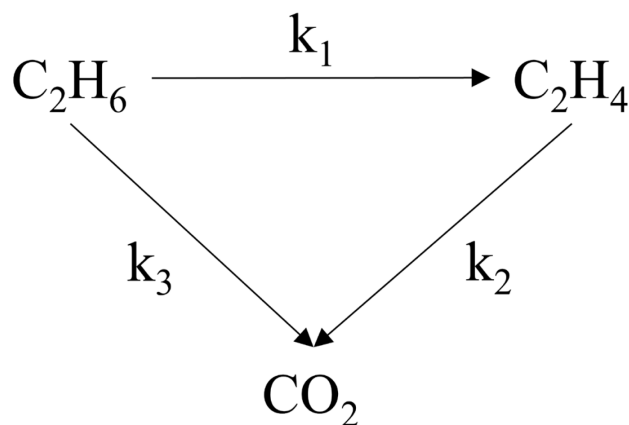


Figure 2.2 – Reaction scheme for the ODH of ethane using a Ni-Sn-O catalyst where k_i represent rate constants [9].

The proposed scheme considers parallel and successive reactions, which were previously enlisted in Table 2.1 and Table 2.2 (see Section 2.1). However, due to experimental observations in previous works [54, 66], chemical reactions involving the formation of CO (see Table 2.2) are not considered [8].

2.3.1 Experimentation

This work is based on previous results where the ODH-C₂ was carried out using an unsupported NiO-SnO₂ as catalyst. Those experiments were performed according to what has been reported by other authors [60], [66] where this catalyst configuration was found to be the optimal one. Furthermore, tests at laboratory scale were carried out under the frame of a collaboration with Universidad Autonoma Metropolitana – Mexico whose intellectual property and experimental data have been utilized at Laboratory for Chemical Technology (LCT) – Ghent University – Belgium for further analysis, including this work.

To performed these experiments, a micro-reactor setup [8] was used where a mixture of ethane, oxygen and nitrogen was used a feedstock. Operating conditions are summarized in Table 2.3.

Table 2.3 – Operating set-up for performing experiments at 1 bar.

Parameters	Unit	Operating Range
Temperature	[°C]	365-480
Ethane molar fraction	[%]	2-14
Oxygen molar fraction	[%]	1.8-9
Space-time	$\left[\frac{\text{g}_{\text{cat}} \text{ S}}{\text{mol}_{\text{C}_2\text{H}_6}} \right]$	15-165

Results of previous test have been used for the construction of a kinetic model using an Eley - Rideal (ER) formalism which has proven to be the most accurate with respect to experimental results [8].

2.3.2 Eley - Rideal formalism (ER)

The principle of this formalism consists on the adsorption of one single molecule onto the catalyst surface while another molecule directly reacts in gas phase without being adsorbed [8, 10]. Table 2.4 shows the reaction mechanism that was consider for the kinetic model. This model was constructed using the following assumptions:

- i. There is only one type of active sites on the catalyst surface;
- ii. oxygen and water are exclusively adsorbed on the active sites;
- iii. steady-state approach is considered;
- iv. superficial reactions are the rate determining steps;
- v. lastly, surface reactions are assumed to be irreversible. These reactions are between adsorbed oxygen and either ethane or ethylene present in the gas phase.

Table 2.4 – Elemental steps for the ODH-C₂ using NiO-SnO₂ as catalyst. Activation energies for direct and inverse reactions, i.e. Ea^d and Eaⁱ respectively, are expressed in (kJ mol⁻¹); while pre-exponential factors are expressed in (mmol g_{cat}⁻¹ s⁻¹) [8].

Step	Elemental reaction	A ^d N _T	A ⁱ N _T	Ea ^d	Ea ⁱ
A	$\text{O}_2 (\text{g}) + 2\text{S} \leftrightarrow 2\text{S}_{\text{oxy}}$	1.92×10^{-1}	5.57×10^8	6×10^{-3}	85.68
1	$\text{C}_2\text{H}_6 (\text{g}) + \text{S}_{\text{oxy}} \rightarrow \text{C}_2\text{H}_4 (\text{g}) + \text{S}_{\text{water}}$	9.20×10^2		66.03	
2	$\text{C}_2\text{H}_6 (\text{g}) + 7\text{S}_{\text{oxy}} \rightarrow 2\text{CO}_2 (\text{g}) + 3\text{S}_{\text{water}} + 4\text{S}$	6.39×10^3		80	
3	$\text{C}_2\text{H}_4 (\text{g}) + 6\text{S}_{\text{oxy}} \rightarrow 2\text{CO}_2 (\text{g}) + 2\text{S}_{\text{water}} + 4\text{S}$	5.53×10^3		82	
B	$\text{S}_{\text{water}} \leftrightarrow \text{H}_2\text{O} (\text{g}) + \text{S}$	1.5×10^{13}	3.13×10^2	99.69	1×10^{-3}

The term S represents an active site onto the catalyst surface and its subindex represent the state of the active site, i.e. free site or associated with another species.

The reaction rate (r_j) of each elemental reaction presented in Table 2.4 are defined by applying the mean-field approximation and the mass action law as represented by Equations (2.1-5). Note that the superscripts d and i represents, respectively, the direct and inverse reaction in step A and B. The formulation of r_j involves a kinetic constant (k_j); the partial pressure of the species involved (p_n); the total concentration of active sites (N_T); the active site fraction (θ_n) and absorption equilibrium coefficients (K_n) for oxygen and water present in reaction A and B, respectively [8].

$$r_A^d = r_A^d - r_A^i = N_T (k_A^d p_{O_2} \theta_S^2 - k_A^i \theta_{oxy}^2) \quad (2.1)$$

$$r_1 = k_1 N_T p_{C_2H_6} \theta_{oxy} \quad (2.2)$$

$$r_2 = k_2 N_T p_{C_2H_6} \theta_{oxy} \quad (2.3)$$

$$r_3 = k_3 N_T p_{C_2H_4} \theta_{oxy} \quad (2.4)$$

$$r_B^d = r_B^d - r_B^i = N_T (k_B^d \theta_{water} - k_B^i p_{H_2O} \theta_S) \quad (2.5)$$

The fraction of active sites associated with oxygen and water is defined by the pseudo-steady-state approximation, as shown by Equations (2.6-7). Since the number of active sites is assumed to be constant during the catalyst life cycle, a global balance of them is represented by Equation (2.8) [8].

$$N_T \frac{d\theta_{oxy}}{dt} = 2 (r_A^d - r_A^i) - r_1 - 7 r_2 - 6 r_3 = 0 \quad (2.6)$$

$$N_T \frac{d\theta_{water}}{dt} = r_1 + 3 r_2 + 2 r_3 - (r_B^d - r_B^i) = 0 \quad (2.7)$$

$$\theta_{oxy} + \theta_{water} + \theta_S = 1 \quad (2.8)$$

Finally, the global reaction rate for each component n (i.e. C_2H_6 , O_2 , CO_2 , C_2H_4 and H_2O) can be determined as combination of each step individually, as suggested by Equation (2.9).

$$R_n = \sum_{j=1}^5 v_{n,j} r_j \quad (2.9)$$

where $v_{n,j}$ is the stoichiometric coefficient of component n in the reaction j .

2.3.3 Kinetic parameters estimation

Although the estimation of the kinetic parameters is out of the scope of this work due to its treatment elsewhere [8], some fundamental aspects need to be mentioned for a general comprehension of the calculation methodology.

The reaction rate coefficients have been calculated using the Arrhenius equation, where each activation energy is estimated by regression, which is carried out by maintaining fixed the pre-exponential factors [68]. This is possible since it has been demonstrated that the first reaction of the sequence presented in Table 2.4 is rate-determinant [69]. The pre-exponential factor for direct reactions are estimated by the transition state theory, which includes the estimation of the entropy change between both states, reactive and transitional. Additionally, the pre-exponential factor for indirect reactions are calculated according to the principle of microscopy reversibility, which involves the calculation of the reaction entropy of each elemental reaction [8].

The estimation of activation energies for each reaction presented in Table 2.4 is carried out through a minimization of the objective function RSS (β). The least square method is utilized to find an appropriate fitting between calculated and observed molar flow rates of each species involved in the kinetic mechanism. A generic expression for the objective function is presented by Equation (2.10):

$$RSS_n = \sum_{n=1}^{n_{calc}} \omega_n \sum_{j=1}^{n_{exp}} (F_{j,n} - \hat{F}_{j,n})^2 \xrightarrow{\beta_1, \beta_2, \beta_3, \dots, \beta_n} \min \quad (2.10)$$

where β is a vector whose coefficients β_i are the optimal parameter values; n_{exp} and n_{calc} are the number of experiments and calculated responses respectively; $F_{j,n}$ and $\hat{F}_{j,n}$ are the experimental and calculated molar flow rates of each component n ; and w_n is the weight associated to the n component.

The molar flow rates are calculated through an isothermal pseudo-homogeneous reactor model where the pressure drop within the fixed bed is assumed to be negligible. It results a system of ordinary differential equations (ODEs), which are solved using proper solver numerical subroutines [70].

2.4 Reactor model

During the process design of a multi-tubular packed bed reactor, the performance of the reactor is generally predicted based on the modelling of a single tube; therefore it is assumed that each tube behaves similarly in terms of concentration and temperature profiles, pressure drop, etc. [14, 15].

Having said this, the ODH-C₂ using a NiO-SnO₂ catalyst was simulated in a single tube of a multi-tubular packed-bed reactor following a rigorous approach presented in previous works [10, 16]. This methodology allows to simulate the non-adiabatic/non-isothermal behaviour of a packed-bed reactor which more accurately approximates real conditions. The heat transfer within the reactor is undertaken by the calculation of effective parameters, i.e. effective thermal conductivity (k_{eff}) and wall heat-transfer coefficient (h_w). These parameters describe the heat transfer in the core of the packed-bed and the heat transport phenomena in the interface

coolant-catalytic bed. A series of reliable engineering correlations have been used to calculate these parameters (see Appendix B).

The hydrodynamics in an industrial-scale packed-bed reactor is undertaken by solving the Navier-Stokes equation including additional terms proposed by Darcy and Forchheimer (NSDF) [17, 18]. This latter equation is simplified by considering the axial velocity component (v_z) as function of the axial and radial coordinate, while the radial velocity component (v_r) is neglected. The hydrodynamics are, therefore, described by the continuity equation and simplified NSDF in its two-dimensional form; respectively, represented by Equations (2.11-12) [19, 11],

$$\frac{\partial \varepsilon_b v_z}{\partial z} = 0 \quad (2.11)$$

$$\begin{aligned} \rho_f \left[\frac{\partial \varepsilon_b v_z}{\partial t} + \varepsilon_b v_z \frac{\partial \varepsilon_b v_z}{\partial z} \right] = & - \frac{\partial \varepsilon_b p_z}{\partial z} + \mu \left[\frac{1}{r} \frac{\partial}{\partial r} \left(r \frac{\partial \varepsilon_b v_z}{\partial r} \right) + \frac{\partial^2 \varepsilon_b v_z}{\partial z^2} \right] - \dots \\ & \dots - \frac{\mu}{K} \varepsilon_b v_z - \frac{\rho_f}{K_z} \varepsilon_b^2 v_z^2 + \varepsilon_b \rho_f g_z \end{aligned} \quad (2.12)$$

where K and K_z are permeability parameters given in terms of Ergun relations [19], ρ_f is the fluid density, μ is the dynamic viscosity, ε_b is the packed-bed void fraction and g_z is the axial component of the gravity acceleration. Initial and boundary conditions are represented by Equations (2.13-17),

$$t = 0; \quad v_z(0, r, z) = v_z(0, r, z)_{ss} \quad (2.13)$$

$$z = 0; \quad v_z = v_{in} \quad (2.14)$$

$$z = L_{re}; \quad \frac{\partial v_z}{\partial z} = 0 \quad (2.15)$$

$$r = 0; \quad \frac{\partial v_z}{\partial r} = 0 \quad (2.16)$$

$$r = R_t; \quad v_z = 0 \quad (2.17)$$

where R_t is the tube radius. Although for simplicity is common to assume a constant radial void fraction profile across the packed-bed, for tube-to-particle diameter ratio smaller than 11 the wall effect begins to influence the ε_b for randomly packed-beds [20]. Thus, a mathematical expression to radially describe the void fraction profile is required when $d_t/d_p < 11$. In this work the profile is constructed using the empirical model developed by de Klerk [21].

When the dimensionless group $[(R_t - r) (d_p)^{-1}] \leq 0.637$, the void fraction as function of the radial coordinate adopts the form represented by Equation (2.18),

$$\varepsilon_b(r) = 2.14 \left(\frac{R_t - r}{d_p} \right)^2 - 2.53 \left(\frac{R_t - r}{d_p} \right) + 1 \quad (2.18)$$

while for $[(R_t - r) (d_p)^{-1}] > 0.637$, the void fraction as function of the radial coordinate is calculated by Equation (2.19),

$$\begin{aligned} \varepsilon_b(r) = \bar{\varepsilon}_b + 0.29 \exp \left(-0.6 \left(\frac{R_t - r}{d_p} \right) \right) \cdot \left[\cos \left(2.3\pi \left(\left(\frac{R_t - r}{d_p} \right) - 0.16 \right) \right) \right] + \dots \\ \dots + 0.15 \exp \left(-0.9 \left(\frac{R_t - r}{d_p} \right) \right) \end{aligned} \quad (2.19)$$

where $\bar{\varepsilon}_b$ is the average bed porosity and d_p is the particle diameter.

Summarizing, Equations (2.11-19) described the fluid dynamics in a single-tube packed-bed reactor in absence of chemical reaction. Nonetheless, a complete mathematical description of the pseudo-heterogeneous model predicts concentration and temperature profiles based on the principle of mass and energy conservation, including effective transport coefficients. On this matter, governing expressions in both gas and solid phase are represented by Equations (2.20-21) and Equations (2.22-23), respectively [10, 15, 19, 11].

$$\varepsilon_b \frac{\partial C_n}{\partial t} + u_0 \frac{\partial C_n}{\partial z} = \varepsilon_b D_z \frac{\partial^2 C_n}{\partial z^2} + \varepsilon_b D_r \left(\frac{\partial^2 C_n}{\partial r^2} + \frac{1}{r} \frac{\partial C_n}{\partial r} \right) + (1 - \varepsilon_b) k_g a_s (C_{ns} - C_n) \quad (2.20)$$

$$\begin{aligned} \varepsilon_b \rho_f C_{pf} \frac{\partial T}{\partial t} + u_0 \rho_f C_{pf} \frac{\partial T}{\partial z} = k_{eff,z} \frac{\partial^2 T}{\partial z^2} + k_{eff,r} \left(\frac{\partial^2 T}{\partial r^2} + \frac{1}{r} \frac{\partial T}{\partial r} \right) + \dots \\ \dots + (1 - \varepsilon_b) h_g a_s (T_s - T) \end{aligned} \quad (2.21)$$

$$(1 - \varepsilon_b) \frac{\partial C_{ns}}{\partial t} = (1 - \varepsilon_b) k_g a_s (C_{ns} - C_n) + \rho_b \sum_{j=1}^r v_{nj} r_j \quad (2.22)$$

$$\rho_b C_{ps} \frac{\partial T}{\partial t} = (1 - \varepsilon_b) h_g a_s (-T_s + T) + \rho_b \sum_{j=1}^r (-\Delta H_j) r_j \quad (2.23)$$

where C_n is the molar concentration of component n ; C_{ns} is the latter analogous for the solid phase; D_r and D_z are, respectively, the radial and axial diffusion coefficients; ρ_b is the density of the packed-bed; C_{ps} and C_{pf} are, respectively, the heat capacity of the solid and gas phase; $k_{eff,r}$ and $k_{eff,z}$ are, respectively, the effective thermal conductivity along the radial and axial

direction; T_s is the temperature of the solid phase; h_g and k_g are, respectively, the interfacial heat and mass transfer coefficients; and a_s is the particle surface area per unit volume of packed-bed.

These set of partial differential equations have their corresponding initial and boundary conditions, represented by Equations (2.24-30) [10],

$$t = 0; \quad C_n(0, r, z) = C_n(0, r, z)_{SS}; \quad C_{ns}(0) = C_{ns}(0)_{SS} \quad (2.24)$$

$$T(0, r, z) = T(0, r, z)_{SS}; \quad T_s(0) = T_s(0)_{SS} \quad (2.25)$$

$$z = 0; \quad u_0 C_{n0} = u_0 C_n - \varepsilon D_z \frac{\partial C_n}{\partial z} \quad (2.26)$$

$$u_0 \rho_f C_{pf} T_0 = v_z \rho_f C_{pf} T - k_{eff,z} \frac{\partial T}{\partial z} \quad (2.27)$$

$$z = L_{re}; \quad \frac{\partial C_n}{\partial z} = 0; \quad \frac{\partial T}{\partial z} = 0 \quad (2.28)$$

$$r = 0; \quad \frac{\partial C_n}{\partial r} = 0; \quad \frac{\partial T}{\partial r} = 0 \quad (2.29)$$

$$r = R_t; \quad \frac{\partial C_n}{\partial r} = 0; \quad -k_{eff,r} \frac{\partial T}{\partial r} = h_w(T - T_{bath}) \quad (2.30)$$

2.4.1 Fortran subroutine

The development of the pseudo-heterogeneous model is able to accurately describe the fluid dynamics and transport phenomena involved in a single tube randomly filled with catalyst pellets. Furthermore, a kinetic mechanism is added to this non-reactive model of the reactor internals, to fully design a mathematical description for the ODH-C₂ using NiO-SnO₂ catalysts.

This model is hence composed by a complex set of parabolic partial differential equations (PDEs), which were solved numerically through axial and radial coordinates using an orthogonal collocation method [19]. The derivative set of ordinary differential equations (ODEs) was solved numerically by the Runge-Kutta-Fehlberg method. Further details regarding the calculation procedure has been widely covered elsewhere [19].

The governing equations of the model have been coded into a subroutine written in Fortran[®] programming language. This subroutine is capable of numerically solving models of significant mathematical complexity, such as the pseudo-heterogeneous reactor model treated in this work. Since a two-dimensional model has been proposed, the subroutine is able to estimate temperature and concentration profiles along the radial and axial coordinates, which is basically the output of the code (see Figure 2.3).

The solver has been condensed into an executable to facilitate the customization of each simulation. In this sense, auxiliary .txt files are used to establish different parametric configurations to run the solver, i.e. inlet composition, catalyst particle diameter, mass flux, operating temperature and pressure, among others. This tool has been the main source for data

acquisition used in this work with the aim of performing a multi-objective optimization at reactor level.

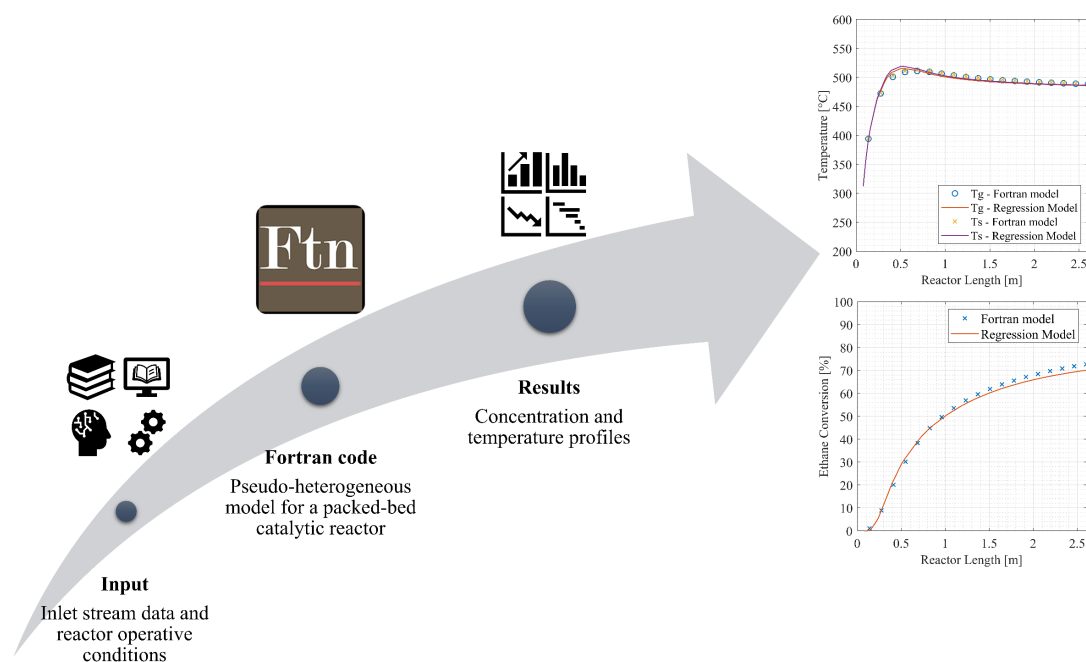


Figure 2.3 – Steps for the simulation of the reactor performance under a set of user-defined parameters. An in-house code developed in Fortran is used as simulation machine.

Due to the complexity of the model, a remarkable computational effort is required to run the code. As a matter of facts, a high-performance laptop (i.e. processor Intel[®] Core[™] i7-7700HQ CPU @ 2.80GHz with 16 GB memory capacity) is able to run up to 4 simulations in parallel using approximately 85% of the CPU capacity, needing 24 hr of time to reach full converge. One of the main goals of this work is, therefore, to develop a mathematically simpler model able to describe the ODH-C₂ on an industrial-scale packed-bed reactor, and to evaluate its performance under different operating conditions.

[This page was intentionally left in blank]

Chapter 3

3. Multiparametric model design

As introduced in the previous chapter, the first approach for a reactor model design is to analyse its performance at a small scale by studying a single tube of the multi-tubular catalytic reactor. Due to reciprocity and geometrical symmetry, the events observed in one tube can be considered to be equivalent to each tube within the reactor. A one-dimension study was carried out along the catalytic bed by taking into account a fixed reactor length (L_{re}) equal to 2.6 m. With respect to the radial coordinate, a dimensionless scale was applied having its origin in the centre of the tube till reach the tube wall (i.e. $r_{ss} = 1$), as shown in Figure 3.1.

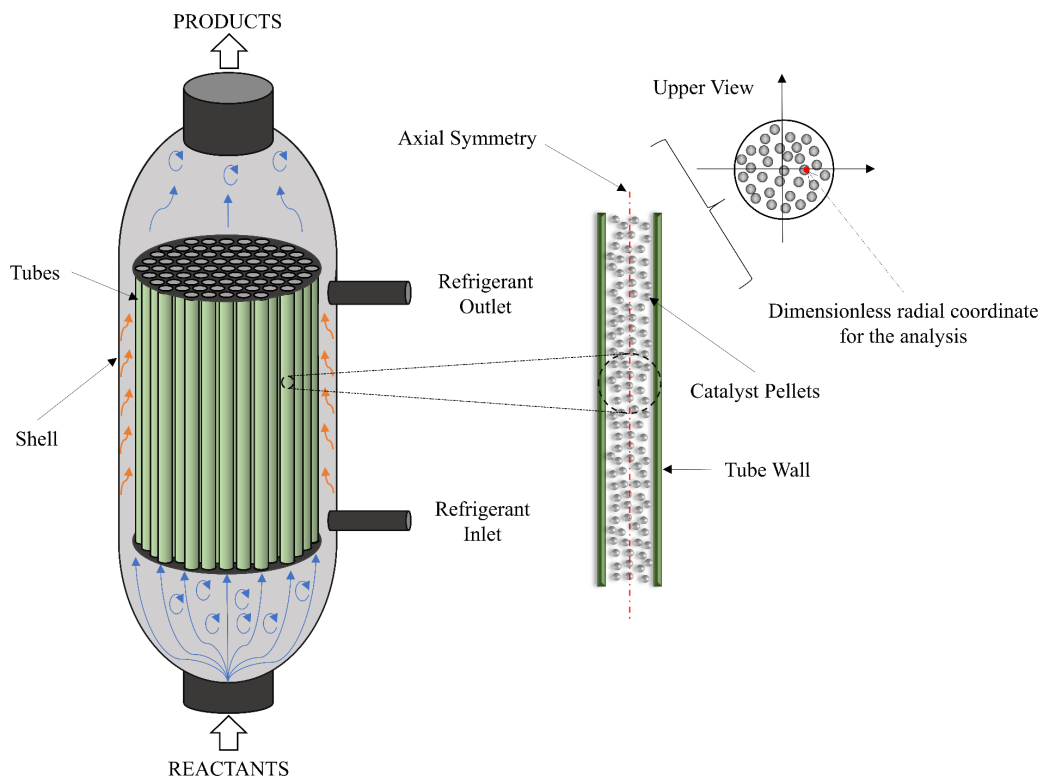


Figure 3.1 – Scheme of a multi-tubular packed-bed reactor. The figure shows the axial symmetry of one tube as well as the dimensionless radial coordinate used for the multiparametric study in this work.

A preliminary multi-parametric analysis was performed with the final goal of reaching the optimal operating conditions to maximize ethylene selectivity and reactants conversion (i.e. ethane and molecular oxygen). The ODH- C_2 was simulated using an in-house code developed in Fortran[®] programming language which describes the pseudo-heterogeneous model presented in the previous chapter. This complex model is able to chemically and physically described the reactions involved in terms of kinetics, hydrodynamics and transport phenomena in a two-dimension approach. Therefore, it is utilized as a reliable source for the data acquisition

procedure. In this way, by changing the initial configuration of the reactor (i.e. inlet compositions, bath temperature, tube-to-particle diameter ratio and mass flux) it is possible to analyse the influence of each parameter towards the overall reactor performance. Furthermore, the temperature profile along the reactor length of both gas and solid phase can be studied in order to establish the conditions which enhances thermal instabilities within the bulk of the catalytic bed.

The mathematical complexity of a two-dimensional pseudo-heterogeneous model guarantees high accuracy while describing both composition and temperature profiles at a considerable computational cost. Nonetheless, for the sake of a practical process simulation at industrial-scale where several processes downstream the ODH-C₂ reactor are included, a simpler model might be implemented. Even though lower computational resources are main requirements, a simpler model should also be able to reproduce trustworthy results with the highest possible accuracy with respect to its counterpart. Lastly, the sensitivity towards different parametric configurations should be statistically equivalent in both models, observing the same effect where identical conditions are imposed within the domain.

Having acknowledged that, a Design of Experiments (DoE) was implemented in order to generate a set of multiparametric equations able to describe the ODH-C₂ in a single reactor tube. Once the accuracy of the new model is verified, an evaluation is conducted in order to analyse the full domain of each parameter of interest with the scope of selecting the optimal operating conditions.

Summarizing, the main objectives of this section are:

- to determine the effect of pre-selected parameters on the overall performance of a multi-tubular packed-bed reactor to study the ODH-C₂ by using NiO-SnO₂ catalysts;
- to construct a simpler mathematical model able to predict the concentration and temperature profiles within the reactor;
- to find an optimal parameter configuration with the scope of maximizing the reactor performance throughout a response surface methodology (RSM) approach.

3.1 Design of experiments

Due to the apogee of technology in terms of informatic systems and computer science, scientist and engineers are using computer simulations to replicate physic models utilizing complex mathematics [71]. The complexity of these models can vary depending on each case-study including linear and nonlinear algebraic equations as well as ordinary and partial differential equations. To sum up, there are uncountable examples of real physical systems where an analytic solution would be extremely complicated to formulate, if not impossible. To solve this, one could perform a design of experiments which is, essentially, a procedure to determine cause and effect relationships whose main objective is to simplify the development of mathematical models [71, 72]. On chemical engineering, most of the experimental work could be optimize in terms of time and resources by a DoE analysis. Some of them are:

- complex physic systems where both linear and nonlinear relationships are observable with many variables interacting to each other;
- routine analysis of all the production chain;
- selection of factors by their significance or effects on measured responses;
- create or simplify a mathematical model, etc.

In general terms, a DoE study can be divided into 8 fundamental steps as shown in Figure 3.2. This pathway is followed independently of the DoE type (i.e. comparative designs, screening designs, response surface methodology or regression modelling).

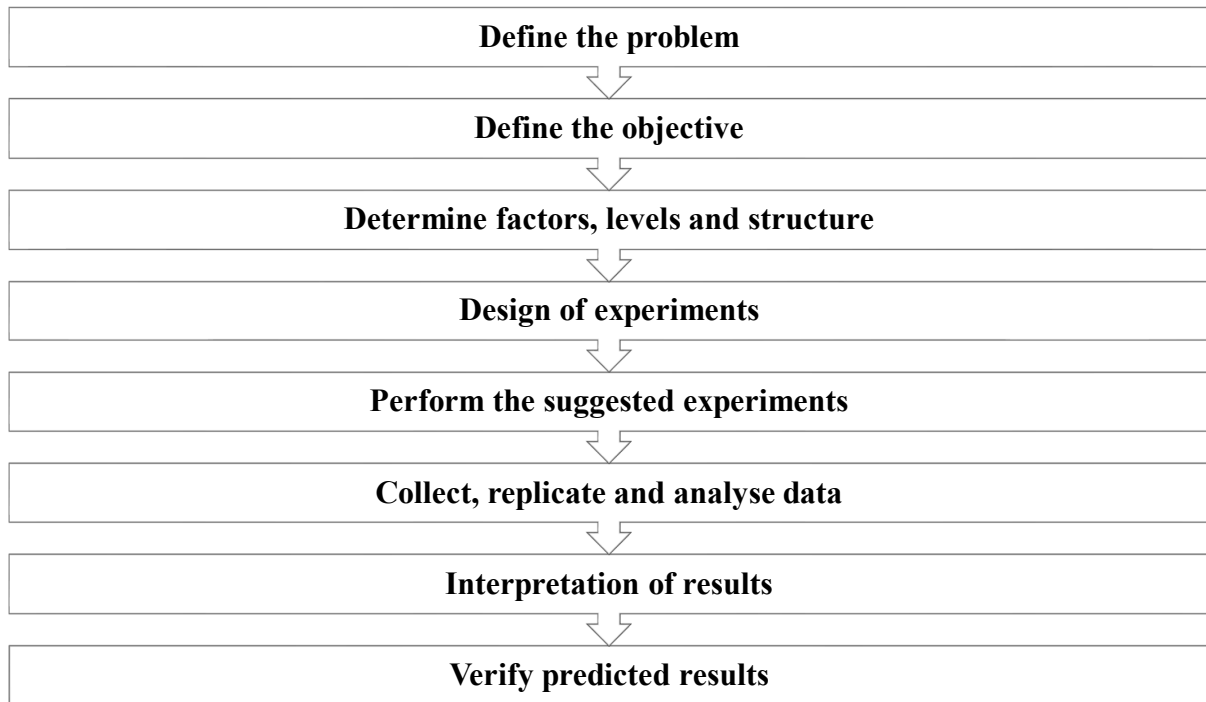


Figure 3.2 – Experimental design stages. Adaptation from [72].

Recapitulating, a DoE study constructs a simple mathematical model which is capable of explaining the contribution of each factor to the system. Nonetheless, statistical tools are used to prove the reliability of the model and to improve its overall accuracy on describing the case-study.

3.1.1 Response Surface Methodology

The response surface methodology (RSM) is a DoE based on the optimization and understanding of a process by the analysis of the output factors [72]. The optimization procedure utilizes mathematical and statistical tools to evaluate the fit of polynomial equations to the data available from experimentation. It has been widely improved since its formulation due to documented evolution of computer science and it has centred the attention of the industrial sector. RSM is hence a highly valuable tool in research activities when it comes to optimization and multiparametric analysis [73]. The general mathematical formula is presented as Equation (3.1), usually referred as mechanistic model [71, 73]:

$$\Phi = f(x_1, x_2, x_3, x_4, \dots, x_j) + \epsilon \quad (3.1)$$

where Φ is the response given by the model which is a pre-defined function of controllable factors (i.e. independent variables) represented by $x_1, x_2, x_3, x_4, \dots, x_j$; while ϵ represents

statistical errors from other sources of variability which are not accounted by the function (e.g. measurement errors). These factors will be selected according to the parameters that better describes the event of interest.

One important observation is related to the units of the independent variables. Normally, several units are involved among the independent variables and, even being the same for some variables, they might be tested over different ranges. To solve this inconsistency one should normalize the parameters before performing a regression analysis. The resulting coded variables are forced to vary from -1 to 1 and thus the units of the parameters become irrelevant [73, 74]. Nowadays, this action is carried out by specialized software and the commonly used expression is presented by Equation (3.2),

$$F = \frac{x - (x_{max} + x_{min}) 0.5}{(x_{max} + x_{min}) 0.5} \quad (3.2)$$

where x is the natural variable, x_{max} and x_{min} represent the range of that natural variable and F is the coded variable.

Because of its simplicity and wide range of application, it is very common to use either first-order or second-order polynomial models to describe the RSM. A first-order model is usually represented by linear functions of independent variables, while a second-order model also includes statistically relevant quadratic and cross-product terms. Equation (3.3) can be therefore written more explicitly as suggested by Equation (3.3) [73],

$$y = \beta_0 + \sum_{i=1}^j \beta_i F_i + \sum_{i,k=1}^j \beta_{ik} F_i F_k + \sum_{i=1}^j \beta_{ii} F_i^2 + \dots + \epsilon \quad (3.3)$$

where β_0 , β_i , β_{ik} and β_{ii} are polynomial coefficients.

The value of the parameters presented in Equation (3.3) are generally estimated through the least square method during a procedure called model fitting [23]. The solution to the normal equations will be, therefore, the least square estimators of the regression coefficients b_0 , b_1 , ..., b_k . Consequently, a similar expression is obtained as shown in Equation (3.4);

$$\hat{y} = b_0 + \sum_{i=1}^j b_i F_i + \sum_{i,k=1}^j b_{ik} F_i F_k + \sum_{i=1}^j b_{ii} F_i^2 \quad (3.4)$$

where \hat{y} is the fitted value and thus, $e = y - \hat{y}$ represents the model residuals.

3.1.1.1 Central Composite Design (CCD)

Having introduced the concept of RSM, the ODH-C₂ is studied through the analysis of surface equations under a central composite design scheme which should be capable of predicting the behaviour of the system under different parametric configurations, thus identifying an optimum operating region within the domain [75].

A central composite design (CCD) has been one of the most used RSM for optimization of several processes due to its simplicity and general applicability on second-order response surface models [72]. Generally, coded factors are utilized for the model construction which can assume low (-1), center (0) and high (1) levels to evaluate the design where both axial and center points are included (see Figure 3.3). The latter ones are added to provide protection against curvature from second-order effects together with a more accurate error estimation [73]; while axial points improve the precision of the model [72].

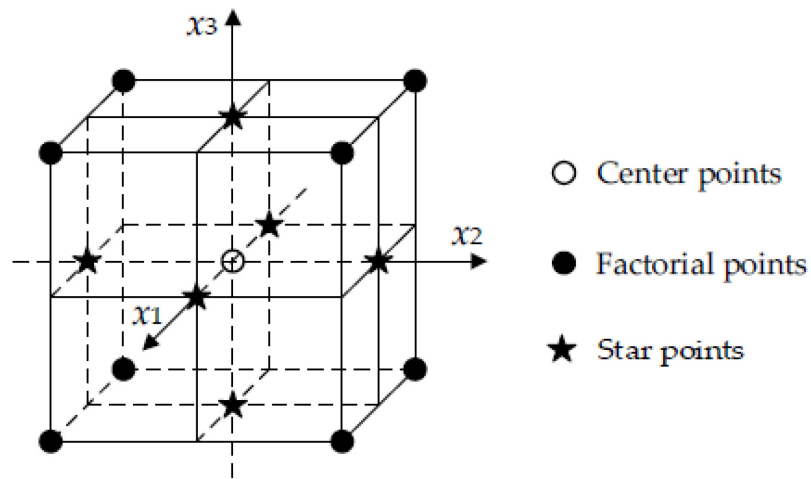


Figure 3.3 – Scheme of a three-factor central composite design [22].

CCD will therefore predict the effect of each factor and the curvature present in the model where the number of experimental samples can be given by $(2^k + 2k + n_{cp})$. In this latter expression, k is the number of factors and n_{cp} represents the number of central points.

3.2 Multiparametric analysis

Having acknowledged the content of Section 3.1, a RSM study was applied in a commercial software JMP 15[®] in order to find the optimal configuration regarding the ODH-C₂ considered in this work. The first step was to select a set of factors that accurately describe the chemical process, and the most important responses. These responses include the variables to be maximized, i.e. the ethylene selectivity and the conversion of ethane and oxygen; in addition to the relevant physical parameter, i.e. the temperature profile of both gas and solid phase. The range of the factors and responses used in this work are summarized in Table 3.2 and Table 3.3.

Table 3.1 – Factors for the development of the multiparametric equations able to describe the ODH-C₂ in an industrial-scale packed-bed reactor.

Factors		Unit	Range	
Description	Nomenclature			
Inlet molar fraction of ethane	$Y_{C_2H_6}$	[%]	2	8
Inlet molar fraction of oxygen	Y_{O_2}	[%]	8	14
Bath temperature	T_{bath}	[°C]	380	480
Tube-to-particle diameter ratio	d_t/d_p	[-]	3	9
Mass flux	MF	[kg m ⁻² hr ⁻¹]	5×10^3	15×10^3

Table 3.2 – Responses for the development of the multiparametric equations able to describe the ODH-C₂ in an industrial-scale packed-bed reactor.

Responses		Unit	Range	
Description	Nomenclature			
Ethane molar conversion	$X_{C_2H_6}$	[%]	0	100
Oxygen molar conversion	X_{O_2}	[%]	0	100
Ethylene selectivity	$S_{C_2H_4}$	[%]	0	100
Gas phase temperature	T_g	[°C]	200	650
Solid phase temperature	T_s	[°C]	200	650

Regarding the domain for each factor, their selection has been effectuated based on practical considerations. The inlet gas mixture is composed mainly by molecular nitrogen (N₂) which provides an inert atmosphere. Values of C₂H₆/O₂ ratio were strictly selected in order to avoid the explosive region of the feed mixture [24]. In this way, $Y_{C_2H_6}$, Y_{O_2} and T_{bath} were considered while studying the kinetic mechanism. With respect to the remaining factors (i.e. d_t/d_p and MF), their relevance towards the maximization of the reactor performance has been proven according to previous contributions [10, 15, 19] and they are, hence, considered in this work.

The reactor dimensions and operating conditions simulated in this work, correspond to common configurations for multi-tubular packed-bed reactors where heterogeneously catalysed oxidation reactions take place (see Table 3.3).

Table 3.3 – Reactor configuration for ODH-C₂ using NiO-SnO₂ as catalyst.

Fixed parameters	Unit	Value	Reference
Reactor length (L_{re})	[m]	2.6	[10, 19]
Packed-bed density (ρ_b)	[kg _{cat} m ⁻³ _r]	75	[8]
Inlet temperature (T_i)	[°C]	200	[11]
Operating pressure (P_{op})	[bar]	1	[10, 19]
Tube diameter (d_t)	[m]	0.025	[10]

The chosen factors must be normalized due to the unit inconsistency, as introduced in Section 3.1.1.1. On this regard, three experimental levels have been selected as low (-1), medium (0) and high (+1) level of independent factors, whose values are summarized in Table 3.4.

Table 3.4 – Experimental design under a central composite design scheme.

Factors		Units	Levels		
			Low (-1)	Medium (0)	High (+1)
F _a	T _{bath}	[°C]	380	430	480
F _b	Y _{C₂H₆}	[%]	2	5	8
F _c	MF	[kg m ⁻² hr ⁻¹]	5×10 ³	10×10 ³	15×10 ³
F _d	Y _{O₂}	[%]	8	11	14
F _e	d _t /d _p	[-]	3	6	9

It is important to point out that there is a nonlinear relationship between the number of trials requested with respect to the number of factors. Under the above mentioned configuration, this case-study required 44 simulations in order to obtain sufficient data to carry out the DoE. The selected model was a CCD composed by five independent factors, two center points ($n_{cp} = 2$) and ten axial points giving, therefore, the number of simulations cited before. These configurations are shown in detail in Table C.1 (see Appendix C), where results from each simulation also enlisted.

On average, each simulation required ca. 20-24 hours to be successfully completed, in spite of some exceptions where the time required was lower, i.e. approximately 4-6 hours. Therefore, the required computational effort varies according to the operating conditions imposed by the user.

Concentration and temperature profiles calculated using the detailed model serve as the response data. While the temperature profile of both phases is directly determined from the model, the concentration of each specie (in kmol m⁻³) needs to be properly manipulated to generate values for the pre-defined responses. On this matter, ethane and oxygen conversion and ethylene selectivity are calculated as shown in Equations (3.5-7).

$$X_{C_2H_6} = \frac{F_{C_2H_6,in} - F_{C_2H_6,out}}{F_{C_2H_6,in}} \times 100 \quad (3.5)$$

$$X_{O_2} = \frac{F_{O_2,in} - F_{O_2,out}}{F_{O_2,in}} \times 100 \quad (3.6)$$

$$S_{C_2H_4} = \frac{F_{C_2H_4,out}}{(F_{C_2H_6,in} - F_{C_2H_6,out})} \times 100 \quad (3.7)$$

The study was carried out by considering a total of 25 points along a single reactor tube (i.e. 25 axial coordinates compressed within the interval $L_{re} = [0, 2.6][m]$) in a fixed dimensionless radial position ($r_{dss} = 0.5$). These points were strategically taken by considering critical zones along the reactor where hot spots are most likely to be produced and thus zones where the model can deviate considerably from the normal operative conditions [25, 26]. Figure 3.4 shows more schematically the chosen axial coordinates.

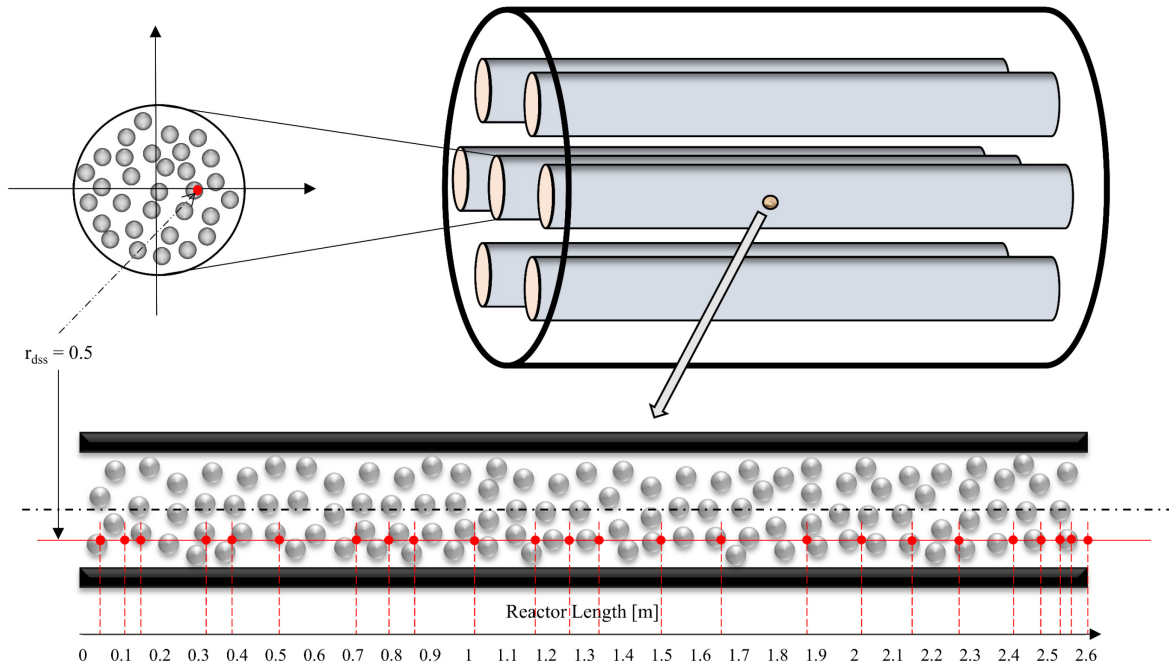


Figure 3.4 – Axial cross-section of a reactor tube filled with catalyst pellets. Selected axial points for the model development are shown. From left to right: $L_{re} = [0.0564, 0.11, 0.15, 0.23, 0.33, 0.39, 0.51, 0.72, 0.79, 0.86, 1.02, 1.18, 1.26, 1.34, 1.50, 1.66, 1.88, 2.02, 2.15, 2.27, 2.41, 2.49, 2.54, 2.56, 2.6]$.

At this point, a DoE analysis is performed at each coordinate of the axial discretization presented in Figure 3.4 (i.e. 25 experimental designs). In this sense, it is possible to recreate complete concentration and temperature profiles along the packed-bed. Having acknowledged that, the complex pseudo-heterogeneous ODH- C_2 reactor model should be reproducible by a set of algebraic equations (see Equation (3.4)), which can be solved with a significant reduction on computational costs. This last improvement is essential for pursuing a multi-objective optimization.

3.3 Parameter significance and model robustness

To be accepted, the new model design must be statistically tested to prove its accuracy while comparing results with the source. This will be the final proof of the model reliability for describing the case-study. In this way, a complete statistical analysis must be performed beforehand to verify the significance of the chosen parameters and the statistical quality of the model. For each response, an analysis of variance (ANOVA) is carried out to study the adequacy of the regression model.

The analysis begins with a statistical significance evaluation of first-order parameters and their respective second-order ones, i.e. quadratic and interaction terms. The objective of this step is to remove the less significant items from the predictive equations as well as providing useful information about what parameters have the highest influence towards the goal of each response.

After evaluating the parameter significance, the next step is to generate the regression coefficients. Coefficients are estimated using the least square method and the t -test is carried out to evaluate its reliability with a 95% interval of confidence.

In order to quantify the quality of fit between predicted and observed values, a set of parity plots and model residuals are accounted. The coefficient of determination (*R-squared*) is calculated and compared with its adjusted form (*R-squared adj.*). There should not be a difference higher than 0.2 between each other in order to be in a reasonable agreement [76]. The global significance of each regression model is also quantified through the F -value, where 4.05 is considered as the minimum threshold for the model predicting adequacy.

3.3.1 Ethane conversion

Although the model has been designed to estimate the ethane conversion along the reactor, at the end what matters the most is its value at reactor output conditions (i.e. $L_{re} = 2.6$ m). The motivation for this is that the final ethane conversion directly determines the reactor performance and thus, intermediate values are not considerably meaningful.

The ANOVA study of the regression model for this response is shown in Table D.1 (see Appendix D). The statistical analysis results indicate that all the main factors are highly significant (p -value < 0.0001) except for F_e (i.e. d_i/d_p). However, this latter parameter has shown a remarkable significance in its quadratic form, i.e. F_e^2 ; being the only quadratic factor statistically relevant. Interaction parameters have also shown to be significant, which means that the regression model should include these second-order parameters to adequately predict the response.

Results from the analysis indicate that d_i/d_p does not have a linear effect towards ethane conversion but it does have a quadratic effect, meaning that this factor is still relevant in the regression model. The second-order effect demonstrates that either a local maximum or minimum is located within the domain of this latter variable.

Factors that have not accomplished the significance level requirements do not represent a reliable source of variability for the response, hence their regression coefficients are excluded from the model. Once this procedure is performed, it is possible to construct a mathematical expression as a function of the coded factors for ethane conversion. The regression model is represented by Equation (3.8).

$$X_{C_2H_6} = 72.99 + 20.38 F_a - 10.11 F_b - 8.77 F_c + 4.30 F_d - 6.23 F_a^2 - 12.10 F_e^2 - \dots \quad (3.8)$$

$$\dots - 4.54 F_a F_b + 4.37 F_a F_c + 2.58 F_a F_d + 3.08 F_b F_c + 2.92 F_b F_d$$

An important verification of the model accuracy is given by the parity diagrams and its respective residual plot (see Figure 3.5). For the majority of scenarios, the model for ethane conversion fits the observed data with an error margin lower than 7%. With respect to the residual plot, there is no evidence of a systematic association between the predicted value and the response residual, meaning that there is not a lack of fit by the model and the error follows a normal distribution.

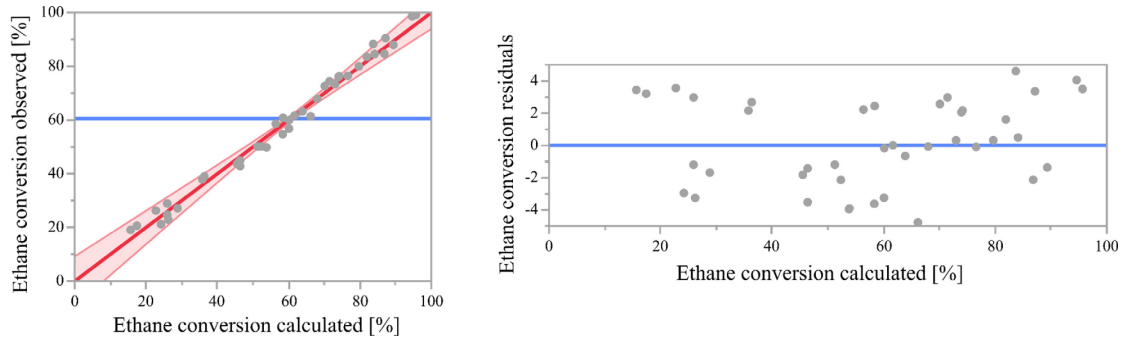


Figure 3.5 – From left to right, ethane conversion prediction plot and its respective plot of residuals.

Table 3.5 summarizes the statistical data of the model where the *F*-value indicates high accuracy for predicting the response. The *R-squared* value indicates that a high proportion of the variation in the response can be attributed to the model rather than to random errors, which is another prove of a good fit capacity by the model.

Table 3.5 – Summary of fit for ethane conversion.

Source	Value	df	Sum of Squares	MS	F-value	Prob > F
Model	-	20	24799.3	1240.0	89.2854	<.0001
Residual	-	23	319.4	13.9		
Total	-	43	25118.8			
R-squared	0.987					
R-squared Adjusted	0.976					

3.3.1.1 Model robustness

A similar procedure was performed for the remaining axial points, under the same criteria for the statistical analysis. A comparison between Fortran simulation data and results from the regression model is used to verify the model reliability

As introduced previously, intermediate values of ethane conversion are not crucial in terms of the reactor performance optimization, where only the final value matters. Yet, those values are

useful to identify possible anomalies of the model while describing both concentration and temperature profiles. On this matter, a set of MATLAB[®] plots were constructed for further analysis and comparison of the 44 experiments with the regression model.

Figure 3.6 shows the evolution of ethane conversion under each factor level configuration; i.e. (-1), (0) and (+1) for each factor simultaneously. Results show an almost identical trend of the ethane conversion along the packed-bed for both the source and the regression model. The local error between the observed and predicted value at outlet conditions is 3.19%, 3.05% and 2.58% in Figure 3.6 (a), (b) and (c), respectively.

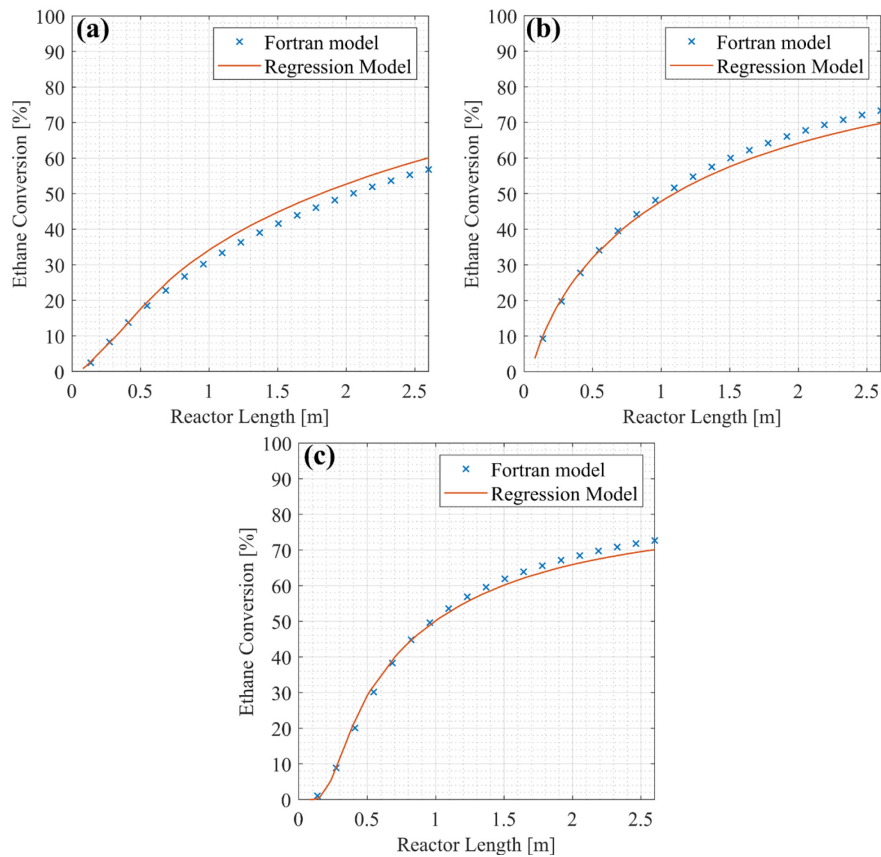


Figure 3.6 – Ethane conversion along the catalytic bed in a single reactor tube. (a) Represents the 29th experiment; (b) represents the 17th experiment and (c) represents the 3rd experiment. See Appendix C for further details regarding each reactor configuration.

In addition to the illustrations presented above, Figure 3.7 (a) and (b) compares the parametric configuration that has shown the highest and the lowest value of ethane conversion, respectively.

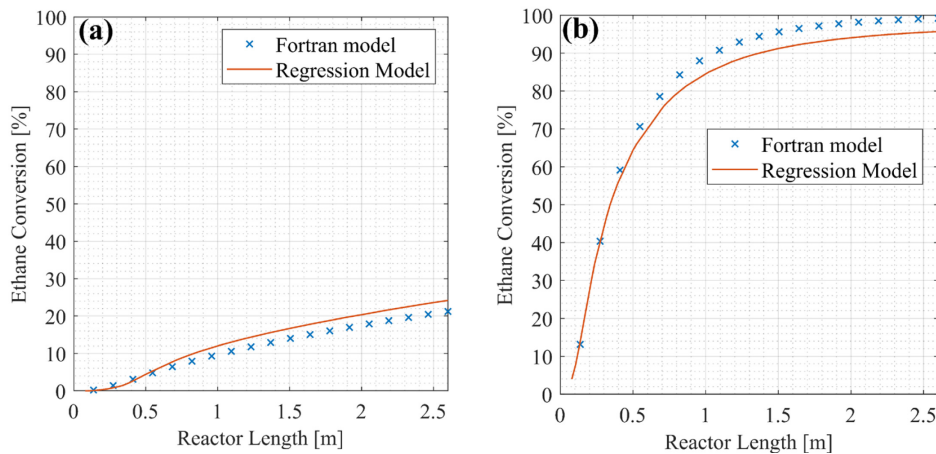


Figure 3.7 – Ethane conversion along the catalytic bed in a single reactor tube. (a) Represents the 6th experiment and (b) represents the 12th experiment. See Appendix C for further details regarding each reactor configuration.

Even though for simplicity the remaining 39 experiments are not plotted, it is important to mention that in all the cases the local error of the regression model with respect to experimental data has been lower than 7%.

3.3.2 Oxygen conversion

Being a response of similar nature, oxygen conversion was studied with the same approach as ethane conversion. Analogously, from the overall reactor performance standpoint, the most important value is the one linked to the reactor outlet.

A second ANOVA study is performed and results are enlisted in Table D.2 (see Appendix D). As expected, similar conclusions can be made regarding this response. The main factors have shown remarkable significance, being d_i/d_p the only exemption with a p -value higher than the significance threshold. As in the previous case, the quadratic form of this latter factor is statistically significant towards oxygen conversion.

Although being responses of similar nature, the number of significant parameters for the regression model is lower with respect to ethane conversion. For instance, $F_a F_c$ and $F_a F_d$ are not any more significant, meaning that the interaction between these two factors does not represent a reliable source of variability for the response. The reason behind this difference, can be linked to the oxygen reaction mechanism. As explained in Section 2.3, the reactive pathway of oxygen is remarkably distinctive from the one of ethane since molecular oxygen firstly interacts with the catalyst surface to replace the lattice oxygen specie. This latter form of the oxidant reacts with ethane which follows a simpler reaction scheme. These notorious difference might incur into a different sensitivity towards the effect of some factors.

Once the significant factors are identified, it is possible to construct the multiparametric model for oxygen conversion. The mathematical expression is represented by Equation (3.9).

$$Y_{O_2} = 65.99 + 23.97 F_a + 19.31 F_b - 8.28 F_c - 6.52 F_d - 14.37 F_e^2 + 6.50 F_a F_b \quad (3.9)$$

Figure 3.8 shows the parity diagram and the plot of residuals. In this case, a higher variability is observed with respect to the model for ethane conversion. Nonetheless, predicted values are within an error margin of ca. 10%; while the model residuals indicates that no correlation exist between predicted data and response residuals.

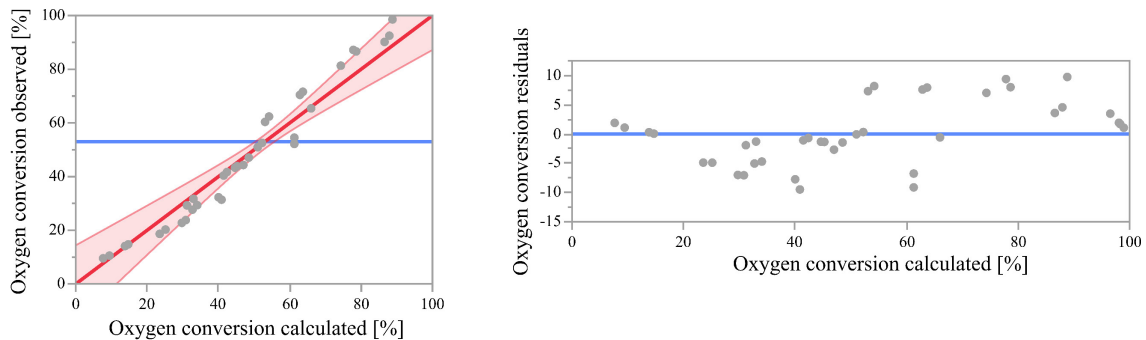


Figure 3.8 – From left to right, oxygen conversion prediction plot and its respective plot of residuals.

The summary of fit for oxygen conversion is presented in Table 3.6. As expected from the parity plot, calculated *R-squared* is lower for oxygen conversion and there is a bigger difference with respect to *R-squared adj.* Nevertheless, the overall statistical description of the model indicates an acceptable level of accuracy.

Table 3.6 – Summary of fit for oxygen conversion.

Source	Value	DF	Sum of Squares	MS	F-value	Prob > F
Model	-	20	39667.1	1983.4	28.6395	<.0001
Residual	-	23	1592.8	69.3		
Total	-	43	41259.9			
R-squared	0.961					
R-squared Adjusted	0.928					

3.3.2.1 Model robustness

The evolution of the response along the packed-bed is further analysed by comparing the conversion profiles (see Figure 3.9). In this case, the local error at reactor outlet conditions is 6.89%, 5.7% and 2.67% in Figure 3.9 (a), (b) and (c), respectively.

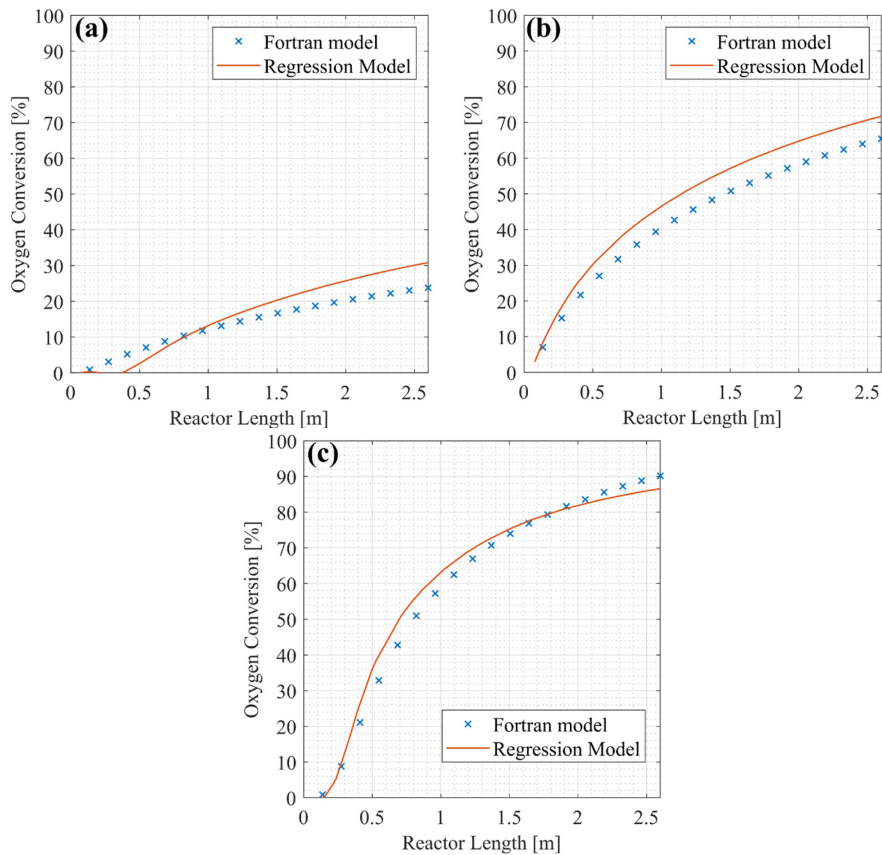


Figure 3.9 – Oxygen conversion along the catalytic bed in a single reactor tube. (a) Represents the 29th experiment; (b) represents the 17th experiment and (c) represents the 3rd experiment. See Appendix C for further details regarding each reactor configuration.

In general terms, the oxygen conversion has presented higher conversion values with respect to ethane under the evaluated range of operative conditions. As a matter of facts, more than one experiment have reached a total oxygen conversion (see Figure 3.10); nonetheless having poor results in terms of ethylene selectivity (i.e. $\sim 50\%$). Furthermore, the lowest oxygen conversion among the experiments have been observed at 5.83%.

The regression model for oxygen conversion has presented its maximum local error while estimating the lowest values of this response (see Figure 3.10 (c)). However, these anomalies are far from the common range of values that guarantees a good reactor performance (i.e. $X_{O_2} > 45\%$), therefore they should not interfere in the multi-objective process optimization.

Among the experiments that showed 100 % of oxygen conversion, all of them have in common the maximum level configuration for T_{bath} and $Y_{C_2H_6}$ (i.e. 480°C and 8%, respectively). This result is totally expected since it indicates that high temperatures and high ethane molar fraction in the feed mixture enhance high oxygen conversion, till the point of reaching the maximum admissible value for this response.

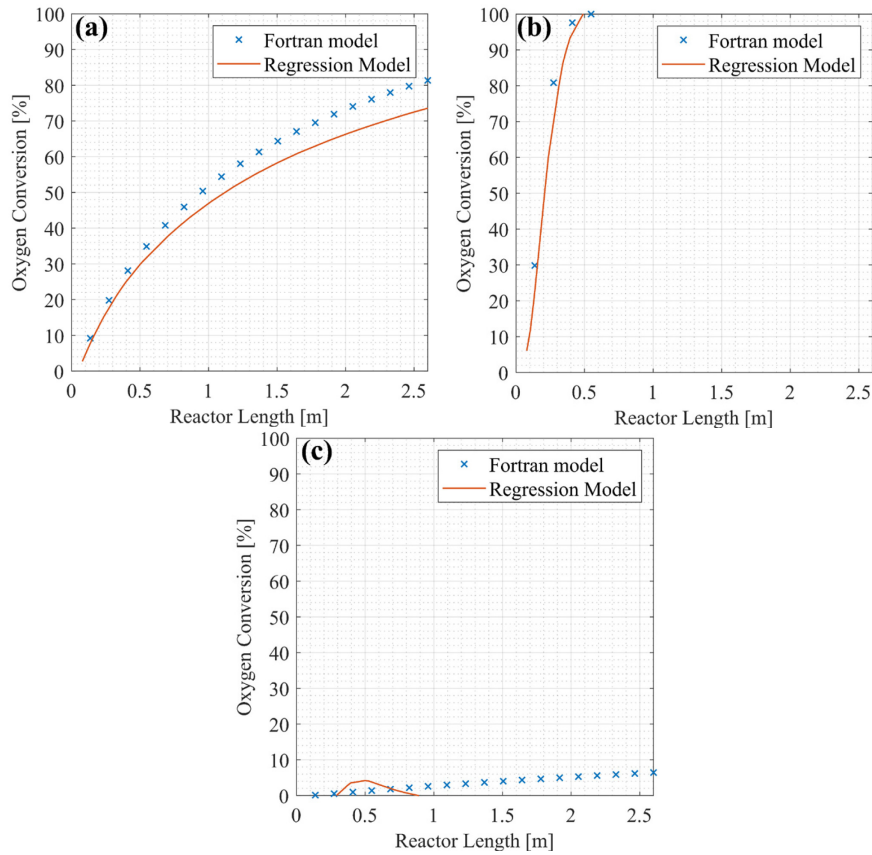


Figure 3.10 – Oxygen conversion along the catalytic bed in a single reactor tube. (a) Represents the 27th experiment; (b) represents the 10th experiment and (c) represents the 15th experiment. See Appendix C for further details regarding each reactor configuration.

3.3.3 Ethylene selectivity

Thereupon the model adequacy for ethane and oxygen conversion is verified, the next step is to design a mathematical description of the reactor product stream quality. In this sense, ethylene selectivity is accounted as the percentage of ethane that has not evolved towards overoxidation. For the sake of the multi-objective optimization at reactor level, a model capable of predicting the overall ethylene selectivity in the resulting product stream is required.

An ANOVA study is conducted as for the previous responses and results are tabulated in Table D.3 (see Appendix D). This response has shown that d_i/d_p has negligible significance in its linear form, while having a slight effect in its quadratic form. Besides, interaction parameters that includes this latter factor are not significance to modeled ethylene selectivity. On this regard, Equation (3.10) represents the regression model for the current response.

$$S_{C_2H_4} = 51.16 - 12.93 F_a + 4.48 F_b + 4.07 F_c - 1.65 F_d + 3.81 F_a F_b + 2.35 F_a F_c - \dots \quad (3.10)$$

$$\dots - 1.40 F_a F_d - 2.85 F_b F_c$$

The multiparametric model accurately fits the observed data, having a margin error of ca. 7% (see Figure 3.11). The model residuals follow a random patron, indicating a normal distribution of the error which, again, is a good sign for the model adequacy.

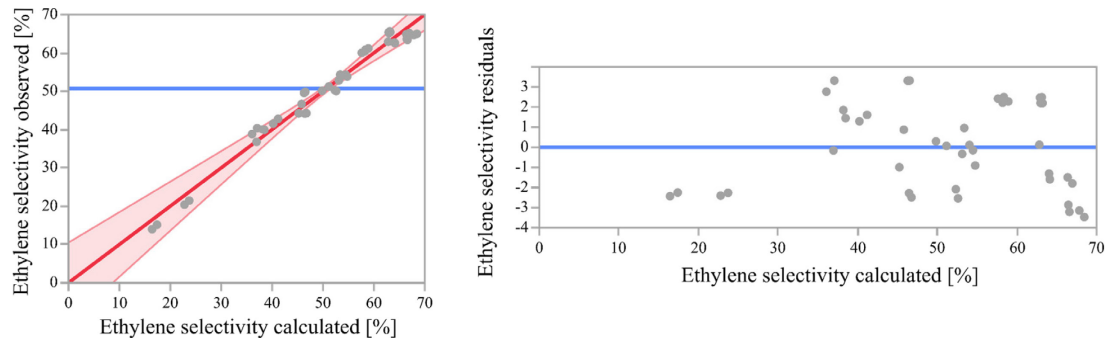


Figure 3.11 – From left to right, ethylene selectivity prediction plot and its respective plot of residuals.

The summary of fit for ethylene selectivity is shown in Table 3.7. The statistic data is in good agreement with the variability shown in the parity plot. Both calculated *R-squared* and *R-squared adj.* are beyond 0.97, which indicates that a high proportion of the observed variance can be explained by the regression model. Additionally, *F*-value points out the global significance of the model being almost 17 times higher than the threshold.

Table 3.7 – Summary of fit for ethylene selectivity.

Source	Value	DF	Sum of Squares	MS	F-value	Prob > F
Model	-	20	8041.2	402.1	48.0477	<.0001
Residual	-	23	192.5	8.4		
Total	-	43	8233.7			
R-squared	0.976					
R-squared Adjusted	0.956					

3.3.3.1 Model robustness

The predictive capacity of the model has presented some instabilities while estimating ethylene selectivity in the surroundings of the reactor inlet. However, the model will gradually gain high stability as it approaches the axial coordinate of interest (i.e. $L_{re} = 2.6$ m). The effect can be observed in Figure 3.12, where factors assume the same configuration as in the analysis of the previous responses. Among the 44 experiments, the maximum local error at reactor outlet conditions was found to be 4.57%. Particularly, Figure 3.12 (a), (b) and (c) present a difference between observed and predicted values of 2.51%, 1.33% and 2.48%, respectively.

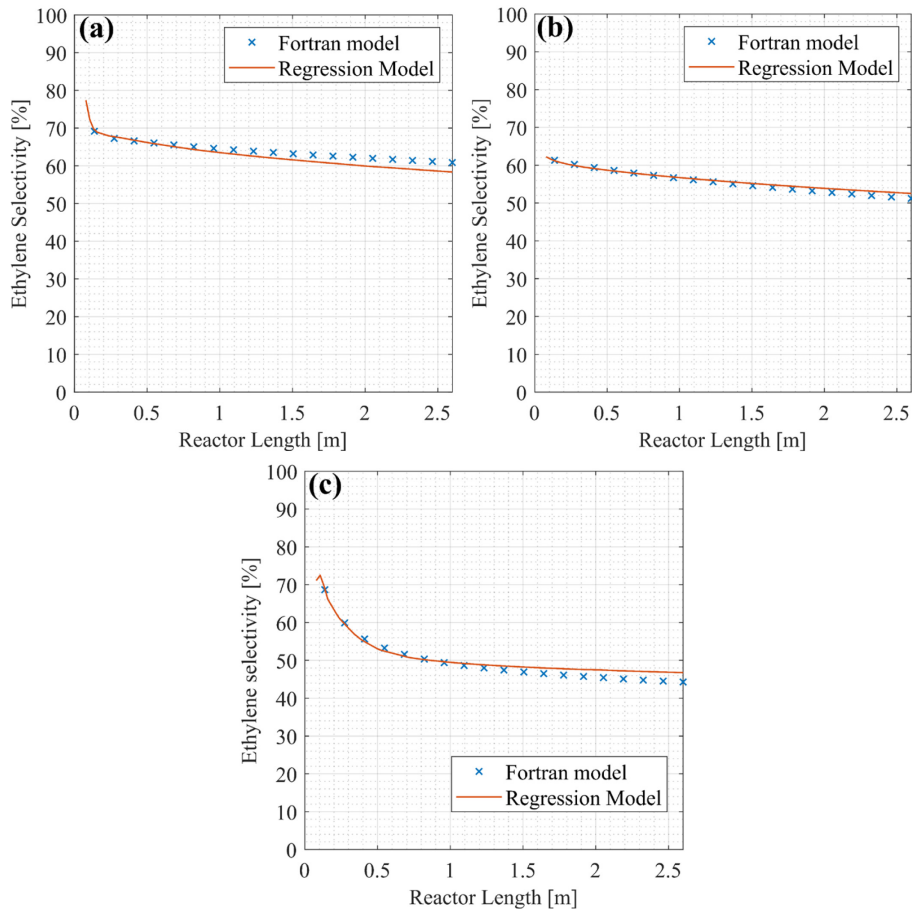


Figure 3.12 – Ethylene selectivity along the catalytic bed in a single reactor tube. (a) Represents the 29th experiment; (b) represents the 17th experiment and (c) represents the 3rd experiment. See Appendix C for further details regarding each reactor configuration.

Experiments showing the best (~ 65%) and worst performance (~ 20%) in terms of ethylene selectivity are schematized in Figure 3.13 (a) and (b), respectively. Note that the unpredictable behaviour close to the reactor inlet suggests that the regression model should not be used to estimate the ethylene selectivity in this region.

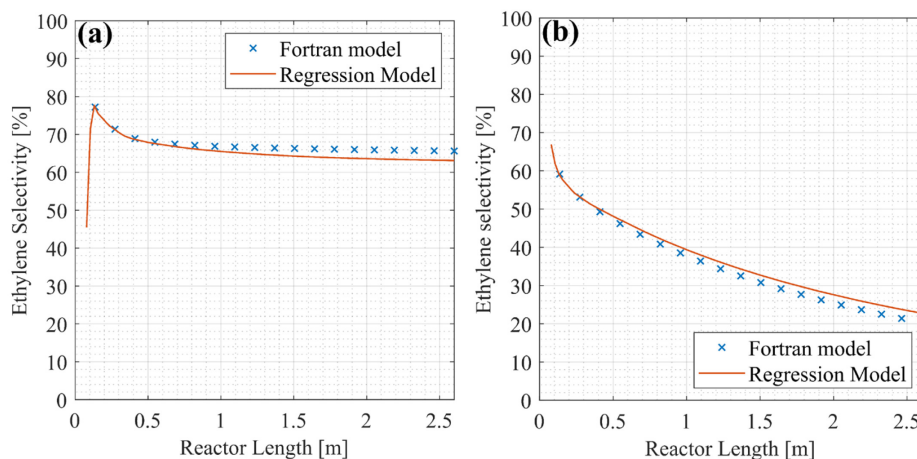


Figure 3.13 – Ethane conversion along the catalytic bed in a single reactor tube. (a) Represents the 33rd experiment and (b) represents the 12th experiment. See Appendix C for further details regarding each reactor configuration.

Although several simulations have been carried out, possible arrangements could have been overlooked. Therefore, an intensive discretization within the selected ranges must be performed in order to cover and evaluate promising configurations that might lead to a even higher ethylene selectivity. This is, in fact, the main topic covered in Chapter 4.

3.3.4 Gas-phase temperature

Heretofore, three multiparametric equations have been developed in order to reproduce the ODH-C₂ reactor performance in terms of the final compositions of its product stream. Although being a key aspect to be considered during a reactor level optimization, the temperature monitoring along the catalytic bed is also essential. In this sense, the temperature profile along the packed-bed has to be known in order to detect anomalies which could lead to mild hot spots formation or even run-away conditions. Therefore, in contrast with the previous responses, the estimation of the temperature profile, i.e. including intermediate axial coordinates, now becomes highly relevant. Nonetheless, the gas-phase temperature at reactor outlet conditions is also an important physical parameter to be considered. In fact, a regression model is utilized for predicting the product stream temperature during the model implementation in a commercial simulation engine, which is one of the main topics treated in Chapter 5.

Results from ANOVA (see Table D.4 in Appendix D) show that the most significant factor able to predict the gas-phase temperature at reactor outlet conditions is T_{bath} . The explanation for this observation is that the temperature of the gas mixture should gradually evolve towards the pre-defined operating temperature as the activity within the packed-bed decreases. However, MF and Y_{O_2} have also presented an slight effect in this latter axial coordinate. This observation is reasonable since the mass flux quantifies the mass flow rate of reactants per reactor cross-sectional area; while the oxygen content is directly involved in the process exothermicity. Although $Y_{C_2H_6}$ is an additional contribution to the process exothermicity, its domain is restricted to lower values with respect to the Y_{O_2} domain; i.e. (2, 8) and (8, 14) in percentual values, respectively; thus having a lower effect towards the response. This observation is not constant all along the packed-bed, in fact the ethane molar concentration shows high significance in the first half of the reactor length, where the highest activity is registered. By considering that oxygen is also involved in additional reactions where ethane does not participate (i.e. oxidation of ethylene), this could indicate that ethylene is being oxidised at the latest axial points of the catalytic bed.

Having acknowledged that, Equation (3.11) represents the regression model for the gas phase temperature at reactor outlet conditions. Note that there is a remarkable difference between the weight of each regression coefficient, highlighting the high influence of T_{bath} in the response prediction. Additionally, there is a marginal contribution of Y_{O_2} towards predicting the final value of the response, therefore oxidation of ethylene is expected to be minimum.

$$T_g = 431.62 + 50.76 F_a + 0.55 F_c + 0.61 F_d + 2.86 F_a^2 + 0.79 F_a F_c + 0.46 F_a F_d + \dots \quad (3.11)$$

$$\dots + 0.50 F_c F_d$$

Since the reactor operates under isothermal conditions, the heat transfer within the catalytic bed should be sufficiently efficient to avoid high temperature increments and possible run-away conditions. On this matter, an important parameter is the particle diameter since the heat transfer is clearly influenced by the void fraction within a reactor tube. This topic will be treated in the incoming sections.

Observed and predicted values by the model are compared including the model residuals (see Figure 3.14). Although on average the margin error was ca. 8%, the multiparametric model has shown a remarkable accuracy for predicting the final temperature of the product mixture, with a maximum local error of ca. 2%. This performance is expected since the number of significant factors is restricted with respect to the models for previous responses.

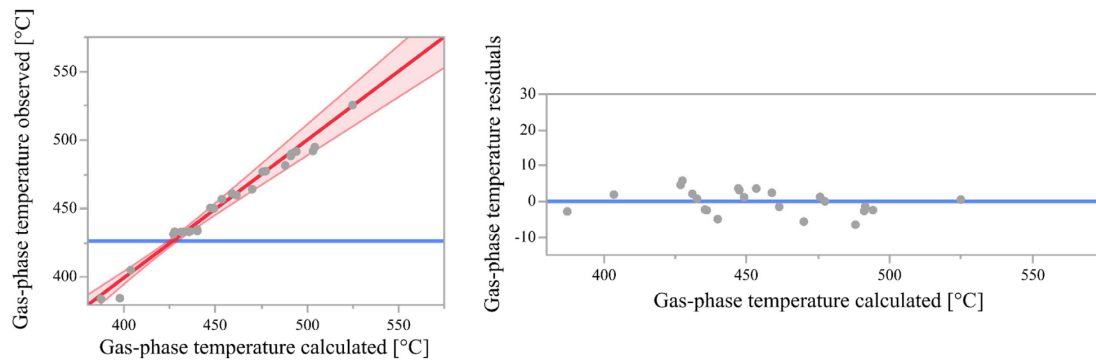


Figure 3.14 – From left to right, gas-phase temperature prediction plot and its respective plot of residuals.

Further statistic data regarding the model is enlisted in Table 3.8. The global significance is the highest among the multiparametric models (i.e. F -value $> 3 \times 10^3$), which is in agreement to the above cited observations. With respect to R -squared and R -squared *adj.*, their values are very close to one with a negligible difference between them, which is evidence of the model adequacy.

Table 3.8 – Summary of fit for gas-phase temperature.

Source	Value	DF	Sum of Squares	MS	F-value	Prob > F
Model	-	20	87710.9	4385.6	3169.45	<.0001
Residual	-	23	31.8	1.4		
Total	-	43	87742.8			
R-squared	0.992					
R-squared Adjusted	0.981					

3.3.4.1 Model robustness

In this section is possible to demonstrate the motivation for constructing a regression model at each point of the axial discretization. On the one hand, under certain conditions the temperature in both gas and solid phase deviate from T_{bath} at intermediate regions in the packed-bed. On the other hand, the final temperature of the gas mixture tends to T_{bath} in all cases (see Figure 3.15). Since the reactions involved are highly exothermic, the deviation from normal operative conditions will always means higher temperatures; including the possibility of reaching the point of catalyst permanent deactivation (i.e. $T_s > 500$ °C), as shown in Figure 3.15 (c).

Therefore, even if the outlet temperature is within normal conditions, an additional verification of the profile along the catalytic bed is compulsory.

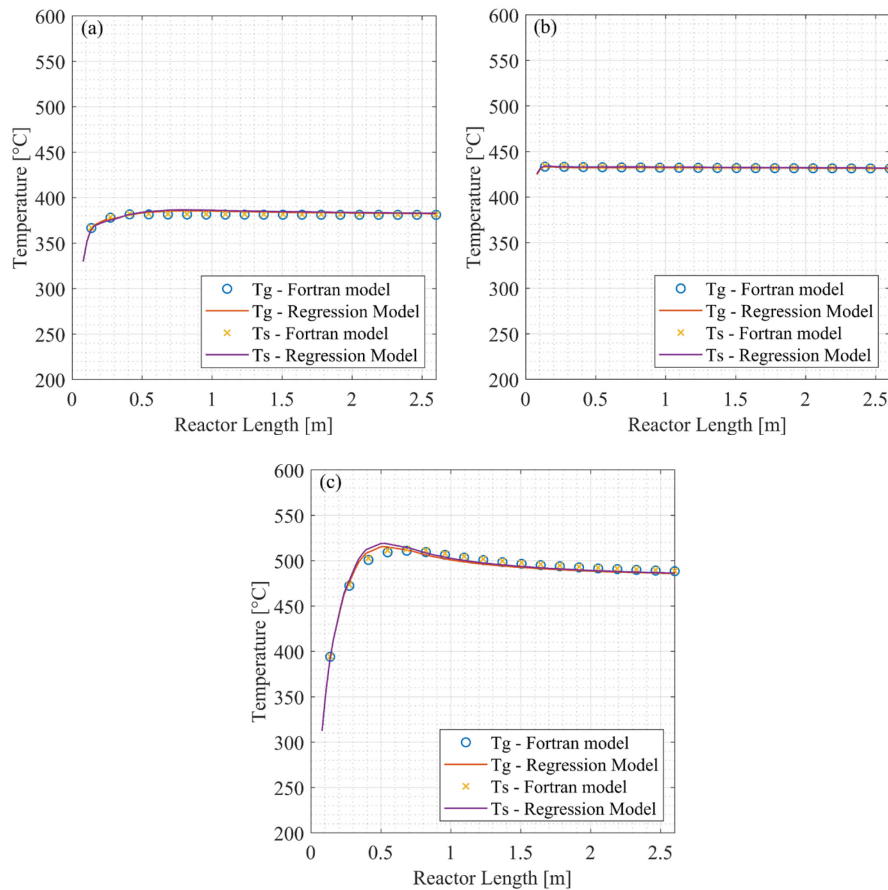


Figure 3.15 – Gas and solid-phase temperature along the catalytic bed in a single reactor tube. (a) Represents the 29th experiment; (b) represents the 17th experiment and (c) represents the 3rd experiment. See Appendix C for further details regarding each reactor configuration.

According to its postulates, a pseudo-heterogeneous model should not present a significant temperature difference between both phases. If that may to happen, it would be a sign of deficient heat transport between both phases; therefore leading to unpredictable thermal instabilities. On this regard, some deviations in both temperature profiles are observed in some experiments as presented in Figure 3.16. Two similar configurations have presented this effect; having in common high working temperature ($T_{\text{bath}} = 480^{\circ}\text{C}$), high ethane molar fraction ($Y_{\text{C}_2\text{H}_6} = 8\%$), high residence time ($\text{MF} = 5 \times 10^3 \text{ kg m}^{-2} \text{ hr}^{-1}$) and big particle diameter ($d_t/d_p = 3$). Hence, the difference relies in the oxygen molar fraction; i.e. 8% and 14% in Figure 3.16 (a) and (b), respectively.

Fortunately, if just one of common factors is coded differently, the model evolves correctly. This is the case of the experiment presented in Figure 3.16 (c) where a smaller particle diameter is utilized (i.e. $d_t/d_p = 9$). Consequently, the heat transfer between the two phases is able to guarantee no noticeable temperature difference.

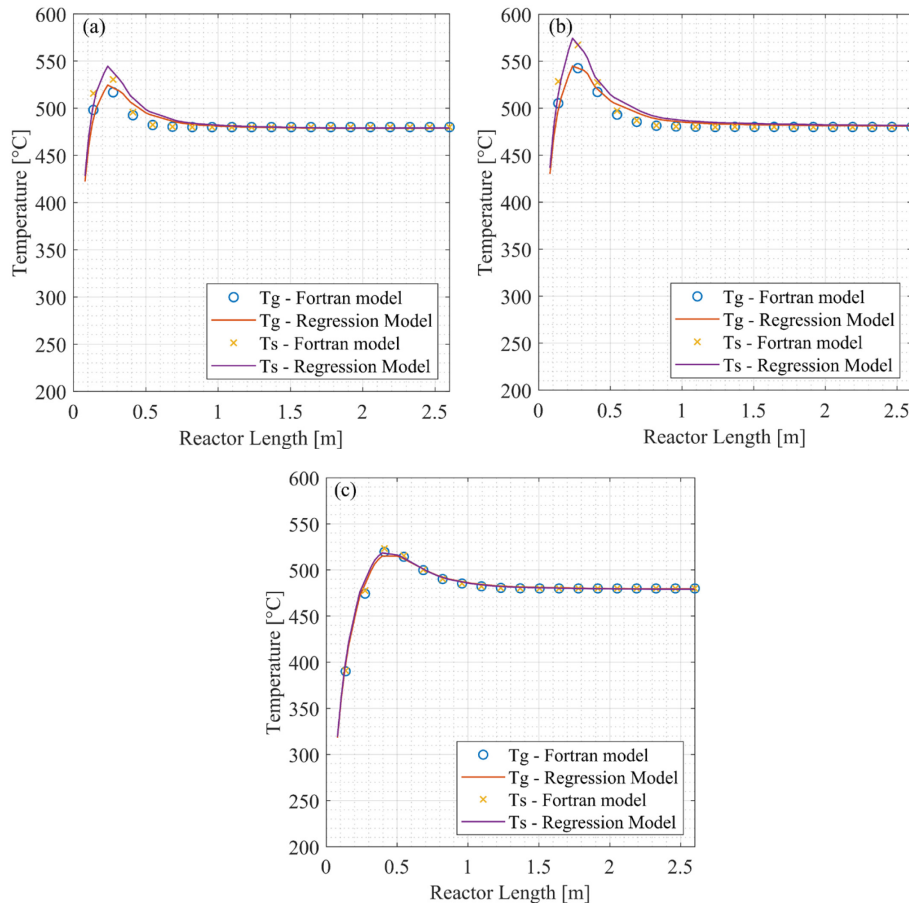


Figure 3.16 – Temperatures profiles of both gas and solid phase. (a) Represents the 10th experiment; (b) represents the 38th experiment and (c) represents the 27th experiment. See Appendix C for further details regarding each configuration.

3.3.5 Solid-phase temperature

This response is intended to be particularly different with respect to the previous one. The study of the temperature profile in the solid phase verifies proper operating conditions under different parametric configurations, i.e. absence of hot spots. Having said this, it turns obvious that there is not a specific motivation on simulating outlet conditions from this response, as it happens with the rest. Therefore, an ANOVA test at $L_{re} = 2.6$ m will not stand out from the remaining 24 axial points since all of them are equally important. Furthermore, the factor significance and how they influence the response prediction are remarkably similar to the information reported in Table 3.11, which is expectable given the pseudo-heterogeneous assumptions in the reactor model design.

The regression model has proved to be very accurate on describing the temperature profile in the solid phase along the axial discretization. The F -value of each multiparametric model has been estimated at each axial coordinate, observing a range of values two orders of magnitude higher with respect to the threshold in all cases.

Particularly, observations have demonstrated that hot spots, if any, are always localized in the first 30% of the total reactor length, which is in good agreement with observations in past contributions [15, 19].

[This page was intentionally left in blank]

Chapter 4

4. Optimization at reactor level

In this chapter, a multi-objective reactor-level optimization is presented using the less-complex model equations developed and verified in the third chapter. The dramatic reduction in computational resources, achieved due to the use of reliable multiparametric equations, permits to evaluate in shorter times the reactor performance under a wide range of operating conditions (within the chosen operative domain. This last aspect is crucial when it comes to whatever system optimization, where many different configurations must be proven.

The main goal is to maximize ethylene selectivity under the highest possible ethane and oxygen conversion. The motivation is that, even if the reactants can be recirculated to the reactor, this process will incur into a higher energy expenses in terms of downstream treatments; making the overall process unsustainable.

In addition to the previous requirement, a verification of stable thermal conditions within the catalytic bed must be granted. To do so, each promising factor combination must not enhance hot spot formation. By hot spot, it is intended an overheating beyond 20°C with respect to the set T_{bath} in at least one point of the packed-bed. Even if the hot spot is not considered critical, i.e. the final temperature does not overcome 500°C able to cause catalyst deactivation, it can still foment thermal instabilities within the reactor tube [26, 27].

4.1 Sensitivity analysis for the decision variables

In order to visualize the effect of the chosen factors, a sensitivity analysis is performed for each response. This evaluation comprised the screening of linear, quadratic and crossed-side effects of the chosen factors with three main objectives: (i) maximize important responses by selecting a promising operative windows, (ii) discard irrelevant ones and (iii) disclose the positive or negative influence of each effect on the responses. A promising multiparametric arrangement should, therefore, accomplish the conditions represented by Equation (4.1).

$$X_{C_2H_6} \rightarrow \max \cup X_{O_2} \rightarrow \max \cup S_{C_2H_4} \rightarrow \max \cup T_s, T_g \rightarrow T_{bath} \forall Dom(L_{re}) \quad (4.1)$$

Preliminarily, an interactive decision tool from JMP 15[®] is utilized to identify the factors having a major effect on the specific response. On this matter, Figure 4.1 presents a set of two-dimensional plots from the prediction profiler tool in JMP 15, where each individual effect can be evaluated.

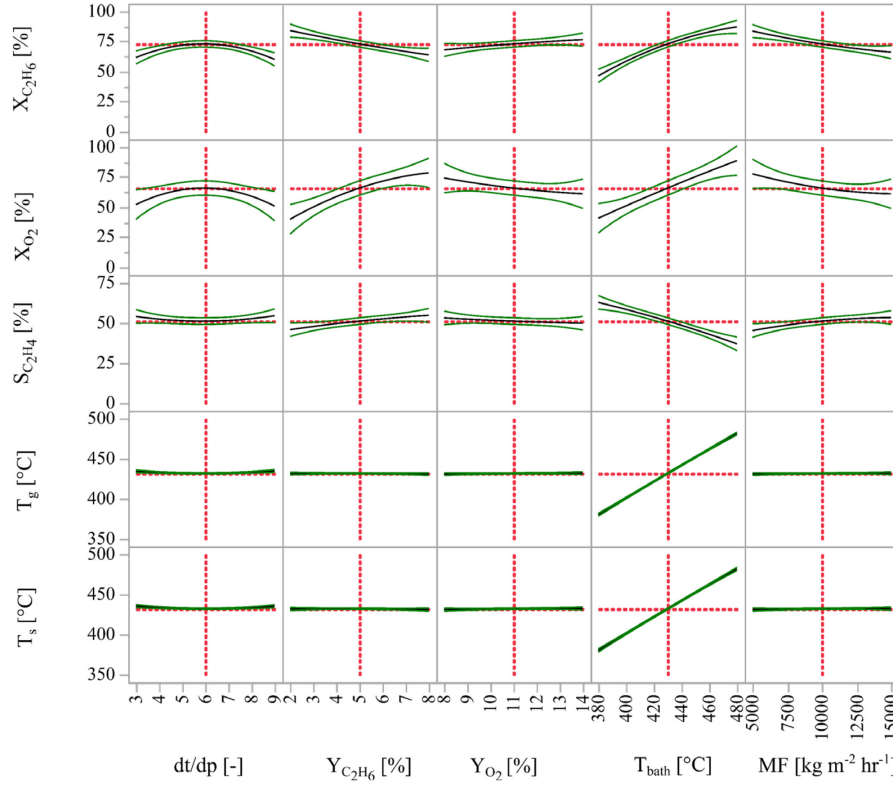


Figure 4.1 – Prediction profiler showing linear effects of independent factors on each model response at $L_{re} = 2.6$ m.

The profiler utilizes the multi-objective regression model to reproduce the catalytic reactor performance under a domain pre-defined by the user. The model is, therefore, ruled by the multiparametric equations derived from the ANOVA analysis conducted in the third chapter of this work, which are enlisted in Table 4.1. Note that the multiparametric equation for T_s at reactor outlet (i.e. $L_{re} = 2.6$ m) is not particularly relevant since, as reported in Section 3.3.5, it contributes to the verification of thermal stability within the packed-bed.

Table 4.1 – Governing equations of the multiparametric model.

Regression model equation	Reference
$X_{C_2H_6} = 72.99 + 20.38 F_a - 10.11 F_b - 8.77 F_c + 4.30 F_d - 6.23 F_a^2 - 12.10 F_e^2 - 4.54 F_a F_b + 4.37 F_a F_c + 2.58 F_a F_d + 3.08 F_b F_c + 2.92 F_b F_d$	Equation (3.8)
$X_{O_2} = 65.99 + 23.97 F_a + 19.31 F_b - 8.28 F_c - 6.52 F_d - 14.37 F_e^2 + 6.50 F_a F_b$	Equation (3.9)
$S_{C_2H_4} = 51.16 - 12.93 F_a + 4.48 F_b + 4.07 F_c - 1.65 F_d + 3.81 F_a F_b + 2.35 F_a F_c - 1.40 F_a F_d - 2.85 F_b F_c$	Equation (3.10)
$T_g = 431.62 + 50.76 F_a + 0.55 F_c + 0.61 F_d + 2.86 F_a^2 + 0.79 F_a F_c + 0.46 F_a F_d + 0.50 F_c F_d$	Equation (3.11)

Through a series of 3-D surface plots generated in MATLAB[®], the combined effect of two independent variables are analysed by maintaining constant the remaining ones. In all cases, only interactions that have presented sufficient statistical significance in the ANOVA test are evaluated. Finally, by using a contour plot overlaying technique, an optimal working zone is selected.

4.1.1 Effects on ethane conversion

Based on the slope of the different linear effects presented in Figure 4.1, it turns out that T_{bath} influence the most $X_{C_2H_6}$; meaning that higher operating temperature enhances ethane reactivity. At the contrary, higher values of both $Y_{C_2H_6}$ and MF will induce a decay in ethane conversion; this is expected since there would be, respectively, an excess of ethane and shorter residence time within the reactor while maintaining constant the remaining factors.

Another observation relays on the parabolic effect presented by d_i/d_p . This effect was anticipated by the high significance observed while performing the ANOVA test, resulting in a significant F -ratio (25.94). Additionally, a slight curvature effect is also shown by T_{bath} but with a much lower significance.

As suggested by the model, interaction effects are crucial while predicting ethane reactivity. Therefore, a series of three-dimensional surface plots are shown in Figure 4.2 where crossed effects are better visualized. For simplicity, the remaining factors which are not accounted in the plot, have been kept at their respective zero-level values; i.e. $T_{bath} = 430^\circ\text{C}$, $d_i/d_p = 6$, $MF = 1 \times 10^4 \text{ kg m}^{-2} \text{ hr}^{-1}$, $Y_{O_2} = 11\%$ and $Y_{C_2H_6} = 5\%$.

Starting with the effect of inlet reactant concentrations, Figure 4.2 (a) shows that higher oxygen concentration enhances ethane conversion. This effect becomes more notorious while operating at higher temperatures, as noticeable by the slope orientation change in Figure 4.2 (e). An interaction with an opposite effect is observed in Figure 4.2 (f), where lower $Y_{C_2H_6}$ values and high temperatures will induce high conversions; as for oxygen, the surface curvature becomes more vertical as temperature increases, thus indicating higher conversion. Although this suggests to work under high oxygen concentration, it may not be suitable in terms of selectivity due to overoxidation of ethane.

The particle diameter has a maximum around 6 which persists independently of the other factors configuration as shown in Figure 4.2 (b) and (d). Extreme d_i/d_p values have a similar influence in the response, while intermediate values, i.e. ~ 6 , generate an increment of ca. 10% in ethane conversion with respect to the boundaries. This observation leads to a symmetric shape of the domain.

Regarding the mass flux, lower values have a positive effect on ethane reactivity due to longer residence times within the catalytic bed. An increment of 15-20 % is observed in the response while screening from upper to lower limit values of MF , as indicated in Figure 4.2 (c).

Summarizing, having in mind all possible configurations available in the chosen operative domain, $X_{C_2H_6}$ values have been observed from 15 to 100%. The regression model predicts that the high values of the response are observed at (i) intermediate particles diameter ($d_i/d_p \approx 6$); (ii) minimum ethane molar fraction ($Y_{C_2H_6} \approx 2$) at high molar fraction of oxygen in the feed mixture ($Y_{O_2} > 13\%$); (iii) high operating temperature ($T_{bath} = 480^\circ\text{C}$); and (iv) high residence time ($MF = 5000 \text{ kg m}^{-2} \text{ hr}^{-1}$). An opposite factor configuration with respect to the previously mentioned one will, consequently, decrease ethane reactivity till reaching ca. 15% of conversion.

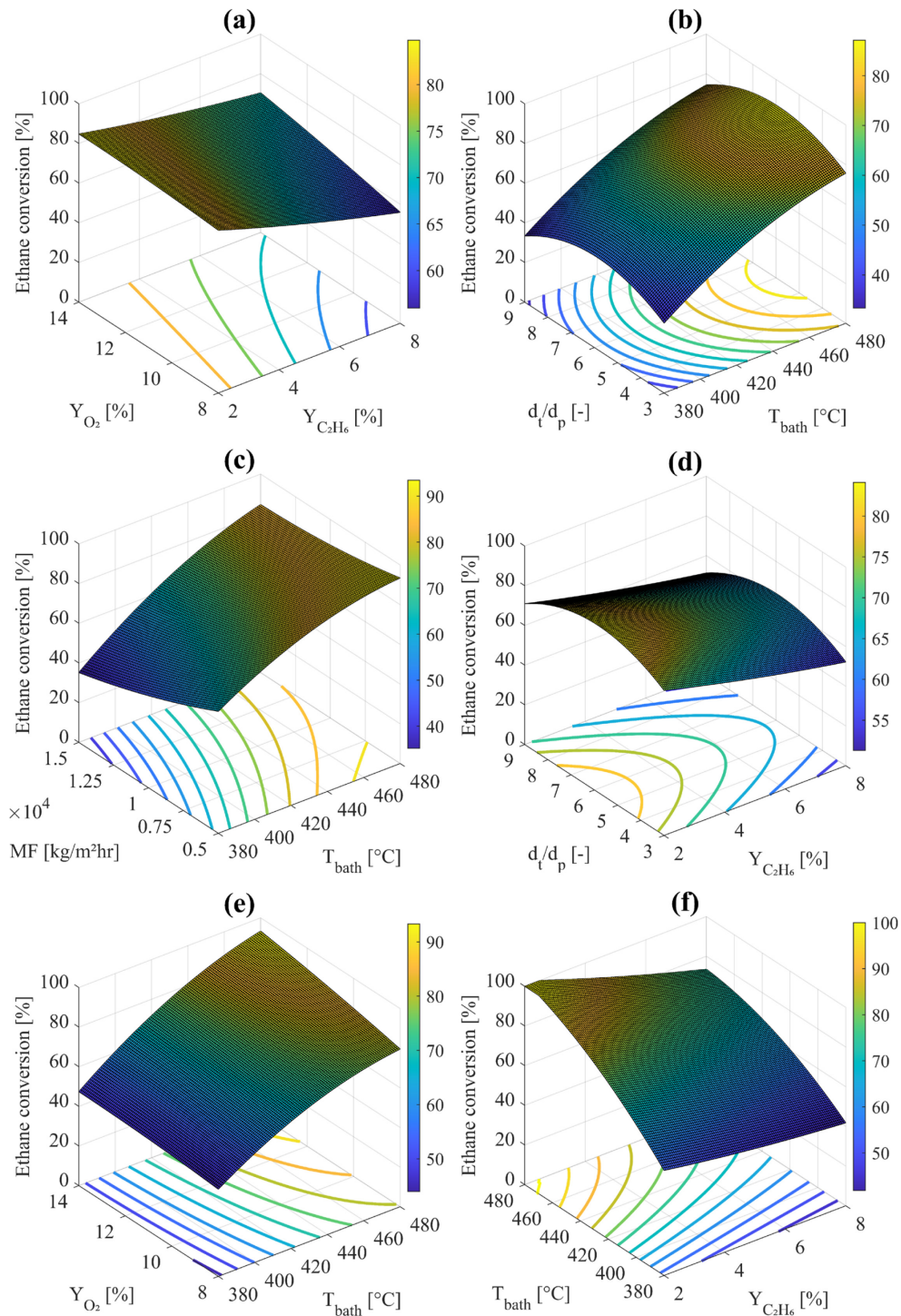


Figure 4.2 – Response surface plots for ethane conversion showing the interaction between two independent factors. The remaining factors (absents on each plot) have been maintained constant at a value equal to their respective zero level (0).

4.1.2 Effects on oxygen conversion

The influence of the different factors in this response has shown some aspects in common with respect to ethane conversion. This is totally expected due to their similar nature as dependent variables. As a matter of facts, only $Y_{C_2H_6}$ and Y_{O_2} have shown an opposite behaviour towards oxygen conversion as one can observed in Figure 4.1.

Due to the reactions involved between these two species, i.e. catalytic oxidation towards ethylene and overoxidation towards CO_2 , there is also a strong influence linked to the operative temperature and the residence time. Furthermore, the curvature effect generated by the particle diameter remains unchanged. In relative terms, there has been a smaller number of significant interactions between main factors for this response. These crossed effects are schematized in Figure 4.3.

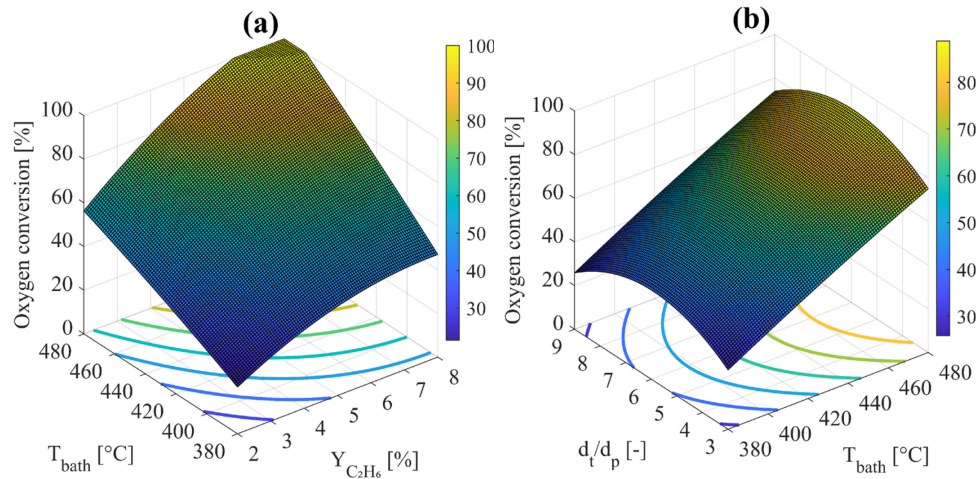


Figure 4.3 – Response surface plots for oxygen conversion showing the interaction between two independent factors. The remaining factors (absents on each plot) have been maintained constant at a value equal to their respective zero level (0).

Figure 4.3 (a) shows an intensive effect in the oxygen reactivity due to the interaction between T_{bath} and $Y_{C_2H_6}$, reaching 100% of conversion close to the upper values of both factors; i.e. $T_{bath} > 470^\circ\text{C}$ and $Y_{C_2H_6} > 6\%$. Complementary, Figure 4.3 (b) has shown the persistence of a maximum in the response when considering $d_t/d_p \approx 6$ and thus, similarities with respect to ethane conversion are highly noticeable (see Figure 4.2 (b)).

After analysing the full spectrum within the domain of independent variables, X_{O_2} can assume values that range from 3% to 100%. The model predicts that high values of X_{O_2} can be obtained at certain parameter configurations that includes (i) intermediate particle diameters ($d_t/d_p \approx 6$); (ii) preferentially, high ethane molar fraction ($Y_{C_2H_6} > 3\%$) and low oxygen molar fraction ($Y_{O_2} < 13\%$) in the feed mixture; (iii) high working temperatures ($T_{bath} > 390^\circ\text{C}$); and (iv) long residence times ($MF < 14500 \text{ kg m}^{-2} \text{ hr}^{-1}$).

4.1.3 Effects on ethylene selectivity

Up to this point, it has been demonstrated that the two reactive species are similarly influenced by the factors, which could potentially define the operative conditions of the reactor. However, Figure 4.1 indicates that ethylene selectivity is inversely influenced by some factors; this is also indicated by the sign of each factor coefficient in the regression model (e.g. -12.33 and 20.38 are, respectively, regression coefficients for the factor T_{bath} within the model for $S_{C_2H_4}$ and $X_{C_2H_6}$). The particle diameter will also influence differently the selectivity towards ethylene, even though its effect is less intense and less significant compared to the previous cases.

The most significant cross interactions between main factors is represented in Figure 4.4. As one can notice, most of the significant interactions are also relevant in terms of ethane

conversion. The direction towards a higher $S_{C_2H_4}$ is, nonetheless, the opposite in all cases. Figure 4.4 (a) shows that ethylene selectivity overcome 60 % when operating at $T_{bath} < 400^\circ\text{C}$ and $Y_{C_2H_6} > 6\%$. This shows that secondary reactions are enhanced by high temperatures, as suggested by the differences in the activation energy for ethylene and CO_2 formation, i.e. ranging from 66 kJ mol^{-1} and $80\text{-}82 \text{ kJ mol}^{-1}$, respectively (see Table 2.4).

Figure 4.4 (b) suggests a milder effect by d_i/d_p regarding $S_{C_2H_4}$. Although a slight curvature effect remains, this influence is considered to be associated with the impact this parameter has in $X_{C_2H_6}$ and X_{O_2} , rather than directly affecting the ethylene selectivity. In other words, it is expected that the catalyst would enhance the selectivity towards the desired product regardless the dimension of the pellets. Nevertheless, a physical influence of d_i/d_p may persist in terms of mass and heat transfer within the catalytic bed since the radial velocity profile within the packed-bed is directly influence by the particle diameter; hence indirectly influencing $S_{C_2H_4}$.

Low values of residence time ($\text{MF} > 8500 \text{ kg m}^{-2} \text{ hr}^{-1}$) keeps CO_2 selectivity below 50% by considering previously mentioned conditions for $Y_{C_2H_6}$ and T_{bath} (see Figure 4.4 (b) and (d)). Oxygen initial concentration has presented a little effect on $S_{C_2H_4}$, influencing in less than 7.5% in the final value of this response (see Figure 4.4 (c)). In spite of that, low concentration of oxygen will reduce overoxidation.

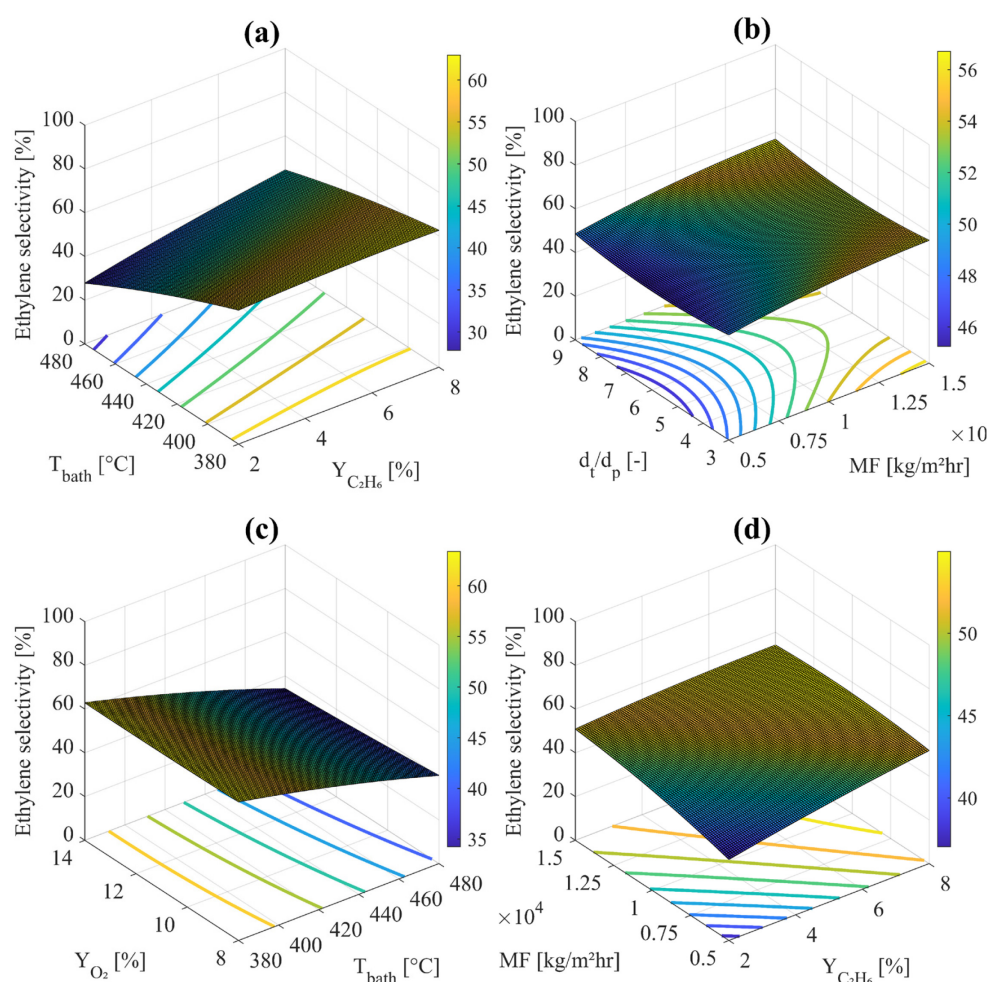


Figure 4.4 – Response surface plots for oxygen conversion showing the interaction between two independent factors. The remaining variables have been maintained constant at a value equal to their respective zero level (0).

Under the studied conditions, values of ethylene selectivity can vary from 13% to a maximum of 66%. The regression model indicates that overoxidation reactions are minimized while operating the reactor at (i) low d_i/d_p (i.e. below 5); (ii) high ethane concentration in the feed mixture preferentially, at low oxygen content ($Y_{C_2H_6} \approx 8\%$ and $Y_{O_2} < 9\%$); (iii) low working temperature ($T_{bath} < 390^\circ\text{C}$); and (iv) short residence times ($MF > 13000 \text{ kg m}^{-2} \text{ hr}^{-1}$).

4.1.4 Effects on the temperature profile

Results analysed heretofore have permitted to elaborate conclusions based on a series of multiparametric equations able to describe the overall reactor performance in terms of the composition of the product stream. Nevertheless, a proper description of the gas-solid-phase temperature profiles requires estimations of intermediate values within the catalytic bed. As a matter of facts, Figure 4.1 indicates that T_{bath} is the only factor that has relevant influence on both gas and solid phase temperature at $L_{re} = 2.6 \text{ m}$, condition that differs in the first 30% of the reactor length.

As firstly introduced in Section 3.3.4, the first third of the catalytic bed is affected to a high reaction rate including, not only the oxidative dehydrogenation of ethane into ethylene, but also overoxidation reactions towards CO_2 . This will negatively affect the heat transfer in the porous media of the catalyst, ending up into a localized temperature increment. As schematized in Figure 4.5, for intermediate axial coordinates, additional factors will play a role for the temperature profile estimation. It has been observed that bigger particle diameters (i.e. low d_i/d_p values) enhances the generation of hot spots within the catalytic bed. The same effect is seen at long values of residence time.

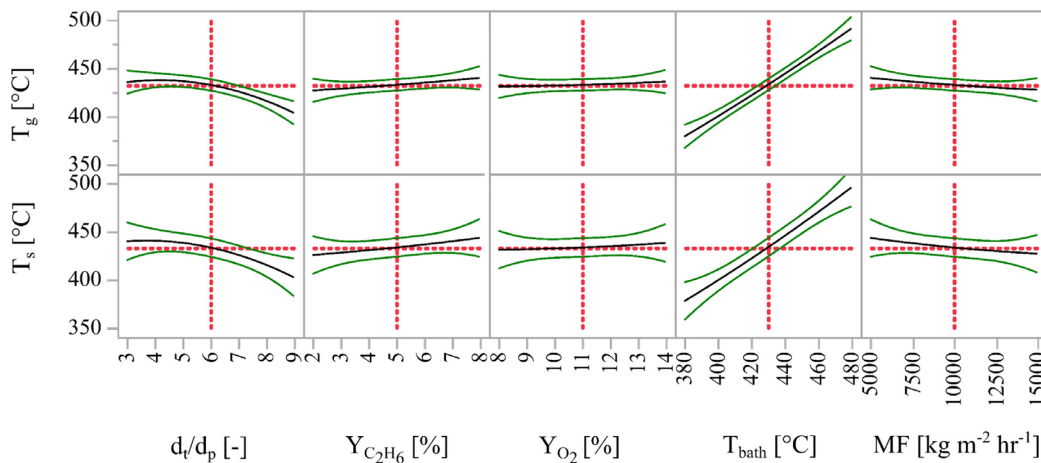


Figure 4.5 – Prediction profiler showing linear effects on both gas and solid-phase temperature at $L_{re} = 0.23 \text{ m}$.

These latter observations are based on the principles of the pseudo-heterogeneous model described in Section 2.4 and could be explained from the standpoint of fluid dynamics. The effective thermal conductivity (k_{eff}) and wall heat-transfer coefficient (h_w) were determined by correlations for the construction of the governing equations of the model. It has been reported that there is a proportional relationship between the particle Reynolds number (Re_p) and both transport coefficients; including the dimensionless numbers of Peclet and Biot (Pe_r y Bi_w , respectively) [77]. Results indicate that the coefficient of proportionality for k_{eff} is bigger than the one for h_w ; therefore, the heat transfer by conduction in the catalyst bulk becomes more

efficient than the heat dissipation by convection as Re_p increases. This is in agreement with the opposite effect observed for Pe_r and Bi_w ; whereas Pe_r increases with Re_p , Bi_w decreases. Consequently, a temperature increment of the catalyst bulk temperature should be observed.

Nonetheless, it is important to mention that most of the previous contributions where heat management in packed-beds is treated, are carried out at constant d_p [25, 26, 27, 77]. Therefore an eventual sensitivity analysis of transport parameters with respect to Re_p is conducted by varying the fluid lineal velocity (u_0) [77]. In this work, however, the Re_p is affected by the d_p and u_0 in the same manner. In other words, as d_p increases, the void fraction within the packed-bed increases (see equation) and so it does u_0 . Having said this, even if the Re_p is not affected by the same parameters in both scenarios, the results in terms of heat management within the packed-bed behaves similarly.

The heat that needs to be dissipated from the reactor will depend on the reaction rates. In the first 30 % of the reactor length, the concentration of the reactants is maximum and thus, the reaction rate will be higher compared to farther axial coordinates. The direct effect of that is a higher heat generation rate and therefore, a higher heat dissipation rate is required to avoid the presence of hot spots. However, since the reactants are gradually consumed along the reactor, the difference between these two parameters will become less pronounced with the axial coordinate till reaching the point where the heat generated is dissipated at the same rate. This phenomena explains the absence of hot spots formation at $L_{re} > 0.75$ m. Regarding $Y_{C_2H_6}$ and Y_{O_2} , higher values lead to a more intensive activity within the reactor; hence, leading to more remarkable differences between T_{bath} the temperature of both phases (i.e. T_g and T_s)

The gradual disappearance of the difference between heat generation and heat dissipation rate is indirectly accounted by the multiparametric model. Figure 4.6 illustrates how the statistical significance of main factors evolves along the axial coordinate when predicting the temperature profile of the solid phase, i.e. T_s .

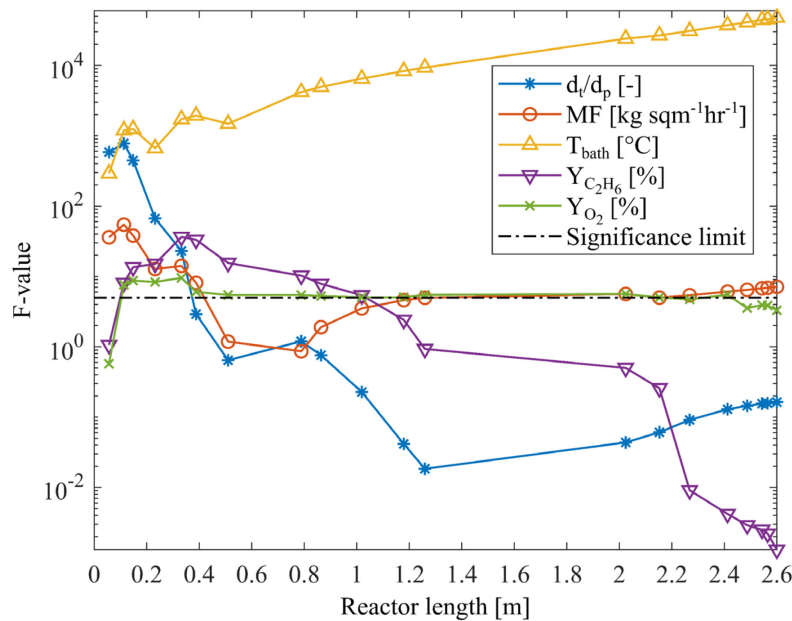


Figure 4.6 – Statistic significance evolution of $Y_{C_2H_6}$, Y_{O_2} , d_i/d_p , MF and T_{bath} along the reactor tube. Significance limit has been established at $Prob > F$ of 0.05.

As noticeable, d_i/d_p and MF are very significant in the reactor inlet surroundings followed by an abruptly decrement of it. These two factors will gain a significance stability in the second

half of the total reactor length. The bath temperature, however, remains with a more pronounced relative significance and its value gradually increases with the reactor length.

4.1.5 Hot spots

It has been mentioned how transient heat transport in a wall-cooled tubular catalytic reactor is determined by the operating parameter configuration. It is clear that the effect of each independent variable in the overall reactor performance, may differ from one axial point to another one. Particularly, their impact on the thermal runaway conditions and hot spots is of crucial importance.

On this matter, due to the exothermic nature of the reactions involved, a temperature rise within the catalytic bulk may cause damage to both catalyst (via sintering) and the reactor itself (via thermal stress). Thermal instabilities englobe hot spots that will not necessarily lead to runaway conditions. Even if the temperature profile within the bulk is far below the critic limit, a temperature difference of 15-25°C with respect to T_{bath} is also undesired. The motivation is that such conditions may create unpredictable operating conditions from the normal reactor performance; hence, making difficult to anticipate the final outcome of the process [26, 27]. In this work, a $\Delta T > 20^\circ\text{C}$ will be considered as a hot spot (i.e. $T_{hs} = T_{bath} + 20^\circ\text{C}$).

As reported in Section 2.2.2.1, NiO-SnO₂ catalysts were synthesised at 500°C. This is, therefore, the critic limit that has to be considered. In this work, that boundary was selected as 495°C in order to establish an error tolerance from the model of $\pm 5\%$. A total catalyst deactivation can, therefore, occur for temperatures beyond this limit.

There have been found several parameters configurations throughout the spectrum that enhance thermal instabilities. Being T_{bath} the most influential factor, hot spots have been observed even at low temperatures (380°C) as shown in Figure 4.7 (a). Under this conditions though, the remaining factors have to assumed specific values; i.e. $d_t/d_p < 4$, $MF < 6 \times 10^3 \text{ kg m}^{-2} \text{ hr}^{-1}$ and high feedstock concentration. Deductively, as long as the operating temperature increases, hot spots become more frequent and intense, even as, the ranges for the remaining factors becomes wider (see Figure 4.7 (b)). An important observation is that critic hot spots ($T_{hs} > 495^\circ\text{C}$) were not detected at $T_{bath} < 440^\circ\text{C}$, regardless the remaining factor configuration.

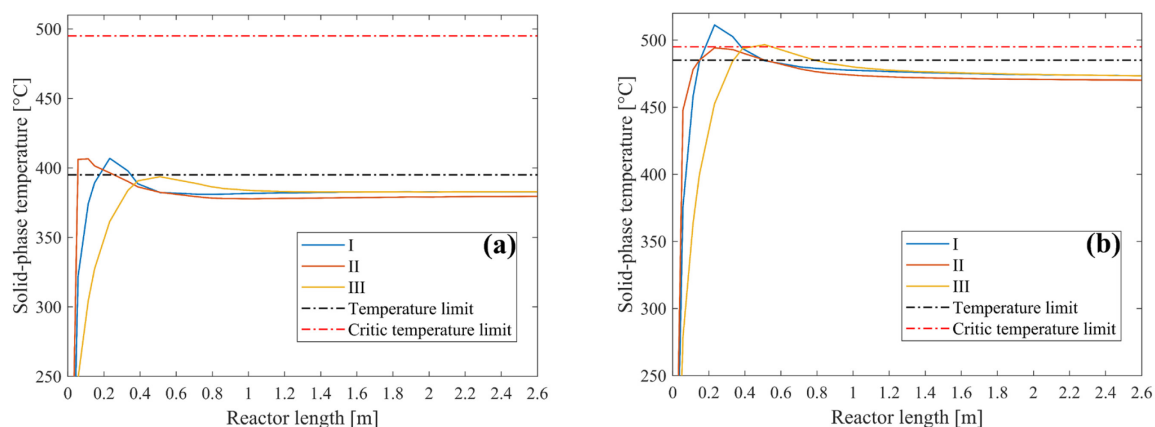


Figure 4.7 – Temperature profile along the catalytic bed under different configurations. (a) Parameters are set at $T_{bath} = 380^\circ\text{C}$, $MF = 5000 \text{ kg m}^{-2} \text{ hr}^{-1}$, $Y_{C_2H_6} = 8\%$, $Y_{O_2} = 14\%$ and $d_t/d_p = [3, 6, 9]$ correspond to (i), (ii) and (iii), respectively. (b) Parameters are set at $T_{bath} = 470^\circ\text{C}$, $MF = 7000 \text{ kg m}^{-2} \text{ hr}^{-1}$, $Y_{C_2H_6} = 6\%$, $Y_{O_2} = 10\%$ and $d_t/d_p = [3, 6, 9]$ correspond to (i), (ii) and (iii), respectively. In both cases, $T_{hs} = T_{bath} + 15^\circ\text{C}$.

Up to this point, it has been demonstrated that there is a vast number of possible parametric configurations able to lead to hot spot formation. Therefore, in order to avoid a thermal stability analysis under conditions that would lead to a poor reactor performance, a proper approach is to firstly identify an area within the domain that could generate a promising outcome. Results from the current section are, nevertheless, useful to anticipate possible thermal anomalies within the reactor.

4.1.6 Combined effect

Due to the multi-factorial nature of the case-study, it becomes challenging to find an unique reactor configuration in which all the desired outcomes are achieved at once. Instead, a compromise between the expected outcomes is generally made in order to define, not an overall optimization point, but a practical one. Particularly, in this work a compromise between selectivity towards the desired product and feedstock conversion is required. As explained in Section 4.1.3, a factor combination that will induce high ethane and oxygen conversion will also deviate the reaction mechanism towards CO₂ formation.

The selection of a promising working zone is carried out through an overlaying technique of several contour plots. This approach is commonly utilized for studies where three-dimensional representations are not enough to cover all the independent variables.

In order to restrict the domain as well as reducing variability, some constrains are imposed based on their relative influence, not only at reactor level, but also taking into account processes downstream the reactor. On this matter, some criteria are pre-defined:

- Selectivity criterion is defined as $S_{C_2H_4} > 62.1\%$. According to the definition given in Equation (3.7), under the latter condition the product yield ratio in mass bases (kg of CO₂ per kg of ethylene produced) remains below unity;
- short residence time is prefer as it leads to a smaller number of tubes per reactor to accomplish an established yield;
- similarly, $Y_{C_2H_6}$ should preferentially be ca. 8% to guarantee an acceptable productivity and minimize separation cost downstream the reactor (i.e. the cost associated to separate the inert fraction of the gas mixture);
- the remaining factors (i.e. d_w/d_p , Y_{O_2} and T_{bath}) have not a specific criterion of selection besides the accomplishment of the above conditions and thermal stability.

Given these conditions, Figure 4.8 illustrates a series of contour plots where a promising operative zone is highlighted. The aim is to determine the optimized working zone for the given parameters even though a specific configuration has been pre-selected for the process simulation in ASPEN Plus. This arrangement, however, can be modified based on the overall process performance, i.e. including separation steps downstream the reactor, where a deeper analysis is conducted to estimate the energy consumption and CO₂ emissions.

A minimum requirement of 30% in ethane conversion have been preliminarily imposed based on common values observed in previous works where Ni-based catalyst for the ODH-C₂ are studied [60]. Additionally, a minimum of 50% is suggested for oxygen conversion. The motivation relies on the energy intensive process for its extraction downstream the reactor (i.e. cryogenic distillation) and how they would eventually impact in the sustainability of the overall process.

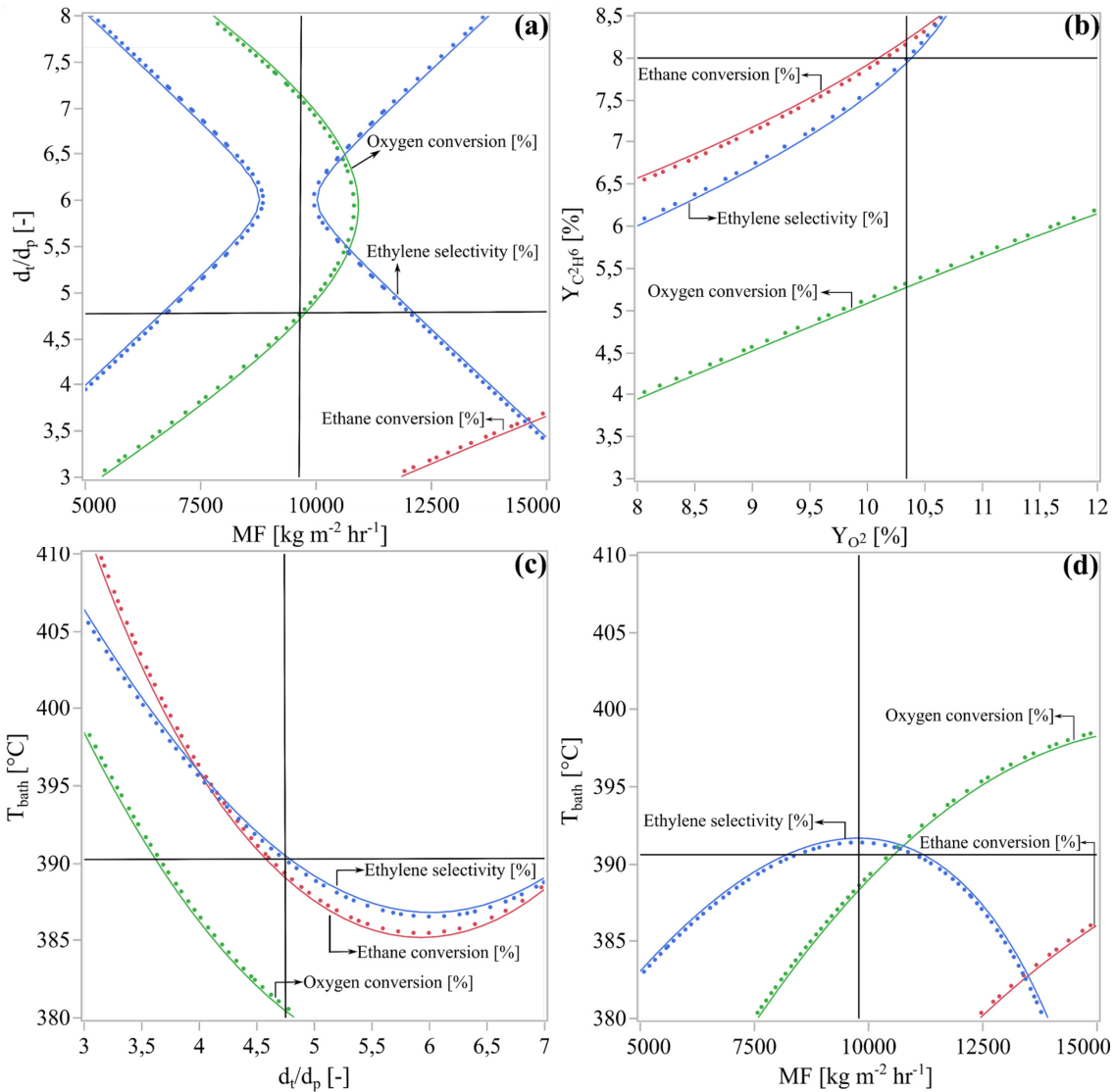


Figure 4.8 – Overlying technique through a series of contour plots. Constrains are defined as: $S_{C_2H_4} > 62.1\%$, $X_{C_2H_6} > 30\%$ and $X_{O_2} > 50\%$. Dots stand for indicating the direction on which pre-defined conditions are accomplished.

Figure 4.8 (a) shows that, under the given constrain of $S_{C_2H_4} > 62.1\%$, is possible to reach intermediate values of MF (up to $1 \times 10^4 \text{ kg m}^{-2} \text{hr}^{-1}$). This condition is favourable to decrease the overall size of the reactor in terms of number of tubes (N_{tu}), thus increasing the feedstock flow rate per reactor cross-sectional area. Shorter residence times are not recommended since ethylene selectivity and reactants conversion decay below the threshold.

Intermediate values of dt/dp (~ 6) leads to a $X_{C_2H_6}$ and X_{O_2} within the predefined ranges (45% and 51.9%, respectively) but at the cost of lowering $S_{C_2H_4}$. However, at $T_{bath} \approx 392^{\circ}\text{C}$ (see Figure 4.8 (c)) overoxidation reactions remain below the threshold. Figure 4.8 (b) shows that $Y_{O_2} \approx 10.3\%$ ensures $Y_{C_2H_6} > 7\%$, which increases the reactor productivity and minimizes the required cross-sectional area.

The above mentioned operative window refers to the reactor optimization in terms of the chemical composition of the feed and product stream. Nevertheless, due to the exothermicity of the ODH- C_2 , a thermal stability analysis is necessary before formulating conclusions. On this matter, all possible parametric configurations within the optimized zone will generate a specific temperature profile along the catalytic bed that must not present thermal instabilities

according to the fundamentals given in Section 4.1.5. Several arrangements have been tested in order to verify if the pre-selected working zone could lead to hot spot formation (see Figure 4.9). Fortunately, the restricted area illustrated in Figure 4.8 has not presented mild hot spots nor critic hot spots formation along the packed-bed.

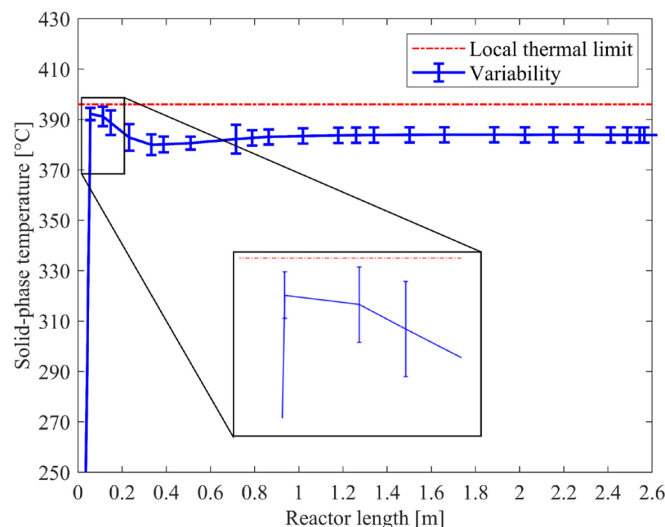


Figure 4.9 – Thermal stability verification.

After the verification of safety conditions from the thermal stability point of view, the adequacy of the optimized region is proven and its implementation in a simulation engine can be performed. The optimized operative zone and its expected outcome is summarized in Table 4.2.

Table 4.2 – Optimized operating conditions and performance of the catalytic reactor.

Source		Optimized range	Expected outcome		
Factor	Unit		Response	Unit	
$Y_{C_2H_6}$	[%]	[7 - 8]	$X_{C_2H_6}$	[%]	[40 - 45]
Y_{O_2}	[%]	[8 - 10.4]	X_{O_2}	[%]	[55 - 59]
d_t/d_p	[-]	[4.7 - 6.6]	$S_{C_2H_4}$	[%]	[62.1 - 64]
T_{bath}	[°C]	[385 - 392]	T_s	[°C]	[381 - 395]
MF	[$kg\ m^{-2}\ hr^{-1}$]	[$8.5 \times 10^3 - 10 \times 10^3$]	T_g	[°C]	[380 - 393]

It is important to understand that, although a specific factorial combination has been selected for the process simulation (see Figure 4.8), further modifications might be possible for improving the overall process performance (i.e. including additional purification steps downstream the ODH- C_2 reactor model). The motivation of providing optimized ranges rather than single values is, indeed, to provide more flexibility while optimizing the complete process.

Chapter 5

5. Reactor model integration and process simulation

In this chapter, a complete process for ethylene production at industrial scale is simulated in ASPEN Plus®. The motivation of using a customizable simulation block is based on describing the ODH-C₂ by the set of multiparametric equations elaborated and verified in Chapter 3. Since the model derives from the pseudo-heterogeneous reactor model, complex kinetics and transport phenomena are implicitly accounted by the governing equations of the new formulation. In this way, not only physicochemical considerations, but also operating conditions (e.g. reactor tube length, catalyst particle diameter, number of tubes, etc) are included in a single block.

Aiming to study a complete ethylene production process, downstream separation sections are added into the simulation environment in ASPEN Plus® (i.e. CO₂ absorption with amines solution and cryogenic product fractionation). An additional section within the simulation environment has been intended to exploit the exothermicity of the set of reactions taking place in the catalytic reactor. Therefore, the sensible heat of the product stream is integrated into a heat exchanger network (HEN) where high-pressure and low-pressure steam is produced. In this way, a complete evaluation of both net energetic requirements and CO₂ emissions are taking into account to compare the performance of this alternative technology with respect to common numbers reported for the well-rooted conventional technology, i.e. ethane and naphtha steam cracking.

5.1 User-defined reactor model

Following the general introduction, the governing equations of the simplified reactor model, have been integrated within the simulator through an USER2 block [78]. These equations are coded in an Excel file where a constant flow of information is established between this latter file and ASPEN Plus. To connect both interfaces, a Fortran subroutine which acts as a “bridge” between the two platforms was implemented, as suggested in Figure 5.1.

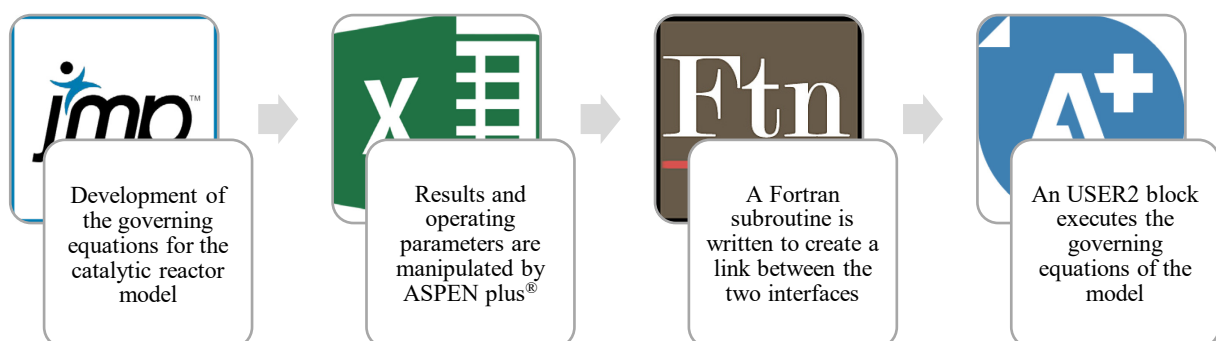


Figure 5.1 – Information pathway while using an USER2 block in ASPEN Plus®.

5.1.1 Excel model specifications

The creation of an Excel workbook is a crucial step for the model customization approach adopted in this work. Once a set of input variables and physical properties have been identified, the user model can be developed within Excel without the need of an iterative compile at each simulator run [79].

When the model is called by ASPEN Plus, the necessary input variables are copied into Excel input sheets in table format (i.e. stream data and physicochemical properties). The numerical data is classified as integer and real number, hence copied to *Aspen_Input*, *Aspen_IntParams* and *Aspen_RealParams* Excel sheets. This classification is given by available templates located within “Engine” folder in the software installation directory. On this matter, the variables for the construction of the Excel model are enlisted in Table 5.1.

Table 5.1 – Excel workbook variables for the ODH-C₂ reactor model. SI is the unit settings given by default.

Aspen_Input		Aspen_RealParams		Aspen_IntParams	
Variable	Description	Variable	Description	Variable	Description
Stream composition	Component mass flow rate	d_t/d_p	Tube-to-particle diameter ratio	N_{tu}	Number of tubes
TOTFLOW	Total mass flow rate	d_t	Tube diameter		
TEMP	Stream inlet temperature	L_{re}	Reactor tube length		
PRESS	Stream total pressure	T_{bath}	Bath temperature		
ENTHALPY ¹	Stream mass enthalpy	MF	Mass flux		
VAP FRAC ²	Vapor fraction				
ENTROPY ³	Stream mass entropy				
DENSITY ⁴	Total density				
MOLE WT ⁵	Average molecular weight				

^{1, 2, 3, 4, 5} These variables can be either provided by the user or calculated during the simulation. In this work, their values are estimated by ASPEN Plus.

These variables have to be manipulated by user-defined mathematical expressions in order to generate the model outcome. In this way, the product stream composition downstream the ODH-C₂ reactor model is calculated by a proper manipulation of the multiparametric equations at $L_{re} = 2.6$ m. One should notice that only the gas phase temperature regression model is needed for this calculation step, while the estimation of the solid phase temperature it has been used for thermal stability verification.

5.1.1.1 Governing equations

A total of five multiparametric equations are coded within an Excel file constituted by four regression models for relevant responses, i.e. $X_{C_2H_6}$, X_{O_2} , $S_{C_2H_4}$ and T_g ; plus, an additional equation to estimate the pressure drop within the packed-bed. This model will be further discussed in the next section.

With respect to the USER2 block, there are basic information that must be provided by the user in order to run the simulation. The number of inlet and outlet streams, the chemical composition of the feed(s), temperature and pressure specifications constitute the bases. In addition to that, a calculation framework is compulsory for the generation of the model outcome. In this work, the reactor model is constituted by two streams; i.e. feed and effluent of the catalytic reactor. Even though the general definition of the responses used in the multiparametric model are useful for the sake of the optimization, a proper manipulation of them must be performed to generate proper results while implementing the model in ASPEN Plus. On this regard, the mathematical expressions to define the reactor model product stream are represented by Equations (5.1-5).

$$F_{C_2H_6,out} = F_{C_2H_6,in} (1 - X_{C_2H_6}) \quad (5.1)$$

$$F_{O_2,out} = F_{O_2,in} (1 - X_{O_2}) \quad (5.2)$$

$$F_{C_2H_4,out} = S_{C_2H_4} (F_{C_2H_6,in} - F_{C_2H_6,out}) \quad (5.3)$$

$$F_{CO_2,out} = 2 (F_{C_2H_6,in} - F_{C_2H_6,out} - F_{C_2H_4,out}) (1 - S_{C_2H_4}) \quad (5.4)$$

$$F_{H_2O,out} = \frac{\dot{m}_{mix} - \dot{m}_{C_2H_6,out} - \dot{m}_{O_2,out} - \dot{m}_{C_2H_4,out} - \dot{m}_{CO_2,out} - \dot{m}_{N_2,out}}{PM_{H_2O}} \quad (5.5)$$

where \dot{m}_i is the mass flow rate of each specie, including the mass flow rate of the inlet stream (\dot{m}_{mix}). Note that the water content of the product stream is defined by a mass balance between the latter and the feed.

The number of tubes (N_{tu}) in the industrial reactor model depends on the inlet mass flow rate which is defined by the user. The link between these two parameters is given by the reactor mass flux. In this way, the former parameter is calculated by Equation (5.6).

$$N_{tu} = \frac{\dot{m}_{mix}}{MF A_{tube}} \quad (5.6)$$

where A_{tube} is the cross-sectional area of each tube within the industrial reactor.

5.1.1.2 Pressure drop estimation

The USER2 block in Aspen plus requires the specification of both, initial and final pressure of the involved streams. Therefore, an additional equation is added to the model in order to estimate the pressure drop within the packed bed. This will allow the simulation engine to calculate further parameters according to the thermodynamic package selected by the user (i.e. UNIFAC with Redlich-Kwong equation of state and Henry's Law).

Several works have been reported in literature where different correlations are used to estimate the pressure drop (ΔP) in packed-beds [80, 81, 82]. Among them, the Reichelt's correlation (1972) [82] has been selected in this work, since it is in good agreement with irregular packed-bed configurations and it takes into account how the ΔP is affected by the wall effect, described in Section 2.4. It presents high accuracy for a wide range of particle Reynolds numbers ($0.01 \leq Re_p \leq 17.635$), tube-to-particle diameter ratio ($1.624 \leq d_t/d_p \leq 250$) and average bed porosity ($0.33 \leq \bar{\epsilon}_b \leq 0.882$) [82].

The pressure drop estimation is carried out through an expression that introduce the concept of dimensionless pressure drop (ψ) for spherical particles, i.e. Equation (5.7)

$$\frac{\Delta P}{L} = \frac{\rho_f u_0^2}{d_p \psi} \quad (5.7)$$

where u_0 is the superficial velocity, and ψ is estimated by the Reichelt correlation [82], as shown by Equation (5.8),

$$\psi = \frac{154 A_w^2}{Re_p} \frac{(1 - \bar{\epsilon}_b)^2}{\bar{\epsilon}_b^3} + \frac{A_w}{B_w} \frac{1 - \bar{\epsilon}_b}{\bar{\epsilon}_b^3} \quad (5.8)$$

where the parameters A_w and B_w are calculated by Equations (5.9-10), respectively.

$$A_w = 1 + \frac{2}{3 \left(\frac{d_t}{d_p} \right) (1 - \bar{\epsilon}_b)} \quad (5.9)$$

$$B_w = \left[1.15 \left(\frac{d_t}{d_p} \right)^{-2} + 0.87 \right]^2 \quad (5.10)$$

The average bed porosity is estimated with the correlation given by de Klerk [21, 82] which shows good predictions for loose irregular packing arrangements, i.e. Equation (5.11).

$$\bar{\epsilon}_b = 0.41 + 0.35 \exp \left(-0.39 \left(\frac{d_t}{d_p} \right) \right) \quad (5.11)$$

In conclusion, the pressure drop estimation is directly influenced by some of the main factors treated in this work (i.e. d/d_p and MF).

5.1.2 Fortran subroutine

As mentioned previously, another important step during the model development is the coding and compilation of an user-defined Fortran subroutine. The latter has been created by following the instructions available in ASPEN Plus manuals [78]. This file uses the extension .f and it allows the simulation engine to read data from the Excel workbook (such as stream parameters) necessary for block calculations. Once results have been obtained by the simulation engine, dependent variables which were pre-defined in the subroutine will be written back in a specific sheet of the Excel workbook (*Aspen_Output*).

5.2 Process simulation

In this section, the main goal is to prove the feasibility of integrating the ODH-C₂ technology within a well-rooted steam cracking facility. In this way, it is possible to study a gradual replacement of critical units of this conventional technology (i.e. cracking furnaces). The integration of this novel technology is supported by the fact that there are specific downstream units in common for both technologies (e.g. C₂-splitter unit) [57]. Having acknowledged this, a higher flexibility can be achieved regarding the scale-up of the process simulated in this work.

The first step is, therefore, to define an objective production scale at which the simulation is performed. On this matter, the ethane capacity of an industrial-scale cracking furnace is taken as reference point, whose common values are 4-40 tons h⁻¹ depending mainly on the type of feedstock (i.e. naphtha or lighter hydrocarbons such as ethane) [35, 36, 37]. It is important to mention that, in a steam cracking plant, several furnaces generally work in parallel in order to cover the necessary ethylene capacity (i.e. up to a million tons per year).

5.2.1 ODH-C₂ reactor block

As introduced in Section 5.1, the reactor model is simulated through an USER2 block [78, 79] which permits several inputs and outputs for more flexibility in case further customizations are needed. Once created the necessary files to run the block (i.e. Excel workbook and Fortran subroutine), the required input data are the name of these latter files and further specifications regarding the involved streams. For the ODH-C₂ reactor model considered in this work, there are only a feed stream and a product stream.

The chosen parametric configuration is within the optimized operating region presented in Table 4.2. Under those conditions, the feed stream was defined to accomplish an ethane capacity of ca. 40 tons hr⁻¹. The reactor model set up from the construction standpoint is, therefore, specified in Table 5.2.

Table 5.2 – ODH-C₂ reactor model pre-defined parameters.

Reactor parameters	Unit	Value
Reactors in parallel ¹	[#]	~ 5
Total number of tubes ²	[#]	1×10 ⁵
L _{re}	[m]	2.6
d _t	[m]	2.5×10 ⁻³

¹ Required number of units to cover one industrial furnace ethane capacity.

² It has been considered 20.000 tubes per industrial ODH-C₂ reactor [83].

Additionally, the required input to run the model in ASPEN Plus is summarized in Table 5.3. Note that some parameters stand for feed stream specifications (i.e. T_{in}, pressure and inlet molar composition), while others stand for further calculations such as the required number of tubes to accomplish the pre-defined ethylene yield. The product stream have presented results in agreement with the conditions specified in Table 4.2, thus evidencing a good performance of the model from the standpoint of the implementation in ASPEN plus[®].

Table 5.3 – ODH-C₂ reactor model: operating conditions and performance.

Operating conditions			Performance		
Parameter	Unit	Value	Parameter	Unit	Value
T _{in}	[°C]	200	T _g	[°C]	392
T _{bath}	[°C]	392	ΔP	[bar]	0.15
P	[bar]	2	X _{C₂H₆}	[%]	47
d _t /d _p	[-]	4.7	X _{O₂}	[%]	56
MF	[kg m ⁻² hr ⁻¹]	9900	S _{C₂H₄}	[%]	62.2
Y _{C₂H₆}	[%]	8			
Y _{O₂}	[%]	10.3			
Y _{N₂}	[%]	81.7			
Total flow rate	[tons hr ⁻¹]	430			

Although the thermodynamic package does not directly influence the chemical composition of the product stream, it will have an effect on the estimation of the thermodynamic properties of the stream, e.g. mass enthalpy. Therefore, it is important to select a suitable numerical solver according to the process being simulated. For the ODH-C₂ reactor block, Peng-Robinson equation of state is used since its adequacy has been already proven for these kind of applications [84, 85].

The planification of the required downstream process is based on the chemical composition of the product stream which is in agreement with the reactor performance seen beforehand. On this matter, Table 5.4 enlisted the component mass flow rate of both feed and product stream.

Table 5.4 – ODH-C₂ reactor model: component mass flow rate.

Mass flow rate (tons hr ⁻¹)	Feed stream	Product stream
CO ₂	0	9.9
C ₂ H ₆	39.9	21.9
C ₂ H ₄	0	10.4
O ₂	59.0	28.3
N ₂	411.2	411.2
H ₂ O	0	28.2
Total flow rate		510.0

By having these results, one should notice that the CO₂ produced per ton of ethylene remains below unity but, nonetheless, is still relatively high (~ 0.95) with respect to common values of steam cracking (i.e. 1.2-1.6) [33]. Furthermore, the reactor model does not include the CO₂ contribution linked to downstream processes yet, which could lead to even higher emissions with respect to the conventional technology. Fortunately, the exothermicity of the ODH-C₂ allows the exploitation of the reaction enthalpy ($\Delta H_r^\circ = -149.6 \text{ kJ mol}^{-1}$) for heating purposes, thus lowering down the net CO₂ emissions.

5.2.2 Steam generation block

The utilization of steam as heating utility is very common in many industrial applications. Its flexibility allows a wide range of working temperature; i.e. from 105°C to 250°C for low-pressure and high-pressure steam, respectively. A conventional steam generation process is roughly composed by a boiler, a heat exchanger and a recirculation network [86]. In this way, water is converted into steam by burning different kind of fuels in the boiler, hence the steam latent heat is exploited as heating utility in the heat exchanger. The exhausted steam is then condensed back into water so it can be recycled again through a pumping network.

The CO₂ emissions linked to steam generation will depend on both power requirements and boiler efficiency. Boilers that burn fossil fuels are highly efficient (~95%) but also more contaminant; while burners that use biomass (e.g. wood chips) have a lower environmental impact with a lower efficiency (~85%) [86]. Due to the availability of a fossil-origin feedstock, the first category is commonly seen within an ethylene production plant. Therefore, this section has the scope to estimate the energy savings while exploiting the exothermicity of the ODH-C₂ by considering a natural gas-fired boiler as reference [28, 87]. The simulation flowsheet is illustrated in Figure 5.2, where each unit of the steam generation block is included.

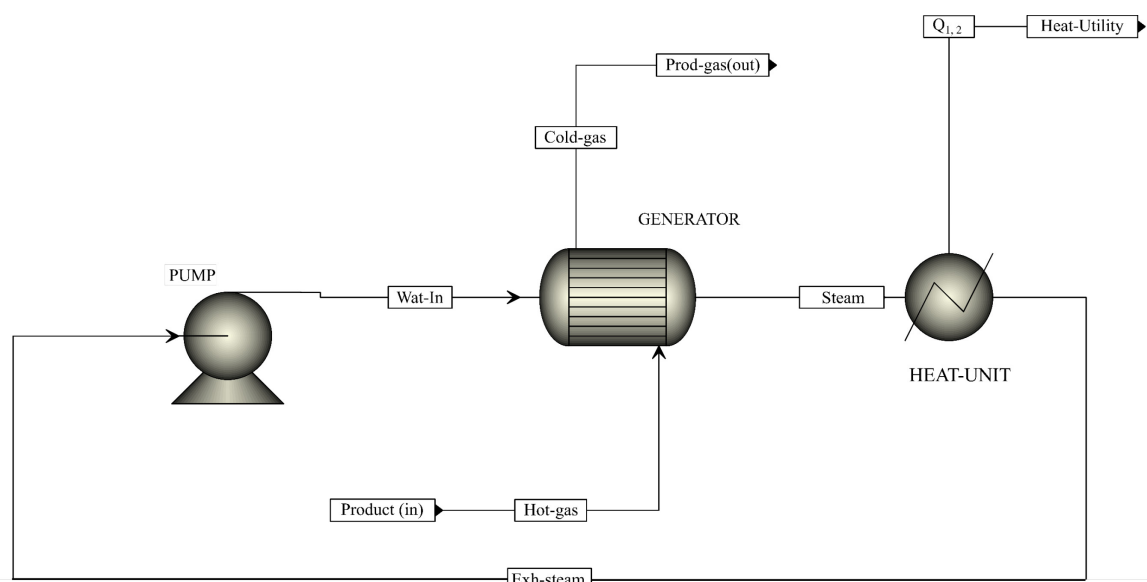


Figure 5.2 – Steam generation block.

As mentioned before, two sections have been created regarding steam generation. Both are constituted by the same units, working at different operating conditions. The steam specifications follow the utility definition given by default in ASPEN Plus. In this way, the pressure and temperature specification of the “Steam” stream in Figure 5.2 will be, respectively, 40 bar at 250°C and 2.5 bar at 125°C for high-pressure and low-pressure steam.

The most important unit is labelled as “Generator”. It represents the heat exchanger where pressurized liquid water arrives from the cold side in order to be totally vaporized into steam. This unit exploits the sensible heat of the product stream coming from the ODH-C₂ reactor, whose temperature is 392°C. The steam is, therefore, generated in the absence of an external source of energy (i.e. natural gas) which incurs into CO₂ emissions savings. Since the reactor effluent must be, nonetheless, cool down for the next downstream process (i.e. CO₂ separation), these two blocks contribute to the energy integration of the overall process.

The simpler heat exchanger unit labelled “Heat-Unit” stands for simulating the heat exchange where a heating utility supply is required. In this way, it is possible to estimate the latent heat of the heating stream under common efficiency values for heating processes. In this work, an efficiency of 90% is assumed at each steam generation block [28].

Additional information regarding each unit have been summarized in Table 5.5. Note that the pump unit has been set up according to the pre-defined pressure discharge (i.e. 40 bar and 2.5 bar for high-pressure and low-pressure steam, respectively) at a mechanical efficiency equal to 85%. This latter conditions is applied to each pump included in the process simulation. The thermodynamic package selected in this section is STEAM-TA, which utilizes ASME 1967 steam table correlations to perform calculations.

Table 5.5 – General information of the steam generation block.

Unit: “Generator”		Unit: “Heat-Unit”	
Parameter	Description	Parameter	Description
Calculation mode	Design	Initial vapor fraction	1
Flow direction	Counter-current	Final vapor fraction	0
ΔT_{pinch}	10°C	ΔP	0.1 bar
Overall heat transfer coefficient (U)	$730.8 \frac{\text{kcal}}{\text{m}^2 \text{ hr K}}$	Efficiency	0.90
Heat duty ¹	$7.82 \text{ GJ ton}_{\text{C}_2\text{H}_4}^{-1}$	Heat duty ²	$7.04 \text{ GJ ton}_{\text{C}_2\text{H}_4}^{-1}$
	$7.32 \text{ GJ ton}_{\text{C}_2\text{H}_4}^{-1}$		$6.62 \text{ GJ ton}_{\text{C}_2\text{H}_4}^{-1}$

^{1,2} These values have been obtained by dividing the global heat duty by the ethylene yield at reactor level (see Table 5.5). From top to bottom, values are enlisted for high-pressure and low-pressure steam generation.

Important information regarding each stream involved in both simulation schemes is enlisted in Table 5.6. Although there are some values in common between the two processes (e.g. vapor fraction and gas flow rate), some others point out the different thermal capacity of both utilities from the standpoint of temperature and pressure working conditions.

Table 5.6 – Stream parameters of the steam generation block ¹.

Parameters	Stream labels				
	Wat-In	Steam	Hot-gas	Cold-gas	Exh-steam
Vapor fraction	[0, 0]	[1, 1]	[0, 0]	[0, 0]	[0, 0]
Temperature (°C)	[250, 125]	[250, 125]	[392, 260]	[260, 137]	[250, 125]
Pressure (bar)	[40, 2.5]	[40, 2.5]	[1.67, 1.47]	[1.47, 1.27]	[35, 2]
Flow rate (ton hr ⁻¹)	[46.1, 33.8]	[46.1, 33.8]	[510, 510]	[510, 510]	[46.1, 33.8]

¹ The first and second value of each vector correspond to data from the high-pressure and low-pressure steam generation block, respectively.

Before concluding this section, one should notice that the final temperature of the ODH-C₂ reactor effluent is 137°C meaning that it could still serve as heating utility for low-demanding processes. In fact, the remaining heat capacity of this stream can be exploited within the CO₂ separation block, where a pre-heating is required for the distillation of the liquid stream downstream the CO₂ absorber.

5.2.3 Compression block

In this section, compression requirements for the process simulation are accounted. Since most of the streams in the process layout are in gas phase, rigorous calculations while estimating the energetic requirements are strictly recommended to guarantee realistic results. Particularly for ethylene production, the process simulation can be performed either at medium-high pressure (> 10 bars) to minimize the volume to be manage, thus decreasing the size of the operation units; or at pressure close to ambient conditions which would be less energy intensive but incurring into a high capital cost. On this matter, Figure 5.3 illustrates how the energy requirements and CO₂ emissions evolves while incrementing the discharge pressure of the compressor.

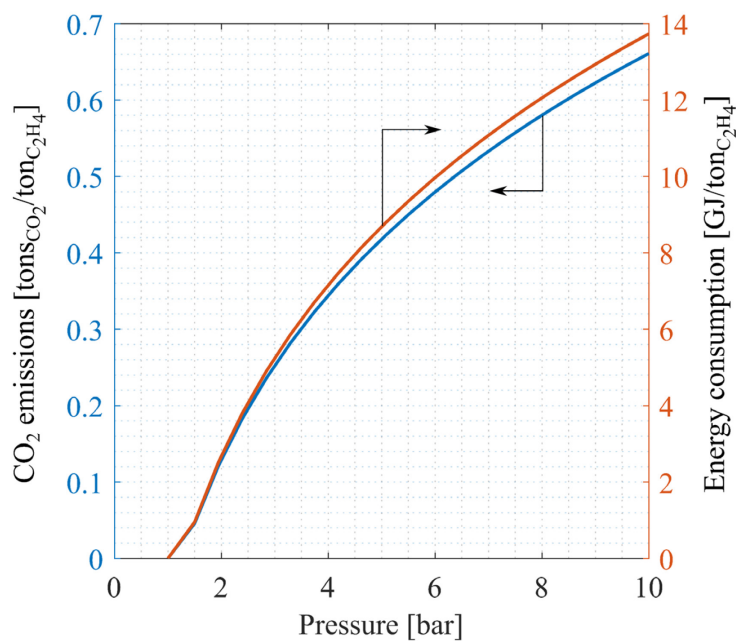


Figure 5.3 – Energy specific consumption and CO₂ emissions as function of a two-stage compressor discharge pressure. The feed (510 tons hr⁻¹) enters the compressor unit after the steam generation block at 35°C.

Given the energy demand of high compression ratios, the discharge pressure has been defined at 2 bar. Furthermore, this choice is in agreement with common pressure operative conditions for the process downstream the steam generation block (i.e. CO₂ extraction), where both the absorber and recovery unit operate at pressures below 2 bar [28].

For simulations at industrial scale, it is advisable to include multi-stage compressor units in the simulation environment (i.e. at least two-stages) [88]. In this way, it is possible to introduce an inter-cooler between stages to cool down the stream, hence minimizing the gas volume and energy requirements. The block has been located downstream the steam generation block (see Appendix E). The inlet stream has been previously treated by a dewatering unit to extract the water fraction generated as a side product. Table 5.7 summarizes the operative conditions and the involved stream parameters.

Table 5.7 – Compression block: operative conditions.

Parameter	Description
Compressor model	Isentropic using ASME method
Number of stages	2
Isentropic efficiency	75%
Inlet mass flow rate	482 tons hr ⁻¹
Fix discharge pressure	2 bar
Compression ratio	1.57
Cooler outlet temperature	35 °C
Cooler utility ¹	Cooling water
Energy consumption	0.98 (GJ ton _{C₂H₄} ⁻¹)
Compressor utility ²	Electricity
Energy consumption	0.97 (GJ ton _{C₂H₄} ⁻¹)

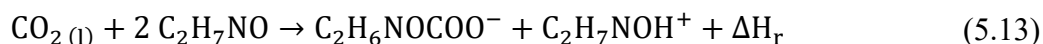
^{1,2} These specific values have been obtained by considering the ethylene yield at reactor level (see Table 5.5). Note that feed-pre treatment expenses are not yet accounted.

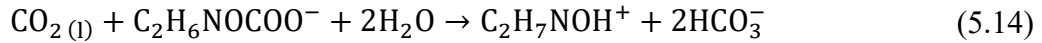
An important observation is the fact of considering zero emissions from the cooler utility. Cooling water from an evaporative draft cooling tower is utilized as coolant [89, 90], therefore ASPEN Plus assumes negligible CO₂ emissions while considering this utility. This advantage is undertaken in the process simulation by utilizing this refrigerant where required; i.e. cooling down up to 35°C.

5.2.4 CO₂ separation block

The separation of the carbon dioxide from the product stream is a crucial step in the ethylene purification process. The removal efficiency of this block should be higher than 99% since even traces of CO₂ could lead to significant ice formation in the upstream process, i.e. cryogenic distillation. A well-rooted process for this scope is the amine-based capture technology, where CO₂ is chemically absorbed in amine solutions within a packed-bed column, also known as absorber. Among different options, monoethanolamine (MEA) has been widely used industrially and commercially, therefore several works have been reported where the latter alkanol-amine is used as standard absorbent for CO₂ capture [29, 91, 92].

When CO₂ is absorbed in the liquid phase, it follows a reaction mechanism composed by three main reactions represented by Equations (5.12-14) [93].





Equation (5.12) represents the physical absorption of CO₂ in the liquid phase, where ΔH_{abs} is the associated heat of absorption; whereas Equation (5.14) represents the chemical absorption of CO₂ in the bulk where several electrolytes species are formed.

Downstream the absorber a stripper is located to released the CO₂ content out from the aqueous solution. This is a very energy intensive process since it consumes more than 80% of the total energy requirements for the CO₂ separation [92], therefore a deep optimization of the stripper working conditions is necessary together with an opportune energy integration.

In this work, the CO₂ separation block has been divided into two subsections. In this way, the absorber and stripping section are simulated under different thermodynamic packages, selected to be in good agreement which each process in particular. This distinction is illustrated in Figure 5.4.

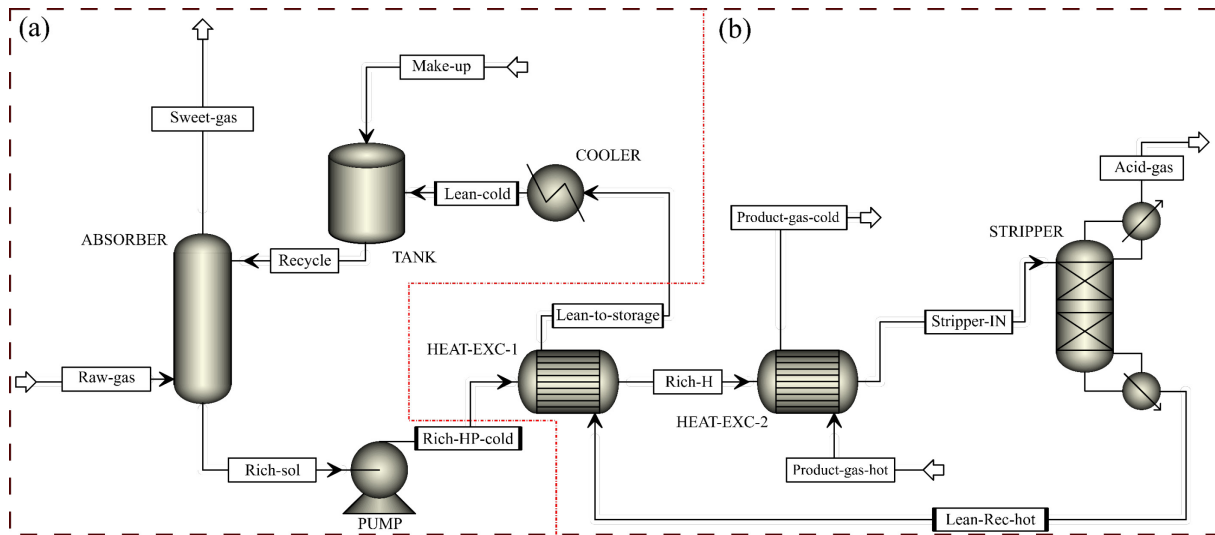


Figure 5.4 – CO₂ separation block. (a) represents the CO₂ absorption section (thermodynamic package: AMINES); while (b) represents the stripping section for CO₂ desorption and MEA recovery (thermodynamic package: eNRTL).

5.2.4.1 CO₂ absorption section

When simulating CO₂ absorption at industrial scale, rigorous calculations are required since the process is highly non-ideal due to interactions in the form of molecule-molecule, ion-ion and molecule-ion. In order to cover those interactions in the simulation, it is important to operate under a accurate calculation method and use a suitable thermodynamic package. On this matter, Rate-based modelling offers accurate estimations with respect to equilibrium models, since it accounts for mass and heat transport limitations [94]. With respect to the thermodynamic package, the Kent-Eisenberg model [95] is available in ASPEN Plus to specifically simulate sweetening processes.

Figure 5.4 (a) represents the simulation block where the absorber is located. This unit consists in a packed column which operates at room pressure and absorption temperatures not higher than 40-60°C to avoid feedstock losses due to the MEA high volatility [96]. At steady-state conditions, the stream labelled as “Recycle” constitutes the lean MEA solution, i.e. aqueous solution of 15% wt. of MEA. Note that to overcome eventual losses of both water and MEA, a

make-up stream is necessary. A large number of runs are required before reaching convergence while considering the whole block (i.e. absorption/desorption). This is linked to the process sensitivity to the solvent content in the absorbent, which can cause divergence. To solve this issue, a set of convergence estimates are generated by running the block without including the recycle stream. In this way, initial points of useful parameters, i.e. temperature and composition of both vapor and liquid phases, are created to facilitate the iterative procedure. Once the simulation is stabilized, the recycle stream can be added to the scheme.

Preliminarily to the simulation of the absorber block, common configurations for sweetening processes found in literature were considered [29, 30]. On this matter, important set up parameters of the absorber are enlisted in Table 5.8. For the first run, initial values for the packed height and column diameter were imposed (15 and 5 m, respectively). The flow rate of MEA solution was defined to stay below the admissible specific pressure drop (334 mm-water m⁻¹) and flooding conditions (i.e. values greater than 85%). These conditions are given by default in ASPEN Plus once the block is configured and it provides feasible operating conditions at industrial scale. Nonetheless, the initial configuration has been further optimized after reaching convergence stability.

Table 5.8 – Fixed parameters of the absorber unit.

Parameter	Description
Unit model	Radfrac
Calculation method	Rated-based
Column type	Packed-bed
Packing type and material	Raschig/ceramic
Void fraction [-]	0.75
Mass transfer coefficient method	Onda-68 [29]
Interfacial area method	
Heat transfer coefficient method	Chilton and Colburn [29]
Pressure drop calculation method	Stichlmair [93]
Liquid and gas phase resistance	Film reactions
Interface factor	1

The packed height is a key parameter while designing an absorption column since it directly influence the mass transfer phenomena between both phases. Another important variable is the required flow rate of MEA solution to achieve high removal capacity. On this matter, the column design has been optimized throughout a sensitivity analysis, where the CO₂ removal capacity has been evaluated as a function of these latter parameters (see Figure 5.5). The analysis has been carried out to remove the CO₂ content from the product stream of the catalytic reactor, whose gas flow rate is 482 tons hr⁻¹ with a CO₂ mass fraction equals to 2.5%. This stream is labelled as “Raw-gas” in Figure 5.4. The CO₂ removal capacity of the column is mathematically represented by Equation (5.15),

$$\%Rem_{CO_2} = 1 - \frac{\dot{m}_{CO_2}^{sg}}{\dot{m}_{CO_2}^{rg}} \quad (5.15)$$

where $\dot{m}_{CO_2}^{rg}$ and $\dot{m}_{CO_2}^{sg}$ are the mass flow rate of CO₂ in the raw-gas and in the sweet-gas streams, respectively.

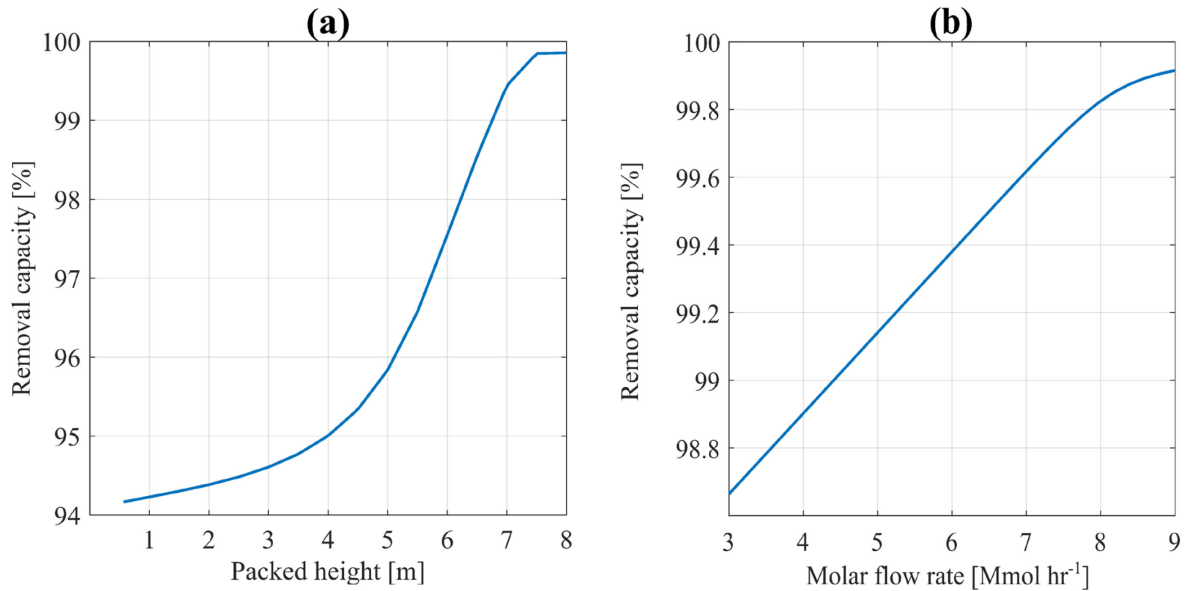


Figure 5.5 – CO₂ removal capacity of the absorber as a function of (a) number of theoretical stages and (b) amine solution molar flow rate. Temperature and pressure conditions are 45°C and 2 bar, respectively.

Figure 5.5 (a) indicates that the initial packed height was overestimated to reach a removal capacity beyond 99% since, under the given operative conditions, ca. 7 m are sufficient. The initial molar flow rate value of the fresh amine solution was 8×10^3 kmol hr⁻¹ which, according to Figure 5.5 (b), it has been also overestimated. The sensitivity analysis indicates that a molar flow rate of 4.5×10^3 kmol hr⁻¹ is sufficient to achieve high carbon removal, almost half of the initial value. Reducing the molar flow rate of the amine solution minimizes the heat duty required in the stripper to liberate the CO₂ content from the rich MEA solution, which is the most energy expensive part of this block. Nonetheless, the reduction of this parameter induces undesired conditions within the absorption column due to a low liquid-to-gas molar flow rate ratio (L/G). In other words, the reduction of the liquid feed in the column enhances greater than 85% values with respect to flooding conditions. This issue can be solved either by increasing the column diameter to reduce the gas molar flow rate per cross-sectional area, or by increasing the working pressure of the column. While the first option incurs into a higher capital cost, increasing the operative pressure of the absorption has been demonstrated to be significant energy intensive (see Figure 5.3).

It turns evident that a compromise has to be made to define the most suitable working conditions. A priori, working conditions indicated in Figure 5.5 (b) would require a column diameter higher than 7 m, which are not commonly seen within the industry [29]; therefore the liquid flow rate should be higher than the minimum. In addition, absorption columns for sweetening process do not generally operate at high pressure since the CO₂ removal is carried out through chemisorption, which is almost unaffected by pressure. Notwithstanding the higher

energy expenses, the only viable option is to operate at higher liquid flow rate (7.5×10^3 kmol hr⁻¹) to guarantee hydrodynamic stability at the given column diameter (5 m). It is important to mention that the heat duty requirements in the desorption section can be supply by using steam as utility (see Section 5.2.2), thus favouring the self-sustainability of this block.

Summarizing, the final operative configuration and performance of the absorption block are given in Table 5.9.

Table 5.9 – Absorber final operative conditions and overall performance.

Operative conditions	Unit	Value
Temperature	[°C]	45
Top-stage pressure	[bar]	1.5
Pressure drop (ΔP)	[bar]	0.06
Diameter	[m]	6
Number of theoretical stages	[#]	14
Packed height per stage (HETP)	[m]	0.50
Raw gas flow rate ¹	[tons hr ⁻¹]	482
Amine solution flow rate ²	[kmol hr ⁻¹]	7.5×10^3
Liquid-to-gas mass flow rate ratio	[-]	0.3
CO ₂ capture	$\left[\frac{\text{mol}_{\text{CO}_2}}{\text{mol}_{\text{MEA}}} \right]$	0.53
MEA losses	[%]	< 1
CO ₂ removal	[%]	99.2

¹ The CO₂ content is 2.5% in mass bases.

² The monoethanolamine content is 15% in mass bases.

The cleaned gas leaves the top of the column with less than 1% of CO₂ in mass bases and traces of MEA. Therefore, a water washing is needed to fully recover it. The resulting stream is composed by air-related species (i.e. N₂ and O₂) and the hydrocarbon fraction, i.e. ethane and ethylene. The final composition is constituted by 87.14% of N₂, 6% of O₂, 2.2% of C₂H₄ and 4.66% of C₂H₆ in mass bases.

5.2.4.2 CO₂ desorption section

The simulation of the stripping section includes the pre-heating treatment of the feed stream (see Figure 5.4). This latter operation is important in order to reduce the required heat duty in the stripper reboiler; thus a common practice is to exploit the sensible heat of the bottom stream (i.e. lean MEA) to pre-heat the rich MEA solution. The temperature range at which the stripper operates is between 100-140°C, therefore the inlet temperature should approach that value as much as possible to minimize the energy expenses.

As anticipated in Section 5.2.2, the ODH-C₂ reactor product stream is cool down till 137°C after passing through the steam generation block. Therefore, the remaining heat load can be exploited to pre-heat the rich MEA solution, i.e. the first heat exchanger located downstream the absorber (see Figure 5.4). On this matter, further details regarding the performance of the pre-heating system have been summarized in Table 5.10.

Table 5.10 – Operating specification and performance of the pre-heating system in the stripping section.

Parameter	Unit: Heat-Exc-1	Unit: Heat-Exc-2
	Description	
Calculation mode	Design	
Flow direction	Counter-current	
ΔT_{pinch}	10°C	
Overall heat transfer coefficient (U)	730.8 $\frac{\text{kcal}}{\text{m}^2 \text{ hr K}}$	
Exchanger area (m ²)	153	133
Cold-side temperature ¹ (°C)	[22, 60]	[60, 99]
Hot-side temperature range ¹ (°C)	[102, 70]	[137, 109]
Heat duty	13.5 GJ hr ⁻¹	16.5 GJ hr ⁻¹

¹The first and the second value of the ranges indicates inlet and outlet conditions, respectively.

Results indicates that significant energy savings are accomplished by the pre-heating system. In specific terms, the first heat exchanger is able to put by ca. 1.30 GJ per ton of ethylene produced; while the second heat exchanger, which integrates part of the heat released in the ODH-C₂ reactor, saves the equivalent of 1.58 GJ per ton of ethylene produced.

The stripper unit consist in a trayed column with a water-cooled partial condenser and a kettle-type reboiler which operates at room pressure. The optimization of this block is based on three parameters; i.e. CO₂ desorption capacity, MEA recovery and heat duty. Therefore, a sensitivity analysis is carried out to evaluate the effect of both, a discrete variable (i.e. number of stages) and continuous variables (i.e. bottom-to-feed ratio, molar reflux ratio and reboiler heat duty). The feed stage in the stripping section is located on the second stage, as the desorption is favoured by less entrainment within the column. The thermodynamic package selected for this section is the electrolyte NRTL model (eNRTL) presented by Chen et.al [97], which is commonly utilized to simulate this kind of electrolyte systems. Respectively, CO₂ desorption capacity and MEA recovery are mathematically calculated as shown by Equations (5.16-17),

$$\%Des_{CO_2} = \frac{\dot{m}_{CO_2}^{ag}}{\dot{m}_{CO_2}^{rich}} \quad (5.16)$$

$$\%Rec_{MEA} = 1 - \frac{\dot{m}_{MEA}^{ag}}{\dot{m}_{MEA}^{rich}} \quad (5.17)$$

where $\dot{m}_{CO_2}^{ag}$ and $\dot{m}_{CO_2}^{rich}$ are, respectively, the mass flow rate of CO₂ in the acid-gas and in the rich MEA solution streams. Analogously, the same definitions apply for \dot{m}_{MEA}^{ag} and \dot{m}_{MEA}^{rich} .

Due to the strong non-ideal behaviour, the reach of convergence will depend of the initial estimation of the above mentioned operating parameters. On this matter, the initial configuration was defined according to previous industrial-scale simulations reported in literature [93]; thus, the first run configuration consisted in 20 equilibrium stages where the feed stream was located in the 2nd stage.

Notwithstanding the latter operative conditions are more generic for an industrial scale process, more detail assumptions can be made regarding the molar reflux ratio (RR) and bottom-to-feed ratio ($B:F$) due to the low CO₂ content of the rich stream (~ 6% in mass bases). Therefore, it is possible to anticipate that the ideal $B:F$ value should be close to one at the lowest possible RR , in order to guarantee high recovery at the lowest possible reboiler heat duty.

Note that this kind of non-ideal systems require a Rate-based calculation approach to pursue a better accuracy, hence the simulation of this part has been performed under this latter condition. Nonetheless, for the sake of generating a set of initial parameters estimates to improve converge (i.e. tentative temperature and composition profiles along the column), a priori the simulation is run under equilibrium conditions.

The first sensitivity analysis was performed to determine the final number of theoretical stages and the best $B:F$ (see Figure 5.6). The MEA recovery grade is highly influenced by the heat duty at the reboiler due to its high vapor pressure, in fact reducing the energy requirements at the stripper also reduces the monoethanolamine losses. Additionally, negligible losses in the hydrocarbon fraction has been observed.

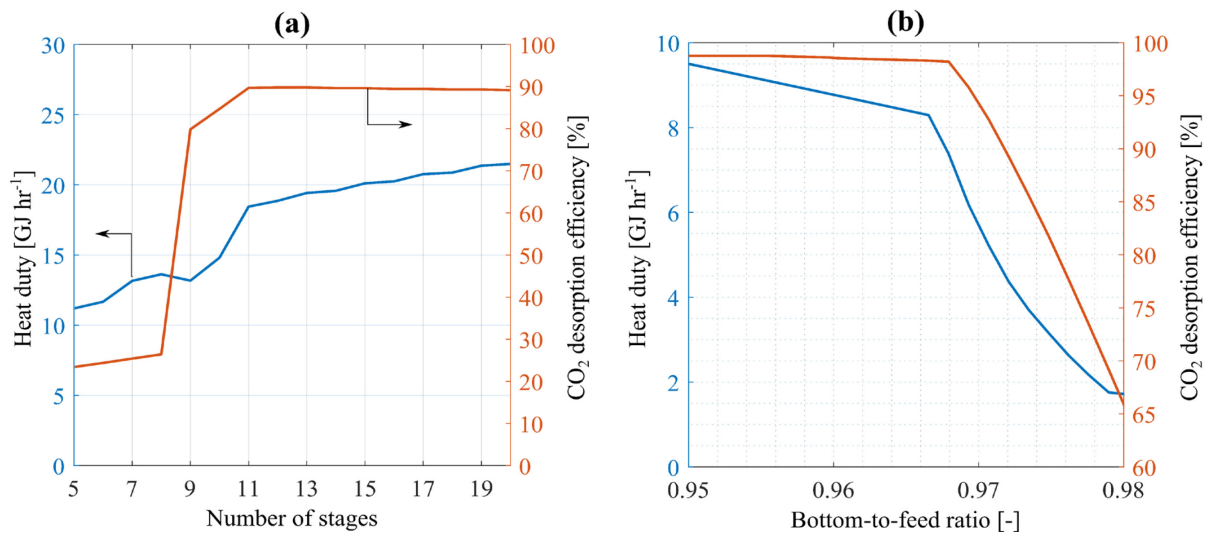


Figure 5.6 – Sensitivity analysis of stripper performance parameters as a function of discrete and continuous variables. Molar RR was maintained fixed at 0.1. Under these conditions, MEA losses were, on average, between 1-2%.

Figure 5.6 (a) indicates that no further improvements in terms of desorption efficiency are observed beyond 11 stages; at the contrary the process becomes more energy intensive under the pre-defined RR and $B:F$ with higher volatility losses.

By specifying 11 stages as new operative condition, Figure 5.6 (b) shows how the $B:F$ influences the overall performance. As introduced before, large bottom rates favours the minimization of the reboiler duty by guaranteeing high removal efficiency. Note that too large

$B:F$ values (> 0.97) do not provide a sufficient residence time to the liquid phase for a complete carbon desorption. Whereas at longer entrainment conditions of the liquid phase (i.e. $B:F < 0.97$), the CO_2 desorption takes place almost entirely. It has been observed that, from a practical standpoint, not further improvements are possible once reaching an overall CO_2 removal of 98%. The molar RR has not presented a significant effect on CO_2 desorption capacity, while it influences the reboiler duty. The reason is that the main refluxed component in the stripper is condensed water which re-enters the column at a lower temperature, hence requiring more energy to compensate the temperature difference to re-establish normal values. Considering that, a fixed value of 0.1 was specified to minimize the energy requirements.

Summarizing, the final operative configuration and performance of the stripper section are given in Table 5.11.

Table 5.11 – Optimized stripper specifications and performance.

Operative conditions	Unit	Value
Temperature	[°C]	90-140
Top-stage pressure	[bar]	1.8
Pressure drop (ΔP)	[bar]	0.09
Diameter	[m]	2
Number of theoretical stages	[#]	11
Molar reflux ratio	[-]	0.1
Bottom-to-feed ratio	[-]	0.965
Reboiler duty ¹	[GJ hr ⁻¹]	37.6
	[GJ ton _{CO₂} ⁻¹]	4.27
Partial condenser duty ²	[GJ hr ⁻¹]	1.17
	[GJ ton _{CO₂} ⁻¹]	0.13
MEA losses	[%]	1-2
CO_2 desorption efficiency	[%]	98

¹ Note that the reported values are gross quantities. Considering the reported reboiler duty, the stripper becomes self-sufficient when considering the generated steam as utility.

² The partial reboiler duty is supplied by cooling water from a natural draft cooling tower. Hence, negligible CO_2 emissions are assumed.

Given the above mentioned operative conditions, the specific reboiler duty is ca. 3.62 GJ per ton of ethylene produce (or 4.27 GJ per ton of CO_2 removed). Considering that the reboiler operates at 140°C, the most suitable utility might be pressurized steam. If the steam was produced by an alternative source (i.e. natural gas), the greenhouse emissions to supply the required energy load would be significant (ca. 2.5 tons of CO_2 per hour). However, an additional thermal integration step can be applied by exploiting the high-pressure steam produced downstream the ODH- C_2 reactor.

As explained in Section 5.2.2, the utility specifications in terms of temperature and pressure (i.e. 250°C and 40 bar) have been defined according to the default specifications in ASPEN Plus. In this sense, it is possible to integrate an user-defined utility by maintaining additional coefficients unchanged (e.g. carbon emission factor and heating capacity). Having said that, Equation (5.18) represents a simple energy balance to estimate the required steam flow rate,

$$\dot{m}_{hps} = \left[\frac{\lambda_{hps}}{\dot{Q}_{reb}} \right]^{-1} \quad (5.18)$$

where λ_{hps} is the latent heat of high-pressure steam (1712.94 kJ kg⁻¹), \dot{Q}_{reb} is the reboiler duty and \dot{m}_{hps} is the mass flow rate of steam. Results indicate that ca. 22 tons hr⁻¹ of high-pressure steam are required to satisfy the energy specifications, which is less than half of the total amount produced in the steam generation section (i.e. 46.1 tons hr⁻¹).

The product streams from the CO₂ separation block (i.e. the full process presented in Figure 5.4) are the stream containing ethylene and ethane which feed the cryogenic separation block; and a residual stream composed mainly by CO₂, water and traces of MEA. This latter stream can be further purify and recompressed for additional applications.

5.2.5 Cryogenic separation block

The product stream of interest coming from the sweetening process is, in practical terms, free of CO₂ (i.e. less than 1% in mass bases). The resulting gas mixture is thereupon fed to a dewatering unit to eliminate the entrained water content within the gas phase. The resulting stream is mainly composed by air-related components (i.e. N₂ and O₂) which constitutes ca. the 90% of the stream flow rate in mass bases. The remaining 10% is constituted by the hydrocarbon fraction, which requires a rigorous separation process in order to recirculate the unreactive ethane back to the catalytic reactor and to obtain an ethylene fraction of commercial standards (i.e. purity higher than 99% in mass bases).

Having acknowledged that, the simulation environment regarding this block is presented in Figure 5.7. The removal of the entrained water from the main stream is followed by an intensive refrigeration process beforehand the first cryogenic separation unit (i.e. flash tank). The first refrigeration unit involves a heat exchanger (“HEAT-EXC-1”), where the cold-side is connected to the top stream of the flash tank, which exits the latter unit at very low temperature (~ 103 K). The bottom effluent of the flash tank is connected to the cold-side of a second heat exchanger (“HEAT-EXC-2”), to minimize the cooling duty requirement in the cooler located upstream the flash tank. Notwithstanding the two heat exchangers, an additional refrigeration step is required to reach the final working temperature of the first separation step.

The flash unit exploits the average boiling temperature difference between the air and the hydrocarbon fraction to separate most of the N₂/O₂ mixture from the latter, which begins to condensate at ca. 143 K. The resulting liquid stream, rich in hydrocarbons, is fed to a cryogenic distillation column to remove the remaining content of air-related components (i.e. ~ 5% in mass bases); this step is expected to be less energy intensive with respect to the first separation unit. The bottom stream is now constituted by the valuable hydrocarbon fraction (i.e. ethane and ethylene) which feeds a second cryogenic distillation unit, commonly addressed as C₂-splitter. As introduced in Section 5.2, this is a potential common point to evaluate the feasibility of the process integration.

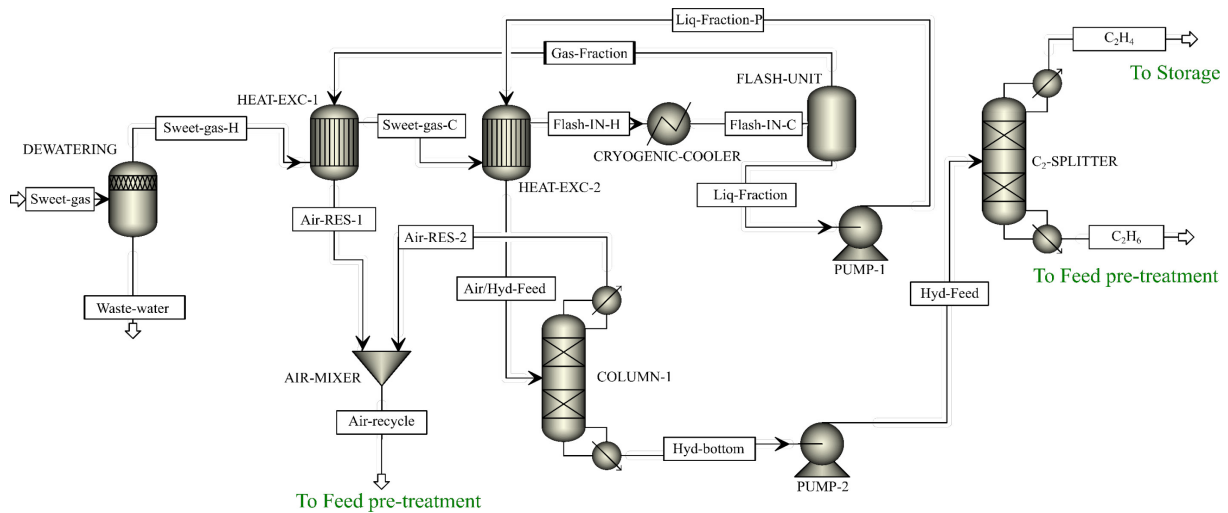


Figure 5.7 – Cryogenic separation block (thermodynamic package: Peng-Robinson).

The process optimization of the cryogenic block has been divided according to the different separation units present in the process flow diagram (see Figure 5.7). On this matter, different operating conditions are studied in order to accomplish the purification standards, i.e. polymer-grade ethylene of 99%, by minimizing both, energy consumption and CO₂ emissions.

The thermodynamic package used in this block includes the Peng-Robinson equation of state as physical property method [98]. Its adequacy to simulate cryogenic processes has been proven in previous contributions [99, 101].

5.2.5.1 Flash separation unit

As introduced in the previous section, the purification of the reactor product stream begins with a cryogenic liquefaction in a flash tank. The motivation of a preliminary separation upstream the cryogenic distillation is justified given the wide boiling point difference between the hydrocarbon fraction (i.e. 184.6 K and 169.3 K for pure ethane and ethylene, respectively) with respect to N₂ (77.35 K) and O₂ (90.2 K). Nonetheless, the main justification for a preliminary separation step is due to the high content of dilutant in the product stream (i.e. N₂). In this sense most of the molecular nitrogen fraction is expected to be separated from the main stream.

The simulation of this unit in ASPEN Plus begins with the identification of the main stream dew point. On this regard, Figure 5.8 illustrates the temperature range at which condensation occurs. A liquid fraction begins to form when the temperature drops below 143.15 K (-130°C) and it becomes richer in hydrocarbons as the temperature decreases up to the point where the more volatile components begin to condensate.

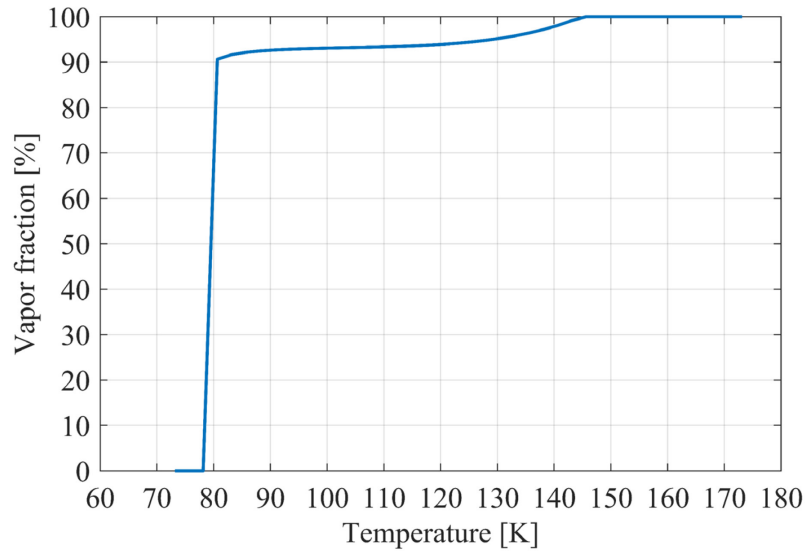


Figure 5.8 – Product stream vapor fraction as a function of the mean temperature at 1.3 bar. The stream is constituted by 87.14% of N_2 , 6% of O_2 , 2.2% of C_2H_4 and 4.66% of C_2H_6 in mass bases.

A sensitivity analysis is carried out to identify the most suitable temperature value for operating the flash unit (see Figure 5.9). On this matter, the objective is to maximize the air separation by minimizing both hydrocarbon losses and the cooling duty. The analysis has shown little influence while expanding the feed stream from 1.3 bar till room pressure.

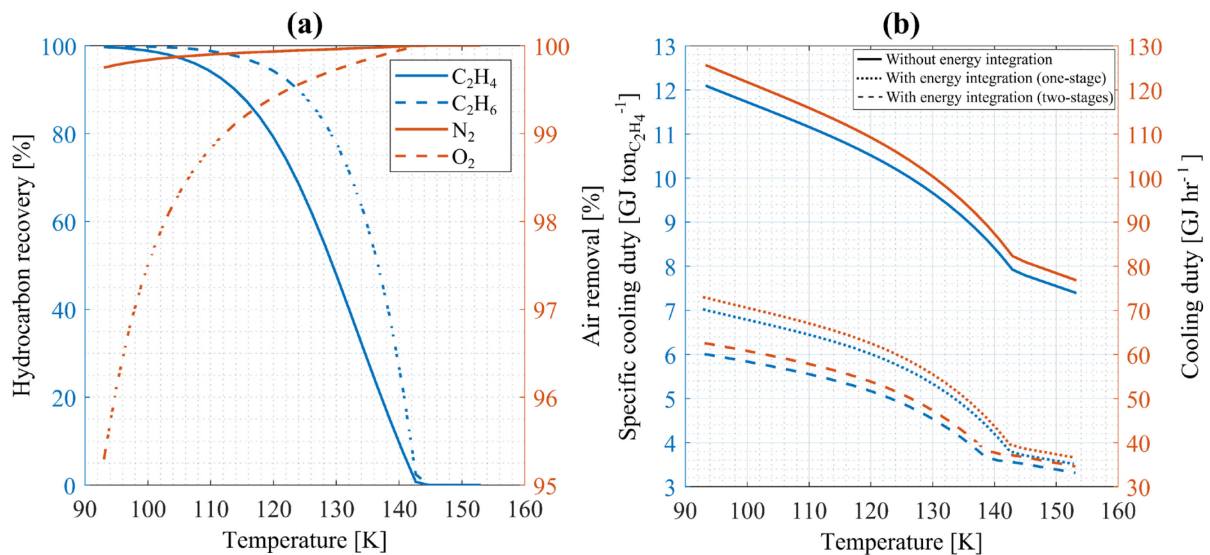


Figure 5.9 – Sensitivity analysis of the flash unit without considering the heat integration. (a) illustrates the overall performance of the flash tank while (b) compares the cooling duty of three different scenarios as a function of the operative temperature. The mass flow rate of the feed stream is 472 tons hr^{-1} , whose composition is constituted by 87.14% of N_2 , 6% of O_2 , 2.2% of C_2H_4 and 4.66% of C_2H_6 in mass bases.

Figure 5.9 (a) illustrates the hydrocarbon recovery and air removal as a function of the operative temperature. The former parameter is calculated as the mass fraction of ethane and ethylene present in the liquid stream exiting the flash unit; analogously, the latter is calculated as the mass fraction of air (i.e. N_2 and O_2) in the gas stream. Figure 5.9 (b) shows the variation of the

required cooling duty as the working temperature decreases. Note that the mass flow rate of ethylene has been kept constant (i.e. 10.4 tons hr⁻¹), since negligible losses of the olefin were observed during the previous upstream processes.

Results from the sensitivity analysis indicates that most of the N₂ content can be eliminated in the flash unit without high losses of hydrocarbons in the gas stream. More specifically, operative temperatures lower than 108 K (-165°C) guarantee more than 99% and ca. 98% separation of the original content of N₂ and O₂ entering the flash unit, respectively. The hydrocarbon fraction have registered less than 2.5% ethylene losses; whereas less than 1% with respect to ethane. It is important to highlight that, even though the process performance is satisfactory, the required energy cost is remarkable. Figure 5.9 (b) indicates that ca. 11.1 GJ of cooling duty per ton of ethylene is consumed to reach such low temperatures when a heat integration system is not accounted. On this regard, a refrigeration system to achieve those requirements is generally constituted by four cascade refrigeration stages where nitrogen-hydrocarbon mixtures are used as refrigerant. The application of this technology has been reported in literature where temperatures up to 100 K were achieved [102]. In this work, a specific pre-defined cooling utility in ASPEN Plus is used to estimate the energy consumption.

The selection of the operating temperature has been motivated by the fact that, on the one hand, more extremes conditions would slightly improve the hydrocarbon recovery at a significant reduction of the air removal capacity due to oxygen condensation. On the other hand, higher temperatures would not guarantee a proper condensation of the hydrocarbon fraction. Having said that, Table 5.12 provides further specifications regarding each stream involved in the flash unit.

Table 5.12 – Stream specifications of the flash unit.

Parameters	Stream labels		
	“Flash-IN-C”	“Gas-fraction”	“Liquid-fraction”
Vapor fraction	1	1	0
Temperature (°C)	309	103	103
Pressure (bar)	1.3	1	1
Flow rate (ton hr ⁻¹)	472	438.7	33.3

A heat integration network is essential to minimize the required cooling duty in cryogenic processes. In this sense, Figure 5.9 (b) presents a comparison between three scenarios (i.e. with and without a pre-refrigeration system) to visualize the improvement in energy requirements. From left to right, the first heat exchanger has been place downstream the dewatering unit where the gas stream is connected to the cold-side; while a second one has been connected in series whose cold-side is connected to the liquid stream exiting the flash (see Figure 5.7). Results indicate that the major improvement is achieved in the first heat exchanger (i.e. a reduction of 4.5 GJ of cooling duty per ton of ethylene; while the second one is capable of saving the additional amount of 0.7 GJ per ton of ethylene. Consequently, the HEN allows to obtain a net cooling duty which is almost half the original value. Further details regarding the configuration of each heat exchanger unit is given in Table 5.13.

Table 5.13 – Specification and performance of the pre-cooling system in the cryogenic block. Location: upstream the flash unit (see Figure 5.7).

Parameter	Unit: Heat-Exc-1	Unit: Heat-Exc-2
	Description	
Calculation mode	Design	
Flow direction	Counter-current	
ΔT_{pinch}	2 K	
Overall heat transfer coefficient (U)	$730.8 \frac{\text{kcal}}{\text{m}^2 \text{ hr K}}$	
Exchanger area (m ²)	153.61	53
Cold-side temperature ¹ (K)	[103, 210]	[103, 195]
Hot-side temperature range ¹ (K)	[309, 208]	[208, 197]
Exchanged duty	49 GJ hr ⁻¹	7.6 GJ hr ⁻¹

¹The first and the second value of the ranges indicates inlet and outlet conditions, respectively.

Note that complex equipment are required for cryogenic heat integration in terms of construction materials (i.e. usually aluminium alloys), which must be resistant to regular thermal stress, and isolation to avoid thermal losses [103]. These specialized heat exchangers are generally built to work at a very precise heat transfer capacity ($\Delta T_{\text{pinch}} \approx 2^\circ\text{C}$), which narrows the operating temperature between the hot-side and cold-side of the equipment.

Summarizing, although a big share of air-related components has been eliminated from the hydrocarbon fraction, there is still a non-negligible fraction of O₂ which requires further treatment. Therefore, another section in the cryogenic separation block includes two distillation columns where the remaining N₂ and O₂ is extracted (i.e. first column) and the resulting hydrocarbon stream is purified to produce high-standard ethylene and ethane (i.e. second column).

5.2.5.2 Cryogenic distillation

The liquid stream entering the first distillation column is constituted by 66% of ethane, 30.7% of ethylene and 3.3% of O₂/N₂ mixture. The remaining fraction of air is completely dissolved in the hydrocarbon mixture and its separation is, therefore, challenging. This justifies the use of a more advanced separation unit such as a distillation column.

Due to the high number of unknown parameters, as an early stage of the process design, the equilibrium stage model is utilized till reaching stable conditions in terms of convergence. Soon after having an initial approximation of main operative conditions, the calculation method is switched to the rigorous Rate-based model [94] aiming to obtain more robust results. This approach is followed to each column within the cryogenic block.

To completely specify a distillation column it is important to visualize the degrees of freedom of the system by considering the known and unknown operating variables. In general terms, the total degrees of freedom is given by $C+6$, where C is the number of components in the feed stream [104]. Therefore, 10 independent variables can be identified in the current stage of the

process simulation (see Table 5.14). Note that additional information for the C₂-splitter design has been also enlisted, which is discussed later in this section.

Table 5.14 – Specifications of independent variables for both distillation columns located downstream the flash unit.

Independent variables	Unit: "COLUMN1"		Unit: "C2-SPLITTER"	
	Degrees of freedom	Specification	Degrees of freedom	Specification
Number of stages	1	Unknown	1	Unknown
Feed stage location	1	Unknown	1	Unknown
Feed flow rate	1	33.3 tons hr ⁻¹	1	31.9 tons hr ⁻¹
Feed temperature	1	-77 °C	1	-14 °C
Feed composition	C-1 = 3	Known	C-1 = 1	Known
Top-stage pressure	1	20 bar	1	30 bar
B:F	1	Unknown	1	Unknown
RR	1	Unknown	1	Unknown

Note that the top-stage pressure (i.e. pressure at the condenser) has been specified at 20 bar. This value is selected in accordance to what has been reported in literature regarding the most common pressure specifications of cryogenic distillation columns (i.e. 20-40 bar) [101, 102]. The design of the distillation column is, therefore, determined by the remaining unknown variables (i.e. number of theoretical stages, feed stage location, *B:F* and *RR*).

The objective of this column is to obtain a high-purity hydrocarbon fraction in the bottom stream, whereas the remaining N₂ and O₂ are concentrated in the distillate. In this sense, the sensitivity analysis is carried out by imposing a set of technical constrains with the scope of maximizing the column performance:

$$y_{N_2}^D, \quad y_{O_2}^D \geq 0.85 \quad \cup \quad y_{C_2H_4}^B, \quad y_{C_2H_6}^B \geq 0.99 \quad \cup \quad \dot{Q}_{duty} \rightarrow \min$$

where \dot{Q}_{duty} is the refrigeration duty; $y_{N_2}^D$ and $y_{O_2}^D$ are, respectively, the mass fraction of N₂ and O₂ in the distillate; while $y_{C_2H_4}^B$ and $y_{C_2H_6}^B$ are, respectively, the mass fraction of ethylene and ethane in the bottom stream. Note that a lower purity of air in the distillate is defined in order to provide more freedom while establishing the best operating conditions (e.g. a compromise might be necessary between required condenser duty and hydrocarbon losses). Since the feed stream is mainly constituted by hydrocarbons (i.e. more than 95% in mass bases), a lower air purity in the distillate still indicates low hydrocarbon losses (< 2%). In this work, hydrocarbon losses are calculated by a simple mathematical expression suggested by Equation (5.19),

$$HYD_{losses} = \frac{\dot{m}_{hyd}^D}{\dot{m}_{feed}} \quad (5.19)$$

where \dot{m}_{hyd}^D is the hydrocarbon mass flow rate at the distillate and \dot{m}_{feed} is the feed mass flow rate.

A first step of the optimization procedure begins by defining the best operative conditions regarding discrete variables (i.e. number of stages and feed stream tray location). On this matter, Figure 5.10 (a) illustrates the variation of the mass fraction of air-related components in the liquid phase and the mass fraction of hydrocarbons in the vapor phase as a function of the number of trays. Note that no further improvements are achieved beyond 18 stages as the profile of each specie remains practically unchanged.

Figure 5.10 (b) represents the variation of the distillate mass composition as a function of the feed stream tray location. The trend indicates that upper stages are the best location for the feed stream (upper than the 7th stage) as the distillate gets concentrated in air-related components and an obvious opposite trend is observed with respect to the hydrocarbon fraction.

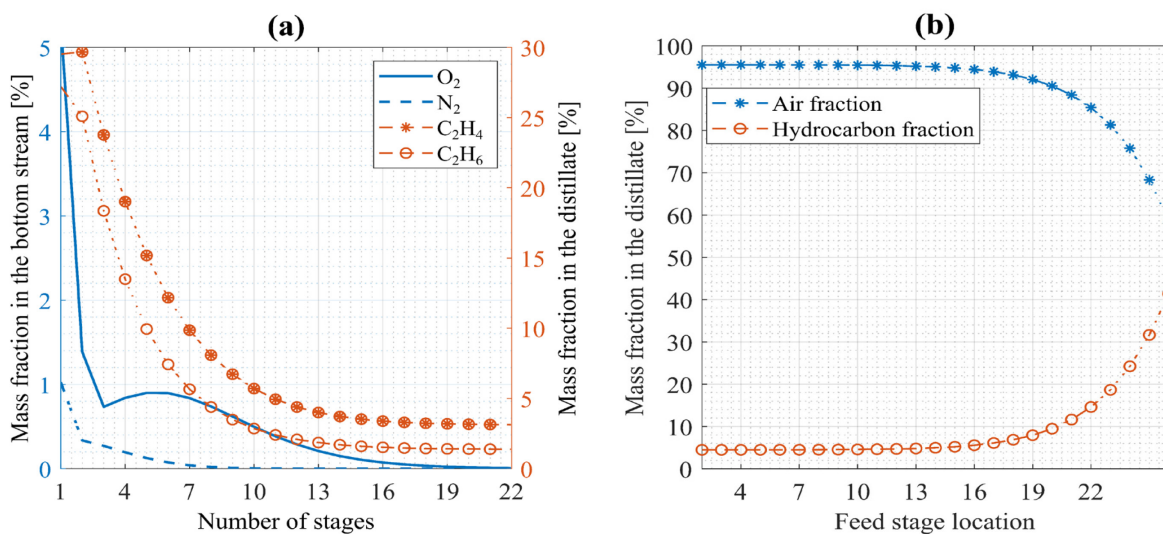


Figure 5.10 – Sensitivity analysis of discrete variables for a cryogenic distillation column design. Purity in the column product streams is plotted as a function of (a) number of stages and (b) tray location of the feed stream.

The second step of the optimization process involves the sensitivity analysis with respect to important continuous variables (see Figure 5.11). From this point onwards, the number of stages and the feed stream location have been maintained fixed at 18 and 7th, respectively. In this way, Figure 5.11 (a) demonstrates the influence of the molar reflux ratio in the distillate air concentration. Values beyond unity have shown no further improvements regarding the latter parameter while, as expected, the required condenser duty increases.

Figure 5.11 (b) shows the effect of $B:F$ in the distillate air purity and the working temperature of the condenser. Although the hydrocarbon purity in the bottom stream accomplishes the imposed constraints in the whole range of $B:F$, only values beyond 0.96 results in air purity higher than 85%; thus, hydrocarbon losses lower than 2%. An important observation is that, the larger the bottom rate (i.e. $B:F \gg 0.961$), the lower the required working temperature at the condenser since the relative composition of light components within the column increases. Therefore, the former parameter should be specified in order to avoid unnecessary extremes temperatures at the condenser.

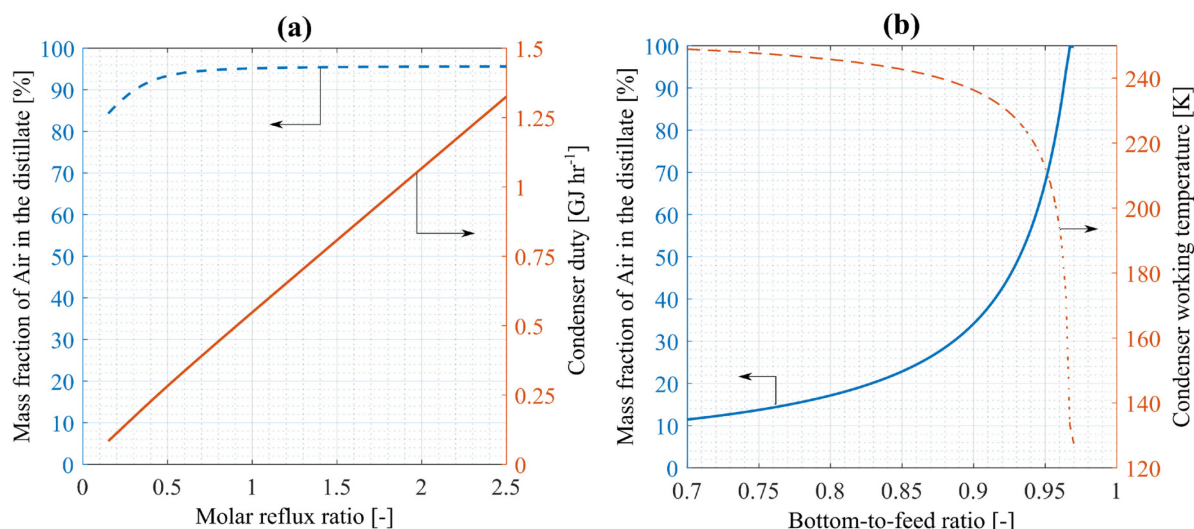


Figure 5.11 – Sensitivity analysis of continuous variables for a cryogenic distillation column design. Air purity in the distillate and condenser duty is plotted as a function of (a) molar reflux ratio and (b) bottom-to-feed ratio. Condenser duty and its working temperature are plotted in (a) and (b), respectively.

Having acknowledged the information given by the sensitivity analysis, the most suitable configuration for the molar reflux ratio and bottom-to-feed ratio is defined at 1 and 0.96, respectively. Under the current parametric specifications, the bottom stream reaches a hydrocarbon purity of 99.8% in mass bases where 31.55% corresponds to pure ethylene. Further information regarding each stream is enlisted in Table 5.15.

Table 5.15 – Stream specifications of the first cryogenic distillation column.

Parameters	Stream labels		
	“Air/Hyd-Feed”	“Air-RES-2”	“Hyd-bottom”
Vapor fraction	0	1	0
Temperature (°C)	-77	-82	-16
Pressure (bar)	20	20	19.85
Flow rate (ton hr ⁻¹)	33.17	13.05	31.87
Composition (% wt.) ¹	66/31/1.6/1.4	3.8/1.2/42/53	68.4/31.5/~ 0/~ 0

¹The reported values correspond to, respectively, %C₂H₆, %C₂H₄, %O₂ and %N₂.

The split of the hydrocarbon-rich stream into its main components, i.e. ethane and ethylene, is carried out in a specialized distillation column commonly known as C₂-splitter. Even though being an essential step of separation in every conventional plant for ethylene production, the complexity and the feed stream composition change according to the feedstock, i.e. ethane or naphtha steam cracking. When ethylene is produced from a heavier hydrocarbon mixture, a well-rooted industrial C₂-splitter is built to separate ethylene from a more complex hydrocarbon mixture, thus leading to a challenging process design [105, 106]. The feed stream is usually constituted by heavier valuable products, i.e. propylene, butene, iso-butene, pentane, among others.

Under these circumstances, the C₂-splitter simulated in this case-study is simplified by the fact of having a far less complex feed stream to be treated. As a matter of facts, the motivation of simulating this distillation unit is to evaluate the feasibility of integrating the ODH-C₂ technology into a well-rooted steam cracking plant from this point onwards. This topic has been already studied by A. M. Gaffney et al. [57], where a comparison between both technologies has been made to establish a good point of integration. In the process simulation reported in this document, that point of integration might be the bottom stream of the first cryogenic distillation column.

The C₂-splitter design follows the same approach as for the first distillation column where, nonetheless, different specifications ought to be accomplished. On this regard, it is important to understand that this should be the last separation step before obtaining an ethylene fraction of commercial standards, while the ethane fraction should also be pure enough to be recirculated back to the catalytic reactor or to other processes. Having said this, the expected outcome from the C₂-splitter is:

$$y_{C_2H_4}^D \geq 0.99 \quad \cup \quad Rec_{C_2H_4} = \frac{\dot{m}_{C_2H_4}^D}{\dot{m}_{feed}} \geq 0.98 \quad \cup \quad \dot{Q}_{duty} \rightarrow \min$$

where $y_{C_2H_4}^D$ is the mass fraction of ethylene in the distillate, $\dot{m}_{C_2H_4}^D$ is the mass flow rate of ethylene at the distillate and \dot{m}_{feed} is the feed stream mass flow rate. Note that up to 2% of ethylene losses are admissible for a more realistic scenario.

Similarly with respect to the previous design, an analysis of degrees of freedom is required to identify the unknown parameters (see Table 5.15). The process design is, in fact, based on the same operative parameters with respect to the first distillation column (i.e. 4 degrees of freedom). Nevertheless, obvious differences are present regarding the feed mass flow rate, inlet temperature, composition and pressure. The latter has been defined according to common values reported in literature [105, 106]. Working at high top-stage pressure (i.e. 30 bar) drastically reduces the cost of refrigeration duty but increases the compression cost, both capital and operative. Nonetheless, the resulting effect has demonstrated to be better while operating at high pressure.

The column optimization begins with a sensitivity analysis of discrete variables (see Figure 5.12). Although being unknown, initial values of $B:F$ and RR have been set in order to obtain preliminary results, i.e. 0.8 and 5 respectively. Figure 5.12 (a) shows that at least 65 stages are required to obtain a distillate of 99% ethylene. With respect to the previous design, more stages are necessary due to the smaller margin in terms of relative volatilities (i.e. boiling point difference between ethylene and ethane of ca. 15°C), which clearly complicates the separation. It is important to notice that, although obtaining a high purity product in the distillate, there are considerable ethylene losses in the bottom stream as the ethane mass fraction is lower than 90%. This observation indicates that the initial estimation of $B:F$ and RR must be revised.

Figure 5.12 (b) indicates that the column should be fed preferentially in mid-low stages in order to achieve both, high ethylene purity in the distillate and high ethane purity in the bottom stream. Note that no further improvements are observed on stages beneath the 30th.

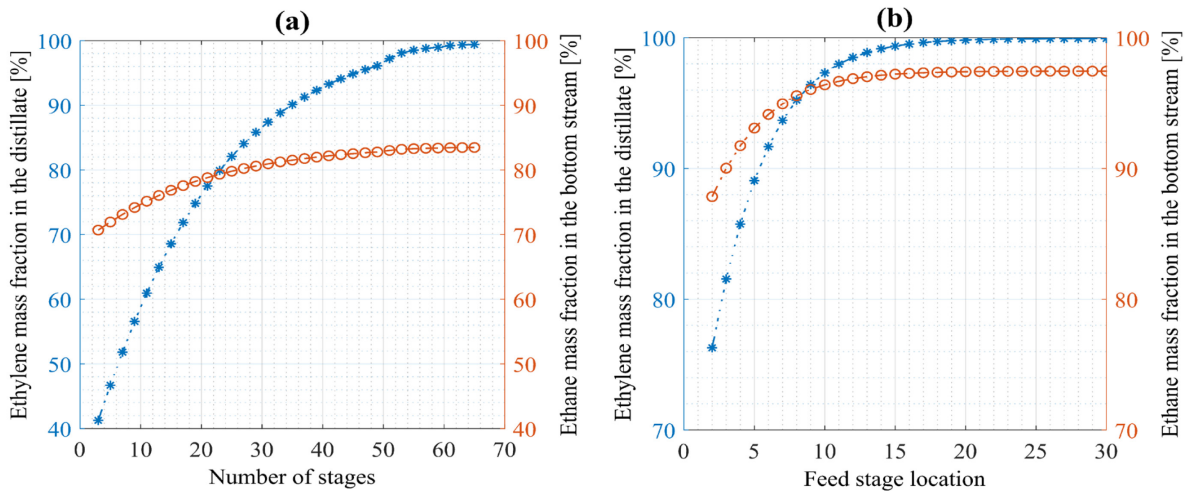


Figure 5.12 – Sensitivity analysis of discrete variables for a C_2 -splitter design. Purity in the column product streams is plotted as a function of (a) number of stages and (b) tray location of the feed stream.

In order to improve the column performance, a second sensitivity analysis is carried out regarding continuous variables, i.e. $B:F$ and RR , as shown in Figure 5.13. Based on the previous results, the following evaluation has been performed at a fixed value of number of stages and feed stream location (i.e. 65 and 30th stage, respectively).

Figure 5.13 (a) demonstrates that there is an opposite effect on both ethylene purity and recovery with respect to $B:F$. The optimal value is, indeed, the intersection between these two slopes (i.e. $B:F = 0.675$) since higher values increase the distillate product but at very low ethylene recovery with respect to the feed stream; consequently, the opposite effect is seen at lower bottom rates.

Figure 5.13 (b) indicates that very large RR are required to achieve an acceptable performance in terms of the product purity and recovery. As expected, there is an almost linear increment of the condenser duty with the independent variable which gradually increases the cost of separation. Therefore the original estimation at the early stages of the optimization must be at least doubled to accomplish the pre-defined constrains (i.e. $RR = 16$).

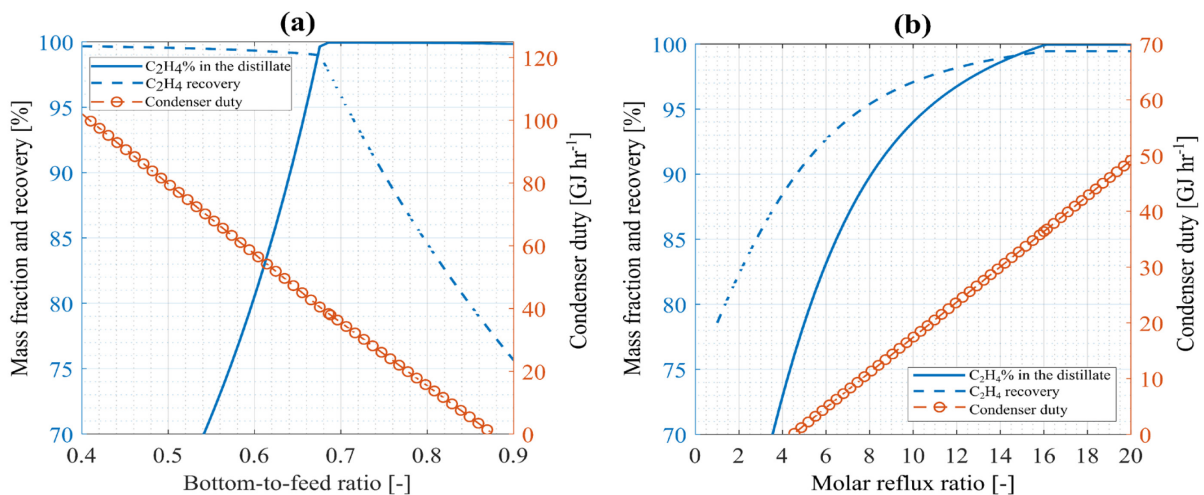


Figure 5.13 – Sensitivity analysis of continuous variables for a C_2 -splitter design. Ethylene recovery and its mass fraction in the distillate are plotted as a function of (a) bottom-to-feed ratio ($B:F$) and (b) molar reflux ratio (RR). The refrigeration load at the condenser is plotted in both graphs.

By addressing the operative specifications reported above, results from the optimization procedure indicates that 99.9% of pure ethylene is obtained in the distillate of the deethanizer, while the bottom stream is constituted by 98.5% of ethane. In addition, ca. 98.3% of the total ethylene fraction fed to the column is recovered in the distillate stream, thus achieving the pre-defined constrains.

It is important to acknowledge that such a high performance at the C₂-splitter requires ca. 40 GJ hr⁻¹ of refrigeration load for producing 9.99 tons of ethylene per hour, which makes it one of the most energy intensive process within the simulation framework considered in the present work. In this sense, the feasibility of integrating the ODH-C₂ technology within a steam cracking facility via the C₂-splitter will be, therefore, the main motivation for pursuing a minimization on the overall energy consumption. This is, nonetheless, one of the main topics treated in the 6th Chapter of this document.

In accordance to what has been reported from the optimization procedure in this section, important specifications of both cryogenic units are summarized in Table 5.16 while additional information regarding streams specifications are enlisted in Table 5.17.

Table 5.16 – Summary of operative specifications and performance of the cryogenic distillation section.

Specification	Unit: "COLUMN1"	Unit: "C ₂ -SPLITTER"
	Description	Description
Calculation mode	Rate-based	
Condenser	Partial	Total
Number of stages	18	65
Feed stream location	4 th stage	60 th stage
Reflux ratio	1	16
Bottom-to-feed ratio	0.961	0.675
Top-stage pressure	20 bar	30 bar
Estimated ΔP ¹	0.15 bar	0.37 bar
Results		
Hydrocarbon losses	1.85%	[-]
Ethylene purity	[-]	99.9%
Ethylene recovery	0.95%	98.3%
Refrigeration duty ²	0.57 GJ hr ⁻¹	39.22 GJ hr ⁻¹
	5.66×10 ⁻⁵ GJ ton _{C₂H₄} ⁻¹	3.93 GJ ton _{C₂H₄} ⁻¹

¹ The pressure drop has been taken from the hydraulic report generated by ASPEN Plus. Values indicates the total pressure drop of the column.

² This parameters is calculated based on the ethylene mass flow rate generated in each unit (i.e. 10.06 tons hr⁻¹ and 9.99 tons hr⁻¹ for "COLUMN1" and "C₂-SPLITTER", respectively).

Table 5.17 – Stream specifications of the C₂-splitter.

Parameters	Stream labels		
	“Hyd-feed”	“C ₂ H ₄ ”	“C ₂ H ₆ ”
Vapor fraction	0	0	0
Temperature (°C)	-14	-12	8
Pressure (bar)	30	30	29.6
Flow rate (ton hr ⁻¹)	31.87	9.99	21.9
Composition (% wt.) ¹	68.4/31.5/~ 0/~ 0	99.9/~ 0/~ 0/~ 0	98.5/1.5/~ 0/~ 0

¹ The reported values correspond to, respectively, %C₂H₆, %C₂H₄, %O₂ and %N₂.

The cryogenic section is the last block of the simulation framework evaluated in the present document. The product streams of this block are constituted by four main streams:

- Two residual streams rich in air-related components, one of which obtained from the separation in the flash unit, while another one results from the first distillation column;
- a third stream generated as bottom product in the C₂-splitter whose major component is ethane and;
- a fourth stream of polymer-grade ethylene exiting the top-stage of the C₂-splitter.

Each of the product streams have obvious different destinations and/or further treatment. The air stream can be recompressed to either be stored or mixed with ethane before being recirculated to the catalytic reactor. The unreacted ethane may have its destination as feedstock for further ethylene production. Lastly, polymer-grade ethylene is usually stored on spherical tanks at high pressure and normal temperature (i.e. 1.83 MPa and 243 K) for its commercialization [107].

Chapter 6

6. Results and discussion

In this chapter an energy analysis is conducted to compare both processes for ethylene production, i.e. ODH-C₂ and steam cracking. Results from the simulation framework will be, therefore, illustrated in order to estimate both gross and net energy consumption per ton of ethylene produced at the simulated plant capacity. The energy distribution is also evaluated in order to identify the most energy intensive operative blocks. The objective is, therefore, to compare these results with common numbers reported in literature for steam cracking; and thus, evaluate the sustainability of the ODH-C₂ in terms of power requirements. On this regard, a well-rooted steam cracking facility operates at a specific energy consumption of 15-25 GJ per ton of ethylene produced [31].

Additionally, a similar study is conducted to contrast the CO₂ emissions linked to both technologies. In order to achieve an accurate estimation of the latter parameter, the net energy consumption is classified by proper utilities according to the scope of each operative unit within the process. The aim is, therefore, to evaluate if the simulated process is able to improve the CO₂ emissions of the conventional technology, whose common values have been reported to be 1.2-2 tons of CO₂ per ton of ethylene produced if including downstream separation processes [32, 33].

The final outcome of both energy evaluation and CO₂ emissions will be always expressed in specific units (i.e. per ton of ethylene produced) in order to normalize the results with respect to the plant capacity.

6.1 Energy distribution and process comparison

Recapitulating, each block within the simulation framework has their own energy expenses associated to different type of utilities. Beginning with the catalytic reactor, the feed gas mixture must receive a pre-treatment in order to accomplish the operative conditions (i.e. $T_i = 200^\circ\text{C}$ and $P = 2$ bar). Due to the exothermic conditions at which the catalytic reactor operates, it can be assumed with high confidence that no notorious energy consumption occurs when the reactor is operating. Note that the molten salt bath is, in fact, constantly exchanging the heat generated by the oxidation. The associated utilities for this block are, therefore, high pressure steam and electricity for the feed mixture pre-treatment.

Downstream the catalytic reactor it is located the CO₂ separation block. As reported before, with the assumption that negligible amounts of MEA is degraded, the energy consumption linked to the absorber/stripper system mainly depends on compression and heat requirements. With respect to the latter, high-pressure steam generated by the exploitation of the reactor exothermicity can be integrated in the stripper reboiler, hence the energy requirements become completely covered.

The last block of the simulation framework covers the cryogenic separation. Due to the extreme working conditions, a proper heat integration in this section is essential in order to minimize the energy requirements and therefore, improving the feasibility of putting the overall process

into practice. Note that, by energy integration, it refers to an internal management of the different units within the block. In other words, there is not a direct pathway to integrate the generated utility (i.e. steam) into the cryogenic separation block. As reported before, the cooling utilities are defined according to the refrigeration requirements of each unit.

The energy distribution within the simulated process is therefore based on the specific utility type and usage at each operating unit. On this regard, the overall energy consumption has been divided into three categories: electricity, heating and cooling. Additionally, the latter is subdivided into cryogenic and conventional refrigeration. This distinction is of key importance since it will have a high influence while estimating the CO₂ emissions. Having said this, Figure 6.1 illustrates the energy distribution according to the above mentioned utilities.

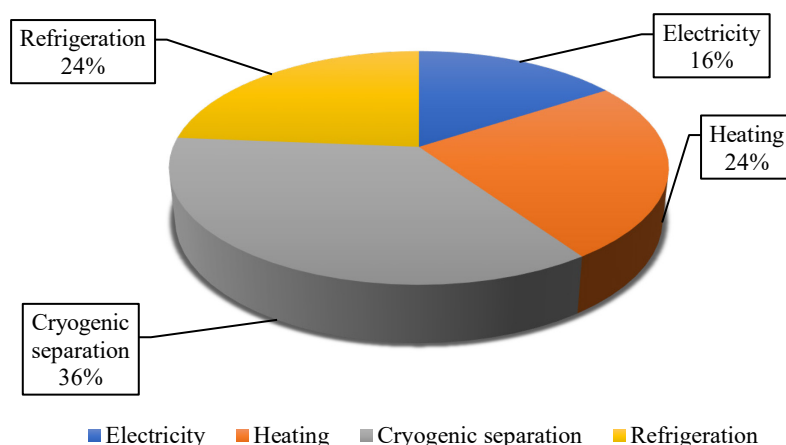


Figure 6.1 – Energy distribution of the ODH-C₂ at industrial scale using NiO-SnO₂ as catalyst. The heating utility does not consider the generated steam.

The category “Electricity” includes the energy requirements linked to compression and pumping. However, the contribution of the latter is almost negligible with respect to the expenses linked to compression (i.e. less than 1%). Note that its overall contribution is considerably high even by taking into account that the maximum pressure of the gas phase was always maintained up to 2 bar. This observation points out that feeding the catalytic reactor with a highly diluted stream might incur into considerable energy expenses in specific terms (i.e. kWh per ton of ethylene produced). In fact, only 18% of the feed stream is constituted by feedstock while the remaining 82% represents the inert fraction, which indicates that most of the compression power is lost by compressing molecular nitrogen. Nevertheless, there are two major constraints that make this effect unavoidable. A physical barrier is imposed by the flammability limit of the gas mixture at the operative range of temperatures; while a technological barrier was demonstrated in Chapter 4, where an acceptable reactor performance is observed under the current feedstock concentration in the feed stream.

Cooling water generated by an evaporative cooling tower is englobed within the category labelled as “Refrigeration”. This type of utility is well-known at industrial level for being a cheap and practically emission-free [89]. Its major use in the simulated process is at the intercooler of the multi-stage compressors. By cooling down the gas stream in an interstage, it is possible to achieve significant electricity savings due to the reduction in the gas volume to be compressed.

The heating utility (i.e. high-pressure steam) is accounted for supplying the required reboiler duty at the stripper located in the MEA recovery section. The pre-heating treatment of the feed mixture is also carried out by using steam. It is considered that the gas mixture is heated up from ambient conditions till the reactor inlet conditions (i.e. from 25°C to 200°C).

Cryogenic separation accounts for the 38% of the total energy consumed in the simulated ethylene production process. Particularly, the C₂-splitter is the second more energy intensive process after the gross air separation at the flash unit (i.e. 55.9 and 39.2 GJ hr⁻¹ of refrigeration duty, respectively). This indicates that ca. 4 GJ of cooling duty are required for producing one ton of ethylene at the simulated process capacity, only by considering the C₂-splitter. This represents approximately 3.4 times the cooling duty of an equivalent unit present in a well-rooted steam cracking facility [31]. The reason for such a difference might be linked to the scale, as it has been demonstrated in practice that cryogenic distillation is affordable at a considerable big-scale (i.e. starting from 100 tons hr⁻¹ of ethylene production) [31].

Having said this, Figure 6.2 reports the energy consumption of each unit according to its respective utility.

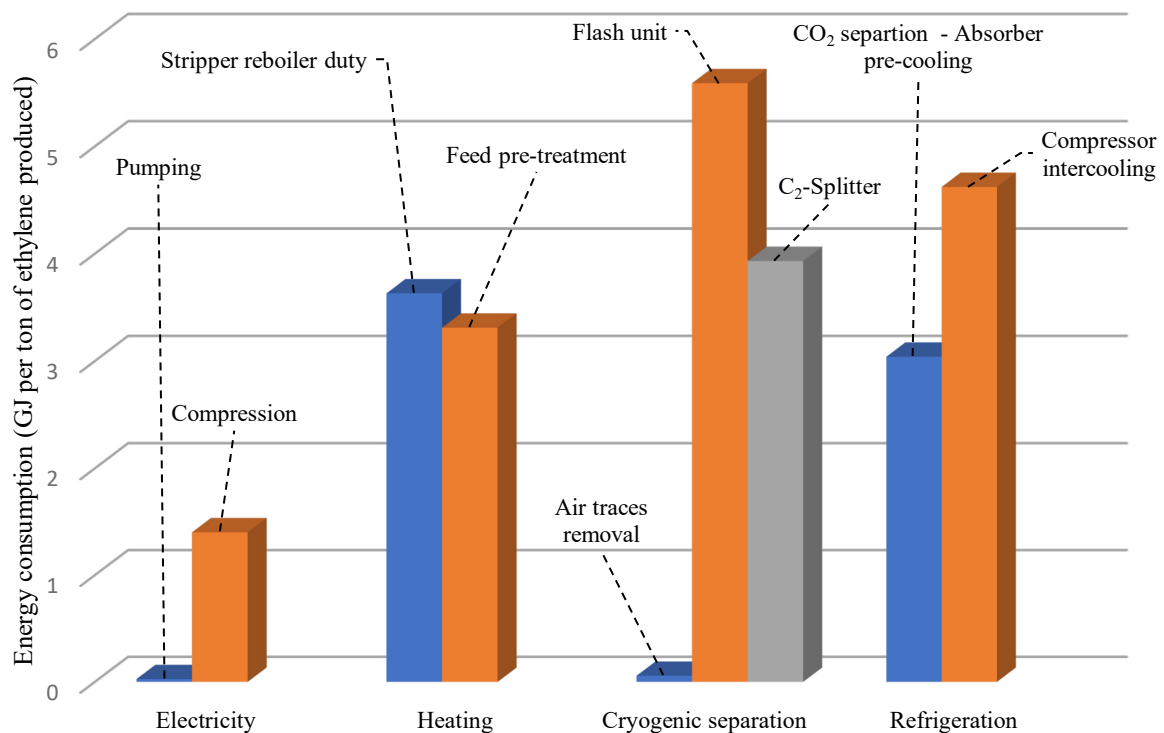


Figure 6.2 – Specific energy consumption of an ethylene production process using ODH-C₂ technology. Values does not represents net results (i.e. steam generation is not included).

Results from the analysis indicates a gross energy consumption of 25.60 GJ per ton of ethylene produced. As previously mentioned, this value is beyond the common numbers of steam cracking technology. However, by considering the steam generation from the catalytic reactor exothermicity, the energetic scenario changes. Given the operative temperature at the stripper reboiler (140°C) and the reactor inlet temperature requirements ($T_i = 200^\circ\text{C}$), it is possible to supply the required heat load by high-pressure steam ($T = 250^\circ\text{C}$, $P = 40$ bar) generated downstream the catalytic reactor. As reported in Section 5.2.2, the available heat load from

high-pressure steam is 7.04 GJ per ton of ethylene which is sufficient to fully covered the heating utility requirements reported in Figure 6.2 (i.e. 6.81 GJ per ton of ethylene). Nonetheless, although achieving a 27.1% reduction, the energy requirements are still considerably high. Under these circumstances, the new energy distribution is illustrated in Figure 6.3.

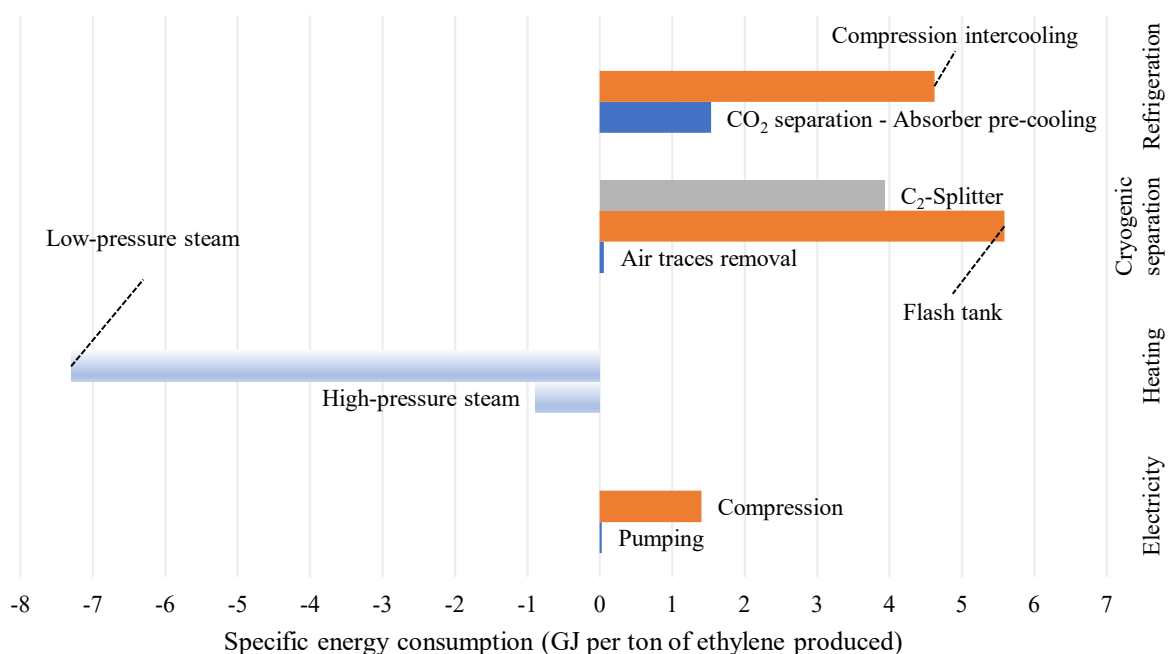


Figure 6.3 – Specific energy consumption of an ethylene production process using ODH-C₂ technology. Net energy requirements are reported with net steam generation. Negative values indicates the remaining heat load after considering the energy integration.

It is important to address that a non-negligible heat load is still available which can be potentially used for further applications. However, there is not an additional process to be consider where steam can be used as utility. Nevertheless, by assuming an integration of the ODH-C₂ technology into a steam cracking plant, the remaining steam can therefore contribute to lower the energy requirements in a steam cracking furnace. As a matter of facts, it is well-known that the conventional process consumes high quantities of steam (i.e. 0.25-0.6 ton of steam per ton of feedstock) [33] and, in addition, the available steam is in good agreement with dilution steam specifications (i.e. 100-190°C at 2-5 bar), which is used as an additive to the hydrocarbon feed in industrial crackers [108, 109]. In order to accurately calculate the energy savings by the use of the available steam, it is important to estimate the energy requirements for producing steam in a conventional boiler. This unit approximates significantly the real working principle of an industrial furnace, where hydrocarbons are used as feedstock and the flue gas sensible heat is used to convert saturated liquid water into steam. In fact, this procedure was already taken into consideration in Section 5.2.2, where the generator estimates the required heat duty to produce steam of pre-defined specifications in terms of temperature and pressure. By assuming dilution steam specifications to be equivalent as the available supply generated by the catalytic reactor, the mass flow rate reported in Table 5.7 (i.e. 33.8 tons hr⁻¹) represents, therefore, a good approximation of the energy savings. Note that an energy conversion efficiency of 90% has been considered, which is lower than common values for

industrial furnaces. The efficiency of this latter unit can be estimated as shown by Equation (6.1) [28].

$$\eta = \frac{T_{FTF} - T_{stack}}{T_{FTF} - T_0} \quad (6.1)$$

where T_{FTF} is the theoretical flame temperature, T_0 is the room temperature and T_{stack} is the stack temperature, whose general value is 160°C. For industrial furnaces, T_{FTF} and T_0 are assumed to be 1800°C and 25°C, respectively; which leads to an efficiency of 92%. This indicates that the heat duty reported in Table 5.7 should be even higher, thus deriving into higher energy savings. Nonetheless, from a conservative standpoint, an efficiency of 90% is maintained for accounting additional heat losses (if any).

With this additional energy savings, the net energy consumption of the simulated process is lowered down to ca. 11-12 GJ per ton of ethylene, which is lower with respect to common steam cracking values.

For a better understanding of the energy demand in both technologies, results from the simulated process are compared with common numbers of a conventional ethane steam cracking plant proposed by V. P. Haribal et al. [31] (see Table 6.1).

Table 6.1 – Comparison of energy demand between a small-scale ethylene production plant using ODH-C₂ technology and an industrial scale ethane steam cracking process.

Section	Specification	Steam cracking	ODH-C ₂
Upstream (GJ ton ⁻¹ _{C₂H₄})	Feed pre-treatment	2.46	3.31
	Reactor	7.43	~ 0
	Steam generation	1.5	-
	Ethane recycle	1.57	0.74
	Propane recycle	0.037	-
Downstream (GJ ton ⁻¹ _{C₂H₄})	Compression / pumping	2.88	4.47
	Steam generation	-	- 13.66
	Demethanizer	0.42	-
	Deethanizer	0.17	-
	Depropanizer	0.037	-
	C ₂ -splitter	1.16	3.93
	C ₃ -splitter	0.037	-
	Deacetylenizer	0.17	-
	CO ₂ separation	-	8.25
	Cryogenic air separation	-	5.6
	Total		15.41

Note that the ethylene yield differs in ca. one order of magnitude in both processes, being 114.2 and 9.98 tons hr⁻¹ of ethylene for steam cracking and the simulated ODH-C₂, respectively. The

former value is the generally expected value from a conventional ethylene production plant, capable of producing up to 1 million tons of this olefin per year.

Notwithstanding the promising outcome of ODH-C₂ technology in terms of energy demand, further savings can be achieved by the integration of the ethane/ethylene mixture on the already installed C₂-splitter unit in a ethane steam cracking plant. This option might not be feasible for a naphtha thermal cracking process where additional products, although valuable, are present. These components come as a result of cracking longer hydrocarbon chains, ending up in a wider range of olefines and alkanes (e.g. C₄, i-C₄, C₅, etc). Even though there are specialized units to separate these chemicals (e.g. debutanizer), they are placed downstream the C₂-splitter. Consequently, an eventual insertion of the pure ethane/ethylene mixture in between the separation procedure may incur into a higher net cost due to the additional separation steps.

6.2 Analysis of CO₂ emissions

The quantification of the total emissions of the process, both direct and indirect emissions, are of crucial importance towards the implementation of this novel technology. Most of the CO₂ production in the dominant technology is indirectly produce at the industrial furnace, where a significant heat load is required to cover the process endothermicity. Steam crackers ranging emissions from 1.2-2 tons of CO₂ per ton of ethylene produced if including additional emissions from downstream separation processes [33]. In addition to that, poisonous gases, e.g. NO_x, are also emitted as a result of the fossil fuel combustion; even though significant efforts have been lately made to reduce those emissions [32]. Given the increasing worldwide environmental regulations, several countries are already imposing taxation to greenhouse gas (GHG) emissions which ranges from 10 to 30 US\$ per ton of CO₂, depending the region [110]. This of course affects the overall profitability of industrial processes, making innovations crucial towards the minimization of GHG emissions.

In this work, it is assumed that natural gas is the primary source of energy to perform each process within the simulation framework. In this way, CO₂ emissions can be estimated based on the energy supplied by natural gas as an ultimate bond of the energy transformation chain. It turns obvious that, as more transformation steps are needed, more energy is required from the primary source to overcome losses linked to those transformations (i.e. energy conversion efficiency); hence incurring into higher GHG emissions. For simplicity, the latter will be calculated based on the net energy consumption described in Section 6.1.

The first contribution to the overall process emissions is accounted at reactor level. Contrary to steam cracking, the ODH-C₂ catalytic reactor directly produced CO₂ as side-product from overoxidation reactions. Even not being a contribution linked to energy consumption, it constitutes a non-negligible fraction of the overall CO₂ produced in the simulated process. According to the optimized reactor operating conditions presented in Section 5.2.1, the specific emissions at reactor level are ca. 0.95 tons of CO₂ per ton of ethylene produced.

Regarding the net GHG emissions downstream the catalytic reactor, Figure 6.2 has anticipated the most energy intensive processes. The net steam generation contributes to minimize the gross emissions at reactor level thanks to the process integration described earlier in this chapter. On this matter, M. A. Gadalla et al. [28] have reported a convenient correlation for estimating CO₂ emissions from primary energy sources, which is represented by Equation (6.2),

$$\dot{m}_{CO_2} = \frac{Q_{fuel}}{NHV} \frac{C_{\%}}{100} R_{cc} \quad (6.2)$$

where \dot{m}_{CO_2} is the mass flow rate of CO₂ in kg s⁻¹, Q_{fuel} (kW) is the heat load from the primary energy source, NHV (kJ kg⁻¹) is the net heating value of the fuel, $C\%$ is the carbon content and R_{cc} is the carbon ratio between the fuel and CO₂. Useful parameters to perform calculations are enlisted in Table 6.2.

Table 6.2 – Natural gas specification to estimate CO₂ emissions [28].

Parameter	Units	Value
Net heating value (NHV)	[kJ kg ⁻¹]	5.16×10 ⁴
C%	[%]	75.4
R _{cc}	[-]	3.67

The required heat load to produced 33.8 tons hr⁻¹ of low-pressure steam has been already reported in Table 5.5 (i.e. 7.32 GJ per ton of ethylene produced). By considering the ethylene yield (10.4 tons hr⁻¹) and a fuel combustion efficiency of 85%, the required Q_{fuel} for steam generation would be ca. 89.56 GJ hr⁻¹ if produced by natural gas combustion. In this way, Equation (6.2) indicates CO₂ emission savings of 4.8 tons hr⁻¹. With a similar reasoning, the remaining fraction of high-pressure steam, i.e. 0.9 GJ per ton of ethylene, can be accounted for further savings (see Figure 6.3). Therefore, the net emission savings due to steam generation downstream the catalytic reactor are 4.9 tons hr⁻¹.

With respect to electricity generation, gas turbines are usually the dominant technology when natural gas is used as primary energy source. The power electricity (W_{el}) delivered by a gas turbine can be estimated based on the heat load generated by the fuel combustion and the Carnot factor (η_c) [28]. The useful power delivered by a gas turbine and η_c can be calculated by Equations (6.3-4), respectively.

$$W_{el} = 0.9 \eta_c Q_{fuel} \quad (6.3)$$

$$\eta_c = \frac{T_{in} - T_{out}}{T_{in} + 273} \quad (6.4)$$

where T_{in} and T_{out} are the inlet and outlet operating temperature values of the gas turbine, respectively. Although those values may vary according to the design and working principle of each turbine, $T_{in} = 1027^\circ\text{C}$ and $T_{out} = 720^\circ\text{C}$ are commonly adopted values when natural gas is used as feedstock, which indicates that $\eta_c \approx 0.24$ [28]. In this way, by coupling Equations (6.2-4), CO₂ emissions linked to electricity requirements are estimated to be 3.5 tons hr⁻¹.

Emissions from the cryogenic separation block are estimated directly from ASPEN Plus utility database. On this matter, the carbon tracking has been performed under the frame of the EU-2007/589/EC regulation which establishes European guidelines for the monitoring and reporting of GHG emissions [34]. Under this framework, the simulation engine estimates a production of 52.5 kg of CO₂ per GJ of cooling duty. Note that this is an approximation since no distinction has been made between the different cryogenic units (i.e. flash tank and C₂-splitter). Having said this, Table 6.1 indicates a specific cooling duty of 6.76 GJ per ton of

ethylene produced (i.e. the sum of the contribution from the flash tank and the well-rooted C₂-splitter from the steam cracking plant).

Having acknowledged the information given up to this points, Figure 6.4 summarizes the CO₂ emissions linked to each block of the simulated process.

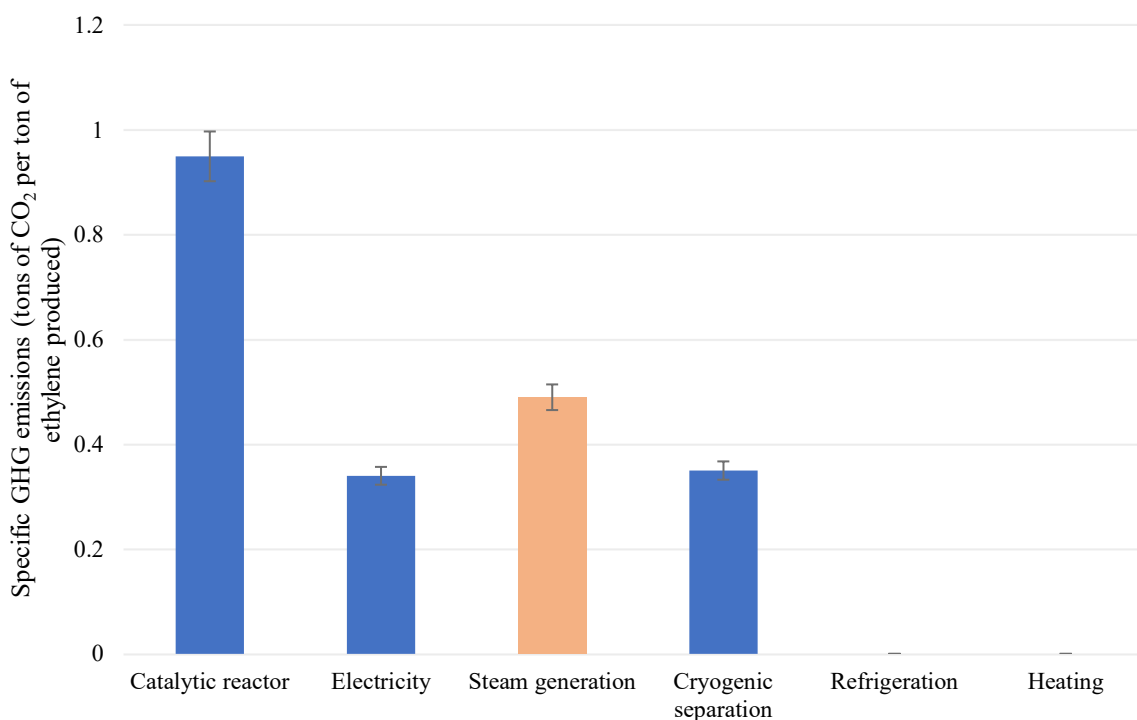


Figure 6.4 – Net specific CO₂ emissions of an ethylene production process using ODH-C₂ technology. Note that the category “Steam generation” has been identified with a different colour to indicate emission savings due to a process integration.

As suggested earlier in this chapter, the cooling utility used in non-cryogenic processes (i.e. stripper condenser duty and compression intercooling) has been opportunely defined as cooling water produced by an evaporative draft cooling tower, which are widely used within the chemical and petrochemical sector. Even though technical details regarding the working principle of this technology is out of the scope of this work, it is important to highlight that it is practically considered an emission-free technology for large productions of cooling water. Its working principle makes it suitable for cooling process up to ambient conditions, i.e. 35-45°C.

Summarizing, results indicate that net GHG emissions are lower with respect to common values reported for steam cracking. Results were observed within the margin of 1.1-1.15 tons of CO₂ per ton of ethylene produced, therefore incurring into emissions savings of at least 50 kg hr⁻¹ with respect to the conventional technology, i.e. more than 1.2 tons of CO₂ per ton of ethylene produced. Note that the variability bars in Figure 6.4 stand for accounting the optimized range of operating conditions at reactor level presented in Section 4.1.6.

Chapter 7

7 Conclusions

Throughout the development of this thesis, a detailed process optimization of the ODH-C₂ has been performed to evaluate its implementation at industrial-scale. A complex pseudo-heterogeneous model describes the working principle of a multi-tubular packed-bed catalytic reactor where NiO-SnO₂ is used as catalyst. This model takes into account both transport phenomena (fluid dynamics and mass/heat transfer) and reliable kinetics, which makes it much more accurate than simpler formulations, e.g. pseudo-homogenous models.

Nonetheless, such a rigorous description of the reactor working principle is paid with a considerable computational cost, which represents the main challenge to conduct a multi-objective process optimization. As a solution, a multiparametric model was designed and statistically verified, aiming to reduced the computational cost when the ODH-C₂ is simulated. In this work, the new model was constructed by using a RSM approach where the governing equations are simpler algebraic expressions, indicating that the model can be run with minimum computational resources. This directly impact in the average time consumption to conduct a simulation; while the pseudo-heterogeneous model requires from 6-24 hr to reach convergence, the multiparametric model is solved in a matter of seconds, thus achieving a time reduction of more than four orders of magnitude.

Notwithstanding the simpler mathematics, the non-ideal consideration of the pseudo-heterogeneous model, i.e. transport limitations and detailed kinetics, are intrinsically covered by the multiparametric model. In fact, its design derives entirely from data generated by the rigorous model. In addition, the ANOVA tests have concluded that the information lost during this procedure is statistically negligible.

During the multi-objective optimization, it has been determined that the ethylene selectivity reaches a maximum of 66%. This value, however, is obtained at a cost of lowering both ethane and oxygen conversion (i.e. 35% and 30%, respectively), thus incurring into a higher operating cost. Given this observation, a compromise has been established by lowering the ethylene selectivity up to 62.2% while increasing the $X_{C_2H_6}$ and the X_{O_2} to 47% and 56%, respectively. This performance at reactor level is achieved by establishing the following parametric set-up: $d_t/d_p = 4.7$, $T_{bath} = 392^\circ\text{C}$, $MF = 9900 \text{ kg m}^{-2} \text{ hr}^{-1}$, $Y_{O_2} = 10.3\%$ and $Y_{C_2H_6} = 8\%$; and it is the chosen configuration for the implementation of the reactor model in ASPEN Plus.

The process simulation in ASPEN Plus has been conducted under a rigorous approach for the process optimization and estimation of energy consumption and CO₂ emissions. The user-defined reactor block has demonstrated that 5 catalytic reactors of 20.000 tubes are required to cover an ethane capacity of 40 tons hr⁻¹ under the above mentioned operating conditions. According to literature [35, 36, 37], this is the feed capacity of at least one industrial cracking furnace within a steam cracking facility. Nonetheless, given the high dilution required in the feed mixture, the overall mass flow rate increases to 510 tons hr⁻¹ where 81.7% correspond to the inert fraction (i.e. N₂). This point clearly represents one of the main limitations of the process from the standpoint of the specific energy consumption in the compression and cryogenic separation block (i.e. 1.4 and 5.6 GJ per ton of ethylene produced, respectively).

The exploitation of the process exothermicity has been a key factor for minimizing the net energy demand. The heat load of the reactor effluent has been sufficient to produce 46.1 and 33.8 tons hr^{-1} of high-pressure steam (250°C at 40 bar) and low-pressure steam (120°C at 2.5 bar), respectively. To sum up, the heat duty required for the feed pre-treatment and the CO₂ separation block (i.e. stripper reboiler duty) is totally covered by the generated steam, which constitutes 24% of the total energy consumption.

The process integration of the ODH-C₂ technology into a conventional steam cracking process has been justified from the standpoint of two operative insights. The first one regards the use of an already installed C₂-splitter unit to minimize the specific energy consumption for the production of polymer-grade ethylene. The second one, points out an additional energy integration by using the generated steam as feedstock for the cracking furnaces (i.e. dilution steam).

As the production scale of the simulated process is ca. one order of magnitude lower than common numbers in a steam cracking plant, the energy consumption at the last cryogenic unit can be minimized by a factor of 3.4 if following the above mentioned pathway. This is, therefore, a key requirement to minimize both energy demand and CO₂ emissions. As a matter of facts, the cryogenic block accounts for 36% and 21% of the overall energy consumption and GHG emissions of the ODH-C₂, respectively.

The remaining fraction of the generated steam, which is not integrated within the ODH-C₂ process itself, is in good agreement with dilution steam used in steam cracking. In this way, this utility can contribute to lower the energy demand of the conventional process; hence, improving the net energy requirements of the ODH-C₂. Under the current operating conditions, this additional saving accounts for ca. 8 GJ per ton of ethylene produced.

Summarizing, the mid-scale ODH-C₂ process has presented a reduction of ca. 15% on specific energy consumption with respect to the conventional steam cracking. This result is obtained if considering an optimistic scenario where an efficient steam cracking plant is used as reference (i.e. 15 GJ per ton of ethylene produced). With respect to CO₂ emissions, results indicate a reduction of 50 kg per ton of ethylene. Note that this value could improve if naphtha cracking is taken as reference. However, the process integration might only be possible if considering an ethane thermal cracking plant, where the working principle and feed composition of the C₂-splitter is equivalent with respect to the simulated process.

In conclusion, the implementation of the ODH-C₂ using NiO-SnO₂ as catalyst has demonstrated promising improvements on sustainable parameters when replacing 10% of the total ethylene production of a conventional ethane thermal cracking plant.

7.1 Future work

Even though the multiparametric model has shown a high accuracy with respect to the complex pseudo-heterogeneous model, the main limitation remains its one-dimensional formulation. In this sense, all the conclusions elaborated throughout this thesis has been formulated according to observation at a fixed radial coordinate ($r_{\text{dss}} = 0.5$). Nevertheless, the low d_i/d_p working conditions enhances high heterogeneity with respect to the radial void fraction profile within the packed-bed. On this regard, de Klerk's correlation [21] demonstrates that significant changes on the void fraction can be obtained if a different radial coordinate is selected. This will surely affect the transport phenomena within the reactor tube, having an influence on the final performance estimation of the catalytic reactor.

As future work, the construction of a similar multiparametric model is proposed at different radial coordinates in order to complement the conclusions elaborated in this thesis. Eventually, it will be possible to fully recreate the pseudo-heterogeneous reactor model, by using simpler algebraic equations. It is important to mention that the design of such a two-dimensional model can be very exhaustive and time-consuming, mostly during the data acquisition step which has been identified as the main bottleneck of the procedure.

Regarding the process itself, ethylene yield and the feed stream dilution have been presented the major challenges for the application of the ODH-C₂ at industrial scale. Therefore, it is proposed that future studies should be conducted aiming to improve these two aspects. In this way, the construction of a multiparametric model including additional independent variables is proposed, e.g. inlet temperature, working pressure and/or catalyst density of the packed-bed. With respect to the feed dilution, further research should be conducted with the scope of replacing N₂ as the inert fraction. A potential alternative should preserve some qualities of N₂ (i.e. low cost and high availability) but guaranteeing a less energy intensive separation from the hydrocarbon fraction.

The above mentioned improvements at reactor level could be the main motivation for conducting a scale-up of the process. In this sense, future work should be focused on increasing the percentage of replacement achieved in this work (i.e. 10%). Eventually, this technology could be presented as a complete alternative for steam cracking.

An additional recommendation regards the performance of a techno-economic analysis. The estimation of both capital investment and operative cost should be the next step after improving the model proposed in this work (i.e. two-dimensional formulation). This future contribution would be a key factor for the implementation of this technology at industrial scale.

Finally, it is important to highlight that this modelling approach can be implemented to evaluate different catalyst configurations for the ODH-C₂. Novel catalysts should maintain some attributes of the NiO-SnO₂, e.g. low working temperatures and high reproducibility; while improving others, e.g. minimization of the CO₂ production at reactor level.

[This page was intentionally left in blank]

References

- [1] E. A. Beever and J. L. Belant, *Ecological Consequences of Climate Change: Mechanisms, Conservation, and Management*. Baton Rouge, UNITED STATES: Taylor & Francis Group, 2011.
- [2] A. Litmus and T. F. O. R. The, “Ethylene: a litmus test for the chemical industry,” *Gulf Petrochemicals Chem. Assoc.*, no. November, p. 8, 2019.
- [3] M. Fakhroleslam and S. M. Sadrameli, “Thermal/catalytic cracking of hydrocarbons for the production of olefins; a state-of-the-art review III: Process modeling and simulation,” *Fuel*, vol. 252, no. January, pp. 553–566, 2019.
- [4] Y. Khojasteh Salkuyeh and T. A. Adams, “A novel polygeneration process to co-produce ethylene and electricity from shale gas with zero CO₂ emissions via methane oxidative coupling,” *Energy Convers. Manag.*, vol. 92, pp. 406–420, 2015.
- [5] I. A. Bakare, S. A. Mohamed, S. Al-Ghamdi, S. A. Razzak, M. M. Hossain, and H. I. De Lasa, “Fluidized bed ODH of ethane to ethylene over VO_x-MoO_x/γ-Al₂O₃ catalyst: Desorption kinetics and catalytic activity,” *Chem. Eng. J.*, vol. 278, pp. 207–216, 2015.
- [6] M. M. Bhasin, J. H. McCain, B. V. Vora, T. Imai, and P. R. Pujadó, “Dehydrogenation and oxydehydrogenation of paraffins to olefins,” *Appl. Catal. A Gen.*, vol. 221, no. 1–2, pp. 397–419, 2001.
- [7] J. S. Valente, R. Quintana-Solórzano, H. Armendáriz-Herrera, G. Barragán-Rodríguez, and J. M. López-Nieto, “Kinetic study of oxidative dehydrogenation of ethane over MoVTenb mixed-oxide catalyst,” *Ind. Eng. Chem. Res.*, vol. 53, no. 5, pp. 1775–1786, 2014.
- [8] C. Alvarado, J. W. Thybaut, J. Poissonnier, and C. O. Castillo-araiza, “Kinetic Analysis of the Oxidative Dehydrogenation of Ethane over a NiSnO catalysts.,” 2019.
- [9] X. Lin, C. A. Hoel, W. M. H. Sachtler, K. R. Poepelmeier, and E. Weitz, “Oxidative dehydrogenation (ODH) of ethane with O₂ as oxidant on selected transition metal-loaded zeolites,” *J. Catal.*, vol. 265, no. 1, pp. 54–62, 2009.
- [10] C. O. Castillo-Araiza and F. López-Isunza, “Modeling the partial oxidation of o-xylene in an industrial packed-bed catalytic reactor: The role of hydrodynamics and catalyst activity in the heat transport,” *Ind. Eng. Chem. Res.*, vol. 49, no. 15, pp. 6845–6853, 2010.
- [11] G. Che-Galicia, R. S. Ruiz-Martínez, F. López-Isunza, and C. O. Castillo-Araiza, “Modeling of oxidative dehydrogenation of ethane to ethylene on a MoVTenbO/TiO₂ catalyst in an industrial-scale packed bed catalytic reactor,” *Chem. Eng. J.*, vol. 280, pp. 682–694, Nov. 2015.
- [12] J. N. Papageorgiou and G. F. Froment, “Simulation models accounting for radial voidage profiles in fixed-bed reactors,” *Chem. Eng. Sci.*, vol. 50, no. 19, pp. 3043–3056, 1995.
- [13] J. J. Lerou and G. F. Froment, “Velocity, temperature and conversion profiles in fixed bed catalytic reactors,” *Chem. Eng. Sci.*, vol. 32, no. 8, pp. 853–861, 1977.
- [14] R. Peláez, P. Marín, F. V. Díez, and S. Ordóñez, “Direct synthesis of dimethyl ether in multi-tubular fixed-bed reactors: 2D multi-scale modelling and optimum design,” *Fuel*

- Process. Technol.*, vol. 174, no. November 2017, pp. 149–157, 2018.
- [15] A. I. Anastasov, “An investigation of the kinetic parameters of the o-xylene oxidation process carried out in a fixed bed of high-productive vanadia-titania catalyst,” *Chem. Eng. Sci.*, vol. 58, no. 1, pp. 89–98, 2003.
- [16] C. O. Castillo-Araiza, H. Jiménez-Islas, and F. López-Isunza, “Heat-transfer studies in packed-bed catalytic reactors of low tube/particle diameter ratio,” *Ind. Eng. Chem. Res.*, vol. 46, no. 23, pp. 7426–7435, 2007.
- [17] A. E. SCHEIDEGGER, *The Physics of Flow Through Porous Media (3rd Edition)*. University of Toronto Press, 1974.
- [18] P. Forchheimer, *Tratado de hidráulica*. Labor, 1950.
- [19] G. Che-Galicia, F. López-Isunza, E. Corona-Jiménez, and C. O. Castillo-Araiza, “The role of kinetics and heat transfer on the performance of an industrial wall-cooled packed-bed reactor: Oxidative dehydrogenation of ethane,” *AIChE J.*, vol. 66, no. 4, 2020.
- [20] S. Bale, S. S. Tiwari, K. Nandakumar, and J. B. Joshi, “Effect of Schmidt number and D/d ratio on mass transfer through gas-solid and liquid-solid packed beds: Direct numerical simulations,” *Powder Technol.*, vol. 354, pp. 529–539, 2019.
- [21] A. De Klerk, “Voidage variation in packed beds at small column to particle diameter ratio,” *AIChE J.*, vol. 49, no. 8, pp. 2022–2029, 2003.
- [22] W. Wang, Y. Cheng, and G. Tan, “Design Optimization of SBS-modified asphalt mixture reinforced with eco-friendly basalt fiber based on response surface methodology,” *Materials (Basel)*, vol. 11, no. 8, 2018.
- [23] J. Tellinghuisen, “Least Squares Methods for Treating Problems with Uncertainty in x and y,” *Anal. Chem.*, vol. 92, no. 16, pp. 10863–10871, 2020.
- [24] D. Razus, M. Molnarne, and O. Fuß, “Limiting oxygen concentration evaluation in flammable gaseous mixtures by means of calculated adiabatic flame temperatures,” *Chem. Eng. Process. Process Intensif.*, vol. 43, no. 6, pp. 775–784, 2004.
- [25] R. Henda, A. Machac, and B. Nilsson, “Heat and mass transport in a nonlinear fixed-bed catalytic reactor: Hot spots and thermal runaway,” *Chem. Eng. J.*, vol. 143, no. 1–3, pp. 195–200, 2008.
- [26] G. W. Koning, “Heat and Mass Transport in Tubular Packed Bed Reactors at Reacting and Non-Reacting Conditions,” *Measurement*, p. 272, 2002.
- [27] A. I. Anastasov, “A study of the influence of the operating parameters on the temperature of the hot spot in a fixed bed reactor,” *Chem. Eng. J.*, vol. 86, no. 3, pp. 287–297, 2002.
- [28] M. A. Gadalla, Z. Olujic, P. J. Jansens, M. Jobson, and R. Smith, “Reducing CO₂ emissions and energy consumption of heat-integrated distillation systems,” *Environ. Sci. Technol.*, vol. 39, no. 17, pp. 6860–6870, 2005.
- [29] Y. Lim, J. Kim, J. Jung, C. S. Lee, and C. Han, “Modeling and simulation of CO₂ capture process for coalbased power plant using amine solvent in South Korea,” *Energy Procedia*, vol. 37, pp. 1855–1862, 2013.
- [30] F. Barzagli, F. Mani, and M. Peruzzini, “A Comparative Study of the CO₂ Absorption in Some Solvent-Free Alkanolamines and in Aqueous Monoethanolamine (MEA),” *Environ. Sci. Technol.*, vol. 50, no. 13, pp. 7239–7246, 2016.
- [31] V. P. Haribal, L. M. Neal, and F. Li, “Oxidative dehydrogenation of ethane under a cyclic

- redox scheme – Process simulations and analysis,” *Energy*, vol. 119, pp. 1024–1035, 2017.
- [32] V. P. Haribal, Y. Chen, L. Neal, and F. Li, “Intensification of Ethylene Production from Naphtha via a Redox Oxy-Cracking Scheme: Process Simulations and Analysis,” *Engineering*, vol. 4, no. 5, pp. 714–721, 2018.
- [33] I. Amghizar, J. N. Dedeyne, D. J. Brown, G. B. Marin, and K. M. Van Geem, “Sustainable innovations in steam cracking: CO₂ neutral olefin production,” *React. Chem. Eng.*, vol. 5, no. 2, pp. 239–257, 2020.
- [34] “EUR-Lex - 32007D0589 - EN - EUR-Lex.” <https://eur-lex.europa.eu/legal-content/EN/ALL/?uri=celex:32007D0589> (accessed Jun. 15, 2021).
- [35] C. Liu, J. Zhang, Q. Xu, and K. Li, “Cyclic scheduling for best profitability of industrial cracking furnace system,” *Comput. Chem. Eng.*, vol. 34, no. 4, pp. 544–554, 2010.
- [36] L. Zhou, K. Li, P. Hang, and G. Liu, “Optimization of the ethane thermal cracking furnace based on the integration of reaction network,” *Clean Technol. Environ. Policy*, vol. 23, no. 3, pp. 879–887, 2021.
- [37] G. Hu *et al.*, “Impact of radiation models in coupled simulations of steam cracking furnaces and reactors,” *Ind. Eng. Chem. Res.*, vol. 54, no. 9, pp. 2453–2465, 2015.
- [38] S. Yolcular, “Hydrogen production for energy use in European Union Countries and Turkey,” *Energy Sources, Part A Recover. Util. Environ. Eff.*, vol. 31, no. 15, pp. 1329–1337, 2009.
- [39] H. Song, E. Dotzauer, E. Thorin, B. Guziana, T. Huopana, and J. Yan, “A dynamic model to optimize a regional energy system with waste and crops as energy resources for greenhouse gases mitigation,” *Energy*, vol. 46, no. 1, pp. 522–532, 2012.
- [40] A. Al-Azkawi, A. Elliston, S. Al-Bahry, and N. Sivakumar, “Waste paper to bioethanol: Current and future prospective,” *Biofuels, Bioprod. Biorefining*, vol. 13, no. 4, pp. 1106–1118, 2019.
- [41] Q. Wang, X. Chen, A. N. Jha, and H. Rogers, “Natural gas from shale formation - The evolution, evidences and challenges of shale gas revolution in United States,” *Renew. Sustain. Energy Rev.*, vol. 30, pp. 1–28, 2014.
- [42] L. F. Pratson, D. Haerer, and D. Patiño-Echeverri, “Fuel prices, emission standards, and generation costs for coal vs natural gas power plants,” *Environ. Sci. Technol.*, vol. 47, no. 9, pp. 4926–4933, 2013.
- [43] Eurostat, “Where does our energy come from?” <https://ec.europa.eu/eurostat/cache/infographs/energy/bloc-2a.html> (accessed May 29, 2021).
- [44] European Chemical Industry Council, “European Market Overview - Petrochemicals Europe - Petrochemicals Europe.” <https://www.petrochemistry.eu/about-petrochemistry/petrochemicals-facts-and-figures/european-market-overview/> (accessed May 29, 2021).
- [45] E. Nduagu, H. Rahmanifard, A. Sow, and K. Marcarenhas, *Economic Impacts and Market Challenges for the Methane to Derivates Petrochemical Sub-sector*, no. 169. 2018.
- [46] J. Moreira, “Steam Cracking: Kinetics and Feed Characterisation,” no. November, pp. 1–5, 2015.

- [47] Y. Wang, S. B. Peh, and D. Zhao, "Alternatives to Cryogenic Distillation: Advanced Porous Materials in Adsorptive Light Olefin/Paraffin Separations," *Small*, vol. 15, no. 25, pp. 1–38, 2019.
- [48] S. Pedram, T. Kaghazchi, and M. T. Ravanchi, "Performance and energy consumption of membrane-distillation hybrid systems for olefin-paraffin separation," *Chem. Eng. Technol.*, vol. 37, no. 4, pp. 587–596, 2014.
- [49] D. Xiang, S. Yang, X. Li, and Y. Qian, "Life cycle assessment of energy consumption and GHG emissions of olefins production from alternative resources in China," *Energy Convers. Manag.*, vol. 90, no. 2015, pp. 12–20, 2015.
- [50] J. Q. Chen, A. Bozzano, B. Glover, T. Fuglerud, and S. Kvisle, "Recent advancements in ethylene and propylene production using the UOP/Hydro MTO process," *Catal. Today*, vol. 106, no. 1–4, pp. 103–107, 2005.
- [51] G. E. Keller and M. M. Bhasin, "Synthesis of ethylene via oxidative coupling of methane. I. Determination of active catalysts," *J. Catal.*, vol. 73, no. 1, pp. 9–19, 1982.
- [52] S. Becker and M. Baerns, "Oxidative coupling of methane over La₂O₃CaO catalysts Effect of bulk and surface properties on catalytic performance," *J. Catal.*, vol. 128, no. 2, pp. 512–519, 1991.
- [53] E. Heracleous and A. A. Lemonidou, "Ni-Me-O mixed metal oxides for the effective oxidative dehydrogenation of ethane to ethylene - Effect of promoting metal Me," *J. Catal.*, vol. 270, no. 1, pp. 67–75, 2010.
- [54] E. Heracleous and A. A. Lemonidou, "Ni-Nb-O mixed oxides as highly active and selective catalysts for ethene production via ethane oxidative dehydrogenation. Part I: Characterization and catalytic performance," *J. Catal.*, vol. 237, no. 1, pp. 162–174, 2006.
- [55] P. T. Bai, B. H. Babu, Y. Ramesh, T. V. Sagar, N. Lingaiah, and P. S. S. Prasad, "Oxidative Dehydrogenation of Ethane and n-Butane on VO_x/Al₂O₃ Catalysts," vol. 118, no. December, pp. 2–6, 2013.
- [56] A. R. Pratt, I. J. Muir, and H. W. Nesbitt, "X-ray photoelectron and Auger electron spectroscopic studies of pyrrhotite and mechanism of air oxidation," *Geochim. Cosmochim. Acta*, vol. 58, no. 2, pp. 827–841, 1994.
- [57] A. M. Gaffney and O. M. Mason, "Ethylene production via Oxidative Dehydrogenation of Ethane using M1 catalyst," *Catal. Today*, vol. 285, no. 2017, pp. 159–165, 2017.
- [58] R. K. Grasselli, "Fundamental principles of selective heterogeneous oxidation catalysis," *Top. Catal.*, vol. 21, no. 1–3, pp. 79–88, 2002.
- [59] R. K. Grasselli, "Site isolation and phase cooperation: Two important concepts in selective oxidation catalysis: A retrospective," *Catal. Today*, vol. 238, pp. 10–27, 2014.
- [60] H. Zhu *et al.*, "Ni-M-O (M = Sn, Ti, W) Catalysts Prepared by a Dry Mixing Method for Oxidative Dehydrogenation of Ethane," *ACS Catal.*, vol. 6, no. 5, pp. 2852–2866, 2016.
- [61] T. Blasco and J. M. López Nieto, "Oxidative dehydrogenation of short chain alkanes on supported vanadium oxide catalysts," *Appl. Catal. A Gen.*, vol. 157, no. 1–2, pp. 117–142, 1997.
- [62] T. T. Nguyen, L. Burel, D. L. Nguyen, C. Pham-Huu, and J. M. M. Millet, "Catalytic performance of MoVTenbO catalyst supported on SiC foam in oxidative dehydrogenation of ethane and ammoxidation of propane," *Appl. Catal. A Gen.*, vol.

- 433–434, pp. 41–48, 2012.
- [63] Ş. B. Ivan, I. Popescu, I. Fechete, F. Garin, V. I. Pârvulescu, and I. C. Marcu, “The effect of phosphorus on the catalytic performance of nickel oxide in ethane oxidative dehydrogenation,” *Catal. Sci. Technol.*, vol. 6, no. 18, pp. 6953–6964, 2016.
- [64] J. M. L. Nieto, B. Solsona, R. K. Grasselli, and P. Concepción, “Promoted NiO catalysts for the oxidative dehydrogenation of ethane,” *Top. Catal.*, vol. 57, no. 14, pp. 1248–1255, 2014.
- [65] B. Solsona *et al.*, “Optimizing Both Catalyst Preparation and Catalytic Behaviour for the Oxidative Dehydrogenation of Ethane of Ni–Sn–O Catalysts,” *Top. Catal.*, vol. 59, no. 17–18, pp. 1564–1572, 2016.
- [66] B. Solsona *et al.*, “Selective oxidative dehydrogenation of ethane over SnO₂-promoted NiO catalysts,” *J. Catal.*, vol. 295, pp. 104–114, 2012.
- [67] R. J. Berger, E. H. Stitt, G. B. Marin, F. Kapteijn, and J. A. Moulijn, “Chemical reaction kinetics in practice,” *Cattech*, vol. 5, no. 1, pp. 30–60, 2001.
- [68] H. Eyring, “The Activated Complex and the Absolute Rate of Chemical Reactions.,” *Chem. Rev.*, vol. 17, no. 1, pp. 65–77, Aug. 1935.
- [69] C. Stegelmann, N. C. Schiødt, C. T. Campbell, and P. Stoltze, “Microkinetic modeling of ethylene oxidation over silver,” *J. Catal.*, vol. 221, no. 2, pp. 630–649, 2004.
- [70] G. Che-Galicia, R. Quintana-Solórzano, R. S. Ruiz-Martínez, J. S. Valente, and C. O. Castillo-Araiza, “Kinetic modeling of the oxidative dehydrogenation of ethane to ethylene over a MoVTeNbO catalytic system,” *Chem. Eng. J.*, vol. 252, pp. 75–88, 2014.
- [71] D. Robinson, “Design of Experiments in Chemical Engineering: A Practical Guide,” *Org. Process Res. Dev.*, vol. 9, no. 2, p. 225, Mar. 2005.
- [72] J. A. Tavizón-Pozos, I. S. Ibarra, A. Guevara-Lara, and C. A. Galán-Vidal, “Application of Design of Experiments in Biofuel Production,” pp. 77–103, 2019.
- [73] R. H. Myers, D. C. Montgomery, and C. Anderson-Cook, *Response Surface Methodology: Process and Product Optimization Using Designed Experiments, 4th Edition*, vol. 705. Hoboken, New Jersey, 2016.
- [74] J. Zhu, S. S. Araya, X. Cui, S. L. Sahlin, and S. K. Kær, “Modeling and design of a multi-tubular packed-bed reactor for methanol steam reforming over a Cu/ZnO/Al₂O₃ catalyst,” *Energies*, vol. 13, no. 3, 2020.
- [75] D. Ba and I. H. Boyaci, “Modeling and optimization i: Usability of response surface methodology,” *J. Food Eng.*, vol. 78, no. 3, pp. 836–845, 2007.
- [76] A. Hemmati and H. Rashidi, “Optimization of industrial intercooled post-combustion CO₂ absorber by applying rate- base model and response surface methodology (RSM),” *Process Saf. Environ. Prot.*, vol. 121, pp. 77–86, 2019.
- [77] G. Che-Galicia, “Comportamiento de un óxido mixto multimetálico (MoVTeNbO) como catalizador para la deshidrogenación oxidativa de etano en un reactor de lecho empacado,” Universidad Autonoma Metropolitana, 2016.
- [78] Aspen Technology Inc., *User Guide Volume 2*, vol. 2. 1999.
- [79] Aspen Tech, “User Unit Operation Models,” in *Aspen Plus User Models*, 2015, pp. 83–133.

- [80] P. G. Carman, "Fluid flow through granular beds," *Chem. Eng. Res. Des.*, vol. 75, no. 1 SUPPL., pp. S32–S48, 1997.
- [81] S. Ergun and A. A. Orning, "Fluid Flow through Randomly Packed Columns and Fluidized Beds," *Ind. Eng. Chem.*, vol. 41, no. 6, pp. 1179–1184, Jun. 1949.
- [82] T. Atmakidis and E. Y. Kenig, "CFD-based analysis of the wall effect on the pressure drop in packed beds with moderate tube/particle diameter ratios in the laminar flow regime," *Chem. Eng. J.*, vol. 155, no. 1–2, pp. 404–410, 2009.
- [83] M. Filho and C. Mcgreavy, "Mathematical modelling for the shell and tube reactor: A tool for computer aided design of industrial reactors," *Comput. Chem. Eng.*, vol. 23, no. SUPPL. 1, pp. S371–S374, 1999.
- [84] L. Pirro, P. S. F. Mendes, B. Kemseke, B. D. Vandegheuchte, G. B. Marin, and J. W. Thybaut, "From catalyst to process: bridging the scales in modeling the OCM reaction," *Catal. Today*, vol. 365, no. March 2020, pp. 35–45, 2021.
- [85] R. Jain *et al.*, "Implementation of a Property Database and Thermodynamic Calculations in OpenModelica for Chemical Process Simulation," *Ind. Eng. Chem. Res.*, vol. 58, no. 18, pp. 7551–7560, 2019.
- [86] E. K. Vakkilainen, "Boiler Processes," *Steam Gener. from Biomass*, pp. 57–86, 2017.
- [87] A. Mahmoud and J. Sunarso, "A comparative study on targeting CO₂ emissions reduction from small-scale utility system," *IOP Conf. Ser. Mater. Sci. Eng.*, vol. 429, no. 1, 2018.
- [88] H. Lugo-Méndez, T. Lopez-Arenas, A. Torres-Aldaco, E. V. Torres-González, M. Sales-Cruz, and R. Lugo-Leyte, "Interstage pressures of a multistage compressor with intercooling," *Entropy*, vol. 23, no. 3, pp. 1–14, 2021.
- [89] L. B. Ma, J. X. Ren, F. Q. Li, L. J. Zhang, and M. Q. Li, "The discussion on cooling optimization of natural draft wet cooling tower," *IOP Conf. Ser. Earth Environ. Sci.*, vol. 199, no. 3, 2018.
- [90] S. Basu and A. K. Debnath, "Main Equipment," *Power Plant Instrum. Control Handb.*, no. 3, pp. 39–146, 2015.
- [91] M. Garcia, H. K. Knuutila, and S. Gu, "ASPEN PLUS simulation model for CO₂ removal with MEA: Validation of desorption model with experimental data," *J. Environ. Chem. Eng.*, vol. 5, no. 5, pp. 4693–4701, 2017.
- [92] F. A. Tobiesen, O. Juliussen, and H. F. Svendsen, "Experimental validation of a rigorous desorber model for CO₂ post-combustion capture," *Chem. Eng. Sci.*, vol. 63, no. 10, pp. 2641–2656, 2008.
- [93] F. Chu, L. Yang, X. Du, and Y. Yang, "CO₂ capture using MEA (monoethanolamine) aqueous solution in coal-fired power plants: Modeling and optimization of the absorbing columns," *Energy*, vol. 109, pp. 495–505, 2016.
- [94] T. A. A. II, "Tutorial 8: Rate-Based Distillation Models," New York: McGraw-Hill Education, 2018.
- [95] D. Pandey and M. K. Mondal, "Equilibrium CO₂ solubility in the aqueous mixture of MAE and AEEA: Experimental study and development of modified thermodynamic model," *Fluid Phase Equilib.*, vol. 522, p. 112766, 2020.
- [96] P. Bröder, F. Owrang, and H. F. Svendsen, "Pilot study-CO₂ capture into aqueous

- solutions of 3-methylaminopropylamine (MAPA) activated dimethyl-monoethanolamine (DMMEA),” *Int. J. Greenh. Gas Control*, vol. 11, pp. 98–109, 2012.
- [97] A. Muhammad and Y. GadelHak, “Simulation based improvement techniques for acid gases sweetening by chemical absorption: A review,” *Int. J. Greenh. Gas Control*, vol. 37, pp. 481–491, 2015.
- [98] M. A. Larijani, M. Bayat, and H. Afshin, “Simulation and performance improvement of cryogenic distillation column, using enhanced predictive Peng–Robinson equation of state,” *Fluid Phase Equilib.*, vol. 489, pp. 117–130, 2019.
- [99] X. Li, J. Li, and B. Yang, “Design and control of the cryogenic distillation process for purification of synthetic natural gas from methanation of coke oven gas,” *Ind. Eng. Chem. Res.*, vol. 53, no. 50, pp. 19583–19593, 2014.
- [100] M. B. Leo, A. Dutta, and S. Farooq, “Process synthesis and optimization of heat pump assisted distillation for ethylene-ethane separation,” *Ind. Eng. Chem. Res.*, vol. 57, no. 34, pp. 11747–11756, 2018.
- [101] U. Shafiq, A. M. Shariff, M. Babar, B. Azeem, A. Ali, and A. Bustam, “Study of dry ice formation during blowdown of CO₂-CH₄ from cryogenic distillation column,” *J. Loss Prev. Process Ind.*, vol. 64, no. February 2019, p. 104073, 2020.
- [102] H. Gurudath Nayak and G. Venkatarathnam, “Performance of an auto refrigerant cascade refrigerator operating in gas refrigerant supply (GRS) mode with nitrogen-hydrocarbon and argon-hydrocarbon refrigerants,” *Cryogenics (Guildf.)*, vol. 49, no. 7, pp. 350–359, 2009.
- [103] D. Popov *et al.*, “Cryogenic heat exchangers for process cooling and renewable energy storage: A review,” *Appl. Therm. Eng.*, vol. 153, no. February, pp. 275–290, 2019.
- [104] M. I. Abdul Mutalib and R. Smith, “Operation and control of dividing wall distillation columns: Part 1: Degrees of freedom and dynamic simulation,” *Chem. Eng. Res. Des.*, vol. 76, no. 3, pp. 308–318, 1998.
- [105] W. L. Luyben, “Comparison of a conventional two-column demethanizer/deethanizer configuration requiring refrigerated condensers with a nonconventional column/rectifier configuration,” *J. Chem. Technol. Biotechnol.*, vol. 91, no. 6, pp. 1688–1696, 2016.
- [106] V. C. Setiawan, I. U. A. Alifah, R. P. Anugraha, Juwari, and Renanto, “Comparison of Model Predictive Controller and Neural Network Controller on Nonconventional Distillation Demethanizer/Deethanizer Rectifier/Column System,” *IOP Conf. Ser. Mater. Sci. Eng.*, vol. 1053, no. 1, p. 012108, 2021.
- [107] X. Xu, F. Wang, M. Huang, J. Bai, and L. Li, “Security quantitative risk analysis of ethylene horizontal tanks of a petrochemical company,” *Procedia Eng.*, vol. 45, pp. 489–495, 2012.
- [108] R. Karimzadeh, H. R. Godini, and M. Ghashghaee, “Flowsheeting of steam cracking furnaces,” *Chem. Eng. Res. Des.*, vol. 87, no. 1, pp. 36–46, 2009.
- [109] T. Ren, M. Patel, and K. Blok, “Olefins from conventional and heavy feedstocks: Energy use in steam cracking and alternative processes,” *Energy*, vol. 31, no. 4, pp. 425–451, 2006.
- [110] C. Mardones and B. Flores, “Effectiveness of a CO₂ tax on industrial emissions,” *Energy Econ.*, vol. 71, pp. 370–382, 2018.
- [111] S. Yagi and D. Kunii, “Studies on effective thermal conductivities in packed beds,”

- AIChE J.*, vol. 3, no. 3, pp. 373–381, 1957.
- [112] T. Katona and T. Nagy, “Full scale wear test with different hose liners,” *KGK Kautschuk Gummi Kunststoffe*, vol. 67, no. 1–2, pp. 22–26, 2014.
- [113] A. Sen Gupta and G. Thodos, “Mass and heat transfer in the flow of fluids through fixed and fluidized beds of spherical particles,” *AIChE J.*, vol. 8, no. 5, pp. 608–610, 1962.
- [114] C.-H. Li; and B. . Finlayson, “Heat Transfer in Packed Beds-A Revolution,” *Chem. Eng. Sci.*, vol. 32, pp. 1055–1066, 1977.

Appendix

This section is intended to provide complementary material to support the covered topics in the main chapters of this document.

A. Nomenclature

List of abbreviations

ANOVA	Analysis of variance
CCD	Central composite design
DF	Degrees of freedom
DoE	Design of experiments
ER	Eley – Rideal formalism
GHG	Greenhouse gas
HEN	Heat exchanger network
HETP	Packed height per stage
MEA	Monoethanolamine
MS	Mean square
MTO	Methanol-to-olefin process
NSDF	Navier-Stokes-Darcy-Forchheimer equation
OCM	Oxidative coupling of methane
ODE	Ordinary differential equation
ODH-C ₂	Oxidative dehydrogenation of ethane (equivalent to <i>DIO-C₂</i> in Italian)
PDE	Partial differential equation
RSM	Response surface methodology
RSS	Objective function
TLE	Transfer line exchanger
USER2	User-defined operation model in ASPEN Plus

List of symbols

A^j	Pre-exponential factor, [$\text{mmol g}_{\text{cat}}^{-1} \text{s}^{-1}$] or [$\text{mmol g}_{\text{cat}}^{-1} \text{s}^{-1} \text{Pa}^{-1}$]
A_{tube}	Cross-sectional area of a reactor tube, [m^2]
a_s	Specific interface area, [m^{-1}]
Bi_w	Biot number, $(R_t h_w k_{\text{eff}}^{-1})$
b_i	Regression coefficients
$C_{\%}$	Carbon content, [%]
C_n	Molar concentration of the component n, [kmol m^{-3}]
C_{pi}	Heat capacity of the i phase, [$\text{kJ kg}^{-1} \text{K}^{-1}$]
D_f	Diffusivity of transferable component in the fluid, [$\text{m}^2 \text{s}^{-1}$] or [$\text{m}^2 \text{hr}^{-1}$]
D_{eff}	Effective diffusivity, [$\text{m}^2 \text{s}^{-1}$] or [$\text{m}^2 \text{hr}^{-1}$]
D_r	Radial diffusion coefficient, [$\text{m}^2 \text{hr}^{-1}$]
D_z	Axial diffusion coefficient, [$\text{m}^2 \text{hr}^{-1}$]
d_p	Particle diameter, [m]
d_t	Tube diameter, [m]
d_t/d_p	Tube diameter-to-particle diameter ratio, [-]
Ea^j	Activation energy, [kJ mol^{-1}]
F_i	Coded factors of the multiparametric model
$F_{j,n}$	Calculated molar flow rate of component n in the case j, [kmol hr^{-1}]
$\hat{F}_{j,n}$	Experimental molar Flow rate of component n in the case j, [kmol hr^{-1}]
F_n	Molar flow rate of the component n, [kmol m^{-3}]
g_z	Axial component of the gravity acceleration, [kg m s^{-2}]
h_g	Interfacial heat transfer coefficient, [$\text{kJ m}^{-2} \text{hr}^{-1} \text{K}^{-1}$]
h_w	Effective wall-transfer coefficient, [$\text{kJ m}^{-2} \text{hr}^{-1} \text{K}^{-1}$]
j_h	Heat transfer factor, $(h C_p^{-1} G^{-1})$
j_m	Mass transfer factor, $(h C_p^{-1} G^{-1} Pr^{2/3})$
K_n	Adsorption equilibrium coefficient for component n, [Pa^{-1}]
$k_{\text{eff},r}$	Effective radial thermal conductivity, [$\text{kJ m}^{-1} \text{hr}^{-1} \text{K}^{-1}$]
$k_{\text{eff},z}$	Effective axial thermal conductivity, [$\text{kJ m}^{-1} \text{hr}^{-1} \text{K}^{-1}$]
k_f	Fluid thermal conductivity, [$\text{W m}^{-1} \text{K}^{-1}$]
k_g	Interfacial mass transfer coefficient, [m hr^{-1}]
k_n	Kinetic constant, [s^{-1}] or [$\text{s}^{-1} \text{Pa}^{-1}$]
L_{re}	Reactor length, [m]
MF	Mass flux, [$\text{kg m}^{-2} \text{hr}^{-1}$]

\dot{m}_n	Mass flow rate of the component n or a mix of them, [kg hr ⁻¹]
NHV	Net heating value, [kJ kg ⁻¹]
N_T	Total concentration of active sites, [mmol g ⁻¹]
N_{tu}	Number of tubes in an industrial-scale multi-tubular catalytic reactor, [-]
Pe_r	Peclet number, $(G C_{pg} R_t k_{eff}^{-1})$
P_{op}	Reactor operating pressure, [bar]
Pr	Prandtl number, $(C_p \mu k_f^{-1})$
p_n	Partial pressure of the component n, [Pa]
p_z	Axial pressure component, [Pa]
\dot{Q}	Heat duty, [GJ hr ⁻¹] or [kW]
R_{cc}	Carbon ratio, [-]
Re_p	Particle Reynolds number, $(d_p \rho u_0 \mu^{-1})$
R_i	User-defined responses of the multiparametric model
R_t	Tube radius, [m]
r_{ss}	Dimensionless radial coordinate, [-]
r_n	Specific reaction rate, [mmol g _{cat} ⁻¹ hr ⁻¹]
Sc	Schmidt number, $(\mu \rho_f^{-1} D)$
SC_{2H_4}	Ethylene molar selectivity, [%]
T_0	Room temperature, [°C]
T_{bath}	Molten-salt bath temperature, [°C]
T_{FTF}	Theoretical flame temperature, [°C]
T_g	Gas phase temperature, [°C]
T_{hs}	Hot spot temperature, [°C]
T_{in}	Inlet temperature, [°C]
T_{out}	Outlet temperature, [°C]
T_s	Solid phase temperature, [°C]
T_{stack}	Stack temperature, [°C]
U	Overall heat transfer coefficient, [W m ⁻² K ⁻¹]
u_0	Superficial velocity [m ³ m ⁻² hr ⁻¹]
v_r	Interstitial radial velocity, [m hr ⁻¹]
v_z	Interstitial axial velocity, [m hr ⁻¹]
$Y_{C_2H_6}$	Molar fraction of ethane in the reactor feed mixture, [%]
Y_{O_2}	Molar fraction of oxygen in the reactor feed mixture, [%]
$X_{C_2H_6}$	Ethane molar conversion, [%]
X_{O_2}	Oxygen molar conversion, [%]

List of Greek symbols

β_i	Polynomial coefficients
ε_b	Packed-bed void fraction, [-]
$\bar{\varepsilon}_b$	Average bed void fraction, [-]
η_c	Carnot efficiency, [-]
$\Delta H_{298\text{ K}}^0$	Standard enthalpy of formation, [kJ mol ⁻¹]
ΔH_{abs}	Heat of absorption, [kJ mol ⁻¹]
ΔH_j	Reaction enthalpy of the reaction j, [kJ kmol ⁻¹]
ΔP	Pressure drop, [bar]
ΔT_{pinch}	Temperature difference at the pinch point, [°C] or [K]
θ_n	Active sites fraction occupied by component n, [-]
λ_n	Latent heat of the component n, [kJ kg ⁻¹]
$\nu_{n,j}$	Stoichiometric coefficient of the component n in the reaction j, [-]
μ	Fluid dynamic viscosity, [Pa s]
ρ_b	Packed-bed density, [kg m ⁻³]
ρ_f	Fluid mass density, [kg m ⁻³]
τ_b	Packed-bed tortuosity, [-]
ψ	Dimensionless pressure drop, [-]
ω_n	Weight factor corresponding to the component n, [-]

B. Effective transport parameters

The effective transport parameters included in the pseudo-heterogeneous reactor model have been calculated through a series of robust correlations reported in literature [111, 112, 113, 114]. These correlations have demonstrated to be suitable for packed-bed reactors as well as taking into account the effect of the velocity profile on the final value of the parameters. Equations present the used correlations:

$$j_m \varepsilon_b = 0.01 + \frac{0.863}{Re_p^{0.58} - 0.483} \rightarrow k_g = \frac{j_m Re_p Sc^{1/3} D_f}{d_p} \quad (B.1)$$

to calculate the inter-phase mass transfer coefficient [113], where j_m is the mass transfer factor, Sc is the Schmidt number and D_f is the diffusivity of transferable component in the fluid;

$$j_h \varepsilon_b = 0.0108 + \frac{0.929}{Re_p^{0.58} - 0.483} \rightarrow h_g = \frac{j_m Re_p Pr^{1/3} k_f}{d_p} \quad (B.2)$$

to calculate the inter-phase heat transfer coefficient [113], where j_h is the heat transfer factor and k_f is the thermal conductivity of the fluid;

$$D_z = \frac{\varepsilon_b D_f}{\tau_b} + 0.5 d_p u_0 \quad (B.3)$$

to calculate the axial mass diffusivity coefficient [112], where τ_b is the tortuosity of the packed-bed;

$$\frac{D_r}{\varepsilon_b} = \frac{D_{eff}}{\tau_b} + 0.1 d_p u_0 \quad (B.4)$$

to calculate the radial mass diffusivity coefficient [112];

$$\frac{k_{eff,r}}{k_f} = \frac{k_0}{k_f} + \left(0.062 - 0.09 \frac{d_t}{d_p} \right) Pr Re_p \quad (B.5)$$

to calculate the effective radial thermal conductivity [112], where the statistic thermal contributions ($k_0 k_f^{-1}$) were calculated from additional correlations reported elsewhere [111]; and,

$$\frac{h_w d_p}{k_f} = 0.17 Re_p^{0.79} \quad (\text{B.6})$$

to calculate the wall heat transfer coefficient [114].

C. Design of experiments: data acquisition

The data acquisition for performing a DoE study was provided by 44 simulations under different parametric configurations. A pseudo-heterogeneous ODH-C₂ reactor model was utilized to perform each simulation at a fixed dimensionless radial coordinate (i.e. $r_{dss} = 0.5$). On this matter, Table C.1 enlists the configuration of each simulation as well as their respective results. In alphabetic order, coded factors (F_i) correspond to T_{bath} , $Y_{C_2H_6}$, MF , Y_{O_2} , and d/d_p respectively; whereas in increasing order, responses (R_j) correspond to $X_{C_2H_6}$, X_{O_2} , $S_{C_2H_6}$, T_g and T_s respectively.

Table C.1 – Configuration of the 44 simulations suggested by JMP 15[®]. Results are shown for $L_{re} = 2.6$ m.

Simulation [#]	Coded factor					Responses				
	F _a	F _b	F _c	F _d	F _e	R _I	R _{II}	R _{III}	R _{IV}	R _V
1	0	0	0	0	+1	59.95	50.96	54.33	434.83	435.15
2	0	0	0	-1	0	67.92	81.35	52.79	431.06	431.35
3	+1	+1	+1	+1	+1	72.66	90.18	44.27	488.41	488.90
4	-1	+1	-1	-1	-1	39.03	62.38	63.39	381.86	382.46
5	-1	-1	-1	+1	+1	58.61	14.13	60.43	381.54	381.66
6	-1	+1	+1	+1	+1	1.22	18.66	65.37	382.28	382.40
7	+1	-1	-1	+1	+1	99.56	43.32	15.15	484.41	484.76
8	-1	-1	-1	-1	+1	54.70	22.76	61.20	381.32	381.42
9	-1	-1	+1	-1	-1	7.15	10.54	64.88	380.76	380.99
10	+1	+1	-1	-1	-1	49.84	100.00	49.59	480.00	480.00
11	+1	-1	+1	+1	+1	84.69	27.69	40.37	485.87	486.22
12	+1	-1	-1	-1	-1	99.17	71.62	20.38	483.20	484.33
13	+1	-1	+1	+1	-1	7.98	29.35	38.83	485.62	487.31
14	0	0	0	0	0	73.31	65.42	51.22	431.44	431.84
15	-1	-1	+1	+1	-1	28.91	6.44	64.69	380.85	381.10
16	-1	0	0	0	0	42.86	31.40	62.94	380.62	380.79
17	0	0	0	0	0	73.31	65.42	51.22	431.44	431.84
18	0	-1	0	0	0	84.59	32.30	46.66	431.00	431.27
19	0	0	-1	0	0	88.31	87.22	44.24	430.93	431.34
20	-1	+1	+1	+1	-1	22.95	20.26	65.17	382.11	382.73
21	+1	0	0	0	0	90.50	98.56	36.80	480.92	481.18
22	+1	+1	-1	+1	+1	76.02	100.00	39.92	480.00	480.00
23	0	0	0	0	-1	1.67	52.57	54.15	434.23	435.58
24	-1	-1	+1	+1	+1	26.30	5.83	64.99	380.88	380.93
25	-1	+1	-1	+1	-1	4.95	41.71	62.54	382.57	383.40

26	-1	+1	+1	-1	-1	20.63	31.72	65.43	381.76	382.27
27	+1	+1	-1	-1	+1	9.97	100.00	49.84	480.00	480.00
28	0	0	0	+1	0	6.49	54.53	50.13	431.68	432.15
29	-1	-1	-1	-1	-1	6.81	23.78	60.86	381.15	381.52
30	+1	-1	-1	-1	+1	8.66	70.45	21.45	484.28	484.63
31	0	0	+1	0	0	61.38	52.17	54.34	431.77	432.12
32	-1	-1	-1	+1	-1	60.85	14.75	60.04	381.35	381.78
33	-1	+1	+1	-1	+1	19.11	29.27	65.62	381.92	382.02
34	+1	+1	+1	-1	-1	50.19	100.00	50.24	480.00	480.00
35	+1	-1	+1	-1	-1	3.52	47.08	41.51	484.73	486.15
36	+1	+1	+1	+1	-1	4.43	92.50	44.17	487.07	489.15
37	+1	+1	+1	-1	+1	50.05	100.00	50.06	480.04	480.04
38	+1	+1	-1	+1	-1	76.32	100.00	40.05	480.00	480.00
39	0	+1	0	0	0	63.23	86.64	53.86	431.28	431.63
40	+1	-1	-1	+1	-1	99.80	43.91	13.99	483.20	484.31
41	-1	+1	-1	-1	+1	37.93	60.39	63.60	382.24	382.41
42	-1	+1	-1	+1	+1	43.70	50.96	62.73	383.02	383.26
43	-1	-1	+1	-1	+1	24.72	81.35	65.17	380.80	380.84
44	+1	-1	+1	-1	+1	79.98	90.18	42.79	484.94	485.24

D. Analysis of variance (ANOVA)

The governing multiparametric equations of the proposed model are constructed based on the effects of independent variables on the pre-selected responses. In this work, a robust regression model is developed by utilizing response surface methodology (RSM), which is considered to be one of the best DoE methods. Nonetheless, the importance and statistical relevance of control parameters must be well-proven [72].

In this sense, the analysis of variance (ANOVA) is essential to test the significance and adequacy of the model as it classifies the variability in two categories: observed and calculated values. A meaningful model requires the experimental errors to be normally and independently distributed with mean zero and variance σ^2 .

The test of significance determines if there is sufficient evidence to reject the null hypothesis regarding regression coefficients. In other words, it proves the existence of a relationship between responses and independent variables. Mathematically, the null hypothesis is represented by Equation (D.1),

$$H_0 \rightarrow \beta_1 = \beta_2 = \dots = \beta_k = 0 \quad (D.7)$$

where rejecting H_0 indicates that at least one independent variable (x_i) is significant for the model. The verification of the null hypothesis is carried out through the F -test, where if F -ratio (i.e. calculated value) exceeds the tabulated value under a certain interval of confidence $(1-\alpha)$, the null hypothesis is rejected. The F -statistic is calculated through Equation (D.2).

$$F = \frac{SSR}{SSE} \frac{(n - df - 1)}{df} \quad (D.8)$$

where, n is the number of test, df is the degree of freedom, SSE is the sum of squares due to the model error and SSR is the sum of squares due to the model residuals. Note that the total sum of squares (SST) is given by each contribution; i.e. $SST = SSR + SSE$.

The coefficient of multiple determination (*R-squared*) is also a commonly used parameter to quantify the adequacy of regression models. For multiparametric models, *R-squared adj.* provides more reliable information for describing the variability by the independent variables. Both are calculated as shown in Equation (D.3).

$$R^2 = \frac{SSR}{SST}; R_{adj}^2 = 1 - \frac{n - 1}{n - p} (1 - R^2) \quad (D.9)$$

where p is the number of parameters included in the regression model. JMP 15[®] has been the informatic tool utilized to perform the analysis of variance for each multiparametric equation of the model developed in this work. Further details regarding the ANOVA of each model response have been enlisted in Table D.1-4.

Table D.1 – Analysis of variance (ANOVA) for the construction of the regression model for ethane conversion. The study has been carried out at $L_{re} = 2.6$ m.

Source		Estimates	SE	Sum of Squares	DF	MS	t-ratio	Prob > t *	F-Value	Prob > F*
Factor	Denomination									
Intercept	b_0	72.99	1.29	-	-	-	56.50	<.0001	-	-
T_{bath}	F_a	20.38	0.64	14121.8	1	14121.9	31.89	<.0001	1016.86	<0.0001
$Y_{C_2H_6}$	F_b	-10.11	0.64	3475.5	1	3475.6	-15.82	<.0001	250.26	<0.0001
MF	F_c	-8.77	0.64	2617.7	1	2617.8	-13.73	<.0001	188.50	<0.0001
Y_{O_2}	F_d	4.30	0.64	627.3	1	627.3	6.72	<.0001	45.17	<0.0001
d_t/d_p	F_e	-0.78	0.64	20.4	1	20.4	-1.21	0.2374	1.47	0.2374
T_{bath}^2	F_a^2	-6.23	2.38	95.5	1	95.5	-2.62	0.0152	6.88	0.0152
$Y_{C_2H_6}^2$	F_b^2	1.00	2.38	2.4	1	2.4	0.42	0.6785	0.18	0.6785
MF^2	F_c^2	1.93	2.38	9.1	1	9.2	0.81	0.4242	0.66	0.4242
$Y_{O_2}^2$	F_d^2	-0.70	2.38	1.2	1	1.2	-0.30	0.77	0.09	0.77
d_t/d_p^2	F_e^2	-12.10	2.38	360.3	1	360.3	-5.09	<.0001	25.94	<0.0001
$T_{bath} \cdot Y_{C_2H_6}$	$F_a F_b$	-4.54	0.66	660.1	1	660.2	-6.89	<.0001	47.54	<0.0001
$T_{bath} \cdot MF$	$F_a F_c$	4.37	0.66	610.3	1	610.3	6.63	<.0001	43.95	<0.0001
$T_{bath} \cdot Y_{O_2}$	$F_a F_d$	2.58	0.66	213.5	1	213.5	3.92	0.0007	15.37	0.0007
$T_{bath} \cdot d_t/d_p$	$F_a F_e$	0.17	0.66	0.893	1	0.9	0.25	0.8021	0.06	0.8021
$Y_{C_2H_6} \cdot MF$	$F_b F_c$	3.08	0.66	302.7	1	302.7	4.67	0.0001	21.80	0.0001
$Y_{C_2H_6} \cdot Y_{O_2}$	$F_b F_d$	2.92	0.66	273.3	1	273.3	4.44	0.0002	19.68	0.0002
$Y_{C_2H_6} \cdot d_t/d_p$	$F_b F_e$	0.29	0.66	2.6	1	2.7	0.44	0.6636	0.19	0.6636
$MF \cdot Y_{O_2}$	$F_c F_d$	-0.31	0.66	3.0	1	3.1	-0.47	0.6436	0.22	0.6436
$MF \cdot d_t/d_p$	$F_c F_e$	-0.29	0.66	2.7	1	2.8	-0.45	0.6598	0.20	0.6598
$Y_{O_2} \cdot d_t/d_p$	$F_d F_e$	-0.07	0.66	0.1	1	0.2	-0.10	0.9174	0.01	0.9174

* Prob > F stands for the probability of observing F value which is greater than F ratio. Prob > F of 0.05 is usually the cut off point to determine the statistical significance. Analogously, the same concept applies for the t-test.

Table D.2 – Analysis of variance (ANOVA) for the construction of the regression model for oxygen conversion. The study has been carried out at $L_{re} = 2.6$ m.

Source		Estimates	SE	Sum of Squares	DF	MS	t-ratio	Prob > t *	F-Value	Prob > F*
Factor	Denomination									
Intercept	b_0	65.99	2.88	-	-	-	22.87	<.0001	-	-
T_{bath}	F_a	23.97	1.43	19541.4	1	19541.4	16.80	<.0001	282.18	<.0001
$Y_{C_2H_6}$	F_b	19.31	1.43	12672.9	1	12672.9	13.53	<.0001	183.00	<.0001
MF	F_c	-8.28	1.43	2328.5	1	2328.5	-5.80	<.0001	33.62	<.0001
Y_{O_2}	F_d	-6.52	1.43	1443.9	1	1443.9	-4.57	0.0001	20.85	0.0001
d_t/d_p	F_e	-0.61	1.43	12.6	1	12.6	-0.43	0.6734	0.18	0.6734
T_{bath}^2	F_a^2	-1.15	5.31	3.3	1	3.3	-0.22	0.83	0.05	0.83
$Y_{C_2H_6}^2$	F_b^2	-6.66	5.31	109.2	1	109.2	-1.26	0.2219	1.58	0.2219
MF^2	F_c^2	3.56	5.31	31.1	1	31.1	0.67	0.5094	0.45	0.5094
$Y_{O_2}^2$	F_d^2	1.80	5.31	8.0	1	8.0	0.34	0.737	0.12	0.737
d_t/d_p^2	F_e^2	-14.37	5.31	507.9	1	507.9	-2.71	0.0125	7.33	0.0125
$T_{bath} \cdot Y_{C_2H_6}$	$F_a F_b$	6.50	1.47	1352.6	1	1352.6	4.42	0.0002	19.53	0.0002
$T_{bath} \cdot MF$	$F_a F_c$	1.56	1.47	77.4	1	77.4	1.06	0.3014	1.12	0.3014
$T_{bath} \cdot Y_{O_2}$	$F_a F_d$	-0.57	1.47	10.5	1	10.5	-0.39	0.7004	0.15	0.7004
$T_{bath} \cdot d_t/d_p$	$F_a F_e$	0.06	1.47	0.1	1	0.1	0.04	0.9652	0.00	0.9652
$Y_{C_2H_6} \cdot MF$	$F_b F_c$	0.05	1.47	0.1	1	0.1	0.03	0.974	0.00	0.974
$Y_{C_2H_6} \cdot Y_{O_2}$	$F_b F_d$	1.08	1.47	37.4	1	37.4	0.74	0.4696	0.54	0.4696
$Y_{C_2H_6} \cdot d_t/d_p$	$F_b F_e$	-0.01	1.47	0.0	1	0.0	-0.01	0.9959	0.00	0.9959
$MF \cdot Y_{O_2}$	$F_c F_d$	0.99	1.47	31.3	1	31.3	0.67	0.5083	0.45	0.5083
$MF \cdot d_t/d_p$	$F_c F_e$	-0.18	1.47	1.0	1	1.0	-0.12	0.9053	0.01	0.9053
$Y_{O_2} \cdot d_t/d_p$	$F_d F_e$	0.05	1.47	0.1	1	0.1	0.04	0.9724	0.00	0.9724

* Prob > F stands for the probability of observing F value which is greater than F ratio. Prob > F of 0.05 is usually the cut off point to determine the statistical significance. Analogously, the same concept applies for the t-test.

Table D.3 – Analysis of variance (ANOVA) for the construction of the regression model for ethylene selectivity. The study has been carried out at $L_{re} = 2.6$ m.

Source		Estimates	SE	Sum of Squares	DF	MS	t-ratio	Prob > t *	F-Value	Prob > F*
Factor	Denomination									
Intercept	b_0	51.16	1.00	-	-	-	51.01	<.0001	-	-
T_{bath}	F_a	-12.93	0.50	5684.2	1	5684.2	-26.06	<.0001	679.28	<.0001
$Y_{C_2H_6}$	F_b	4.48	0.50	683.6	1	683.6	9.04	<.0001	81.69	<.0001
MF	F_c	4.07	0.50	564.5	1	564.5	8.21	<.0001	67.46	<.0001
Y_{O_2}	F_d	-1.65	0.50	92.0	1	92.0	-3.32	0.003	11.00	0.003
d_t/d_p	F_e	0.22	0.50	1.6	1	1.6	0.44	0.6661	0.19	0.6661
T_{bath}^2	F_a^2	-1.27	1.84	4.0	1	4.0	-0.69	0.4978	0.47	0.4978
$Y_{C_2H_6}^2$	F_b^2	-0.88	1.84	1.9	1	1.9	-0.48	0.6383	0.23	0.6383
MF^2	F_c^2	-1.85	1.84	8.4	1	8.4	-1	0.3266	1.00	0.3266
$Y_{O_2}^2$	F_d^2	0.32	1.84	0.3	1	0.3	0.18	0.8622	0.03	0.8622
d_t/d_p^2	F_e^2	3.10	1.84	23.7	1	23.7	1.68	0.106	2.83	0.106
$T_{bath} \cdot Y_{C_2H_6}$	$F_a F_b$	3.81	0.51	465.6	1	465.6	7.46	<.0001	55.64	<.0001
$T_{bath} \cdot MF$	$F_a F_c$	2.35	0.51	177.4	1	177.4	4.6	0.0001	21.20	0.0001
$T_{bath} \cdot Y_{O_2}$	$F_a F_d$	-1.40	0.51	63.1	1	63.1	-2.75	0.0115	7.54	0.0115
$T_{bath} \cdot d_t/d_p$	$F_a F_e$	0.09	0.51	0.3	1	0.3	0.18	0.8564	0.03	0.8564
$Y_{C_2H_6} \cdot MF$	$F_b F_c$	-2.85	0.51	259.3	1	259.3	-5.57	<.0001	30.98	<.0001
$Y_{C_2H_6} \cdot Y_{O_2}$	$F_b F_d$	-0.43	0.51	6.0	1	6.0	-0.84	0.4077	0.71	0.4077
$Y_{C_2H_6} \cdot d_t/d_p$	$F_b F_e$	-0.17	0.51	1.0	1	1.0	-0.34	0.7386	0.11	0.7386
$MF \cdot Y_{O_2}$	$F_c F_d$	0.55	0.51	9.7	1	9.7	1.08	0.2925	1.16	0.2925
$MF \cdot d_t/d_p$	$F_c F_e$	0.01	0.51	0.0	1	0.0	0.01	0.9887	0.00	0.9887
$Y_{O_2} \cdot d_t/d_p$	$F_d F_e$	0.01	0.51	0.0	1	0.0	0.02	0.9867	0.00	0.9867

* Prob > F stands for the probability of observing F value which is greater than F ratio. Prob > F of 0.05 is usually the cut off point to determine the statistical significance. Analogously, the same concept applies for the t-test.

Table D.4 – Analysis of variance (ANOVA) for the construction of the regression model for gas-phase temperature. The study has been carried out at $L_{re} = 2.6$ m.

Source		Estimates	SE	Sum of Squares	DF	MS	t-ratio	Prob > t *	F-Value	Prob > F*
Factor	Denomination									
Intercept	b_0	431.62	0.41	-	-	-	1058.45	<.0001	-	-
T_{bath}	F_a	50.76	0.20	87587.0	1	87587.0	251.59	<.0001	63299.59	<.0001
$Y_{C_2H_6}$	F_b	-0.33	0.20	3.8	1	3.8	-1.66	0.1113	2.74	0.1113
MF	F_c	0.55	0.20	10.3	1	10.3	2.73	0.0119	7.46	0.0119
Y_{O_2}	F_d	0.61	0.20	12.7	1	12.7	3.03	0.0059	9.18	0.0059
d_t/d_p	F_e	0.19	0.20	1.2	1	1.2	0.92	0.3677	0.84	0.3677
T_{bath}^2	F_a^2	-0.89	0.75	2.0	1	2.0	-1.19	0.2451	1.42	0.2451
$Y_{C_2H_6}^2$	F_b^2	-0.53	0.75	0.7	1	0.7	-0.71	0.4862	0.50	0.4862
MF^2	F_c^2	-0.32	0.75	0.2	1	0.2	-0.42	0.6761	0.18	0.6761
$Y_{O_2}^2$	F_d^2	-0.30	0.75	0.2	1	0.2	-0.4	0.6951	0.16	0.6951
d_t/d_p^2	F_e^2	2.86	0.75	20.2	1	20.2	3.82	0.0009	14.59	0.0009
$T_{bath} \cdot Y_{C_2H_6}$	$F_a F_b$	-0.93	0.21	27.8	1	27.8	-4.49	0.0002	20.12	0.0002
$T_{bath} \cdot MF$	$F_a F_c$	0.79	0.21	20.0	1	20.0	3.8	0.0009	14.43	0.0009
$T_{bath} \cdot Y_{O_2}$	$F_a F_d$	0.46	0.21	6.7	1	6.7	2.19	0.0387	4.81	0.0387
$T_{bath} \cdot d_t/d_p$	$F_a F_e$	0.08	0.21	0.2	1	0.2	0.38	0.7081	0.14	0.7081
$Y_{C_2H_6} \cdot MF$	$F_b F_c$	0.31	0.21	3.0	1	3.0	1.48	0.1514	2.20	0.1514
$Y_{C_2H_6} \cdot Y_{O_2}$	$F_b F_d$	0.47	0.21	7.1	1	7.1	2.27	0.0328	5.16	0.0328
$Y_{C_2H_6} \cdot d_t/d_p$	$F_b F_e$	-0.02	0.21	0.0	1	0.0	-0.1	0.9242	0.01	0.9242
$MF \cdot Y_{O_2}$	$F_c F_d$	0.50	0.21	8.1	1	8.1	2.42	0.0238	5.86	0.0238
$MF \cdot d_t/d_p$	$F_c F_e$	-0.04	0.21	0.1	1	0.1	-0.19	0.8504	0.04	0.8504
$Y_{O_2} \cdot d_t/d_p$	$F_d F_e$	0.05	0.21	0.1	1	0.1	0.24	0.8161	0.06	0.8161

* Prob > F stands for the probability of observing F value which is greater than F ratio. Prob > F of 0.05 is usually the cut off point to determine the statistical significance. Analogously, the same concept applies for the t-test.

E. Process simulation in ASPEN Plus®.

Figure E.1 illustrates the simulation environment of the overall process for ethylene production by the ODH-C₂. Note that each section has been simulated in different “Hierarchy” blocks in order to specify a suitable thermodynamic package for each subprocess. The reactor block may require more than one unit depending on the stipulated ethylene yield. In this simulation framework, the USER2 block accounts for several reactors working in parallel according to the required number of tubes, i.e. 2×10^4 per reactor unit.

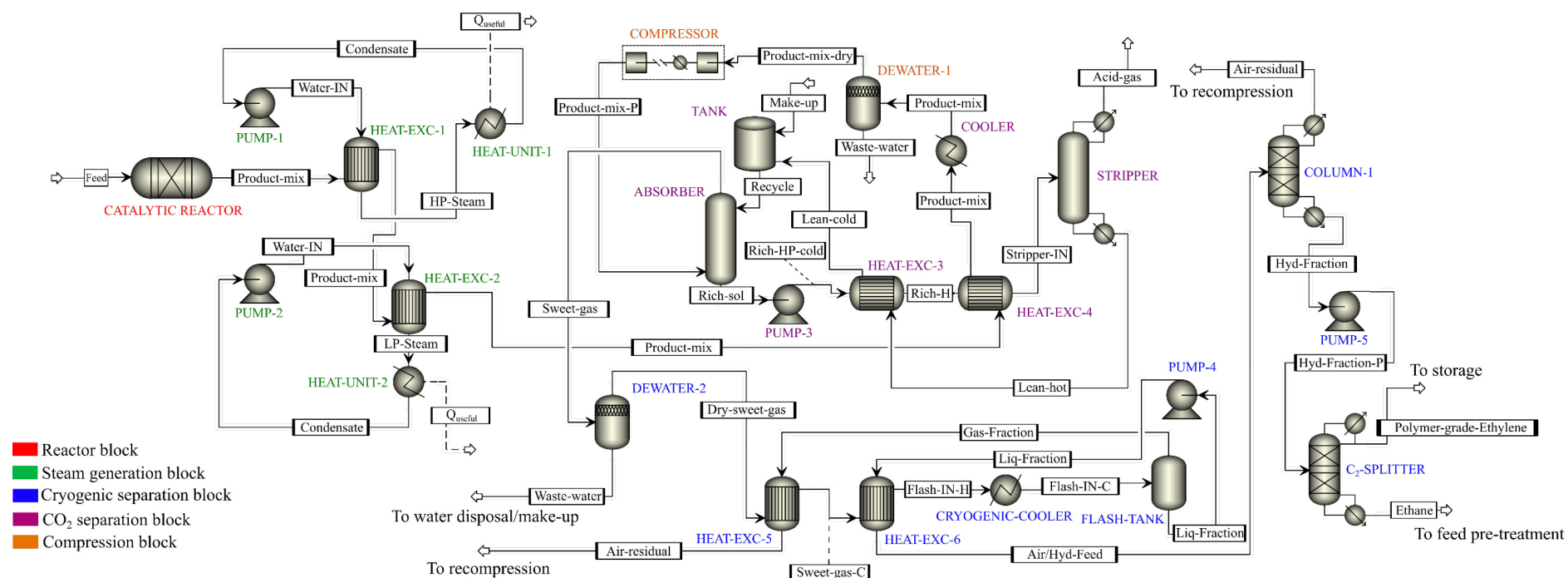


Figure E.1 – Block flow diagram of the overall process for ethylene production by the ODH-C₂ using NiO-SnO₂ as catalyst.

Acknowledgements

These few lines are dedicated to the people that, from different perspectives, have contributed to this priceless personal achievement.

First, I would like to thank my coach, Carlos Alvarado Camacho, and my supervisor, Jeroen Poissonnier. Thank you very much for your constant guidance and support throughout the development of this thesis. Thanks for the countless and constructive catch-up meetings, for being always available and for allowing me to learn on daily bases during this period.

I would like to express my most sincere gratitude to Professor Joris Thybaut, who was my first contact at Ghent University. Thank you for letting me be part of an unique academic experience in this prestigious institution.

Special thanks to Professor Stefania Specchia, who has been my academic advisor and supervisor at Politecnico di Torino. Thank you for being always available and for every piece of advise given during my double degree program.

I could not finish without thanking the main pilar in my life, my family. To my parents and sister, who have been always there to support me and guide me no matter how optimistic or challenging the scenario was. By looking back, I am totally sure that all of this would not have been possible without you. Words will never be enough to express my gratitude.